Scalable Synthesis of Less-Toxic Colloidal Copper Indium Sulfide Quantum Dots and Application to Optoelectronic Device Architectures

by

Yaxin Zheng

A thesis
presented to the University of Waterloo
in fulfillment of the
thesis requirement for the degree of
Doctor of Philosophy
in
Electrical and Computer Engineering (Nano)

Waterloo, Ontario, Canada, 2021

Examining Committee Membership

The following served on the Examining Committee for this thesis. The decision of the Examining Committee is by majority vote.

External Examiner: Paul Charpentier
Professor, Western University

Supervisor: Siva Sivoththaman
Professor, University of Waterloo

Internal Member: William Wong
Professor, University of Waterloo

Internal Member: Zbigniew Wasilewski
Professor, University of Waterloo

Internal-External Member: Yuning Li
Professor, University of Waterloo

Author's Declaration

I hereby declare that I am the sole author of this thesis. This is a true copy of the thesis, including any required final revisions, as accepted by my examiners.

I understand that my thesis may be made electronically available to the public.

Abstract

The consequences of mankind's extravagant energy consumption has loomed over humanity for much of the twenty-first century. As societies realize the increasing urgency of transitioning to renewable energy sources, solar energy has been progressively adopted worldwide. Like most electronic devices, solar cells, photodetectors, and other commercial light sensing and management devices are primarily based on silicon. Due to disadvantageous intrinsic traits, silicon is inefficient at optoelectronic applications. Significant efforts have been exerted towards the discovery and implementation of alternative semiconductor materials. However, due to its abundance and compatibility with established manufacturing processes, silicon has proved difficult to dethrone.

In the last two decades, application of nanomaterials have become a particularly notable topic among device and electrical engineers. For solar cells, the utility of nanomaterials occupy an area known as "Third Generation" solar cells, which is defined by the use of novel architectures and materials to overcome the intrinsic limits of bulk semiconductor materials. Among nanomaterials applied for light management devices, quantum dots (QDs) are one of the most significant areas of research. High-performance photovoltaic (PV), photodetector, light emitting, and other light management devices have been achieved from QDs, which have now graduated from the realm of research devices to commercial application. Early successes were primarily achieved using Cd- and Pb-based QDs. Still to this day, the best performance benchmarks in photovoltaics and photodetectors have been set by PbS QDs. However, the known toxicity of these elements poses significant controversy in their adaptation, precluding their commercialization.

This thesis explores the application of less-toxic copper indium sulfide (CIS) QDs for photovoltaic and photodetector device architectures. Although less investigated than binary QD materials, cupric chalcopyrites display significant optical and structural properties that are flexibly tuned for a variety of applications. In this work, a low-temperature, one-pot, non-injection, temperature-ramped method is presented for high-throughput synthesis of CIS QDs. Exploration of cationic stoichiometry and temperature conditions yielded a comprehensive model to explain the properties and behaviours displayed by the QDs during synthesis and application. CIS/ZnS core/shell QDs were developed from these QDs, resulting in increased tunability, higher stability, and enhanced emission intensity and lifetime. This synthesis procedure reliably yielded QDs tunable from visible to near-infrared (544-800 nm), with photoluminescence quantum yield (PLQY) of up to 20% for core/shell QDs.

Furthermore, a synthesis process is presented for zinc copper indium sulfide (ZCIS) QDs, a more stable quaternary variant of CIS QDs incorporating Zn passivation within the core. As the Type I core/shell configuration formed by the CIS/ZnS QDs poses issues with carrier confinement and transport, it cannot be utilized for device purposes. Inspired by the benefits of zinc incorporation for core CIS QD stability, zinc alloying was devised as a method to leverage the benefits of zinc incorporation. A similar one-pot, low-temperature ZCIS synthesis procedure was developed, which reliably produced almost 1 g of intensely emissive ZCIS QDs. Cationic stoichiometry and overcoating were investigated to elucidate their effect on the QD lattice and subsequent parameters.

A ligand-exchange process is presented, allowing the functionalization of the as-synthesized, solution-dispersed colloidal QDs for compatibility with film formation. Long, non-polar 1-dodecanethiol (DDT) ligands, which are critical to the scalable one-pot synthesis, were exchanged for short, polar 3-mercaptopropionic acid (MPA) ligands, which allowed the formation of uniform QD solids onto ZnO surfaces. This ligand functionalization is integral to the utility of the QDs in the advantageous metal oxide/QD heterojunction device structure. QD film formation methods were further explored to determine film formation parameters and practices that would best aid in the production of uniform, regular CIS QD solids of sufficient thickness. Sputtered and sol-gel ZnO films were also investigated for enhancement of the ZnO/CIS QD interface. ZnO/CIS QD diodes were fabricated to evaluate the results of the film development processes. Devices with diodic I-V behaviour and response to illumination were achieved.

The key to silicon's persistent presence in the optoelectronics industry is the fabrication processes and techniques utilized in device production, which have evolved to be inseparable from its use. Although many novel materials and architectures have been developed for photovoltaic and photodetector devices, their inability to depose silicon stems from their incompatibility with existing manufacturing practices. For nanomaterials and QDs, the nonchalant manner in which they are applied to device fabrication in research and prototyping environments draws doubt of their performance, leading to reluctance for commercial acceptance. Therefore, the establishment of repeatable, reliable, standard fabrication procedures for nanomaterial devices is a significant tenet of this thesis work. Through photolithography and shadow mask patterning, small, regular, 5 μm-diameter device areas were defined onto standard 2.2 × 2.2 cm^2 substrates. All steps of the fabrication process were designed to be compatible with existing industry fabrication technologies, paving a smoother transition to commercial production. This work yielded small-area ZnO/CIS QD heterojunction devices on standard substrates, with strong response to illumination. The processes and technologies developed in this work are applicable in the investigation and formation of a variety of nanomaterials-based electronic and optoelectronic devices, amenable to the realization of commercially feasible nanodevices.

Acknowledgements

First things first, I would like to thank my supervisor, Dr. Siva Sivoththaman. I am grateful for his guidance and trust, and I have thrived as a researcher under his mentorship. It has been an absolute privilege to have you as my supervisor, and I could not have wished for a better PI. Thank you for everything. I would also like to thank Dr. William Wong for his helpful advice and support throughout my academic career, from his time as my professor during my undergrad, to his role as a member of my dissertation committee. Furthermore, I would like to thank the other members of my dissertation committee: Dr. Zbig Wasilewski, Dr. Yuning Li, and Dr. Paul Charpentier for their constructive suggestions and guidance, which have served to improve the quality of this work.

Next, I would like to acknowledge the members of Center for Advanced Photovoltaics and Display Systems (CAPDS), who created a collaborative and supportive environment for my research. I would especially like to thank Dr. Bahareh Sadeghimakki for her keen insight, wonderful advice, and supportive guidance throughout this journey. Bahareh, you are a brilliant mentor, and you have helped me become the researcher I am today. I would like to give a special thank you to Dr. Roohen S. Tarighat, for his ingenuity, from which my (and everyone's!) research has greatly benefited. Big thanks to my officemates Dr. Hrilina Ghosh, Dr. Zhen Gao, and Fangyan Sun; I am so grateful for your friendship, and for the conversations, laughter, and letting me into the office when I locked myself out. I would also like to acknowledge Kristin Buttenhoff, Jacob Brunning, Evan Piano, and Yizun Wang for their excellent work in QD development, which has aided in the completion of thesis. Finally, thank you to my colleagues Wayne Wang, Dr. Nasim Bakhshizadeh, Jon Atkinson, Jun Wang, Dr. Navid Jahed, Dr. Maziar Moradi, Joseph Street, and many others, for their support during this degree.

Thank you to my wonderful friends, especially Lux, Patsy, Adam, Annia, Tasfin, Sabrina, Hummer, Elizabeth, Lili, Takin, and PT, who have provided me with valuable encouragement, sustenance, and technical assistance throughout this journey. This would have been much harder without you.

I would like to recognize my father, Shize Zheng and my mother, Dr. Yonghua Cheng. Dad, thank you for the countless sacrifices you have made that have allowed me to pursue my interests and reach where I am today. Mom, your brilliance as an engineer and a researcher have always driven me to better myself, and will continue to inspire me as I move onto the next stage. I could not have done this without you.

Last but not least, thank you to my Lord and Saviour, Jesus Christ, for giving me the opportunity to go on this amazing adventure, and the strength to finish it.

Table of Contents

List of Tables

List of Figures

List of Key Abbreviations

AFM	Atomic Force Microscopy
CIS	Copper Indium Sulfide
CQD	Colloidal Quantum Dot
DAP	Donor-Acceptor Pair
DDT	1-Dodecanethiol
DMD	Digital Micromirror Device
DMEM	Dulbecco's Minimum Essential Medium
DSSC	Dye Sensitized Solar Cell
EDS	Energy-Dispersive X-Ray Spectroscopy
EQE	External Quantum Efficiency
ETL	Electron Transport Layer
FIB	Focused Ion Beam
FTIR	Fourier Transform Infrared Spectroscopy
HRTEM	High Resolution Transmission Electron Microscopy
HTL	Hole Transport Layer
ICP-MS	Inductively Coupled Plasma Mass Spectroscopy
$\mathbf{In(Ac)_3}$	Indium Acetate
IQE	Internal Quantum Efficiency
IR	Infrared
ITO	Indium Tin Oxide
LED	Light-Emitting Diode
MEG	Multi-Exciton Generation
MLA	Maskless Aligner
MPA	3-Mercaptopropionic Acid
NC	Nanocrystal
NIR	Near-Infrared
NP	Nanoparticle
OA	Oleic Acid
ODA	Octadecylamine
ODE	1-Octadecene
QD	Quantum Dot
QDPV	Quantum Dot Photovoltaics
QDSC	Quantum Dot Solar Cell
QDSSC	Quantum Dot-Sensitized Solar Cell
QE	Quantum Efficiency

PEB	Post Exposure Bake
PL	Photoluminescence
PLQY	Photoluminescence Quantum Yield
PV	Photovoltaic
RMS	Root Mean Square
RPM	Rotations Per Minute
SEM	Scanning Electron Microscope
SPR	Surface Plasmon Resonance
TCSPC	Time-Correlated Single-Photon Counting
TEM	Transmission Electron Microscopy
TOP	Trioctylphosphine
UV	Ultraviolet
UV-Vis	Ultraviolet-Visible Spectroscopy
VLSI	Very Large-Scale Integration
XPS	X-ray Photoelectron Spectroscopy
ZCIS	Zinc Copper Indium Sulfide
$\mathbf{Zn(SA)_2}$	Zinc Stearate

Chapter 1

Introduction and Motivations

1.1 Evolution of Photovoltaics and Photodetectors

From the advent of the industrial revolution, the devastation that mankind has unleashed upon the planet has necessitated the harnessing of renewable energy sources. Anxiety over the inevitable consequences of our hubris has escalated in recent years, and sustainability has become a central focus in technological research and development. Among renewable energy sources, solar energy has long reigned as the centerpiece of development. Due to its abundance, cleanliness, and accessibility, harvesting solar energy has been a widely investigated topic across the globe. Significantly, solar energy is environmentally benign, as it is not volatile, does not have any fuel risk or constraints, and does not produce pollutants during operation [23], making it a less controversial source of energy than its more volatile contemporaries.

The first generation of photovoltaic (PV) devices were made from inorganic, crystalline bulk semiconductor materials. These bulk cells displayed advantageously high carrier mobility, good light absorption, and high thermal and light stability. Although crystalline silicon continues to dominate the photovoltaics market, its intrinsic limitations, including its fixed, indirect bandgap and limited internal quantum efficiency [24], hinder its performance in optoelectronic applications. As first generation bulk crystalline PV devices fell out of fashion, cheaper thin film "second generation" solar cells emerged. Their lower prices and mass-production possibilities lead to their status as attractive alternatives to bulk semiconductors. However, due to the significant losses resulting from their intrinsic material compositions [25], neither first nor second-generation solar cells can exceed the Shockley-Queisser efficiency limit of 43% [26]. Thus, solar researchers moved onto third generation photovoltaics, defined by the integration of innovative architectures and novel quantum nanostructures which are not confined by the inhibitions of bulk materials. The development of nanomaterials-based solar cells became particularly attractive, due to their unique photon conversion and absorption properties, which provide the possibility of surpassing Shockley-Queisser limits.

Among nanomaterials, semiconducting quantum dots (QDs) are of particular interest for photovoltaic, photodetector, and light-emitting devices due to their advantageous optical and electrical properties [3][18][27][28][29][30][31][32][33][34][35]. Quantum dots boast favourable attributes such as opto-electrical tunability [32][34][35][36][37][38][39][40][41], low-cost, high-volume production [31], good photostability [42], high absorption coefficients [38][43], and ability to improve photovoltaic efficiency via multi-exciton generation [36][44][45][46]. Development of colloidal quantum dots (CQDs) has piqued particular interest among the scientific community, as it allows flexible adjustment of many properties during their bottom-up synthesis, resulting in easy-to-handle, customized QDs in solution. These tunable QD "inks" are useful for a wide range of light-absorbing applications.

Tangential to PV, QDs are incorporated in other optoelectronic devices, with QD-based photodetectors being particularly notable. Photodetectors are one of the most versatile class of optoelectronic devices, used in a multitude of applications including imaging [24][36][47][48], spectroscopy [24][30][36][48], communications [24][30][33][36][47], biological sensing [33][47], thermal sensing [33][49], surveillance [24][48], security switching [30], and more. QD-based photodetectors show desirable spectral selectivity [48]; based on the active QD material, they can be employed for detection of ultraviolet (UV), visible, and infrared (IR) wavelengths [18][45] and beyond, outside the range of detection for silicon [50]. The development of economical, solution-processed QDs is advantageous for the low-cost, large-scale fabrication of photodetectors sought across multiple fields [33].

While many exciting materials and structures have been painstakingly developed by device scientists and engineers, crystalline silicon holds a monopoly in the world of consumer electronics. The continued dominance of crystalline silicon is attributed to the difficulty of applying nanostructures to mass-fabrication and up-scaling. To gain traction in the consumer market, facile, straightforward nanomaterials synthesis methods must be developed for compatibility with very large-scale integration (VLSI). Furthermore, due to the small overlap between nanotechnologists and health scientists, the safety risks posed by these novel materials are not well-known, leading to reluctance of adoption. However, based on the prevalence of nanotechnology in every area of technological development, a nanotechnological future is absolute.

1.2 Application of Quantum Dots to Photovoltaics and Photodetectors

Quantum dots are minuscule, tunable semiconductor nanomaterials with powerful optical and electrical properties. Quantum dots are notable for their promising application to a diverse collection of fields ranging from optoelectronics [16][28][51][52][53] to biomedical imaging [54][55]. Advantageously, many properties such as bandgap [35][44][47][56][57], photoluminescence (PL) emission, absorption [18][24], and solvent compatibility are adjusted during synthesis, with many properties dependent on QD size [24][30][32][34][36][50]. QDs are excellent candidates for many applications, especially in light management technologies such as PV, photodetectors, displays, and light filtration [31][41].

Bottom-up synthesis methods are the most commonly employed, resulting in colloidal quantum dots that are utilized much in the manner of inks. As smaller structures require less material and cheaper production, inorganic semiconductor quantum dots are viable replacements for expensive, high-grade semiconductor bulk materials. In contrast to the high costs associated with traditional silicon processing and fabrication [24], colloidal quantum dots are compatible with low cost, large-scale, solution-based manufacturing [18][24][31][32][36][47][58]. The versatility, detectivity, and low-cost production of CQDs make them desirable in various photodetector and photovoltaic applications [24][33][34][48][49].

The formation of QDs is diverse, as they can be fabricated based on any semiconductor composition. Compound semiconductor configurations are overwhelmingly employed over single-element QDs. The most widely researched colloidal QDs for optoelectronics are in the II-VI and IV-VI groups, primarily based on cadmium and lead [56][59][60]. PbS and PbSe QDs have been successfully incorporated in high-efficiency photovoltaics and photodetectors [24][33][34][36][50][61], utilizing the Pb compounds' high molar absorption coefficient and wide bandgap tunability [30][47][24]. Due to their intense, sharp emissions, CdSe QDs have been largely applied towards light emitting diodes (LEDs). However, the known toxicity of elemental Cd and Pb poses concerns for large-scale production [36][62][63][64][65], especially considering the nanomaterials' ease of aerosolization and capacity to impart toxicity regardless of functionalization [63][66]. Apprehension over QD aerosolization and exposure in processing and testing facilities, risks in large-scale deployment, and limited end-of-life recycling options hinder commercial viability [67][68].

Although Cd- and Pb-based QDs continue to enjoy investigative attention from researchers, efforts of commercialization have largely moved away from their use, towards less-toxic compounds. I-III-VI quantum dots, including copper indium sulfide ($CuInS_2$;

CIS), $CuInSe_2$ (CISe), $AgInS_2$ (AIS), and $AgInSe_2$ (AISe) [2][69][70][71], have attracted considerable attention due to their tunable opto-electrical properties [2], low bandgaps [72][73], lower toxicity [67], and diverse applicability [53][54]. Furthermore, it has been shown that employing different molar ratios of Group I, III, and VI elements allow significant flexibility over the structure and optical properties of the resulting QDs [74]. High-throughput synthesis of CIS QDs has previously been reported [2], making it promising for manufacturing. As the mainstream commercial applications of QDs expand, the development and enhancement of less-toxic QDs is paramount.

1.3 Motivation for this Research

1.3.1 Developing Facile Synthesis Processes for Less-Toxic QDs

As the environmental and economic consequences of non-sustainable technologies become progressively apparent, there is increased urgency for efficient solar energy harvesting methods. The application of nanomaterials to photovoltaics and photodetectors is an enticing prospect in aiding sustainable technology development. Unlike many fussy nanostructures with elaborate synthesis procedures requiring expensive, high-maintenance equipment, bottom-up solution-based synthesis of colloidal quantum dots are fairly straightforward. Advantageously, these solution-processed QDs are compatible with large-area, large-scale processes, making them ideal for commercial device production.

The most commonly investigated quantum dots are based on toxic cadmium (CdSe, CdS, CdTe) and lead (PbS, PbSe). While these QDs are known for their performance and stability, their toxicity poses barriers to the commercialization of QD-based technology. Their synthesis also requires sensitive, precise injection of volatile and reactive materials, making up-scaling and mass-production an impossibility. The serious health and environmental risks presented by devices employing these materials impede their applicability towards technologies available to the general public [31][35][36][56][66]. Facile, one-pot, high-throughput synthesis processes of non-toxic QDs, conducted under safe conditions with low reaction temperatures, are ideal.

Due to their lower toxicity, I-III-VI QDs are investigated as safer, more suitable alternatives to Cd- and Pb-based QDs. Among I-III-VI QDs, development of cupric chalcopyrites, especially CIS QDs, have been exceptionally promising [56][75]. The bulk form of $CuInS_2$ possesses a direct bandgap of approximately 1.5 eV [31][44], optimal for absorption and solar conversion across the visible spectrum [56][68][75][67]. Due to the attractive opto-electrical properties of CIS QDs, including high absorption [24][35][56][58][67][68], chemical and radiation stability [58][67][68], wide range optical tunability [31][65][67], and long lifetime [31], they are considered one of the most promising novel materials for photovoltaic and photodetection applications [75][76][77][78]. Furthermore, CIS QDs can be produced by using non-injection synthesis methods, which are compatible with high-throughput and scalable processes [31][65][79][80]. The simple, scalable synthesis of CIS QDs make them more compatible with large-area manufacturing environments. Devices based on CIS QDs have shown comparable performance to Cd, Pb-based QD devices [35][44][56]. CIS QDs are a safe option for synthesis and device implementation.

Prior to the emergence of third generation photovoltaic technologies, the CuIn(Ge)(S,Se) (CIGS) family of semiconductors, which encompasses CIS, were successfully applied to second generation thin film solar cells. Furthermore, these I-III-VI chalcopyrites have taken the form of multinary semiconductor quantum dots, for a range of applications unsuitable for Cd- and Pb-based QDs [67]. The 1.05-1.5 eV wide, tunable bandgaps of these materials are ideal for the visible spectrum [75][67], displaying high absorption coefficients[56][67][68], good radiation stability [67][68], and promising characteristics for photon conversion [67]. Unfortunately, bulk phase cupric chalcopyrites, such as CIGS thin films, have proclivity for instability. In CIS bulks, Cu_xS and In_2S_3 phases separate due to the cations, which have tendency to form independent bonds with S (resulting in separate Cu-S and In-S bonds). CIGS films are notorious for clusters, domains, and non-uniformities, making fabrication processes expensive [81]. For these reasons, CIGS thin film solar cells lost favour as third generation PV gained prominence. Conversely, the dual-cationic structure of cupric chalcopyrite materials becomes favourable in the nanoscale, as it can be leveraged to tailor the QDs.

The many advantageous and curious optoelectronic properties displayed by CIS QDs motivates their further development for light management device applications. As they show many traits that make them compatible with large-scale PV and photodetector integration and fabrication, continued improvement is a worthy undertaking. Specifically, synthesis processes should be developed to achieve facile, high-throughput synthesis that is amenable to industrial production. Furthermore, strategies must be established to overcome the disadvantageous of their complex, defective lattices. The formation of high-quality CIS QDs is paramount to their translation to uniform, device-quality QD films for implementation in commercial PV, photodetector, and light management devices.

1.3.2 Developing Reliable QD Device Fabrication Processes

In the march of progression for light management technology, the poor optoelectronic properties displayed by silicon materials have been deemed increasingly inadequate. In the research community, QDs have been cemented as a dominant alternative for light emission, detection, and harvesting. As QD usage becomes more widespread, there is strong motivation towards the development of novel and less-toxic QDs, including CIS. However, the investigation of these relatively novel materials poses many uncertainties in the course of device implementation. Incorporation of novel QDs in light management devices necessitates the development of reliable processes in every step of material synthesis and device fabrication, to eliminate ambiguities posed by fabrication. Achieving reliable QD devices is paramount to QD commercialization.

Nanoparticles (NPs) have transitioned from research labs into the marketplace for a multitude of applications [64][82][83][84][85]. Large-scale nanoparticle and QD production are required for many fields, including photovoltaics, photodetectors, displays, light management, power generation, energy storage, and medicine [39][40][82][84] . In contrast to conventional bulk silicon devices, which are usually fixed in a planar configuration upon rigid substrates [3], nanomaterial devices require more complex processing. As there are limitations that make nanomaterials incompatible with the VLSI processes and equipment used in commercial silicon devices, nanomaterial devices tend to be implemented on a smaller scale. Nanomaterial devices entails exhaustive, multi-step fabrication (mainly solution processing) and assembly of the discrete components. Although this is acceptable in research environments, it is far too bothersome for manufacturing [3]. Complex fabrication reduces the repeatability of the process, bringing forth additional uncertainties regarding device performance.

Furthermore, considerations towards safety and prevention of exposure are a necessity in the development of large-scale fabrication processes for QD devices. As nanomaterials are associated with inherent toxicity, this raises concerns regarding production safety. Even nanoparticles comprised of materials that are classified as non-toxic as bulks, such as Si, are implicitly toxic due to their small size [86], which allows easy aerosolization. Currently, safe handling procedures are addressed on a case-by-case basis and are mostly limited to small-scale, research settings [82]. The millimeter to centimeter-size scale on which research is conducted makes exposure risks more manageable. There are no adequate standardized safety guidelines for handling nanomaterials at the large scale required in industrial processes [85][87]. Safety is paramount in utilization of nanomaterials [86], and standardized processes must be developed to mitigate exposure.

The processability of CQDs make them advantageous for low-cost, large-area, large-scale devices on a variety of substrates [31][88]. The handling and manipulation of bottom-up CQDs are fairly straightforward. QDs are compatible with a flexible range of substrates, presenting architectural possibilities beyond the traditional rigid bulk semiconductor devices [3]. Furthermore, their solution processability allows them to be handled much in the manner of inks, allow large-scale implementation and flexible customization. Therefore, CQDs are the most likely candidates to succeed in commercially processed devices. The design of systematic, repeatable fabrication processes for CQDs is paramount to the future of QD devices in industry.

1.4 Objectives of this Research

This PhD project focuses on the synthesis and application of copper indium sulfide quantum dots for photovoltaic and photodetector device architectures. As such, the main objectives of the research were defined in four categories: QD synthesis, QD film formation, characterization, and device design and fabrication. They are outlined further in the following sections.

1.4.1 QD Synthesis

The development of scalable, bottom-up synthesis for less-toxic quantum dots is imperative to industrial production. Although quantum dots are available for purchase, the small selection sold by suppliers are expensive with little allowance for customization, making in-house synthesis more practical. In this research, a facile, low-temperature, high-throughput synthesis process was developed for less-toxic CIS QDs. Significant development of the QDs was completed, with exhaustive investigation on the impact of synthesis temperature and precursor variation on the QD structure and properties. Furthermore, surface functionalization and alloying procedures were developed to improve the stability and performance of the QDs. Finally, a theoretical model was developed to understand the formation of the QDs and their optical behaviours.

1.4.2 QD Solid Formation

The formation of CQD solids is significant to the application of QDs in solid state devices. However, the 1-dodecanethiol (DDT) ligands utilized in the facile CIS QD synthesis process is incompatible with film formation and interfacing with common electron transport materials. Therefore, a ligand exchange process was developed to replace the DDT ligands with shorter 3-mercaptopropionic acid (MPA) molecules, which are more conducive to QD film formation. Methodologies of QD film formation were studied in effort to obtain smooth, crack-free, uniform QD solids. As well, ZnO films were developed for fabrication of

ZnO/QD heterojunction devices. The ZnO/CIS QD interface was investigated to optimize vertical carrier transport, while the CIS QD film was studied to improve carrier mobility through the QD solid.

1.4.3 Characterization

To ensure the quality of the synthesized quantum dots, QD films, and other materials used in device formation, optical, structural, and electrical characterization were performed. The QDs were optically characterized via photoluminescence, ultraviolet-visible spectroscopy (UV-Vis), and Fourier transform infrared (FTIR) spectrometry. Structural characterization of QD solids, ZnO films, and ZnO/QD heterojunctions were primarily performed using atomic force microscopy (AFM), scanning electron microscopy (SEM), transmission electron microscopy (TEM), and energy-dispersive X-ray spectroscopy (EDS). Electrical characterization was performed using illuminated current-voltage (I-V), dark I-V, and photoconductivity studies. Additionally, toxicity studies were performed to investigate the safety and exposure risks of this research.

1.4.4 Device Design and Fabrication

To eliminate ambiguities posed by fabrication, it is important that standardized, reliable processes are utilized in the fabrication of novel, nanomaterials-based devices. Currently, fabrication of QD and other nanomaterials devices in research labs tend to utilize questionable, multi-step assembly processes with poor repeatability. This is unacceptable in industry, which emphasizes the importance of repeatable, standardized fabrication protocols. The fabrication of nanomaterial devices should strive for the same process control. As the use of novel QDs and nanomaterials themselves bring forth ambiguities, it is important to eliminate questions of device performance related to poor fabrication practices. A planar heterojunction ZnO/CIS QD device architecture was designed and investigated, then scaled down to micro-scale dimensions through photolithography and patterning. Tools and procedures were designed to ensure repeatability and scalability, producing reliable micro-scale devices on cm-scale substrates compatible with standardized fabrication facilities. The repeatability of the process eliminated uncertainties regarding device fabrication, allowing more focus on optimizing factors that contribute to improving device performance.

1.5 Organization of Thesis

Chapter 1 is an introduction to this research, presenting a general overview of the area, as well as the motivations that drive this work.

Chapter 2 presents a literature review of relevant topics required to understand this research. In particular, this chapter provides background on progress in quantum dots and QD light management devices, including QD PV and QD photodetectors.

Chapter 3 focuses on the development of facile, low-temperature, high-throughput synthesis of CIS QDs. A bottom-up method of synthesis was developed, and the resultant QDs were optically, elementally, and structurally characterized. Various parameters of synthesis, including temperature, precursor stoichiometry, and T-ramping, were investigated to determine the impact on the synthesized QDs. Ultimately, it was found that a Cu-deficient precursor ratio, in conjunction with gradual T-ramping, produced the highest-quality QDs. Theoretical models were developed to propose explanation for QD formation, as well as their optical mechanisms.

In Chapter 4, an overcoating technique was established for fabricating CIS/ZnS core/shell QDs. Due to the lattice complexities in CIS QDs, surface nonidealities arise, leading to sub-optimal optical properties. Thus, ZnS overcoating was developed to improve surface passivation and stability of the core CIS QDs. Reaction conditions, including precursor stoichiometry and synthesis temperature, were optimized to improve the quality of the resultant core/shell QDs. It was found that Zn-excess precursor ratios significantly improved optimal properties, especially lifetime. A theoretical model was developed for the mechanisms of overcoating, wherein it was proposed that Zn cations diffuse into the CIS core during overcoating, giving way to unique optical properties and a graded, alloyed Cu/Zn-CIS/ZnS core/core/shell structure.

Chapter 5 explores the functionalization of CIS QDs for device applications. The long, non-polar DDT ligands used in synthesis are incompatible with formation of metal oxide/QD heterojunctions, which are significant in achieving QD-based devices. Additionally, due to the imposition of a carrier-confining structure, core/shell CIS/ZnS QDs are not conductive to formation of conductive QD films. Therefore, a ligand exchange process was developed to replace the as-synthesized DDT ligands on core CIS QDs with shorter, bifunctional MPA. The ligand exchange allowed successful achievement of good quality ZnO/CIS QD heterojunctions, which are applicable for PV and photodetector devices.

Chapter 6 presents the development of a synthesis strategy for alloyed zinc copper indium sulfide (ZCIS) QDs, in effort to exploit Zn-associated enhancement without an overcoat that hinders carrier transport. Similar to the process for CIS QDs, a low-temperature, scalable, high-throughput synthesis strategy was developed for ZCIS QDs. Variation of cationic precursor ratios were studied to determine the impact on the quaternary ZCIS lattice. As with CIS, it was found that Cu-deficient ratios resulted in ZCIS QDs with the most advantageous optical properties. The QDs were successfully applied to a ZnO/ZCIS QD diode, which showed preliminary response to illumination.

In Chapter 7, CIS and ZCIS CQDs were applied towards formation of QD solids. Strategies of QD film formation was studied and evaluated, to determine the impact of various common film formation methodologies on QD solid morphology. In particular, dip-coating was studied to explore the self-assembly formation of crystalline, uniform CIS and ZCIS QD solids. The impact of various parameters, including rate of withdrawal, number of dipping cycles, and annealing temperature, were explored to study the impact on the resultant QD solid. Ultimately, it was found that dip-coating could not produce films of sufficient thickness for QD device application. However, the observation of factors which impact film uniformity and crystallinity was valuable for subsequent device studies.

Chapter 8 presents the fabrication of a simple, large-area, planar device based on a ZnO/CIS QD heterojunction. Using vacuum deposition and solution casting processes amenable to VLSI, a photodetector device was successfully fabricated. In addition to refining the main ZnO/CIS QD heterojunction, other aspects of the device, including an MoO_3 hole transport layer (HTL) and metallization, were studied and optimized. The device was characterized using optical and elemental methods, providing clarity on the structure of the individual films comprising the device structure, as well as the interfaces present. The device showed response to visible and UV illumination.

Chapter 9 describes the design and fabrication of a small-area ZnO/CIS QD heterojunction photodetector device. Although the planar device displayed promising results, the lack of repeatability in forming a large-area device led to the design of a much smaller active area fabricated onto a standard 2.2×2.2 cm^2 substrate. Insulating SU-8 and photolithography were utilized to define 5 μm-diameter wells (19.63 μm^2 active device area) onto standard cm-scale substrates. A QD injection system was designed and developed to confine QDs within a small area, producing QD films with better uniformity and repeatability. This reliable fabrication process allows the use of standardized fabrication masks and equipment with the atypical small-area device, achieving repeatable device structures. The resultant devices showed good response to illumination, and the highest ON-OFF ratios compared to other devices fabricated in this work.

Chapter 10 presents an investigation of the exposure risk and biological toxicity of the QDs investigated in this work. *In vitro* cytotoxicity studies were conducted on HeLa cells, to compare the impact of common CdSe QDs and CIS QDs on cell death. Additionally, studies were conducted to determine the risk of aerosolization and worker exposure in QD research and processing environments. The findings in this chapter were significant to determining the feasibility of continuing this research, as well as designing and evaluating the processes and studies conducted in the remainder of this work.

Chapter 11 summarizes the results achieved in this work and provides outlook and recommendations for the future of CIS QDs and CIS-based optoelectronic devices.

Chapter 2

Background and Literature Review

Crystalline nanostructures of semiconductor materials are of great interest in optoelectronics research. One nanostructure investigated for third generation photovoltaics is the semiconductor quantum dot, which exhibits a number of attractive properties for light management applications. The quantum dot's small size and large surface-to-volume ratio lends to three-dimensional quantum confinement of carriers, resulting in remarkable properties and behaviour [25]. Some of its most touted properties include size-tunable photoluminescence emission, high photoluminescence quantum yield (PLQY), broad excitation spectrum, multiple exciton generation (MEG), and resistance to photobleaching [89][90][91]. This chapter provides background on the synthesis and application of QDs for photovoltaics and photodetector applications. This literature review begins with an overview of quantum dot structures, continues with exploration of solution-based quantum dot synthesis, and concludes with a summary of progress in quantum dot-based devices.

2.1 Quantum Dots

Quantum dots are a family of materials with size-dependent optical and electrical properties, which can be tailored for a wide range of applications [90][92]. Quantum dots are structurally composed of a metalloid crystalline core with a shielding overcoat [64]. They assume a variety of shapes, including spherical, cubic, tetragonal, and rodded, as shown in Fig. 2.1 [1]. Physical characteristics such as size, shape, defect, composition, crystallinity, surface composition, and doping greatly influence the behaviour of QDs.

Due to quantum confinement, QDs are not governed by the rules of classical physics,

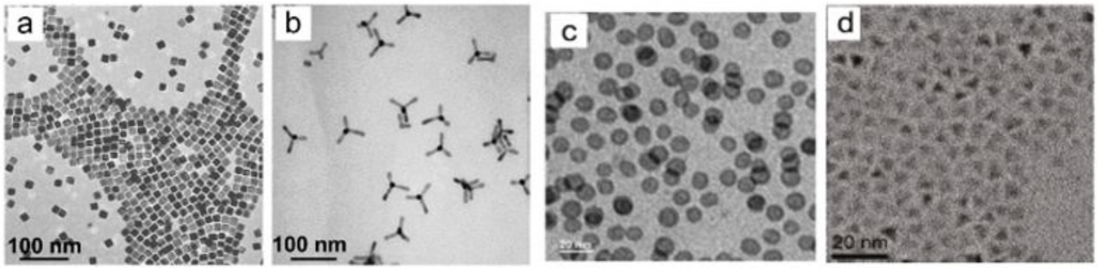

Figure 2.1: Quantum dots of different shapes and materials, including (a) PbSe cubes, (b) CdSe tetrapods, (c) hollow iron oxide spheres [1], and (d) tetrahedral CIS/ZnS [2].

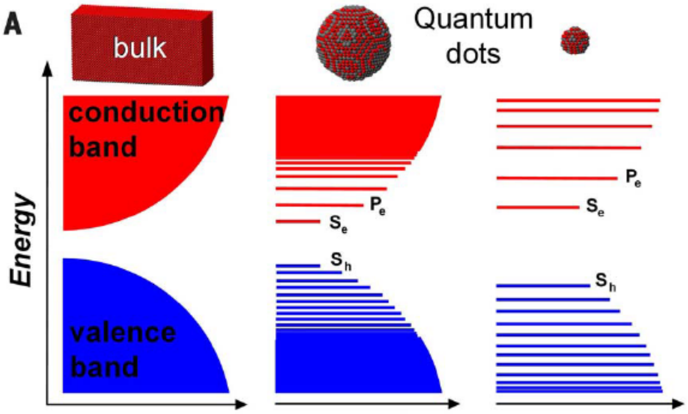

Figure 2.2: Comparison of electronic states in bulk materials and QDs [3].

imbuing them with extraordinary properties that significantly differ from their bulk counterparts [4]. QDs are composed of far fewer atoms than bulks, resulting in fewer energy states. As there is less overlap of the energy states, this produces discrete states for carrier occupation, rather than continuous bands for carrier locomotion [3]. As QD sizes increase, more atoms are added, contributing to more energy states that overlap, resulting in the energy states becoming more band-like [3]. Fig. 2.2 illustrates the band structure differences between bulk materials, and small and large QDs. The majority of the notable QD properties arise from their unique energy state configurations.

QD dimensions range from 2-3 nm to under 30 nm [1][4], placing them between atomic-molecular and bulk. QD optical, electrical, and magnetic properties are primarily influenced by the energy difference between their unoccupied and occupied molecular orbitals ("bandgap"). Increasing QD sizes tend to redshift emission and absorption. This is be-

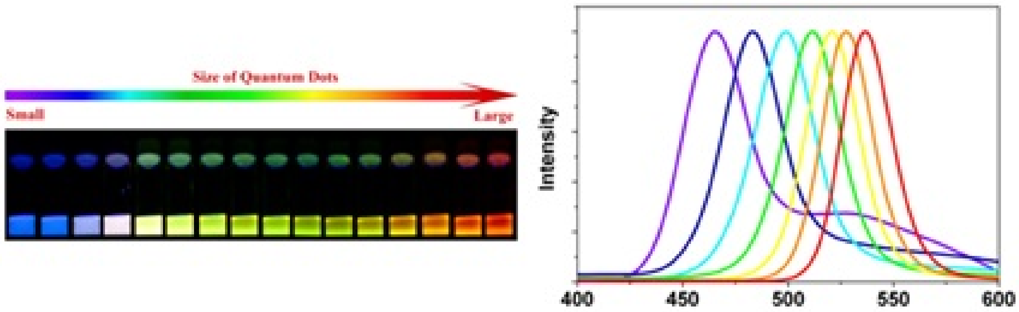

Figure 2.3: CdSe QDs displaying size-dependent photoluminescence emission [4].

cause, due to the scarcity of atoms in the nanostructure, the addition of each atom impacts the QD much more significantly than in bulk materials. The increase in atoms causes the electronic band structure in larger QDs to become more band-like, leading to a smaller separation between unoccupied and occupied molecular orbitals (i.e., a smaller bandgap). Different material compositions are capable of having bandgap values (and therefore emission and absorption) within a specific range; Fig. 2.3 shows variation in emission by size. For example, CdSe-based QDs are noted for having emission in the visible range, while Pb-based QDs typically have bandgaps that place their emission in the infrared.

Quantum dots are often viewed as a lower-cost alternative to expensive, process-intensive bulk semiconductor materials. Highly fluorescent Group II-VI QDs such as CdSe, CdTe, and PbS are the most commonly applied in research of electronics, optoelectronics, and medical biology [93]. However, despite early excitement over the advantageous performance and stability of these QD materials, their actual consumer applicability has been limited due to concerns over toxicity [74]. Increased research efforts have been dedicated toward QDs based on less-toxic materials. Group III-V quantum dots such as GaAs, InP, and InAs share the direct bandgap, high mobility, and reliable doping of their bulks, while being less expensive to manufacture than their high-purity bulk counterparts [94]. Apart from binary structures, ternary I-III-VI semiconductor quantum dots such as $CuInS_2$ and $AgInSe_2$ show advantageous absorption, emission, and lifetime [78][67][95], making them particularly ideal for photovoltaic and optoelectronic applications. Non-toxic, environmentally benign ternary QD structures are of significant interest among device engineers [96]. Of I-III-VI QDs, cupric chalcopyrite QDs such as copper indium sulfide have increasingly gained attention among the photovoltaics community due to their solar-compatible absorption spectra [74][81] and large extinction coefficients [81][97]. The biological stability [98] and comparative non-toxicity [63][99] of CIS QDs make them a suitable alternative to Cd-

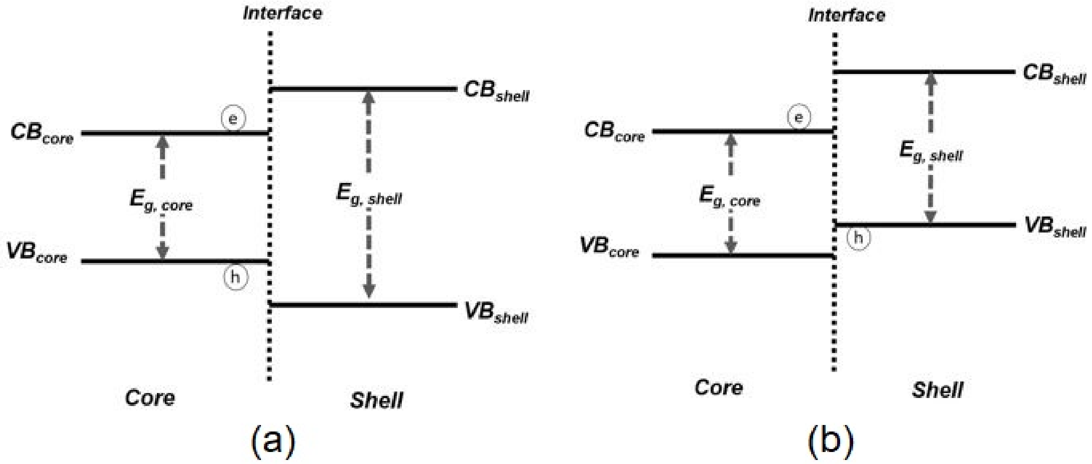

Figure 2.4: Bandgap diagrams of (a) Type I and (b) Type II core/shell QDs.

and Pb- containing QDs in light management applications.

2.1.1 Quantum Dot Surface Passivation

As their surface-to-volume ratios are so large, QDs are strongly influenced by surface functionalization. QDs tend to possess a high density of carrier-trapping surface sites and states, with many dangling bonds and uncoordinated surface atoms [3][4]. Therefore, surface passivation is necessary. Surface-passivating inorganic overcoats, which cover the entirety of a QD's surface, can impart high emission, stability, and high quantum yield [89]; they improve QD optical properties by carrier confinement, dangling bond saturation, and reduction of surface states [4]. Core/shell QDs are typically classified as either Type I or Type II. Type I QDs are configured with a wider bandgapped shell semiconductor straddling a small bandgapped core, as shown in Fig. 2.4(a). Type II quantum dots form a staggered alignment, with the band edges of the core material offset (usually lower) from the band edges of the shell (Figure 2.3(b)).

Overcoating is often leveraged to improve a quantum dot's stability and optical properties. Type I core/shell structures are effective in carrier confinement within the cores, as the band edges of the core are wrapped by the bandgap of the shell [3]. Although not conducive to carrier conduction, this is effective in correcting intrinsic deficiencies and suppressing single-dot blinking, as demonstrated by Chen et al's work with Type I CdSe/CdS QDs [100] and Hollingsworth group's work with "giant" CdSe QDs comprising multiple passivating shells [101]. Type II configurations selectively confine one type of carrier within the core, an effective strategy in reducing recombination in devices that rely on single-carrier mobility. This type of configuration is seen more often in device applications, such as Ivanov et al's synthesis of Type II core/shell CdS/ZnSe QDs with efficient separation of electrons and holes between the core and shell [7], or Zhao et al's fabrication of solar cells using hole-confining Type II CdTe/CdSe core/shell structures [12]. Deviation from traditional Type I and Type II configurations can produce unique architectures, such as Zhong et al's inverse Type I CdS/CdSe QD, which uses a wide bandgap/small bandgap core/shell configuration to control carrier localization [12]. Intricacies in band alignment are correlated to shell thickness and can decrease quantum yield [102]. In particular, large core-shell QDs are disadvantageous due to having poor size distribution and broad PL spectra [100]. Thick capping layers may cause misfit locations to form, negating the benefits of surface passivation [4]. Most importantly, thicker shells hinder conductivity of QD films, as they provide larger barriers to tunnelling of carriers from the QD core [3]. Such factors must be considered when selecting shell materials for overcoating.

While core/shell structures are greatly advantageous for stability, many device applications forgo overcoating to avoid issues with carrier conduction. Ligand functionalization is another significant method of surface passivation in QDs. The term "ligand" denotes a class of molecules bonded to a central metal core though attractive interaction. For quantum dots, ligands are organic molecules that bind to its surface to control growth and stability, prevent agglomeration [1][3][103][104], and influence fluorescence and quantum yield [105]. The surface imperfections in QDs lead to formation of trap states within the bandgap (Fig. 2.5) [3]. Such states easily capture carriers and promote fast electron-hole recombination, leading to non-radiative recombination pathways, which compete with desirable radiative recombination [3]. Ligand molecules can bind to the dangling bonds and surface imperfections that create these states, pushing them beyond the band edges such that they cannot act as detrimental traps [3].

Ligands are significant to QD interactions with and reaction to the surrounding environment [3][105]. The polarity of a ligand imparts solubility onto the QD, and significantly determines its wettability to a substrate. Most surface ligands are composed of long hydrocarbon chains, which are advantageous for solution stability, but hinder uniform film formation. The most common ligands found on colloidal QDs are oleic acid (OA), trioctylphosphine oxide (TOPO), 1-dodecanethiol, oleylamine, and hexadecylamine [105]. When the as-synthesized ligands are not ideal, they may be "exchanged" for more suitable ligands, provided the new ligands have stronger affinity to the surface. MPA is a common

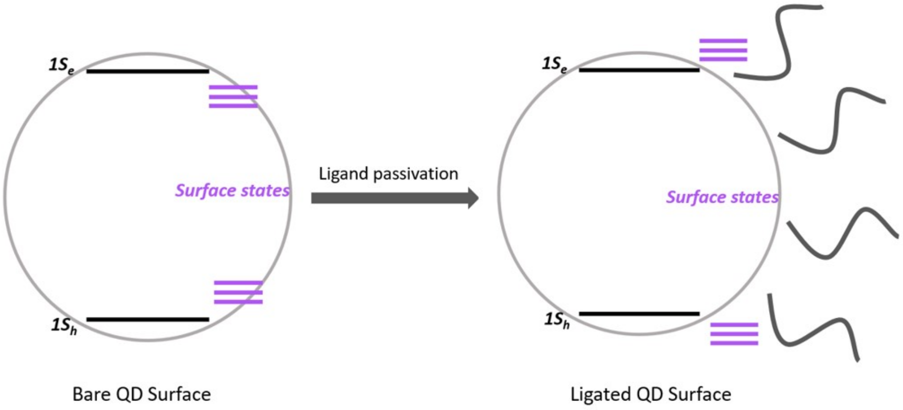

Figure 2.5: Ligands contribute to surface passivation through eliminating surface states.

ligand for QDs intended to form interfaces with metal oxides. 1-ethandithiol (EDT) is a common non-polar alternative; its high concentration of hole carriers and electron traps makes it attractive for photodetection applications that require preferential carrier trapping [47]. Iodide and halide passivation via tetrabutylammonium iodide (TBAI) ligands have also become commonplace. Halide ligands are smaller and can sterically conform onto the QD surface to passivate traps and surface trenches that MPA cannot fit into [106]. Iodides have advantageous desorption kinetics that allow efficient stabilization of QD surfaces [90][107]. Recently, more conductive inorganic and metallic ligands have risen in prominence in effort to improve conductivity between QDs [3][94]. Finally, some have explored the use of multiple ligand strategies to passivate all forms of unwanted surface states [106]. Generally, desirable ligands have strong adherence to a QDs surface, provide colloidal stabilization, enable stable electronic communication between QDs, and constructively supplement core properties. Ligands that are able to cross-link to form tightly packed, electronically coupled QD networks are advantageous for device applications.

Beyond polarity and passivation, ligands affect QD energy levels. The band-tuning effects of adsorbed ligands arise from the formation of microscopic surface dipoles that modify the energy level alignment at the QD/ligand interface [108]. Changing the ligands, especially the chemical binding groups attached to the QD surfaces, results in modifying the QD/ligand surface dipole, producing a shift in the vacuum energy, and therefore, valence band and conduction band maxima [5]. Bawendi's group investigated the effects of thiol, amine, and halide ligands on the energy levels of PbS QDs; Fig. 2.6 shows their findings. Ligand exchange was found to shift the band level of the QDs by as much as 0.9

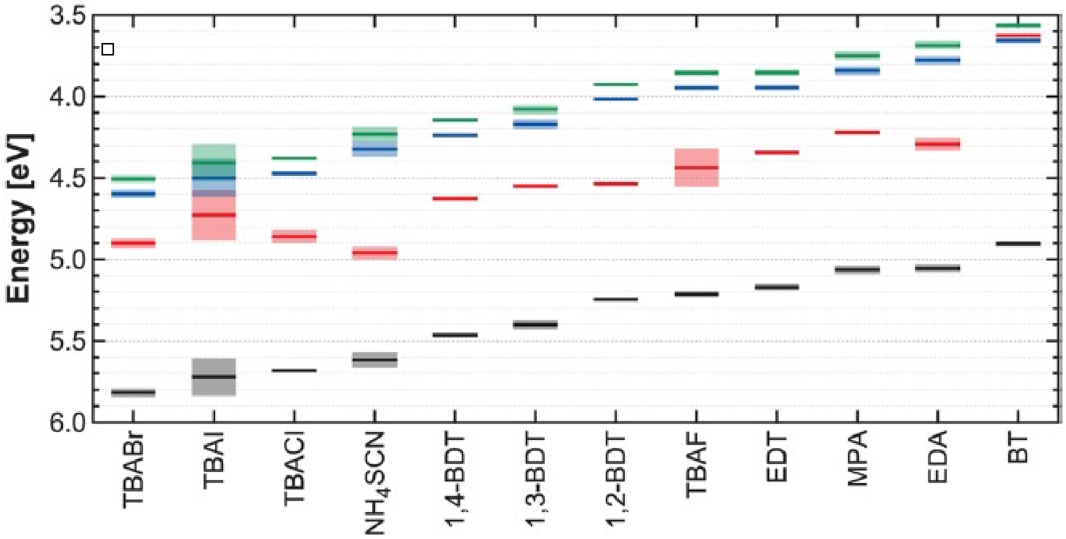

Figure 2.6: Effect of ligand exchange on energy levels of PbS QDs [5].

eV, significantly impacting bandgap engineering.

Soreni-Harari et al conducted similar research on ligand exchange in InAs, finding that the energy levels of the QDs could be shifted as much as 0.3 eV [108]. It was concluded that the properties of the isolated ligand molecule does not largely correlate with its influence on QD energy levels. Therefore, inspecting the properties of the independent ligand is not helpful in determining its effect on QD band levels. Energy level position is impacted by the interactions between the ligand's anchor group and the QD surface where it is bound. QD band levels are susceptible to the influence of these surface effects because interactions on their abundant surfaces affect the entire volume of the nanoparticle [108]. However, due to the complexity of interactions and screening effects on and within QDs, it is difficult to exactly control band alignment using ligand functionalization.

Aside from ligand influence on the QD bandgap, it is notable to recall that in QD device structures, carriers transport in and out of QDs via their ligands. Conduction between neighbouring QDs is significantly impacted by the uniformity and arrangement of the QD solid, which is determined by ligands. Conduction at QD device junctions is contingent on the band alignment at the interface, which are managed by ligand properties. As such, the carrier locomotion between QDs and their neighbours are effectively controlled by their ligands. Therefore, ligand selection and control is one of the most significant aspects of consideration in QD device design and fabrication.

2.2 Quantum Dot Synthesis

Like most nanomaterials, synthesis of QDs is classified into two categories: top-down (synthesis through cleaving of bulk materials) and bottom-up (growth from raw precursors). Bottom-up synthesis has dominated since the beginning, as early methods of QD growth were accomplished through molecular beam epitaxy and Stranski-Krastonov growth [109]. Quantum dots have been successfully synthesized via a multitude of strategies, including lithography [110], plasma synthesis, via gaseous precursors in microdischarge reactors [111], and using low-pressure non-thermal plasma [112]. As QD research matured, preference shifted towards synthesis methods that support large-volume, high-throughput production.

The most common technique is pyrolysis, in which solid- and liquid-phase precursors are combined and heated, decomposing and reforming into colloidal nanoparticles [11]. The resultant QDs are dispersed in solvent and deposited onto substrates to form films [3][105]. Colloidal QD synthesis via pyrolysis holds similarities to established chemical synthesis procedures, making it popular among chemists [1][4][6]. Furthermore, colloidal synthesis allows complete control over the QD characteristics via synthesis conditions including temperature, growth time, precursors, environment, and more. These QD "inks" are compatible with large-volume, low-cost production, and suitable for roll-to-roll manufacturing, making them feasible for industrial production [113].

In QDs applied towards electronic devices, strategies such as successive ionic layer adsorption and reaction (SILAR) and chemical bath deposition (CBD) are sometimes utilized instead of pyrolysis. Such processes entail submersion of the substrate into precursor solutions to allow nucleation and particle growth of QDs; in CBD, this is usually extended immersion in one QD precursor solution, while SILAR requires sequential, repeated dipping in multiple solutions to grow a QD film ion-by-ion [104]. These methods allow the direct growth of QDs onto substrates, which advantageously mitigate issues with QD attachment associated with CQD deposition. However, CBD and SILAR are time-consuming and resource-intensive, resulting in defective, inefficient films with poor QD thickness [104] and size control [114]. Therefore, colloidal QD growth is preferred due to the ease of production and allowance for greater tunability [113][115][116][117]. Although scalability of production, QD robustness, and production under ambient environment are issues that require further addressing [113], CQD inks are the most compatible with manufacturing. The following sections further discuss solution-based colloidal quantum dot synthesis.

2.2.1 Colloidal Quantum Dot Growth

The essence of CQD synthesis via pyrolysis entails adding metal-organic and ligand precursors to surfactants and solvents, then heating the synthesis chamber to a high temperature under vigorous stirring [6][11]. Under sufficient temperature and mixing, nucleation occurs, and precursors become colloidal nanocrystals that increase in size over time. The resulting colloidal quantum dots are extracted, purified, and dispersed in an appropriate solvent [105]. While the basis of all pyrolysis involve the addition of solid precursors to solvents, the specifics of the QD synthesis procedure varies depending on material, desired ligands, and the intended application. A notable technique is hot-injection, in which precursor solutions are separately prepared, and rapidly injected into solvent that has been heated to very high temperatures (in excess of 300°C) [1][100]. Hot-injection is sometimes preferred due to more precise control over the growth stages, but is infeasible for scaled-up production, as it requires high precision and poses safety concerns. In contrast, one-pot synthesis procedures require all precursors to be added to the reaction chamber and heated, without further injection during the procedure. The reaction proceeds on its own when the conditions for QD formation kinetics are reached. For device engineers, development of straightforward, scalable methods such as injection-free and one-pot synthesis is desirable.

The growth of a monodisperse colloid occurs in two steps: a nucleation event, then subsequent slower, controlled growth on the nuclei. Initial size distribution depends on nucleation time, which is controlled by maintaining the rate of precursor addition below precursor consumption [6]. Nucleation and growth time should be balanced at approximately the same rate. If nucleation occurs too quickly, bulk crystals will form instead of the desired nanocrystals, and if nucleation occurs too slowly, the precursors will form molecular clusters [1]. This initial period of nucleation and growth is referred to as focusing of the size distribution, or simply “focusing”. During focusing, monodispersity is fairly high, as all of the nanocrystals in solution grow at a uniform rate [6]. Following focusing, quantum dot synthesis enters the “defocusing” regime, which is dominated by Ostwald ripening. During defocusing, smaller nanocrystals dissolve due to their high surface energies, and their elemental constituents redeposit on larger nanocrystals. As synthesis proceeds, the total number of nanocrystals in the solution decreases, while the remaining nanocrystals grow larger in size [1][6]. The formation of colloidal nanoparticles is sometimes referred to as the Nano-Ostwald ripening model [1]. Fig. 2.7(a) presents a schematic diagram of the quantum dot growth process, which occurs in the setup shown in Fig. 2.7(b). Figure 2.7(c) shows that as synthesis proceeds, quantum dots become bigger, with redshifted emission.

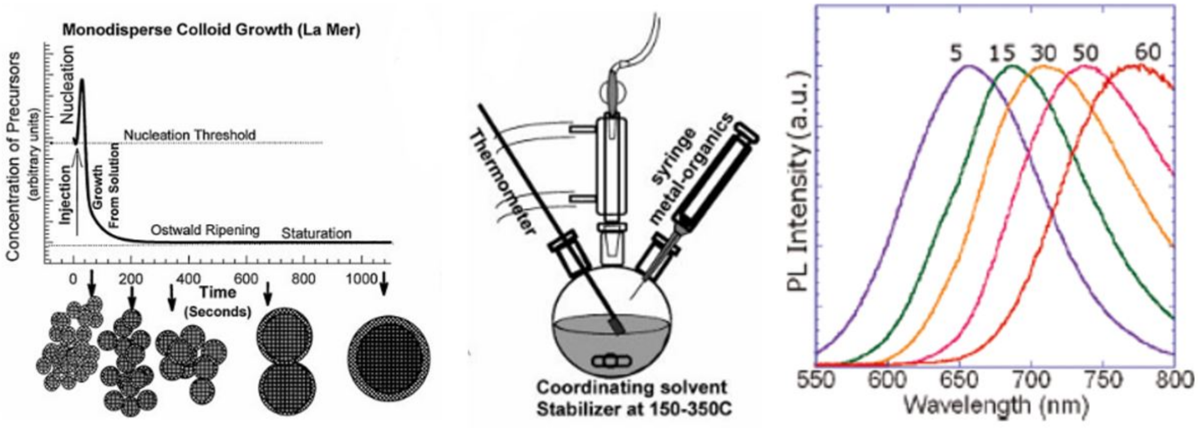

(a) (b) (c)

Figure 2.7: Colloidal QD synthesis: (a) Nucleation and growth of monodisperse quantum dots in solution-based colloidal synthesis [6]. (b) Three-neck flask used for synthesis of colloidal quantum dots [6]. (c) Redshifting emission spectra of CIS QD synthesis conducted between 5 minutes to 60 minutes [2].

2.2.2 QD Overcoating

Colloidal QDs are surface-passivated with ligands, which allow them to remain stable in solution. However, more robust surface coverage may be preferred, leading to overcoated core/shell QD structures. In the formation of core/shell QDs, the overcoating of the shell is typically performed after the core is synthesized and purified. As shell materials tend to have larger bandgaps than the core, with a significantly different lattice constant, the cores lattice may be strained during growth, impacting the absorption and emission spectra of the final structure [4]. Typically, the QD grows larger following overcoating, as shown in Fig. 2.8(a) and 2.8(b), but cation inter-diffusion and other core-shrinking effects can produce a smaller quantum dot, as shown in Fig. 2.8(c) in comparison to 2.8(d) [73][95][118]. Shell thickness is tuned by controlling temperature and precursor loading [89]. To be compatible for overcoating, the surface energies of the core and shell material must be similar, and the shell materials barrier for heterogeneous nucleation should be lower than barrier for homogeneous nucleation [6].

Colloidal QD overcoating begins with heating purified core quantum dots in solvent to a sufficient temperature conducive to epitaxial growth onto their surfaces. The precursors

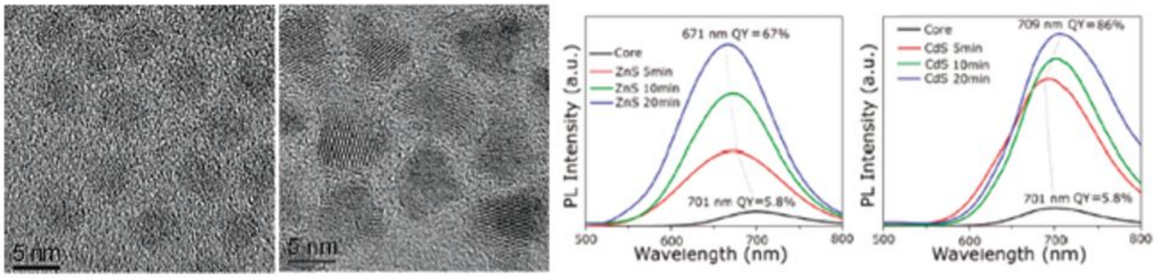

(a) (b) (c) (d)

Figure 2.8: (a) HRTEM images of CdS and (b) CdS/ZnSe QDs [7]. (c) PL spectra of CIS QDs overcoated with ZnS shell(d) CdS; the ZnS overcoat causes blueshift [2].

for the shell material are gradually added, allowing time for nucleation onto the surface of the core crystal. The rate of precursor addition should be fast enough for nucleation onto the core, but not so quick that the overcoat precursors agglomerate and nucleate amongst themselves. Temperature control is also significant, as high temperatures facilitate surface diffusion of shell. Although overcoating at higher temperatures creates thicker shells and larger QDs, the resulting overcoat may lack uniformity due to faster growth [89].

2.2.3 QD Solids

For solid state device applications, colloidal QDs are deposited onto a substrate to form films [3]. The properties of the QD solid relate to the intrinsic optical and structural characteristics of the QDs themselves. The QD solution impacts film formation, as the arrangement of individual QDs onto the substrate depends on the QD size, monodispersity, and stability within the solvent [3]. The ligand plays an overwhelming role in the formation of QD solids, dictating the interaction of QDs amongst themselves, and with the substrate material. It is not typical for as-synthesized QDs to be applied towards QD solids, as the long, insulating ligands that keep them colloidally suspended in solution are detrimental to ordered film formation. External factors such as solvent characteristics, evaporation rate, and ambient environment also determine the quality of the QD film. QD solids are fundamental in the fabrication of QD-based devices.

2.3 Device Applications of Quantum Dots

Although silicon continues to dominate as the semiconductor of choice in electronic devices, alternative materials have gained strong traction due to its optical shortcomings. Although virtually unheard of outside of academic research just a decade ago, the general public has become aware of QDs' existence through the commercial availability of QD displays and other consumer goods. The QD market is expected to reach a value of US $9 billion by 2024, growing at a compounded annual growth rate of 27% from 2019. Fig. 2.9(a) shows the recent and projected market presence of the quantum dot market based on applications. Asia Pacific and Middle East dominate the global QD market, but North America is expected to contribute further over the next several years [9].

The majority of QD applications revolve around display technologies, and it is expected that they will continue to be the primary employers of QD technology. Light management applications such as photovoltaics, lighting, and sensing are expected to gain prominence over the next decade, eventually holding equal shares of the QD market. As QDs possess particularly advantageous photoluminescence emission and quantum efficiency, it is unsurprising that the majority of QD applications revolve around their optical capabilities. QDs have significantly progressed in the past decade, from sub-20% photoluminescence quantum efficiency (PLQE) in 2006, to achieving near-unity PLQE in 2016. With the current progress and extensive research efforts made in this area, the potential for a QD-dominant optoelectronics market is promising.

2.3.1 QD-Based Light-Emitting Diodes

Light detection, emission, and control applications of quantum dots are intensively investigated among the research community. Aided by their high luminous efficiency and narrow linewidth, QDs are frequently applied towards light-emitting diodes [10][78]. The small size of QDs can prevent light scattering, and they are particularly useful for white LEDs due to their strong retention of the green and red spectral regions [78]. Fig. 2.10(a) shows a typical schematic for a simple QD-based single-wavelength LED, which sandwiches a thin layer of light-emitting QDs between two carrier-injecting transport layers [1]. QDs of different sizes can be mixed to produce multi-wavelength emitting LEDs of different colours. Unfortunately, while numerous and varied CQD LEDs are found in literature, they show poor carrier injection and subpar lifetimes. In effort to improve performance, more complex structures with multiple carrier blocking and transport layers, and architectures such as distributed Bragg reflectors and quantum wells, have been applied to various success

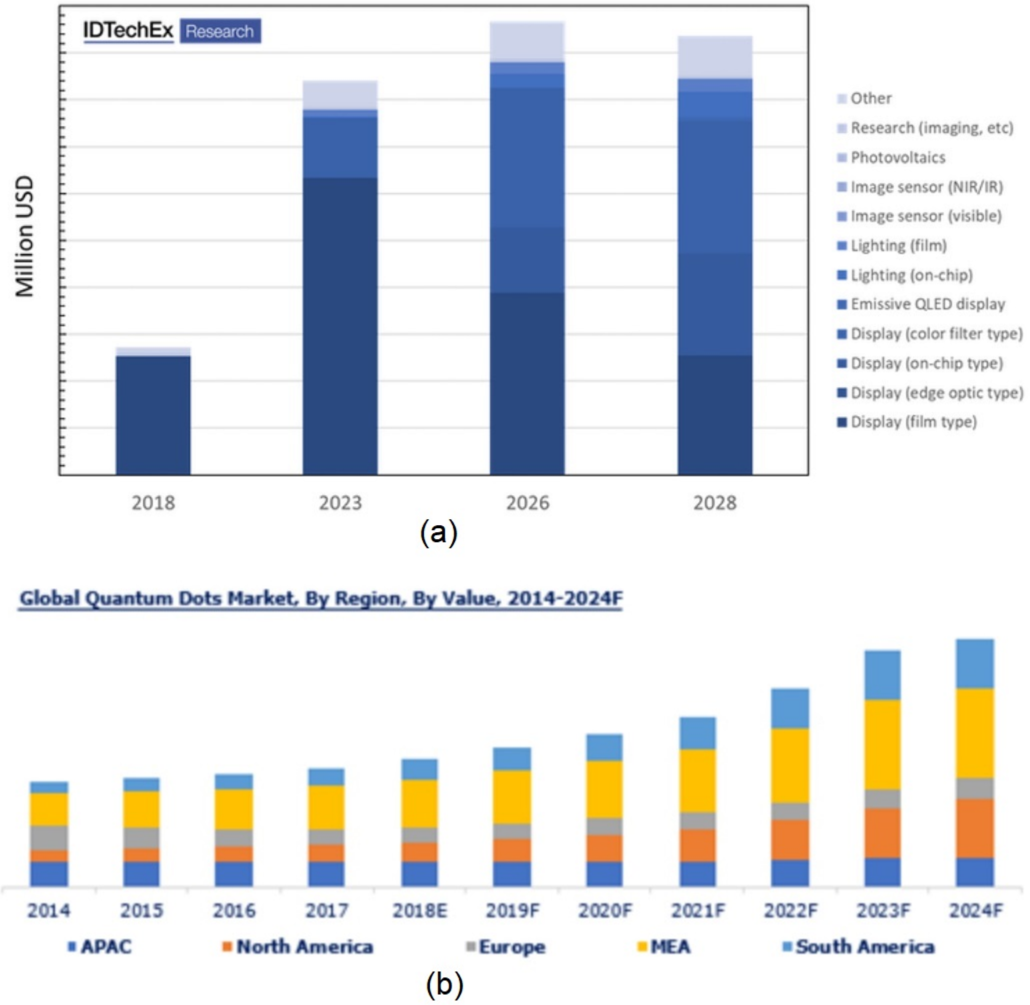

Figure 2.9: Market predictions for (a) QDs devices [8] and (b) the global QD market [9].

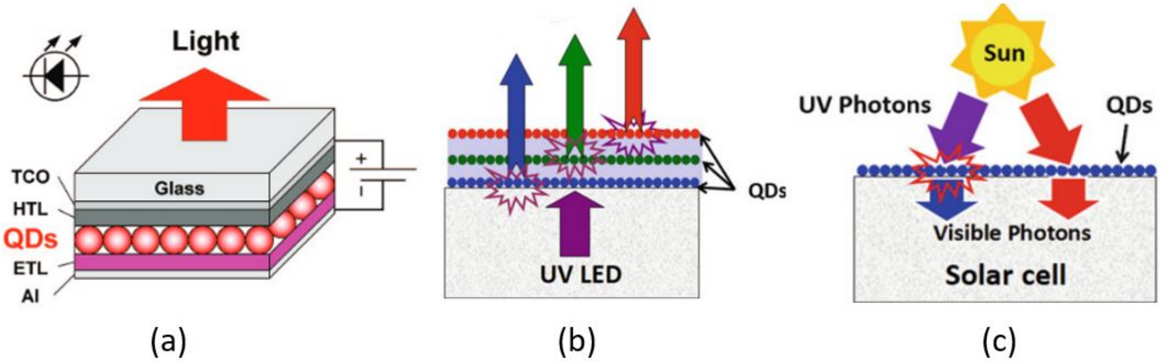

Figure 2.10: QDs in light management devices: (a) QDs as emitters [1] and (b) colour converters in LEDs [10]; (c) QDs as luminescence down conversion layers [10].

[10][28]. Inorganic-organic devices combining organic HTL with QDs have shown particular benefit to electroluminescence efficiency [28].

The superior optical characteristics of QDs make them efficient for optical applications such as filtering and conversion. Fig. 2.10(b) shows the utility of multiple QD layers as colour converters for a commercial LED. In such applications, QDs are mixed with resins and cured onto an existing blue- or UV-emitting LED as optical filters to produce LEDs with varied emission (typically white LEDs) [119][120][121]. The strong absorption and narrow emission capabilities of QDs also make them appropriate as conversion and concentrators for solar cells [102][122]. In luminescence down-conversion (LDC) and up-conversion, materials modify incoming photon wavelengths to optimize the absorption and performance of a device [25][41]. QDs are suitable for down-conversion, as they can absorb photons with energies higher than its bandgap, reliably emitting photons with energy equivalent to its bandgap. QD LDC was applied by Lin et al, using a layer of CQDs to down-shift UV photons to visible photons for more efficient absorption [10]. In Sadeghimakki et al's 2013 work (Fig. 2.10(c)), an internal quantum efficiency improvement of 100% was achieved for bare silicon solar cells enhanced with down-converting CdSe/ZnS QDs [122]. In these light management applications, QDs do not perform electrical functions, and are sealed within resins, spin-on-glass, or other transparent, non-conductive materials to avoid chemical and mechanical degradation.

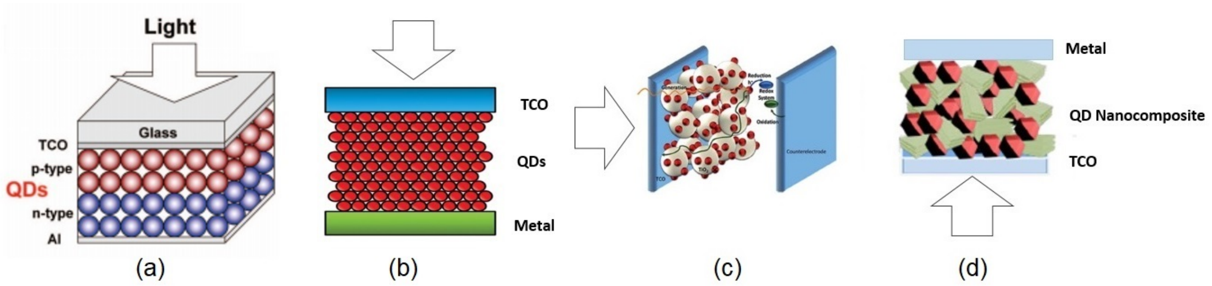

Figure 2.11: Common QD solar cell structures: (a) Heterojunction [1], (b) Schottky (modified from [11]), (c) QDSSC [12], and (d) bulk heterojunction (modified from [13]).

2.3.2 Progress in Quantum Dot Solar Cells

Solar cells are one of the largest fields of research incorporating quantum dots. Requiring less material and tedious fabrication conditions than bulk semiconductors, quantum dot solar cells are a green solution in an industry that values sustainability. QDs can be applied in multiple areas of the photovoltaic structure, including photonic down-conversion, explored above. However, the designation of "quantum dot solar cell" generally implies the use of the QDs as absorbers.

Solid state QD photovoltaic architectures can take the form of Schottky, heterojunction, and bulk heterojunction structures, illustrated in Fig. 2.11. Quantum dot-sensitized solar cells (QDSSCs), analogous to bulk dye-sensitized solar cells, are liquid interface devices that form the fourth major category of QD PV (2.11(c)) [11]. QDs are applied in conjunction with other nanomaterials, such as nanowires, graphene, and perovskites, especially in bulk heterojunction and QD-sensitized architectures [123]. As absorbers, QDs display multiple functions not found in bulk semiconductors. One phenomenon is exploited by QD-based hot-carrier solar cells, which operate by directly extracting high energy carriers [124], efficiently using the high-energy photons to increase conversion efficiency, lower cost, and reduce thermalized energy loss [124]. Quantum dots have also been utilized in multi-exciton generation solar cells to leverage the areas of the spectrum with low semiconductor response [124]. However, the performance of MEG by QDs during photovoltaic applications has so far been dubious, likely due to defect density and non-optimal cell fabrication.

The quantum dot sensitized solar cell dominates as one of the most common configurations for QD-based photovoltaics. The basic structure of the QDSSC is a translation of the TiO_2 photosensitizer/organic dye absorber/solution electrolyte structure of the traditional dye sensitized solar cell (DSSC), but with highly-efficient QDs replacing messy, fast-evaporating organic dyes. The photoanode is comprised of QDs absorbed within the porous TiO_2 structure, forming bulk heterojunctions throughout, allowing carriers generated by the QDs to be quickly separated and transported into the TiO_2. Although record efficiencies have been dominated by heterojunction PV structures, [125], QDSSCs efficiencies are comparable; the current quantum dot photovoltaic (QDPV) photovoltaic conversion efficiency (PCE) record is 18.1% [125], while the highest PCE for QDSSCs is 13.08% [126]. The greatest issues arise from incident light absorption, recombination, QD degradation, and counter electrode compatibility [12], mainly stemming from the liquid electrolytes used in QDSSCs. Liquid electrolytes have been the most efficient in hole conduction, as they act similarly to bulk heterojunction structures, forming a percolative network throughout the photoanode structure to quickly separate holes from the QD absorber. However, this also allows fast recombination throughout the photoanode, reducing solar cell efficiencies. Additionally, common electrolytes such as I^-/I_3^- corrode the TiO_2/QD photoanode [104], requiring atypical alternatives. From the perspective of manufacturing, the use of liquids are not desirable, as liquid components are difficult to assemble, and poses stability issues due to leakage and evaporation. Gel and solid electrolyte-based QDSSCs are an ongoing area of investigation but have not shown similar success [104].

The current QDPV PCE record is held by Ulsan National Institute of Science and Technology; their reported 18.1% efficiency is a significant improvement from the sub-1% efficiency reported 15 years prior [90][125]. The previous two records were held by Hao and Sanehira, both using perovskite QDs to achieve PCE of 16.6% and 13.43%, respectively [14][15]. Both cells utilized a simple heterojunction architecture, with a metal oxide/perovskite QD interface (SnO_2/QDs for Hao et al, TiO_2/QDs for Sanehira et al) and the same conductive polymer HTL on top of a transparent conductive oxide. Although inorganic lead halide perovskite QDs have greatly elevated the performance of QD solar cells, it is important to note that the performance is not comparable to bulk perovskite PV, which surpassed 16.6% efficiency in 2014, and currently holds a 25.5% efficiency [125].

Prior to the work of Hao and Sanehira, QD solar cells based on PbS QDs reigned the best research cell efficiency chart, without exception [125]. The earliest efficiency achievements were demonstrated by NREL, using ZnO/PbS QD heterojunctions. The majority of the record-breaking cells were fabricated by Sargent's group, which primarily increased cell efficiencies through QDs-enhancing functionalizations. Sargent group contributed significantly to enhancement of PbS QDs, developing methods of halide incorporation to passivate surface traps, which have served to incrementally improve record cell efficiencies [90][106][127][128][129]. Architectures to improve the metal oxide/QD interface [130] and enhance QD absorption [34] were also successful, while maintaining the primary depleted

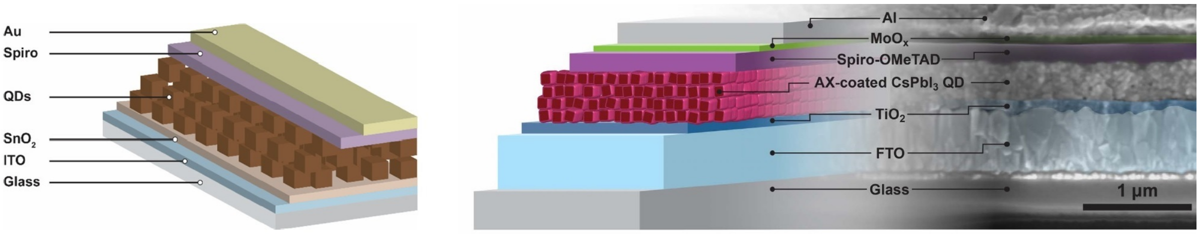

(a) (b)

Figure 2.12: Perovskite QDPV achieved record PCE of (a) 16.6% [14] and (b) 13.43% [15]

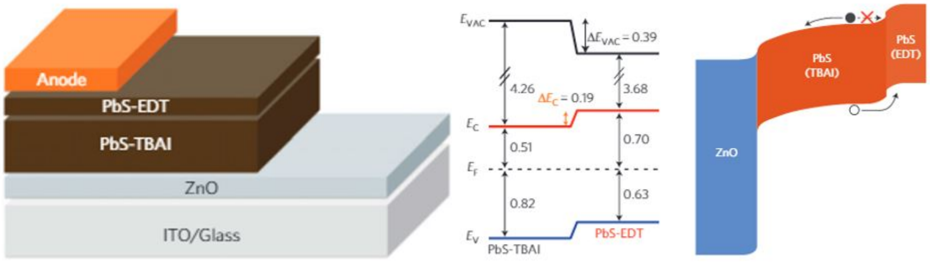

(a) (b)

Figure 2.13: (a) QD solar cell using PbS QDs as absorber and electron-blocker [16]. (b) Band diagrams of the QD/QD heterojunction [16].

heterojunction solar cell structure.

In 2014, Bawendi's group fabricated a PbS QD-based solar cell that achieved a record power conversion efficiency of 8.55% [16][125]. Although it was overtaken in the following year, this work was significant in promoting the use of QD/QD interfaces for charge separation. The primary heterojunction was formed between solution-processed ZnO nanocrystals and inorganic halide-passivated PbS quantum dots, but several layers of EDT-ligated PbS QDs were incorporated; a schematic is shown in Fig. 2.13(a). The EDT ligation of the PbS QDs changed the band alignment, efficiently blocking electrons and separating carriers. The formation of interfaces between the same inorganic QDs negated issues of stability and material incompatibility, while ligand exchange allowed tuning of the band alignment (Fig. 2.13). The use of halide/EDT-ligated PbS QD/QD interfaces subsequently rose in prominence among those endeavouring to produce QDPV with record efficiencies [127][128][129][131][132].

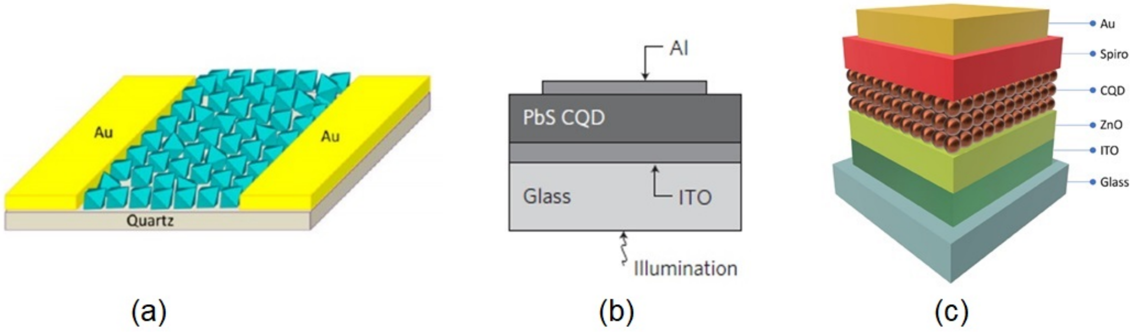

Figure 2.14: Simple QD infrared photodetectors with (a) $CuInSe_2$ QDs deposited onto pre-patterned electrodes [17], (b) PbS QDs in a vertical architecture between two contacts [18], and (c) PbS QD photodetector with various carrier transport layers [19].

2.3.3 Progress in QD Photodetectors

Photodetectors are another area of device application in which QDs have shown significant potential. QDs' size-tunability is a great asset in their application to photodetectors, allowing them to absorb a greater range of the light spectrum and achieve high detectivity at low cost. Narrow-bandgap QDs such as PbS and InAs are particularly useful due to their ability to absorb infrared and far-infrared wavelengths, which are untapped by commercially available Si-based photodetectors [1][133]. Fig. 2.14(a) presents a lateral structure of QD photodetectors, in which a layer of CQDs are deposited onto a substrate with pre-patterned electrodes. The conduction in these devices is lateral, making the uniformity of the CQD solid essential to charge transport and response [17]. This simple lateral, planar device architecture is effective as proof-of-concept for the employment of novel QD materials. Specific detectivity in the order of 10^{13} Jones have been achieved in such configurations, for photodetectors based on PbS QDs [88].

Vertical photodetector architectures are more desirable, as they reduce the carrier transport distance before collection by electrodes. In its simplest form, a Schottky device is formed, in which a layer of CQDs is inserted between two metallic contacts, one of which is a transparent conductive oxide to allow light penetration (Fig. 2.14(b)). Heterojunction architectures, often with multiple layers of electron and hole transporting materials, as shown in Fig. 2.14(c), are more typical in the realization of sophisticated photodetector devices. Although there is more complexity in fabrication, the improved charge separation and reduced recombination afforded by such architectures significantly improves performance over single-layer devices [47]. Schematics with metal oxide/QD heterojunction has produced photodetectors with high detectivity as high as 10^{12} to 10^{13} Jones [19][50]. QD/QD heterojunctions have also been utilized, in which QDs with doping established through ligand functionalization, are combined to form devices with QD/QD interfaces, resulting in high specific detectivity in the range of 10^{12} Jones, fast response time [134], and high ON-OFF ratios [47]. Vertical architectures allow for more control over the device, and strategies such as interface passivation and functionalization significantly reduces traps and recombination to enhance device response [135]. However, compared to lateral photodetector schematics, vertical architectures significantly increase the probability of device shorts [33].

The fabrication of QD-based photodetectors is similar to QDPV and suffers from similar obstacles. Fabrication challenges regarding scalability, process reliability, and formation of reliable QD solids are the main barriers to the commercialization of QD devices. Compared to QDPV, QDs play one more significant role in photodetectors, as they determine the absorption spectrum, and therefore, the selectivity of the ensuing device. The range of detection of QD photodetectors are based on the QD size [30], and thus, tailoring QD properties affects the response of the photodetectors. QD-based photodetectors hold significant advantages in sensitivity over silicon photodetectors, as PbS QD photodetectors are capable of detection beyond the 940 nm limit of silicon detectors [134], while the tunability of other QDs allows detection of visible and UV wavelengths.

2.3.4 QD Nanocomposites

As conductivity losses due to poor carrier transport and recombination is a large issue in QD solids, many QD-based devices combine QDs with conductive polymers, shown in Fig. 2.15. Conductive polymers such as poly[2-methoxy-5-(2-ethylhexyloxy)-1,4-phenylenevinylene] (MEH-PPV), poly(methyl methacrylate) (PMMA), and others have been used in conjunction with QD photodetectors and devices to improve conductivity and charge separation, benefiting both photodetector and photovoltaic performance [12][19][21][30][33][36]. Polymers are either mixed with QDs to form a nanocomposite (Fig. 2.15(a)) or incorporated as a separate layer to form a heterojunction with QDs (Fig. 2.15(b)). As shown in Fig. 2.15(c), the typically much higher lowest unoccupied molecular orbital (LUMO) of these polymers prevent electrons entering the polymer from the QD's conduction band (CB), while the relatively matched highest occupied molecular orbital (HOMO) and valence band (VB) levels allow for hole conduction [20][21].

QD/polymer nanocomposites are advantageous through the creation of many heterojunctions throughout the bulk of the absorber ("bulk heterojunctions"), which significantly

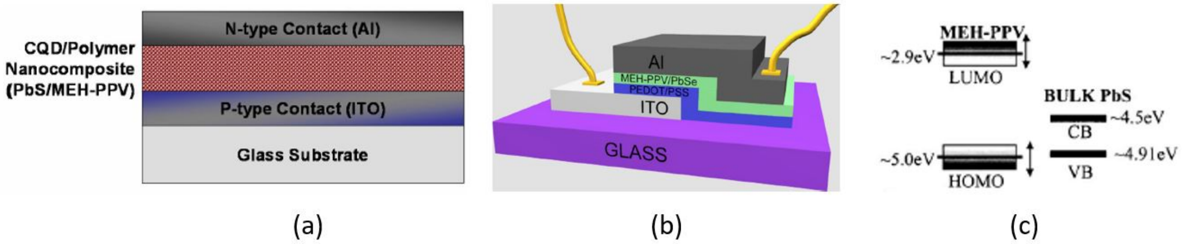

Figure 2.15: Simple QD infrared photodetectors based on (a) PbS QDs/MEH-PPV nanocomposite [12], and (b) PbSe QDs/MEH-PPV junction [20]. (c) Electron-blocking mechanism of MEH-PPV for PbS [21].

enhances charge separation and transport [13]. Nanocomposites have also been formed with QDs and other conductive materials, including metal nanoparticles and graphene [33]. The plentiful distribution of heterojunctions improves carrier transport over planar configurations, but may impart QDs with its partner's undesirable traits. The low mobility and instability of organic polymers results in decreased carrier mobility and faster degradation of the composite compared to standalone inorganic QDs [3]. The large surface energy differences between the organic/inorganic polymers and QDs results in poor interpenetration. Additionally, the increased frequency of these heterojunctions increases instances of interfacial charge recombination as well as separation [13]. Creating bulk heterojunctions with metal NPs mitigates the issues posed by organics, but also results in the production of traps for hot carriers [47]. Other conductive materials such as graphene aid in improving separation and transport, but may disadvantageously cause conduction to become too high, resulting in high dark currents that lead to poor device sensitivity and low ON-OFF ratios [47]. These disadvantages must be considered before ceding QDs to nanocomposites for bulk heterojunction structures.

2.3.5 Cupric Chalcopyrite QD-Based Devices

Heretofore, all record efficiency QD solar cells have been based on lead-containing PbS and perovskite QDs [125], benefiting from their advantageous optical properties and mature fabrication techniques [134]. However, the continued research focus on Pb-based QD applications hinders the goal of QD devices for consumer applications. Lead is well-known for its environmental and biological toxicity. The many advantageous physical, chemical, and optical properties of lead has resulted in its usage in many industries throughout history, causing it to be one of the largest global environmental pollutants [136]. Pb exposure causes damage to the central nervous system, renal system, reproductive system, and circulatory system, among others. Pb is associated with decreased cognitive performance in both children and adults, leading to behavioural issues and learning deficits in the former, and dementia in the latter [136]. Lead-containing nanomaterials cannot be safely applied to consumer goods made available to the general public.

Pb-based QDs are attractive due to its excellent absorption of the abundant near infrared (NIR) spectrum, producing photodetectors and solar cells with exceptional performance [47][134]. It is tantalizing to pursue Pb-based QDs for photovoltaic and photodetection applications; no other QDs have achieved equal performance. However, the notable toxicity of lead, combined with the inherent toxicity of nanomaterials [137][138], poses alarming implications for the commercialization of Pb-based nanoparticles and QDs. Therefore, the research of less-toxic QDs is critical to the future of consumer QD devices.

Cupric chalcopyrite QDs are promising as a less-toxic alternative to PbS QD absorbers. The (Zn)CuIn(S, Se) family of QDs have been applied with great success in QDSSC structures, keeping pace with the record-breaking efficiencies achieved by Pb-based QDPV. Pan et al's 2014 QDSSC used Type I CIS/ZnS QDs, which successfully achieved a 7.04% efficiency, at a time when the record efficiency for QDPV was 8.55% [16][56]. In 2015, Kim et al applied CISe QDs to a QDSSC with an efficiency of 8.1%; the record efficiency for QDPV was approximately 9% at that time [125]. In 2016 and 2017, ZCISe-based QDSSCs attained 11.61% and 12.56% efficiency, respectively, while the benchmark was between 10.6% and 13.3% [15][35][104][128]. The current record efficiency QDSSC is also based on a cupric chalcopyrite QD; in 2019, Zhang et al fabricated QDSSCs with a 13.08% efficiency using alloyed $\mathrm{ZnCIS_xSe_{1-x}}$ QDs [126].

Simulations by Scheunemann et al found that in planar metal oxide/CIS QD heterojunctions, carriers are lost beyond 40 nm of the interface, resulting in reduced collection [139]. For these reasons, the more plentiful interfaces formed by QDSSC structures have been more desirable for cupric chalcopyrite QDs. Conversely, as liquid electrolytes cause difficulties with fabrication and stability [104], it is more prudent to investigate solid state architectures. Furthermore, the majority of record efficiency QD solar cells have been based on metal oxide/QD heterojunctions. As (Zn)CI(S,Se) QDs are much less commonly applied towards heterojunction architectures, more investigation is required in this area. Even compared to other QDs, CuInS QDs show significantly defective structures, with deep traps that reduce carrier mobility [140]. CIS QDs' odd surface properties pose difficulties in forming high-quality interfaces. CuInSe QDs have shown better crystallinity, but the presence of Se does not fully mitigate toxicity concerns.

Similar to QD PV, although PbS QDs are also primarily employed in QD-based photodetectors, some success has also been achieved with solid state photodetectors based on CIS QD films. CIS QD photodetectors mainly have lateral architectures, whose small but present response to illumination have sufficed as proof-of-concept [141]. More sophisticated lateral structures have been demonstrated, with employment of a bi-layer to enhance detection, such as Hong et al's incorporation of up-conversion nanoparticles with CIS/ZnS QDs, which demonstrated sensitivity to NIR illumination [142]. Huang et al presented a lateral device employing a film of CIS CQDs, formed onto SnS_2 and pre-patterned Au/Cr electrodes, which showed high responsivity and enhanced photocurrent compared to devices lacking CIS QDs [58]. For lateral devices, the crystalline film formation of the CQD solids is extremely significant, due to the lateral traversal of carriers for collection. More sophisticated heterojunction photodetector structures, which have shown better performance, are mainly the domain of PbS-based QD devices. Although advanced device structures incorporating cupric chalcopyrite QD nanocomposites have produced devices with high photocurrent gain [143], responsivity [144], detectivity [36], and fast response [145], the issues arising from nanocomposite materials still pose issues for commercialization. Research of CIS QDs in sophisticated, multi-layered photodetector architectures are comparatively rudimentary, and require significant investigation.

In the pursuit of device improvement, success arises from improvement of both material and architecture [104]. Although great strides have been made on Pb-based QD photovoltaics, their toxicity and environmental contamination make their continued development problematic for commercial optoelectronics, motivating the investigation of less-toxic alternatives. The QDSSC architectures utilized for (Zn)CI(S,Se) QDs are not sustainable for large-scale manufacturing and commercialization. Therefore, QDPV based on metal oxide/CIS QD heterojunctions are a promising area of investigation. Research efforts must approach this problem systematically from two perspectives: enhancing the defective surfaces and lattices of cupric chalcopyrite nanoparticles, and seeking improved architectures for CIS-based QD devices. The intrinsic advantages of QDs have continuously propelled interest in QD-based photovoltaics and devices, leading this field to progress rapidly over the last decade. Although more progress is needed for CIS QD-based heterojunction photovoltaic and photodetection devices, it is a worthy undertaking to secure a future with sustainable, mass-producible QD devices. The extraordinarily fast pace of nanotechnology research provides a favourable outlook for the future of mass-produced, market-dominant quantum dot-based devices.

Chapter 3

Synthesis of Core Copper Indium Sulfide Quantum Dots

Achieving safe and large-scale production of QDs is critical for industry applications. Top-down QD synthesis methods are typically low-yield and do not allow impactful tailoring of QD properties, making them unsuitable for large-scale adaptation. While bottom-up colloidal QD synthesis is the most facile method of QD production, the synthesis of toxic Cd- and Pb- based QDs involve hot-injection processes at high temperatures, posing great safety risk in industrial processes. Therefore, a methodology for scalable, one-pot synthesis of core CIS quantum dots was developed in this work. The synthesis was completed at lower reaction temperatures than previously reported in literature, and yielded gram-scale throughput of QDs. The resulting quantum dots showed intense photoluminescence, achieving a maximum PLQY of 10%. The synthesized core CIS QDs were evaluated using optical, structural, and elemental characterization. Synthesis via low-temperature regime processes, wide range of tunability in the visible-to-IR range, and intense and long-lived emissions make these less-toxic, CIS-based QDs attractive for large-area, scaled-up device applications such as photovoltaics, light-emitting diodes, sensors, and bioimaging. The following sections present the development and investigation of the one-pot, non-injection, low-temperature synthesis of less-toxic CIS QDs.

3.1 CIS QD Structure and Mechanisms

Unlike the more common binary QDs, cupric chalcopyrite QDs possess unique ternary structures that allow greater structural and compositional flexibility. It has been shown that for such QDs composed of multiple cations, employing different molar ratios of Cu, In, and S precursors allow control over their growth rate, as well as structural and optical properties [146]. Thus, the optoelectronic properties of CIS QDs can be manipulated by adjusting the composition of their complex lattices via elemental stoichiometry. Although there is no consensus on the optimal Cu:In precursor ratio, which may vary for different processes, Cu-deficient ratios have been preferred due to favourable generation of radiative optical pathways [146][147]. There is some evidence that increasing sulfur precursors also leads to improvement in optical behavior [148], although not to the extent achieved via cation ratio variation. This section analyzes the unique aspects of CIS QDs' structures and their impact on optical mechanisms. The understanding of CIS QDs presented in this section is critical to the development of effective synthesis strategies.

3.1.1 The CIS QD Lattice

Cupric chalcopyrite bulks are not new to the world of optoelectronics devices, as they occupy an important place among thin film materials used for Gen II solar cells. The CIGS family materials have a chalcopyrite lattice, a tetragonal crystal structure derived from the zinc-blende system [149]. Unlike II-VI semiconductors (such as CdSe and PbS), CIS and other cupric chalcopyrite QDs are a two-cation compound, with each cation forming separate bonds with the S^{2-} anion. These bonds give rise to two new ionic compounds within the CIS system: Cu^{+}-S^{2-} bonds become Cu-S^{-} donors while In^{3+}-S^{2-} become In-S^{+} acceptors. The Cu-S bond is approximately 5% smaller than the In-S bond, causing lattice distortions if either cation is placed on sites intended for the other [149]. The lattice of ternary I-III-VI semiconducting QDs such as CIS accommodate many off-stoichiometric compositions, allowing more flexibility than their binary II-VI counterparts [149]. Due to the differences in the lengths between Cu^{+}-S^{2-} and In^{3+}-S^{2-} bonds, changing the cationic stoichiometry (Cu/In ratio) results in changes to the lattice, and therefore QD bandgap [150]. The unit cell parameter for CIS QDs is given by Equation 3.1 [149]:

$$d = \frac{a}{\sqrt{h^2 + k^2 + \frac{l^2}{(c/a)^2}}} \tag{3.1}$$

In this relation, d is interplanar spacing, a and c are unit cell parameters, and h, k, l are Miller indices. In a tetragonal lattice, $a = b$ and all angles are 90°. Changes to the Cu and In precursor ratio produces Cu or In vacancies, and interstitials of the more abundant

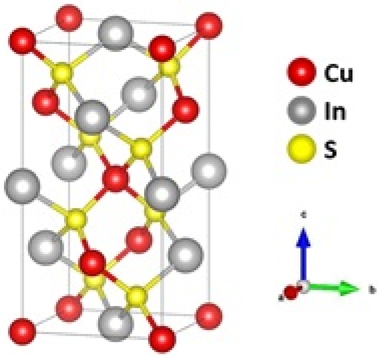

Figure 3.1: CIS QD lattice, referenced from [22].

cations positioned in sites intended for the deficient cations. Substitution of In at Cu sites (or vice versa) produces deformations of the lattice, and changes a and c. Fig. 3.1 depicts the unit cell of a CIS QD chalcopyrite lattice. Due to the combative dual-cationic system of its lattice, CIS QDs are very defective, with significant trap formation [140]. The intrinsic defects and cationic off-stoichiometry of CIS QDs contribute significantly to unique features of their optical properties [56][68][149], which deviate from that of their simpler binary counterparts.

3.1.2 Emission in CIS QDs

Unlike bulk semiconducting materials, CIS QDs radiative emission is primarily defect-dependent, resulting from internal donor-acceptor pair (DAP) recombination through trap states, rather than band-to-band recombination [114]. Instead of relaxing from the conduction band to valence band, excited electrons in CIS QDs descend from a donor trap state near the conduction band to an acceptor trap state near the valence band, producing emission (Fig. 3.2). DAP recombination in CIS QDs occurs from donor sulfur vacancies (V_S) and In interstitials in Cu (Cu_{In}), to acceptor copper vacancies (V_{Cu}) [93][149].

There are two main recombination pathways in CIS QDs: non-radiative surface traps and radiative internal states [31]. Non-radiative recombination occurs via pathways provided by surface trap states, and compete with radiative internal DAP recombination. To better understand the recombination mechanism in CIS QDs, a conceptual sketch map of its energy band structure is presented in Fig. 3.2.

Radiative recombination is increased by i) reducing non-radiative recombination states and ii) increasing radiative DAP recombination states. Non-radiative recombination path-

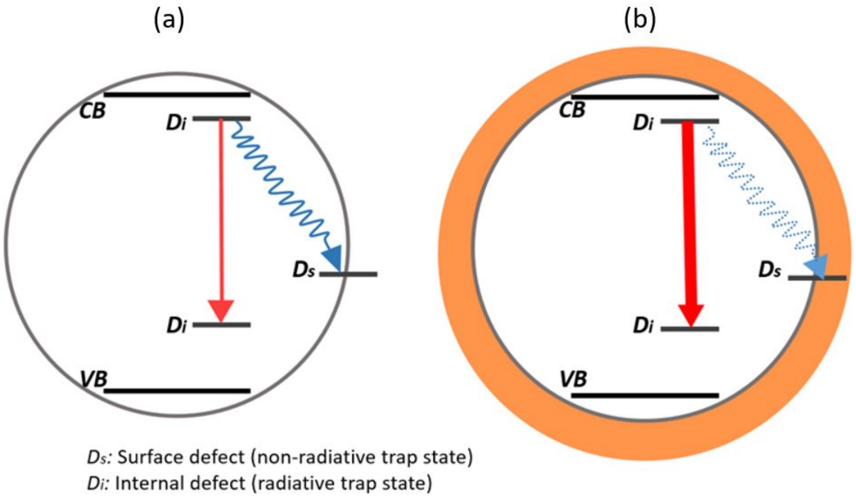

Figure 3.2: Energy band structure for CIS QDs (a) before and (b) after surface passivation.

ways are removed by passivating the surface to eliminate surface traps, via strategies such as overcoating or surface reconstruction (illustrated in Fig. 3.2(b); discussed further in upcoming chapters). As a result, recombination via radiative channels dominate, leading to improved optical quality of the QDs [2][151]. Radiative internal DAP states are increased by manipulating precursor stoichiometry, but as emission weakens with overabundance of DAP states (due to mutual quenching), there is a limit to the optical enhancements achieved with creating more states [149]. Furthermore, emission is also affected by temperature, as CIS QDs are susceptible to "thermal quenching effects", where non-radiative transitions in CIS QDs increase with temperature [78].

CIS QDs display characteristically broad emission, with extreme Stokes-shifting with respect to absorption. This mainly stems from the DAP recombination [68][67][75][78][152]. As the internal defect states involved in the radiative recombination occupy a broader range of energies, it follows that the resultant transitions also have more variations in energy compared to band-to-band transitions of bulk semiconductors.

3.2 Synthesis of Stoichiometric CIS QDs

Due to the expected wide-spread use of nanomaterials, scalability, throughput, and safety are major considerations in creating QDs for industry applications. Synthesis of less-toxic QDs at lower temperatures is favored due to simplicity, control, and safety. As CIS QDs belong to a less-developed area of nanomaterial research, their synthesis and functionalization is less adequately covered than their more established II-VI counterparts. The following sections present the non-injection, one-pot synthesis of CIS-based QDs in the low reaction temperature regime, with gram-scale throughput. The synthesis procedure is first discussed in detail, followed by optical characterization. Subsequent subsections provide detailed analysis of reactions taking place throughout the process, in effort to better elucidate the nature of ternary cupric chalcopyrite QDs.

3.2.1 Synthesis Setup

Synthesis of the CIS QDs is executed inside of a three-neck glass reaction flask (Cole Parmer) under an oxygen- and moisture-free atmosphere. A Schlenk line connected to a nitrogen gas line and a vacuum pump is used to maintain an inert atmosphere inside of the reaction flask. Although the synthesis process can proceed under ambient when provided with the correct kinetic conditions, this more intricate setup protects QDs from humidity degradation, as QD adsorption of H_2O from ambient humidity undesirably shifts band properties and compromises charge transport [113].

The vacuum line is connected to a condenser, which is used to condensate and return evaporated precursor materials to the reaction flask. A cold trap connected between the condenser and vacuum line is used to further capture and densify fumes before they reach the exhaust. Water is flowed through the condenser, above the reaction chamber, in order to cool the condenser. The entire setup is housed within a fume hood. Fig. 3.3(a) shows the synthesis setup schematic.

The reaction flask is mounted onto a stirring heating mantle (Cole Parmer); an RF coil stirring controller (Cole Parmer) with a magnetic stirrer, and a proportional-integral-derivative (PID) controller (Omega) are used to regulate stirring and temperature, respectively (Fig. 3.3(b)). The heating mantle is filled with silica beads to ensure even heat distribution around the base of the flask, and the top of the flask is bundled in synthetic insulation. The center neck of the flask is connected to the condenser, which in turn connects to the Schlenk line; vacuum is applied through this neck. Nitrogen flow is controlled through one of the side necks connected to the Schlenk line. When performing synthesis, a thermocouple is inserted through this neck to monitor the temperature; this thermocouple is connected to the PID controller to ensure accurate T input. The final, unconnected neck is used for extraction and insertion under an inert atmosphere; it is sealed with an airtight rubber septum with a fold-over skirt. This schematic is designed to contain the

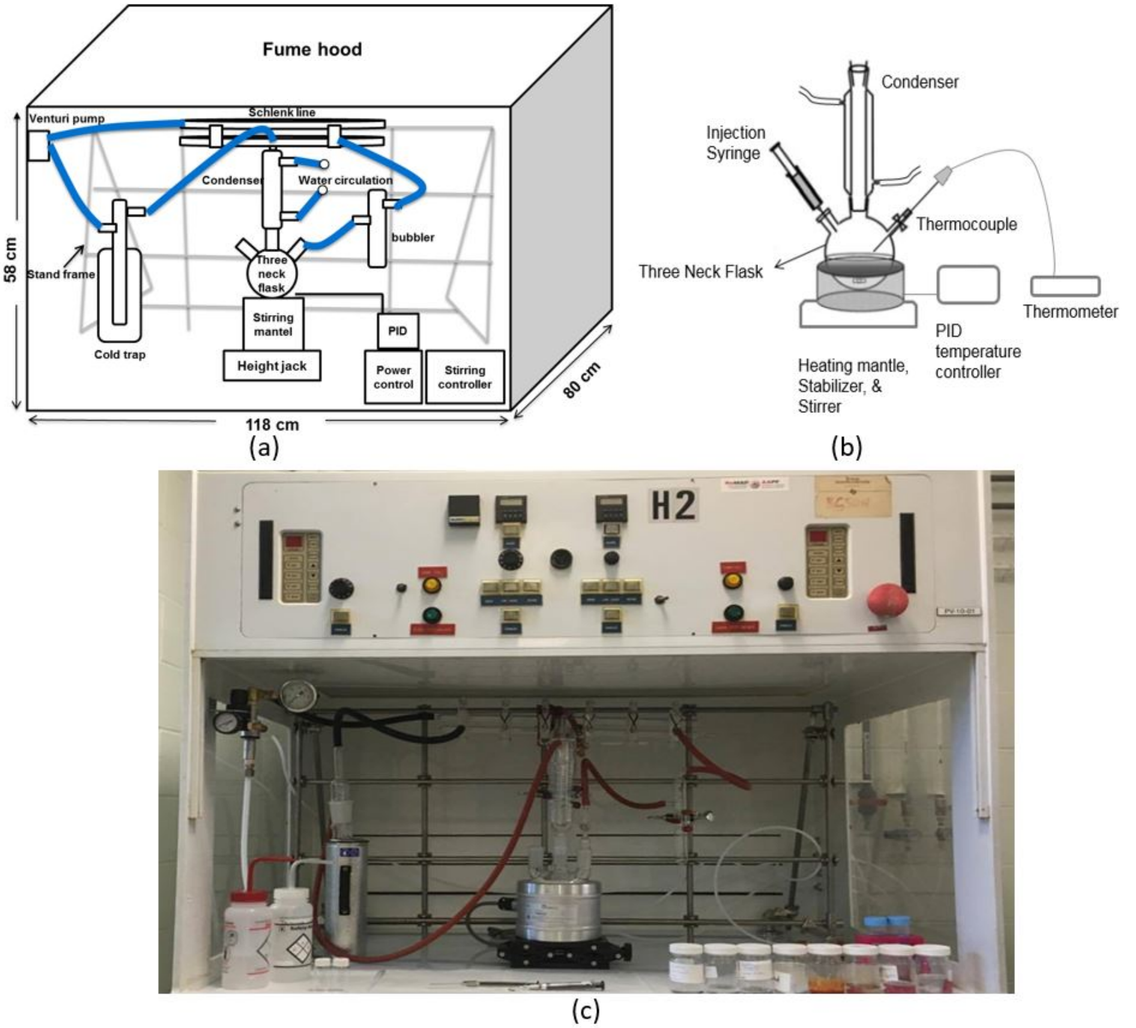

Figure 3.3: Diagrams of (a) synthesis tower used in QD synthesis and (b) reaction flask; (c) photograph of synthesis tower.

reaction within the flask, thus minimizing exposure and contamination. Fig. 3.3(c) shows a photograph of the synthesis setup.

3.2.2 CIS QD Synthesis Procedure

In a typical synthesis with a stoichiometric 1:1 ratio of Cu:In precursors, 1 mmol (0.19 g) copper iodide (CuI), 1 mmol (0.292 g) indium acetate ($In(Ac)_3$), and 5 mL 1-dodecanethiol are added to the 3-neck reaction flask. Other stoichiometries will be discussed in later sections. The flask is sealed and degassed for 15 minutes, followed by 20 cycles of nitrogen purging. In the initial phase of growth, the stirring heating mantle is set to input to obtain a solution temperature of 80°C inside the chamber. From room temperature, the solution reaches this temperature in approximately 15 minutes. The reaction is kept at this temperature for 30 minutes, until the precursor mixture decomposes into a transparent, nearly clear liquid, indicating the onset of nucleation. The one-pot nature of this synthesis is enabled by DDT, which serves multiple functions as the sulfur and ligand precursor, solvent, reaction control, and stabilizer [141].

From the initial growth at 80°C, the solution temperature is gradually raised to 120°C degrees in 5-10°C increments, with 10-20 minutes of growth time between each temperature. Throughout the growth process, the QD solution undergoes a visual color change from green, to yellow, orange, red, dark red, and finally, black. Fig. 3.4 shows the colour progression of synthesized CIS QDs, as stills obtained from film. The increasingly red-shifting solution colour correlates to increase of nanoparticle size, and indicates colloidal nanocrystal growth. The solution temperature is kept at 120°C for the last phase of growth. Maintaining a steady final temperature is significant in ensuring the yield of high-quality of colloidal CIS quantum dots.

As CIS quantum dots increase in size over the duration of synthesis, extraction time and synthesis length depends on the desired quantum dot emission wavelength. Fig. 3.5(a) shows aliquots of CIS QDs extracted after growth times of 5-140 min following nucleation. Fig. 3.5(b) and (c) show the normalized emission and absorption of QDs withdrawn at different points of growth. Photoluminescence was investigated using a fluorescence spectrometer (Edinburgh Instruments) with a 450W Xenon lamp as the excitation source. Upon excitation at 380 nm, the emission was recorded using a cooled photomultiplier detector. Absorption spectra were recorded using a UV-vis spectrophotometer (Perkin-Elmer Lambda 1050). QD concentrations of 10 mg/mL and 1 mg/mL were used for emission and absorption measurements, respectively. Lower concentrations were used for absorption to avoid detector saturation. Broad, visible to infrared spectra in the 600-800 nm range

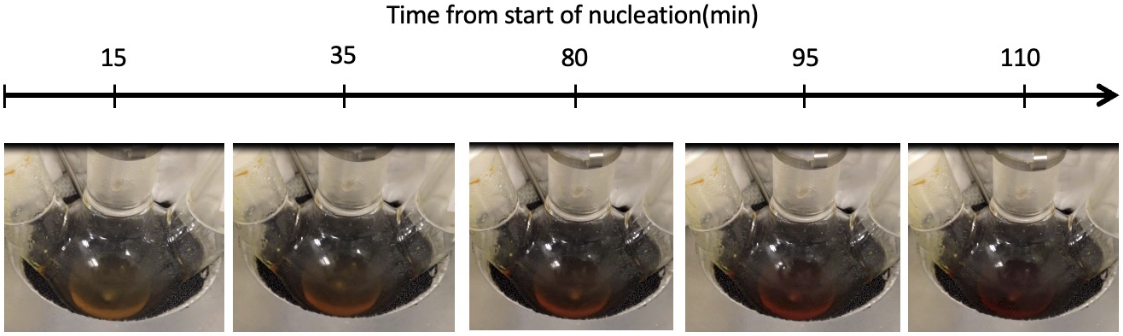

Figure 3.4: Colour change of synthesized CIS QD solution, indicating quantum dot growth.

(yellow to infrared) were obtained. The characteristic broad emission of the CIS QDs, stemming from DAP recombination, is apparent. The emission spectra is significantly Stokes shifted from absorption spectra. Some emission spectra appears dual-peaked due to lattice defects, which produce more mid-gap states, and solution polydispersity; this is remedied through more careful control over the temperature during synthesis.

The synthesis reaction is halted by briefly immersing the flask into a cool water bath, or injecting with cold solvent (hexane). The synthesized CIS quantum dots are extracted through the stopper-sealed neck using a clean syringe. The freshly synthesized colloidal CIS quantum dot solution is dispersed in hexane, precipitated with addition of anti-solvents (acetone or ethanol), and purified using centrifugation (8000 rpm at 5 min over several cycles). Finally, the precipitate is dried under nitrogen, and re-dispersed in hexane. This process is capable of producing as much as 800 mg of QDs per run. The synthesized DDT-ligated core-only CIS QDs will remain stable for several weeks.

3.2.3 Regimes of Colloidal CIS QD Growth

The colloidal, one-pot synthesis of CIS QDs is given in 4 regimes: Decomposition, Nucleation, Ripening, and Termination. Each regime is determined by the reaction temperature within the flask, notably the temperature upon which nucleation occurs (T_n) and the terminal temperature upon with QDs overshoot the optimal size and become unstable (T_t). The reaction temperature dictates the kinetics of each regime.

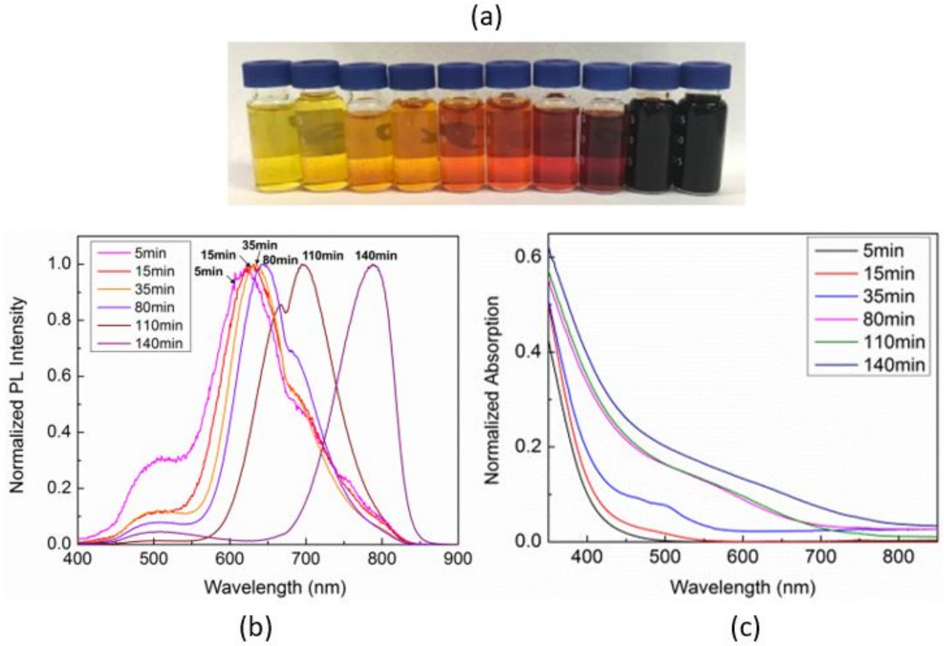

Figure 3.5: (a) Core CIS QD solutions with corresponding (b) emission and (c) absorption spectra; growth time refers to time from nucleation. The shoulder at 670 nm originates from a step in quantum efficiency of the detector.

I. Decomposition, $\boldsymbol{T} < T_n$

The synthesis reaction begins when the solid cationic precursors dissolve into the DDT. With heating and stirring, CuI, $In(Ac)_3$, and DDT decompose to their elemental and molecular components. This is the Decomposition Regime, in which QDs have not yet began to form, but the precursors separate, releasing the Cu^+, In^{3+}, and S^{2-} ions that form the basis for the CIS QD cores. At this point, the synthesis solution is thick, bright yellow, and slightly powdery.

II. Nucleation, $\boldsymbol{T} = T_n$

As T passes reaches T_n (80°C for the CIS QDs presented in this work), the synthesis solution enters the Nucleation Regime, in which nanocrystal cores begin to form. This initial stage of QD growth is also known as focusing of the size distribution, or "focusing". The clarifying of the synthesis solution signals transition from Decomposition Regime to Nucleation Regime. At this stage, the QDs in solution are overall fairly small; monodispersity and nanocrystal concentration is high. Notably, if temperature variations exist within the reaction vessel, partial nucleation will occur. In this situation, portions of the synthesis solution with fully decomposed precursors will begin nucleation, while masses of congealed, non-decomposed precursors will remain until they are broken down. This results in uneven nucleation and polydispersity within the solution, and should be avoided.

III. Ripening, $T_n < \boldsymbol{T} < T_t$

As nucleation saturates, QDs enter the Ripening Regime, also referred to as "defocusing" or "Nano-Ostwald Ripening". In this regime, smaller QDs decompose due to their high surface energies, contributing their elemental components as raw material to increase the size of larger nanocrystals. The total number of QDs in the system decreases, while the average QD size increases. In this stage, the synthesis solution undergoes a visual colour change, corresponding with increased size and redshift of PL emission. This regime requires the gradual, consistent increase of input temperature beyond T_n. The reaction may be halted in this regime when the desirable colour is obtained.

IV. Termination, $T_t \leq \boldsymbol{T}$

CIS QDs possess an optimal size, in which all precursors are completely consumed, and their surfaces are optimally passivated with the DDT ligands. The optimal size corresponds

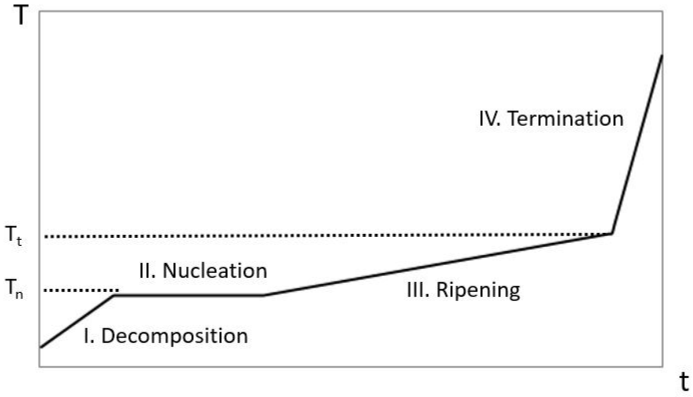

Figure 3.6: Regimes of CIS QD Synthesis.

to a specific terminal temperature (T_t, approximately 150°C here), beyond which improperly passivated, overly large QDs with poor solubility and incomplete surface passivation are obtained. Higher temperatures may even decompose attached ligands and precipitate them in reaction mixture, where they do not contribute to QD surface passivation [95]. Thermal runaway occurs beyond T_t, eventually sintering the QDs and decomposing them.

Fig. 3.6 illustrates the four synthesis regimes. Time is arbitrary; the onset temperature of each regime is the most significant in determining QD growth. QD growth can complete in under 10 minutes to over several days, contingent on rate of temperature increase. Although the duration of the reaction does not determine the onset of each regime, the speed of synthesis significantly affects the quality of the QD lattice, discussed later.

3.2.4 Optimal Sizing

The synthesis reaction is typically halted before reaching the terminal temperature, curbing the size and emission of the QDs. As seen from the normalized emission presented in Fig. 3.5(b), the emission curves obtained for QDs with emission between 650 and 800 nm are the most selective (80-140 min), showing the highest intensities. The best PL intensity and PLQY were achieved for the dark-red QDs with emission peak at 700 nm, corresponding to a growth time of 110 min after nucleation. Based on the quality of the QDs' optical properties, this was identified as the optimal size for QDs synthesized using the stoichiometric ratio presented above. At this stage of growth, the QD size, precursor consumption, and DDT ligand coverage of QD surface is near-optimal. The range of

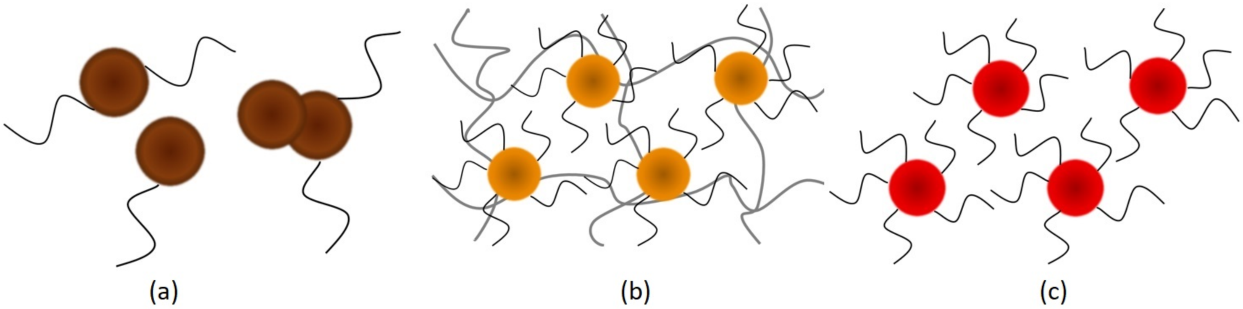

Figure 3.7: Ligand coverage and QD stabilization for QDs that are (a) too large, (b) too small, and (c) optimal.

optimal QDs size varies with cationic stoichiometry.

Beyond the optimal size, the QDs emit in the infrared wavelength range. Although they are still capable of emission, dispersion of these QDs in solvent results in a sabulous, gritty solution in which they cannot stay suspended. The QDs grow too large for sufficient surface passivation, resulting in QDs agglomerating and fusing together. This is due to two reasons: i) complete consumption of DDT precursors, and ii) lack of surface sites for ligand attachment. As QDs become larger, the different facets are exposed, and more facets with fewer sites for ligand binding appear [129]. Increased addition of DDT precursors does not resolve this issue, as the surfaces of the large QDs do not have sufficient binding sites, and excess DDT would simply remain within the solution as an unwanted by-product of the reaction. The QDs have poor stability and sub-par optical performance. The correlation between QD size and ligand coverage is shown in Fig. 3.7.

QDs extracted at much shorter wavelengths become gelatinous when dispersed in solvent. Beneath this optimal size, emissive QDs are obtained, but their intensity is much smaller compared to the emission of optimally-sized QDs. This is consistently observed in literature, in which CIS QDs with shorter peak emission wavelengths tend to be optically inferior [121]. At sizes smaller than the optimal size, the passivation sites on the smaller QD surfaces become saturated with bonded DDT, and excess DDT remains in the solution. As well, the excess DDT cross-link with each other, other organic by-products, and ligands attached to QDs, forming strong, insulating networks of bonded polymers, which trap the QDs and decrease optical performance. The trapped QDs can be extracted by continuous purification of the QD solution to break down the cross-linked DDT matrix, but this is time-consuming, and presents the threat of stripping ligands from the surfaces of the QDs.

When QDs are grown to optimal size, the precursor DDT is adequately consumed, and the small amount of excess DDT and other unreacted by-products are easily removed through purification. The surface traps become modified and reduce in concentration in presence of sufficient thiol groups, resulting in good surface coverage. DDT optimization is important for achieving high-quality core QDs. The quality of these QDs are affirmed by their excellent optical performance.

3.2.4.1 Impact of QD Size on QD Films

Solutions containing non-optimally sized QDs form poor-quality films. In a synthesis reaction that is halted before the QDs reach optimal size, the QDs are trapped in cross-linked organic DDT matrices. This translates to a glossy film with poor solvent evaporation due to solvent trapping by the DDT matrix. This makes application and manipulation difficult; the QD films do not stabilize and are removed from the substrate easily. The uniformity and smoothness of the films are very poor, as the long DDT molecules' winding nature make it difficult to control QD position on the substrate surface. Some areas have large clusters of QDs intertwined in the DDT matrix, while other areas have insufficient coverage, leaving the substrate bare. These films have poor conduction due to the insulating DDT molecules, which provide large interdot separation.

QDs that are grown too large form cracked, discontinuous films with poor QD distribution across the substrate. These large QDs have poor surface ligand coverage, and are fused and agglomerated in solution. The poor solution dispersion leads to difficult control over their film formation properties. Their poor surface properties result in the formation of amorphous films with poor substrate coverage, leading to great risks of device shorting in vertical architectures.

3.3 Effect of Temperature on CIS QD Growth

Reaction temperature, T-ramp profile, reaction time, precursor concentration and flow rate, and surfactant content are the main synthesis parameters that affect the growth rate and quality of the quantum dots. Among these, reaction temperature is particularly notable contributing to the structural and optical properties of CIS QDs, as it determines kinetics of precursor decomposition, core nucleation, and size distribution. High-T synthesis results in faster growth of large QDs with narrow bandgaps, crystalline structures, narrow emission peaks, and gradient composition [120]. However, undesirable reactions can also arise from such processes, such as precipitation of decomposing ligands within the reaction mixture [95]. It is critical to achieve careful control of temperature throughout the duration of QD synthesis. The low reaction temperature of this synthesis process is advantageous, as it prevents undesirable reactions and unwanted precipitation of ligands [120].

From a purely kinetic view, sufficient thermal energy must be provided to trigger the onset of each temperature regime, but the duration of each thermal regime is inconsequential. However, the duration of each regime has significant effect on the lattices, and therefore the structural and optical properties of QDs. The temperature ramping profile, which determines the duration of each regime, is highly significant in influencing the environment of QD growth, and therefore, contributes to determining the growth rate, shape, and quality of the QDs [153].

CIS QD synthesis was conducted under two temperature ramping schemes: abrupt and gradient. In abrupt T-ramping, the initial temperature set point is intentionally positioned beyond the nucleation temperature, directly to a value beyond the Ripening Regime ($T_t < T$), and halted before sintering. CIS QD synthesis completes more quickly using abrupt temperature ramping, the higher the set temperature, the faster the growth.

In the gradient T-ramping scheme, the temperature is increased slowly, allowing a duration of soaking at temperatures within each regime. The recipe presented in Section 3.2.2 uses gradient ramping. Although the specifics of duration is dependent on each synthesis, this entails a first set point to the nucleation temperature, followed by a soak duration until all precursors have decomposed and nucleation has occurred. Subsequently, the temperature is slowly increased (5-10°C increments for 5-10 min in this work) to allow the QDs to slowly grow larger. The final temperature should not exceed the terminal temperature. Fig. 3.8 shows two typical abrupt and gradient T-ramp profiles. It can be seen that the gradient T-ramping scheme extends the synthesis time to nearly three times the length of the abrupt T-ramping scheme.

The products of the two different ramping schemes show variation, as the temperature ramping determines growth rate and QD shape and quality [153]. In abrupt T-ramping, higher temperatures and faster growth speed combine to produce improperly formed, low-quality CIS QDs with poorer lattices and less ligand passivation sites on their surfaces. The abrupt scheme provides a large amount of thermal energy in a relatively short duration, which does not allow sufficient time for the cations comprising the QD lattice to traverse to optimal, energetically favourable positions in the lattice. Meanwhile, the slower growth and more gradual thermal energy input of gradient T-ramping affords more opportunity for cations to traverse to energetically favourable positions, as well as providing in-situ annealing that results in lattices with fewer defects and better crystallinity. Ligand coverage is also better on QDs grown using gradient T-ramping; the less defective surfaces provide more passivation sites that allow greater ligand coverage.

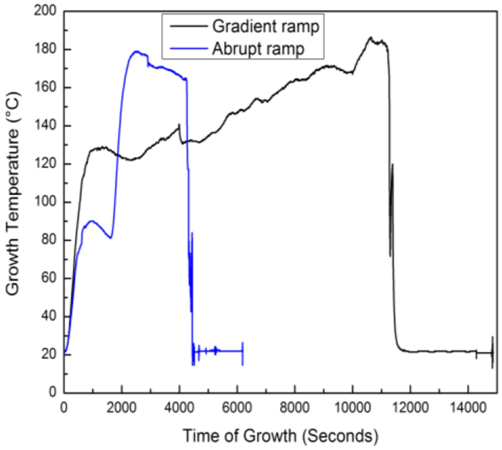

Figure 3.8: Abrupt and gradient temperature ramping profiles for CIS QD growth.

Both abrupt and gradient T-ramping pass through all of the QD formation regimes, but this will occur so quickly in abrupt ramping, that it is nearly impossible to halt the reaction at the desired optimal size, before the QDs reach the Termination Regime. The gradient T-ramping scheme is more desirable, as slower synthesis allows more control over the reaction, without overshoot of the desired QD size. If thermal runaway occurs, the synthesis reaction can exit gradient T-ramping and enter abrupt T-ramping at any point of the reaction. High temperatures decompose the QDs, resulting in destabilization and agglomeration due to insufficient ligand coverage [67]. Temperature must be carefully controlled to prevent overshooting the nucleation and terminal temperatures.

Photoluminescence emission and absorption spectroscopy were used to compare the quality of the quantum dots produced using the abrupt and gradient temperature ramping profiles. The absorption, PL, and decay lifetime of core CIS QDs synthesized using gradual and abrupt T-ramps are shown in Fig. 3.9. Time-resolved spectroscopy was investigated using a fluorescence spectrometer (Edinburgh Instruments) with a pulsed LED of 375 nm wavelength, 5 MHz repetition frequency, and 943.3 ps pulse width. The decay curves were obtained by time-correlated single-photon counting (TCSPC) method with a pulsed laser (EPLED) used for excitation at a wavelength of 380 nm, with 5 MHz repetition frequency, pulse width of 943.3 ps, 20 μw power, and 10 nm bandwidth. The decay data was fitted to decay functions using fluorescence analysis software technology software (FAST, Edinburgh Instrument), which allowed more than four decay constants to be obtained by multi-exponential tail fitting analyses, ensuring that $\chi^2 < 1.3$. QD concentrations of 50 mg/mL and 4 mg/mL were used for PL/lifetime and absorption measurements, respec-

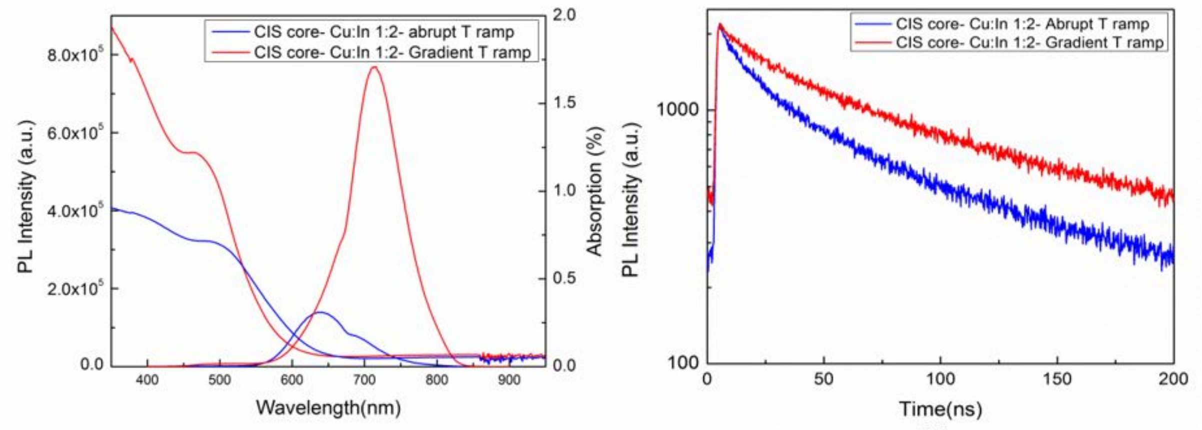

(a) (b)

Figure 3.9: (a) Absorption, PL, and (b) decay lifetime spectra of the CIS QDs synthesized using abrupt and gradient T-ramps.

tively. Cu:In molar compositions of 1:2 were used for both, as the difference in QD quality between abrupt and gradient T-ramping was not as apparent for the 1:1 stoichiometric ratio; precursor stoichiometry will be further discussed in later sections. The PL of the core QDs grown using gradient T-ramp showed almost 10-fold improvement compared to those produced by abrupt T-ramp. The slow growth provides in-situ gradual annealing, allowing for increased crystallinity, yielding core QDs with fewer vacancies and defect sites, and more effective ligand coverage. The results indicate that the ramping rates have greater impact than the final growth temperature, and are key in developing processes in the low-T regime. Large Stokes shifts of 230 nm and 140 nm can be seen for the QDs grown using gradient and abrupt T-ramps, respectively.

Photoluminescence quantum yield was obtained using an integrating sphere, with the Edinburgh PL/FL system. PLQY of 5% was obtained for core CIS QDs grown with abrupt T-ramp. Core CIS QDs with PLQY of 10% and improved lifetimes were obtained using the gradient T-ramp. Therefore, gradient ramping was adapted as the primary method of temperature ramping. The synthesized QDs remained stable when tested even after several weeks. No significant change was observed in the stability of the QDs grown using the two temperature ramp profiles.

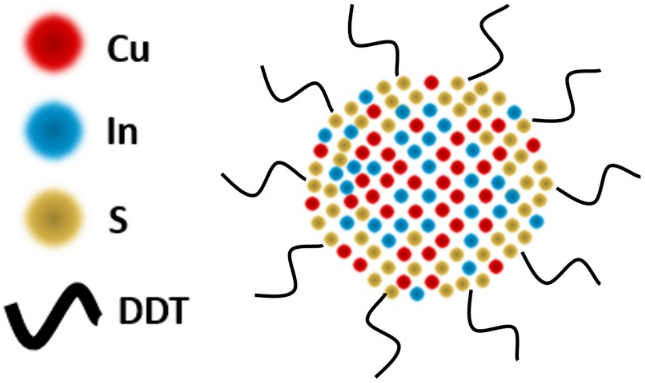

Figure 3.10: Schematic of graded lattice of CIS core QDs. This schematic is illustrative; the core contains sulfur, but to a less concentrated degree than the surface.

3.4 Cationic Stoichiometry

The two-cation system of the CIS QD core gives rise to its flexible and off-stoichiometric lattice. Both Cu^{+} and In^{3+} are electron donors which form separate bonds with the accepting S^{2-} anion. Furthermore, DDT precursor serves as both sulfur and ligand source. As the DDT ligand attaches onto the QD surface via its thiol group, CIS QDs tend to have a greater S concentration on its surface. This leads to a graded structure shown in the schematic in Fig. 3.10, with a more metallic core and greater concentration of sulfur on the surface.

As the flexibility of the ternary CIS QD lattice accommodates significant off-stoichiometric variations, the optical and electrical properties of the QDs can be tuned by changing the stoichiometric ratio of Cu:In cations. Eq. 3.2 above showed the interplanar spacing to be a function of unit cell parameters a and c, which are both impacted by the bonding lengths between bonding species. Because of the difference between the lengths of Cu-S and In-S bonds, changing their ratio induces changes to the lattice. The extent of lattice deformation can be quantized by two parameters: tetragonal strain (η) and anion displacement (u). The tetragonal strain parameter describes the crystal distortion of the tetragonal lattice compared to a standard zinc-blende phase; it is given as Equation 3.2 [149]:

$$\eta = \frac{c}{2a} \tag{3.2}$$

Cell parameter a, corresponding to the shorter edge of the tetragonal lattice along the x-axis, decreases as Cu:In ratio is increased. c (parallel to the z-axis), the "height" of the tetragonal lattice, increases with Cu:In ratio; a and c are inversely affected by Cu deficiency [149]. This can be understood from viewing the placement of Cu and In atoms in Fig. 3.1. Increasing the Cu:In ratio induces excess Cu, which would become interstitials at In sites. As Cu-S bonds are shorter than In-S, this produces a compressive strain that elongates c and reduces a. Tetragonal strain approaches unity as Cu:In approaches 1:1, and for Cu-excess stoichiometric ratios [149].

Equation 3.3 provides a quantitative calculation for anion displacement, u, which describes the number of anions displaced from an ideal tetrahedral lattice site [149]:

$$u = \frac{1}{4} + \frac{{R_{CuS}}^2 - {R_{InS}}^2}{a^2} \tag{3.3}$$

R_{CuS} and R_{InS} give the lengths of Cu-S and In-S bonds, respectively. Anion displacement is maximum (0.239) at Cu-deficient ratios, minimizing at Cu:In 1:1 and slightly increasing with excess Cu [149]. Viewing Fig. 3.1, Cu deficiency results in In cations inserted at Cu sites, replacing Cu-S bonds with longer In-S bonds that produce a tensile strain and cause lattice deformation. Therefore, both Eq. 3.2 and 3.3 indicate that changes in the Cu:In ratio contribute to deformations in the CIS chalcopyrite lattice [149].

The CIS QD recipe presented earlier utilizes a stoichiometric 1:1 Cu:In precursor ratio. However, in the majority of this work, off-stoichiometric, Cu-deficient 1:2 ratios were primarily used. In Cu-deficient CIS QDs, Cu vacancies and In interstitials are preferably generated, producing radiative recombination pathways and improving the QD optical quality [148]. Thus, Cu-deficient Cu:In molar ratios were studied to determine the effect on the synthesized QDs' optical, electrical, and structural properties. The results are presented in the following sections.

3.4.1 Copper Deficiency

Inducing copper deficiency in synthesis produces lattice deformations that affect the optical properties of the resultant CIS QDs. In addition to lattice distortion, Cu-deficient CIS QDs generates increased Cu vacancies and In-in-Cu site interstitials. As DAP states form from $2\mathrm{V}_{\mathrm{Cu}}^{-} + \mathrm{In}_{\mathrm{Cu}}^{2+}$ pairs, Cu deficiency promotes the increased formation of radiative recombination pathways [31][114][148][149]. For this reason, Cu-deficient stoichiometry are

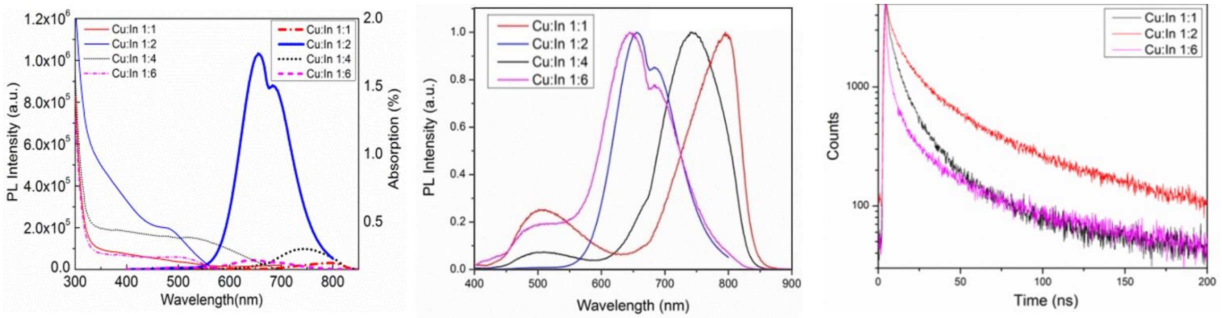

(a) (b) (c)

Figure 3.11: Optical characterization of synthesized CIS QDs: (a) PL emission and absorption measurements of CIS QDs synthesized with Cu-deficient ratios, and (b) comparison of emission peak positions. (c) Lifetime measurements performed for CIS QDs synthesized with different precursor ratios.

preferable for synthesis [146][147]. The use of Cu-deficient stoichiometry leads to improved PLQY [149] and higher luminescence [154]. Cu deficiency corresponds to In-excess and In occupation of M^1 metal sites, which produces higher lifetimes and better photoluminescence emission [154].

Cu deficiency is typically induced through addition of excess In precursors rather than removal of Cu precursors; each excess In atom induces two Cu vacancies [154]. It is recommended to use excess In while keeping Cu constant (i.e., 1 mmol:2 mmol Cu:In rather than 0.5 mmol:1 mmol), to ensure that there is sufficient input of In cations to occupy vacant Cu sites. It has been shown that temperature has effect on stoichiometry [31], in which the precursor composition may be kept constant while the reaction temperature is changed to tune the lattice composition [155]. However, as the reaction is sensitive to changes in temperature, stoichiometry tuning via precursor composition is the recommended method for lattice tuning.

3.4.2 Blueshift Induced by Copper Deficiency

Fig. 3.11 shows the absorption, PL, and lifetime of the CIS core QDs synthesized using various Cu:In molar ratios. QD concentrations of 50 mg/mL and 4 mg/mL were used for PL/lifetime and absorption measurements, respectively. It can be seen that, of the 4 ratios investigated (1:1, 1:2, 1:4, 1:6), a ratio of 1:2 Cu:In yielded quantum dots with the highest PL intensity and lifetime; this is in close agreement with theory [31][74][148][154].

It can also be seen in Fig. 3.11(a) that varying Cu:In composition at a fixed growth time and temperature produces QDs with different emission peaks, indicating that the bandgaps of the QDs are tunable via varying reactant composition. Inducing Cu deficiency via In excess produces some blueshifting in CIS QDs and produces 4.5-6.5 nm QDs with emission in the range of 650-750 nm. These results suggest that variation in Cu:In ratio can be leveraged for tuning the bandgap and subsequent emission properties of CIS QDs. The ratio of the Cu:In precursors does not necessarily correspond to the same ratio of Cu:In atoms in the synthesized cores.

The blueshift of absorption and emission in CIS QDs, produced by Cu deficiency, is noted in literature [31][149]. It stems from Cu deficiencies in CIS lattices, corresponding with a decrease of orbitals originating from Cu, thus producing a weakened repulsion between the Cu *d* orbital and S *p* orbitals. This subsequently causes lowering of the acceptor states, a hybrid of Cu *3d* and S *3p* orbitals, leading to an overall wider "bandgap" [78][146][148][152]. At the same time, In results in induction of more In-S bonds, which stretch the lattice to widen the separation between conduction and valence bands [149]. Therefore, the energy between the radiative recombination states is increased, resulting in emission of higher energy photons with shorter wavelengths. The production of larger bandgaps, and subsequent blueshift through In-excess stoichiometry is a noted phenomenon in other ternary chalcopyrite QD structures [154].

In the results shown in Fig. 3.11, the 1:2 ratio produces the highest-quality QDs, despite having less Cu deficiency than 1:4 and 1:6 ratios. This is attributed to insufficient DDT and over-deficiency of Cu in the 1:4 and 1:6 ratios. Due to the high molar mass of In(Ac)_3, indium-excess synthesis greatly increases the amount of solid precursors that must be dissolved. In this study, the DDT volume was fixed at 5 mL, which was insufficient to dissolve the more In-abundant ratios. In order to decrease the solid precursor mass, synthesis was performed using lower molar masses of CuI and In(Ac)_3 at the same relative ratios (i.e., 0.25 mmol:1 mmol instead of 1 mmol:4 mmol), but the poor quality of the resultant QDs indicated instability due to over-deficiency of Cu. Although small amounts of Cu deficiency (such as 1:2 Cu:In) distorts the lattice to within acceptable bounds, compositions with too little Cu weakens and collapses the lattice, making it thermally unstable and prone to quenching [78]. Very Cu-deficient QDs show particular susceptibility to thermal quenching compared to other ratios [78].

3.4.3 Anionic Precursor Variation

Throughout the investigation of temperature and cationic stoichiometry, the DDT was kept at a constant volume of 5 mL. Synthesis conducted with lower DDT volumes of 1 mL and 3 mL produced lower-quality QD solutions with less uniformity, higher viscosity, and organic debris. Thus, a minimum of 1 mmol each of CuI and $In(Ac)_3$, and 5 mL of DDT, must be used during synthesis for sufficient CIS quantum dot growth. Based on the results of this study, the 1:2 Cu:In ratio produced with 5 mL DDT under gradient T-ramping, was primarily used for ongoing core CIS QD synthesis and investigation.

3.5 Structural and Elemental Analysis of CIS QDs

Structure, size, and morphology of the synthesized QDs were studied by high resolution transmission electron microscopy (HRTEM, ZeissLibra200MC). Transmission electron microscopy, provided in Fig. 3.12, was used to visually investigate the structure, dispersity, and crystallinity of the synthesized CIS quantum dots. The core QDs appear quite polydisperse. The spherical shape and crystalline structure of the QDs are visible in the HRTEM image (top inset); from here, it can also be deduced that the CIS core QDs are approximately 4 nm in size. Diffraction patterns (bottom inset) also demonstrate the QDs to have good crystallinity. The TEM images shown here present QDs grown using gradient temperature ramping. TEM images of CIS QDs grown using abrupt T-ramping showed crystalline structures, but the gradient T-ramp structures had stronger diffraction patterns, indicating that the crystal quality is improved to some degree.

Elemental analyses were performed using energy-dispersive x-ray spectroscopy (EDS; Bruker Quantax) and inductively coupled plasma mass spectrometry (Agilent 7700). Elemental analysis of the CIS quantum dots was performed using EDS (Fig. 3.12(b)); Cu, In, and S were detected in the core CIS samples. Inductively coupled plasma mass spectroscopy (ICP-MS) was performed on drop-cast QDs to study the effects of T-ramp profile on stoichiometric ratio of QDs (Fig. 3.12(c)). A Cu:In:S ratio of 1:2:0.2 was detected for the quantum dots synthesized via gradient temperature ramping, corresponding with a core structure of $CuIn_3S_{0.4}$. The Cu:In:S ratio was 1:3:0.4 for the CIS QDs synthesized using abrupt temperature ramping, corresponding more closely to a core composition of $CuIn_2S_{0.2}$. It can be seen that neither are stoichiometrically exact, and Cu:In precursor ratio does not solely determine the elemental composition of the core CIS QD [156]; the T-ramp profile influences stoichiometry to some extent. This stoichiometric deviation from the elemental ideal is attributed to the complicated lattice imperfections found within CIS QDs, partially caused by distortion of their tetragonal lattices.

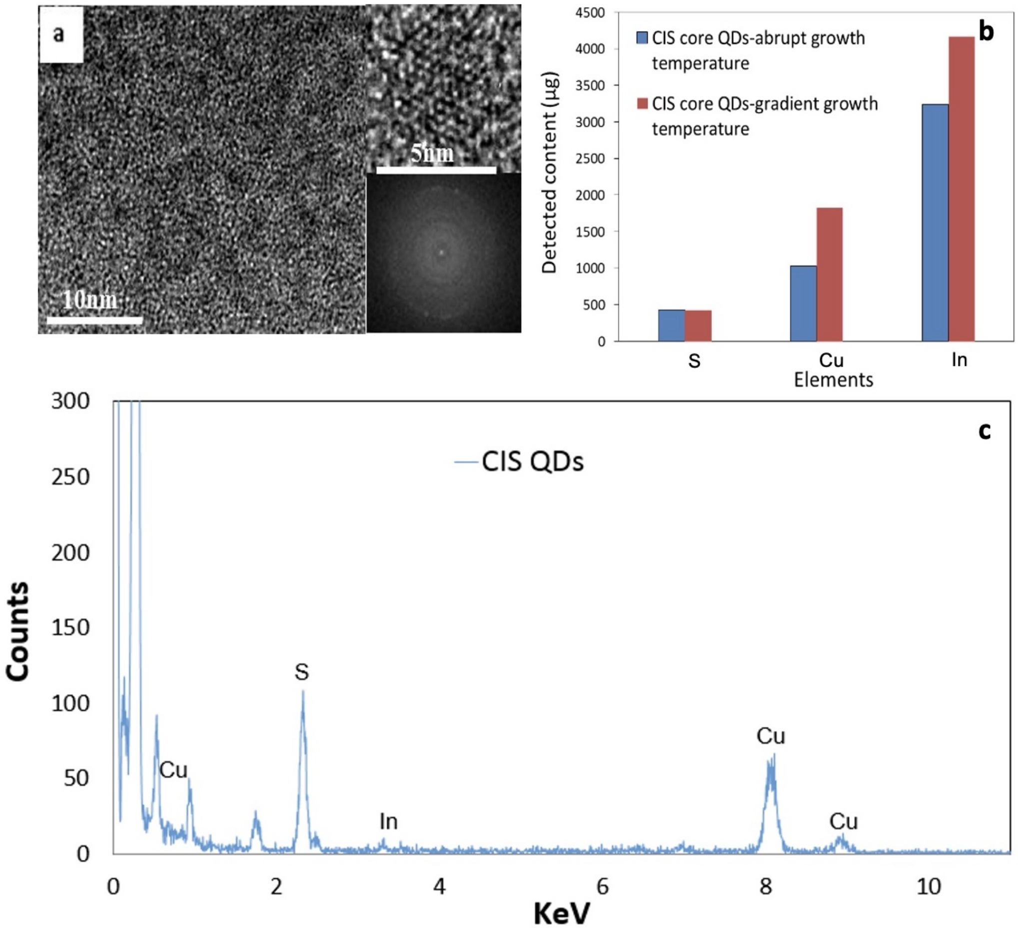

Figure 3.12: (a) TEM images of the synthesized CIS QDs. Insets show QDs' diffraction pattern (bottom) and HRTEM image (top). (b) ICP-MS characterization of CIS QDs grown using different temperature ramping profiles showing different stoichiometry. (c) EDS of synthesized core CIS QDs.

3.6 Conclusions

CIS quantum dots were synthesized at low temperatures using a one-pot process, displaying high PL emission and a maximum PLQY of 10% through optimizing QD elemental composition and growth temperature. Four regimes of colloidal CIS QD growth were identified, with their kinetics determined by the reaction temperature. The effects of temperature during growth were systematically investigated, and found to have significant effect on the surface passivation of resultant QDs. Gradient T-ramps with gradual temperature increase during growth produced core CIS QDs with more ligand coverage and fewer defects. It was determined that these ternary QDs show optimal properties at a specific size, with the most complete ligand coverage, associated with the best colloidal stability and film quality. The impact of cationic stoichiometry on CIS QD properties were investigated. Precursor molar ratios of 1:2 for Cu:In resulted in the strongest efficiency of CIS QDs. The improved quality of the CIS QDs are attributed to the preferential copper deficiency and more efficient growth during a gradual temperature ramping schematic. Based on these results, QDs synthesized with a molar ratio of 1:2 Cu:In, using a gradient ramping method to gradually increase the temperature during growth, were applied to continued materials investigation and device implementation.

Chapter 4

Synthesis of Core/Shell CIS/ZnS Quantum Dots

Although the synthesized core CIS QDs show advantageous optoelectronic properties, their complicated ternary lattices and presence of non-radiative surface recombination pathways lead to non-optimal behaviour. The extensive surfaces of CIS QDs are riddled with traps and recombination states, which detract from radiative emission. The complicated, dual-cationic lattices of QDs are inherently defective, leading to effective emission at only one optimal size. These issues significantly impact the application of CIS QDs in photovoltaic, photodetection, and light-emitting devices. Overcoating is a common methodology for engineering quantum dot properties, including bandgap adjustment and surface passivation. Overcoating eliminates undesirable surface states by removing dangling bonds and surface states [44][78][157], promoting radiative recombination [2][151] and producing more desirable optical properties. Core/shell structures contribute to QD coupling [3], which enhances the electronic behaviour of QD solids. Core/shell structures allow control over carrier confinement, and improve the long-term air-stability of QDs.

For CIS QDs, overcoating with a ZnS shell improves PL emission, increases lifetime, and promotes stability. ZnS is chemically stable and nontoxic [67], making it suitable in this work. Therefore, a method for solution-based ZnS overcoating of CIS QDs was developed, presented here. A controlled, drop-wise shell growth process was implemented to achieve more flexibility in emission wavelengths. Parameters such as core quality, reaction temperature, and overcoat precursor composition were explored to determine their impact on CIS/ZnS growth. The following chapter presents the methodology for formation of high-quality CIS/ZnS QDs.

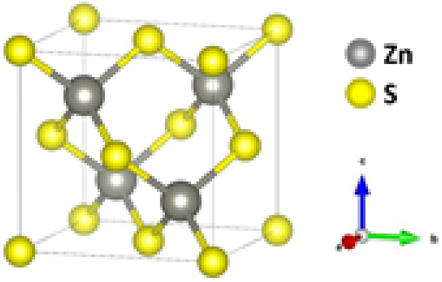

Figure 4.1: Zinc blende lattice of ZnS.

4.1 Overcoating of Stoichiometric ZnS Shell

ZnS is a wide-bandgapped semiconductor with a zinc blende lattice, as shown in Fig. 4.1. CIS and ZnS are fairly compatible, with a small lattice mismatch of 2-3% between their similar chalcopyrite and zinc blende structures [65][67]. CIS/ZnS is categorized as a Type I alignment, in which the band edges of the core is wrapped by the shell, confining both electrons and holes. Type I configurations are conducive to QDs with high PLQY, reducing exchange interactions and radiative recombination rates. ZnS shells passivate surface defects on CIS QDs, eliminating undesirable non-radiative recombination pathways and improving optical properties [31][65]. Zn-incorporated CIS QDs possess less surface defects and show enhancement compared to core-only CIS QDs [78][157]. This section presents a procedure for ZnS overcoating of CIS QDs. The impact of ZnS on the optical properties of the QDs are investigated and mechanisms of passivation are proposed.

4.1.1 ZnS Overcoating Procedure

The overcoating procedure uses the same Schlenk line setup as the core CIS QD synthesis in the previous chapter. CIS/ZnS core/shell QDs are created by incorporating a ZnS precursor solution into pre-synthesized CIS QDs. To prepare the synthesized CIS cores for overcoating, 4 mL of ODE and 1 mL of the concentrated, purified core CIS QD solution is added to the reaction flask. Ambient purging is completed according to the core synthesis procedure in the previous chapter, to remove unwanted oxygen and moisture. The temperature of the solution is gradually raised to 150°C, upon which the ZnS overcoat solution is added drop-wise, at a rate of ≈1 drop per second. Overcoating begins immediately. The same temperature is maintained throughout the reaction. As the reaction proceeds, the solution begins to blueshift from the starting colour (red cores were primarily used in this work, as they show the most optimal structural and optical properties), to orange, yellow, and down to green. Emission wavelengths smaller than green were not achieved, as the core material is completely consumed. Like the core procedure, the reaction is halted via water bath or injection of cold solvent when the desired QD emission colour is obtained [31]. The process must be monitored carefully to ensure that it is terminated at the correct wavelength. Upon completion of the growth, the core/shell CIS/ZnS QDs are subsequently washed via centrifugation with ethanol, and re-dispersed in hexane.

The ZnS overcoat solution is prepared using 0.4 mmol (0.253 g) zinc stearate ($Zn(SA)_2$), 0.4 mmol (0.0128 g) sulfur, 4 mL 1-octadecene (ODE), and 5 mL trioctylphosphine (TOP; ligand). The overcoat solution is thoroughly mixed using ultrasonication for 90 minutes, upon which the precursors are dissolved and the solution becomes a uniform, white, milky solution. Up to 9 mL of the ZnS overcoat solution is produced. The entire volume does not need to be used at once; the solution is stable for several weeks, and one bottle of precursor can be used over multiple runs of overcoating. The $Zn(SA)_2$:S ratio presented here provides equal amounts of the cationic and anionic precursors (0.4:0.4 mmol, or, 1:1 ratio of Zn:S); other ratios will be further discussed in subsequent sections.

4.1.2 Blueshifting of CIS/ZnS Emission

The notable blueshifting emission of CIS/ZnS QDs deviates from other Type I core/shell QDs, such as CIS/CdS, whose emissions redshift, corresponding to increased particle size [152]. The cause of the blueshift has been attributed to four processes: i) zinc inter-diffusion, ii) surface reconstruction, iii) surface cation exchange, and iv) core S consumption. These factors mainly generate blueshifting by decreasing the size of the core QD; however, some blueshifting is attributed to modification of primary recombination mechanisms. The blueshifting in CIS/ZnS QDs is some combination of all four processes.

(i) Zinc Inter-diffusion

This mechanism proposes ionic Zn movement from the wider bandgapped ZnS (∼3.6 eV) shell to the smaller bandgapped CIS (∼1.5 eV bulk) core [156]. During the ZnS overcoating, Zn^{2+} ions diffuse into the CIS core, removing Cu^{+} and In^{3+} ions [72][158], physically reducing the size of the QD [152]. This decreased size impacts the electronic band structure, resulting in blueshift [67][152][158]. Fig. 4.5 illustrates Zn inter-diffusion.

Zinc inter-diffusion is considered to be the dominant mechanism of blueshift in CIS/ZnS QDs. In addition to decreased QD size, the blueshift induced by zinc inter-diffusion is also

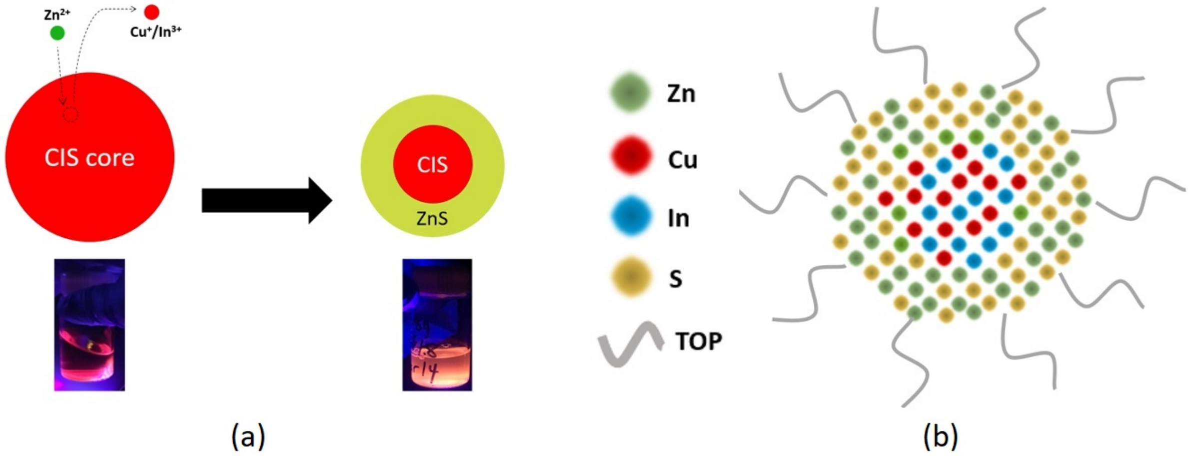

Figure 4.2: (a) Blueshifting caused by Zn^{2+} cation exchange with Cu^{+} or In^{3+} during the overcoat process. (b) Schematic of CIS/ZnS structure; the core size becomes decreased due to surface reconstructing from the ZnS.

attributed to improved recombination mechanisms. Zinc inter-diffusion fills copper vacancies and removes indium interstitials, decreasing the donor states in DAP recombination, which stems from internal defect states. This leads to more CB-to-V_{Cu} band-to-acceptor recombination mechanisms, which produce more blueshifted emission due to the higher energy of the transition [78].

(ii) Surface Reconstruction

Overcoating reconstructs the QD surface [67][158], disturbing the atomic arrangement by removing organic DDT ligands and replacing them with inorganic ZnS. The more stable composition of the ZnS compound removes surface states that contribute non-radiative recombination pathways. This also serves to decrease the overall physical size of the QDs, resulting in enhanced, blueshifted emission.

(iii) Surface Cation Exchange

This is a variation of the first phenomenon, in which Zn cation exchange specifically occurs on the QD surfaces, removing surface Cu^{+} and In^{3+} cations and reducing the overall QD size [65][158]. The surface-specific Zn inter-diffusion form alloyed Zn-CIS locally at the

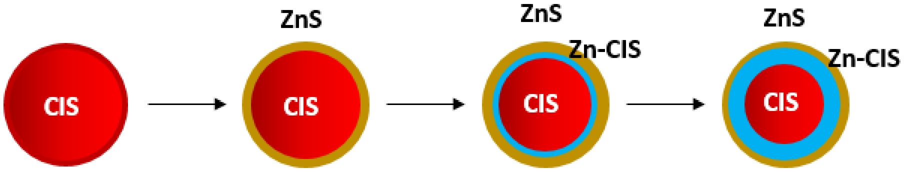

Figure 4.3: Formation of a graded Zn-CIS shell during ZnS overcoating of CIS.

CIS/ZnS interfaces, with a wider bandgap compared to CIS deeper in the core (Fig. 4.3) [78]. The structure of the CIS/ZnS core/shell QD can be considered to have a more graded CIS/ZCIS/ZnS composition, rather than distinct boundaries between the CIS core and ZnS shell [31][74]. The production of the graded structure results in greater passivation.

(iv) Core S Consumption

During overcoating, S atoms from the core contribute to the construction of the shell [31]. This results in a decreased QD size, which causes blueshift of emission. This phenomenon will be further discussed in the subsequent section.

4.1.3 Sulfur Source

Unexpectedly, the elemental S contained in the ZnS precursor solution is not the main source of S during ZnS shell growth. The sulfur primarily originates from the thiols comprising the core QDs' DDT ligand, as well as the bulk of the core itself. The dominant source of S is determined by method of temperature ramping during core growth, which dictates DDT coverage. Fig. 4.4 conceptually illustrates the mechanism of ZnS shell formation onto core CIS QDs grown using different T-ramping profiles.

QDs grown using gradient T-ramping have more crystalline lattices with better-passivated surfaces abundantly covered by DDT ligands. In such QDs, the DDT ligands are the primary source of the S in the shell. Sulfur is stripped from the thiol terminal groups in the DDT molecules, which become displaced when ZnS nucleate onto the QD surface. The remainder of the organic ligand is not needed, and becomes discarded during purification.

In QDs grown using abrupt T-ramping, the fast growth process results in weak and less-stable bonds in the core structure, with a low percentage of ligand coverage on the

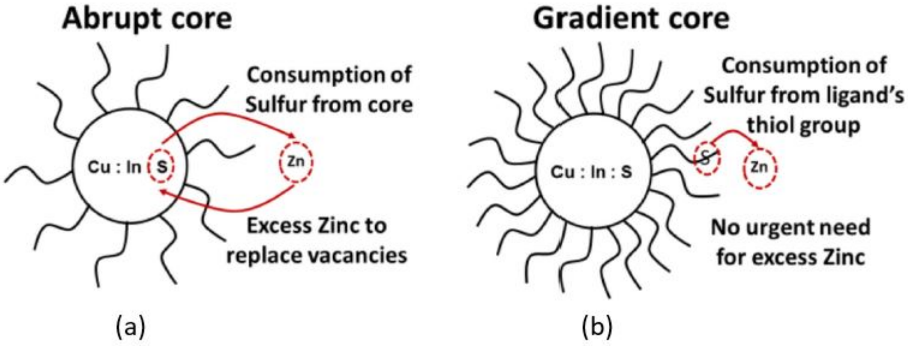

Figure 4.4: Conceptual mechanism of ZnS shell formation on core CIS QDs grown using (a) abrupt and (b) gradient temperature ramp profiles.

surface. The ligands do not provide sufficient S for shell growth, and S must be drawn from within the QD core as the dominant sulfur source. This process breaks Cu-S and In-S bonds, which create defects that form non-radiative recombination pathways, leading to low lifetime. Core/shell QDs synthesized from gradient T-ramped QDs are preferable.

4.1.4 Optical Tuning via Overcoating

The photoluminescence emission of synthesized, uncoated CIS quantum dots is shown in Fig. 4.5, overlaid with the emission of the same quantum dots after briefly overcoating with ZnS. It can be seen that there is a 10-fold improvement in the PL efficiency, as well as a 160 nm peak position blueshift. Compared to core CIS, the synthesized CIS/ZnS QDs have higher quantum yield and photostability.

It is known that the core CIS QD is only optimal within a small range of sizes, corresponding to specific emissions (typically red). Shorter emission wavelengths cannot be effectively obtained in CIS core QDs, but the blueshifting associated with overcoating provides CIS-based QDs with more emission flexibility. Due to the improved surface passivation and more optimal lattices achieved through Zn-S bonds, the PL emission spectra of CIS/ZnS QDs is narrower and more intense compared to the emission properties displayed by core QDs. Thus, overcoating provides a method for tuning the fairly rigid emission of CIS QDs beyond the “optimal” wavelength.

In order to observe the blueshifting of the CIS/ZnS structures being formed, aliquots were extracted at 5 min and 10 min (after ≈60 min of growth, when the rate of blueshifting

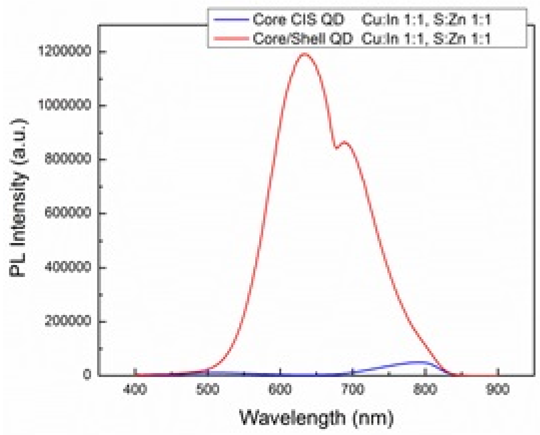

Figure 4.5: PL spectra of synthesized core CIS and CIS/ZnS QD overcoated with a stoichiometrically balanced Zn:S ratio.

slowed) intervals. A 1 min wait-time was implemented between drop-wise addition of ZnS solution and extraction of each aliquot, to ensure the overcoat material was sufficiently incorporated into the solution. The corresponding emission and absorption spectra is shown in Fig. 4.6; QD concentrations of 5 mg/mL and 1 mg/mL were used for emission and absorption measurements, respectively.

Systematically tuned emissions over a wide range (544-650 nm) that extended to the shorter wavelengths were observed with up to 10-fold increase in PL intensity. Brightly-emitting orange, yellow, and green QDs were obtained (Fig. 4.6(a)). Emission of shorter wavelengths were not possible; extending the overcoat reaction beyond this range completely consumed the CIS QD cores, leaving ZnS nanoparticles with their characteristic broad emission in the blue wavelength range. The first extracted peak position (3.5 min) showed a 150 nm shift compared to the CIS core (≈680 nm), and a PLQY up to 20% was obtained. Notably, the peaks are sharper and narrower than obtained for even the best core CIS QDs. Thus, ZnS shell growth advantageously allows a much higher degree of emission tunability to be achieved.

4.1.5 Overcoat Injection

The rate of shell precursor injection is significant in controlling the core/shell quality. Although more tedious, drop-wise precursor addition is preferred to high-volume, instantaneous addition. When the overcoat solution is added in a controlled rate (1 drop/s) as

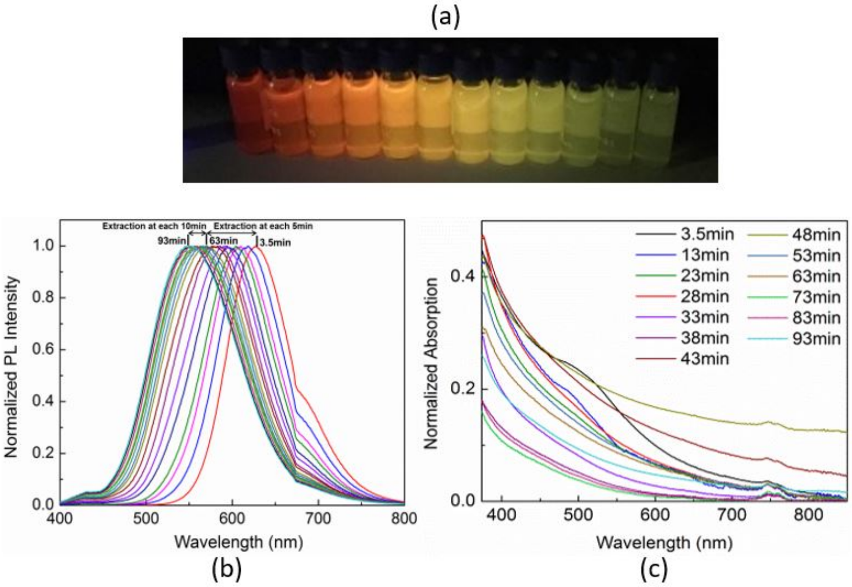

Figure 4.6: (a) Vials of CIS/ZnS QDs extracted at different growth times, and their corresponding (b) emission and (c) absorption spectra.

described previously, it is possible to extend the synthesis of core/shell QDs to shorter wavelengths, as short as 544 nm. Compared to faster growth, the drop-wise methodology maintains QD efficiency throughout the process [31].

Slow addition corresponds to slower growth that results in higher-quality shells; the continuous thermal energy provided throughout the process contributes in-situ annealing, which improves QD lattice crystallinity over extended duration. Instant, high-volume addition promotes less crystalline growth, inducing interactions that cause the QD core to resize too quickly, making it more difficult to halt the reaction at the desired time. As well, QDs within the solution are overcoated (and therefore resized) at different rates, resulting in significant polydispersity. Fig. 4.7 shows the effect of controlled addition of the overcoat solution compared to uncontrolled (or quick) injection.

The PL intensity of the CIS/ZnS QDs produced using uncontrolled injection decreased dramatically after a short growth period of 40 min, with a longer final wavelength than core/shell QDs grown using the drop-wise method. The core was completely consumed after 60 minutes, coinciding with total absence of PL emission intensity. In contrast, the QDs produced using prolonged injection continued to blueshift in emission, and could be extracted after 90 min, resulting in the shortest emission peak of 544 nm (left-most peak

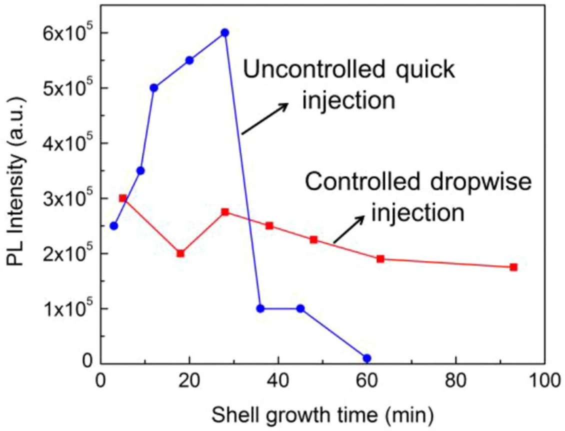

Figure 4.7: Comparison of controlled and quick ZnS precursor injection.

in Fig. 4.6(b)). Due to the better emission characteristics and control, subsequent studies used drop-wise injection.

4.1.6 Temperature Dependence of Optical Properties

Temperature significantly determines the decomposition kinetics of the ZnS precursor solution. Overcoating at higher temperatures promotes Zn inter-diffusion, improving core/shell structures [31]. However, overcoating at overly high temperatures causes nucleation of the shell precursors, leading to nonepitaxial shell growth [119]. Controlling the overcoat temperature is important to ensure crystalline, monodisperse CIS/ZnS QDs.

To study the effect of shell growth temperature on the properties of core/shell QDs, ZnS shells were grown onto core CIS QDs synthesized using gradient T-ramp. Overcoating temperatures ranging from 70°C to 160°C were investigated; the same temperature was maintained throughout the reaction. The Zn:S precursor molar ratio was kept constant at 8:1; precursor stoichiometry will be discussed in the next section. Fig. 4.8 presents the lifetime of CIS/ZnS QDs grown at increasingly higher temperatures and extracted after a fixed growth time (10 min). The concentration of QDs was kept constant at 10 mg/mL for the measurements. The PL and lifetime of the obtained CIS/ZnS QDs were most optimal at the two highest shell growth temperatures, 130°C and 160°C. Core/shell CIS/ZnS QDs with PLQY of 20% was obtained at a maximum temperature of 160°C.

Reaction temperatures higher than 100°C allows better consumption and inter-diffusion of Zn precursors during alloying and shell formation, resulting in good-quality core/shell

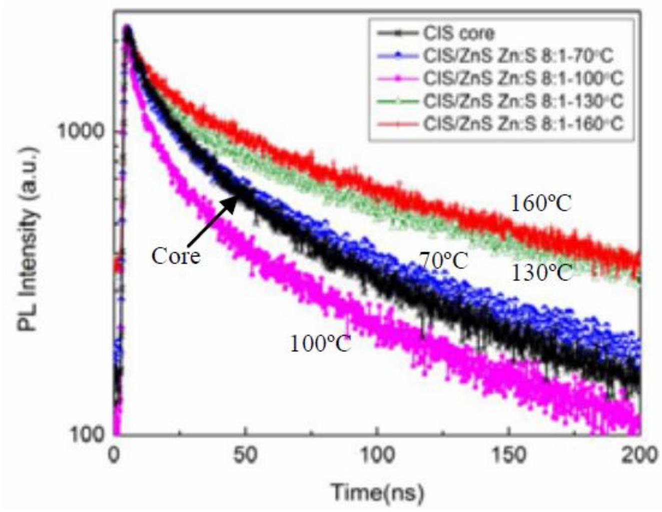

Figure 4.8: Lifetime of the CIS/ZnS QDs produced at different shell growth temperatures.

structures. This is consistent with the findings of this study, in which the overcoating temperatures equal to or lower than 100°C showed lifetimes equivalent to the defective core's lifetime. The higher temperatures provide sufficient thermal energy to allow shell crystallization kinetics to proceed. It should be noted that 130-160°C is considered to be in the low-T regime compared to most prior work on QD synthesis. These temperatures are low enough that the overcoating reaction is not driven to complete too quickly, and shell materials are afforded sufficient opportunity to traverse to energetically favourable positions on the core surface. Prolonged precursor addition via the drop-wise method, combined with maintenance of the reaction at the optimal growth temperature, results in a longer synthesis duration that yields tunability and higher-quality core/shell QDs. Based on the findings of this study, overcoating temperatures between the optimal range of 130-160°C (mainly 150°C) was used in subsequent study of CIS/ZnS QDs.

4.2 ZnS Precursor Stoichiometry

Precursor composition is significant in determining the structural, and subsequent optoelectronic properties of quantum dots. This was observed previously for the core CIS QDs, in which varying Cu:In ratios had profound effect on the optical behaviour of the QDs. Likewise, the optical properties of core/shell CIS QDs also have dependence on the Zn:S precursor ratios.

Overcoat solutions with different Zn:S composition ratios were investigated for shell growth, and various composition ratios of Zn:S precursors were investigated to determine the optimal recipe for the ZnS overcoat solution. The procedure described above presents overcoating using a strochiometrically balanced $Zn(SA_2)$:S ratio (0.4 mmol:0.4 mmol, herein referred to as 1:1). Based on this 1:1 ratio, the zinc stearate and sulfur precursors were subsequently doubled, quadrupled, and octupled, while keeping the other solid precursor constant at 0.4 mmol. The TOP and ODE precursors were also kept constant. Sulfur-excess (0.4 mmol:0.8 mmol, i.e., 1:2 Zn:S molar ratio or greater) or zinc-excess (0.8 mmol:0.4 mmol, i.e., 2:1 Zn:S or greater) solutions were appropriately prepared by multiplying the molar masses of the sulfur or zinc stearate as required. Increasing the amount of zinc stearate notably results in a more opaque, viscous precursor solution, while S-excess precursor solutions do not appear visually different from the 1:1 ratio. As with varying Cu:In ratio, the ratio of Zn:S precursor do not necessarily correspond to the elemental composition of Zn:S atoms in the shell.

It was established that the T-ramping used for core preparation significantly affected the results of overcoating. In QDs produced through gradient T-ramping, which have higher surface ligand coverage, the displaced ligands are the primary source of sulfur. For abrupt T-ramped QDs, the sulfur must be provided from the core; as a result, these core/shell QDs are more defective and unstable. Although elemental sulfur in the ZnS precursor solution is not a significant source of sulfur, S-excess precursor stoichiometries were nevertheless examined to determine anionic precursor variation on core/shell structures. This section investigates the effect of precursor stoichiometry on core/shell QD structures. The ZnS overcoating of abrupt and gradient T-ramped, Cu-deficient core CIS QDs were studied separately, and presented in their respective subsections.

4.2.1 Core QDs Grown with Abrupt T-Ramps

Core CIS QDs with a 1:2 Cu:In ratio were synthesized using abrupt T-ramping, then overcoated with different Zn:S ratios. Fig. 4.9, shows the absorption, PL intensity, and lifetime of core/shell QDs with Zn-excess Zn:S precursor ratios. QD concentrations of 10 mg/mL and 4 mg/mL were used for PL/lifetime and absorption measurements, respectively. All other parameters, including overcoat time and temperature, were kept constant. The length of each overcoating process was adjusted to keep the emission wavelength fairly constant across different ratios.

Core CIS QDs have a proclivity for dual-peak emission, attributed to lattice defects and polydispersity. This is particularly prevalent in abrupt T-ramped QDs, which are grown

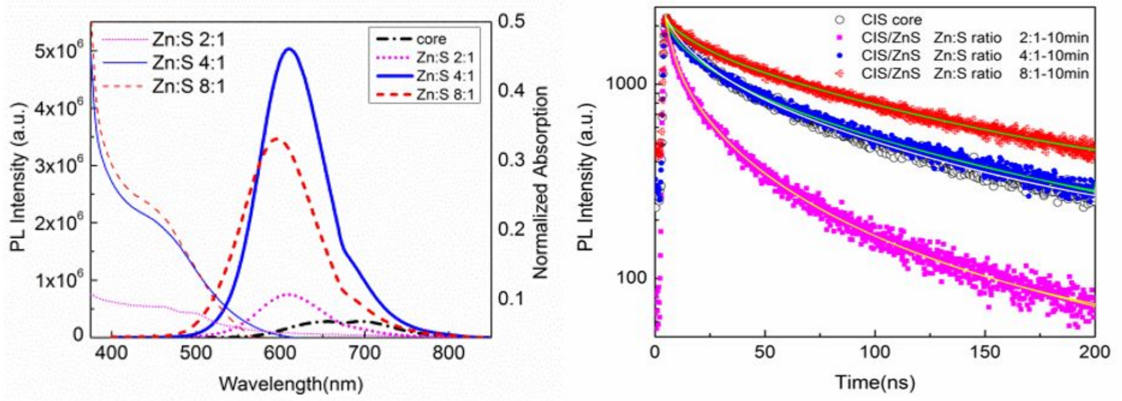

(a) (b)

Figure 4.9: Abrupt T-ramped CIS QDs overcoated using various Zn:S ratios optically evaluated using (a) PL and UV-Vis absorption spectroscopy and (b) lifetime measurements. The labeled Zn:S ratios indicate the added Zn:S precursors, not the stoichiometric composition of the shell.

quickly at high temperatures. In Fig. 4.9(a), the core QD shows a visible dual-peak at 650 and 720 nm. For all Zn-excess ratios, upon overcoating, the intensity of the core's primary 650 nm emission peak greatly increased and slightly blueshifted, attributed to Zn inter-diffusion. The secondary peak at 720 nm neither blueshifted nor increased, instead tapering as a weak shoulder. As the appearance of the 720 nm peak is associated with the inhomogeneity of QDs and defect sites arising from the small CIS cores, its disappearance after overcoating is indicative of core passivation.

In ratios with excess Zn, there is greater inter-diffusion of Zn to the core. This is poignant for abrupt QDs, as the process of overcoating draws sulfur from its bulk, resulting in a weakened lattice. Greater Zn diffusion aids in stabilization of these S-depleted cores. Additionally, as proposed above, the inter-diffusion of Zn shifts the dominant recombination mechanism from defect-dependent DAP to CB-to-V_{Cu}, which more closely resembles band-to-band mechanism. Optical properties are enhanced as a result.

To further explore the effect of Zn:S compositional ratio on the quality of CIS/ZnS structures, S-excess shell precursors were utilized for overcoating. The addition of excess S produced some improvement in PL, but to a lesser extent compared to excess Zn. For lower Zn:S (S-rich, Zn-deficient) ratios, the lifetime of the QDs remained unchanged. As the elemental S in the ZnS precursor is not a significant source of sulfur for the shell, it is unsurprising that its inclusion excess does not have a meaningful impact on QD properties.

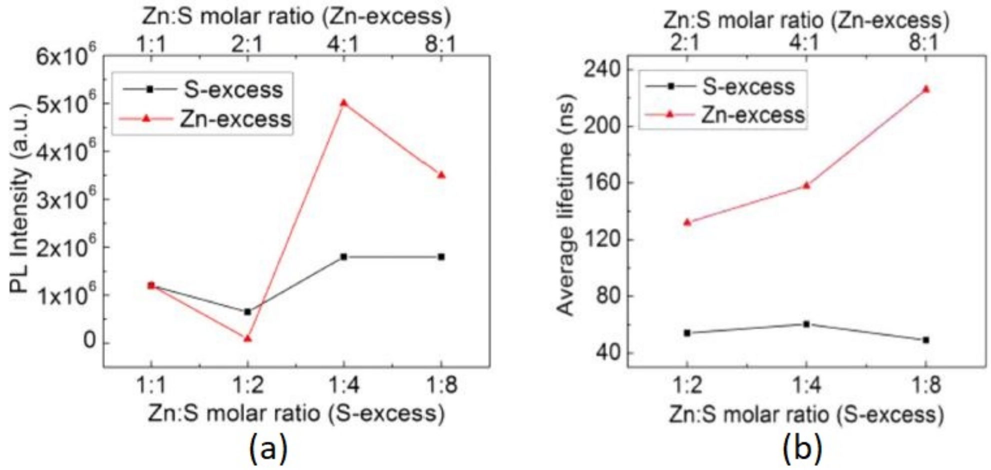

Figure 4.10: Comparison of (a) PL intensity and (b) decay lifetime of CIS/ZnS QDs grown using shell overcoat solutions with different Zn:S molar ratios.

The complete PL and lifetime data are shown in Fig. 4.10, respectively, for solutions with S-excess and Zn-excess precursors.

The two recombination pathways that contribute to the PL decay lifetime of CIS QDs also guide the emission properties of core/shell CIS/ZnS QDs. Table 4.1 presents lifetime components extracted from multi-exponential fitting analyses for core/shell CIS/ZnS QDs produced using various Zn- and S-excess ratios. Here, β represents the pre-exponential factor, τ represents the decay lifetime component in ns, and χ^2 is defined as the fit quality factor, which should fall below 1.3. Short-lived lifetime components (τ_1 , τ_2), in the range of few tens of nanoseconds, are associated with surface trap states; the long-lived component (τ_3) in the range of hundreds of nanoseconds, is associated with internal defects. Lifetime values for core CIS QDs are also given for comparison. Lifetime was increased from 84.33 ns for the core CIS QDs, to 246 ns for the best quality core/shell QDs. The results also illustrate that when S-excess precursors are used for shell growth, the excitons with short-lived emission in the range of few tens of nanoseconds (∼15.93 ns) dominate the PL.

The best lifetimes were achieved by overcoating core QDs with Zn-excess precursors. In this case, the excitons with long-lived emissions in the range of hundreds of ns (∼246 ns) are dominant, specifically at an optimal Zn:S ratio of 8:1, enhancing both PL and lifetime. Zinc-excess shells reduce the contribution from the fast decay and results in close to single-exponential decay. As conceptually presented in the previous chapter, in core/shell CIS/ZnS QDs, surface trap states are eliminated through surface passivation.

Table 4.1: Decay lifetime components for CIS and CIS/ZnS QDs.

Sample	B_1	τ_1	B_2	τ_2	B_3	τ_3	$\langle\tau\rangle$	χ^2
CIS core	207.80	2.85	780.29	16.41	1050.6	84.33	75.33	1.01
CIS/ZnS 2:1	853.99	2.81	690.43	11.39	212.35	167.91	132.47	1.07
CIS/ZnS 4:1	328.36	1.75	353.12	10.97	829.60	157.9	153.04	1.06
CIS/ZnS 8:1			635.41	43.94	1058.5	246.0	226.43	1.04
CIS/ZnS 1:2	614.43	2.69	844.23	13.62	747.18	65.34	54.07	1.01
CIS/ZnS 1:4	637.63	2.79	853.58	15.93	637.80	75.14	60.39	0.98
CIS/ZnS 1:8	643.62	2.9	963.45	14.94	614.84	64.59	49.76	1.00

As a result, relaxation via the slower internal defects channel becomes dominant, and radiative emission dominates. Through overcoating, CIS-based QDs can show even longer lifetimes than CdSe-based QDs [41]. PLQY of 12.5%, 17.98%, and 19.89% were obtained for the CIS/ZnS QDs with Zn:S ratio of 2:1, 4:1, and 8:1, respectively. QD solutions with a concentration of 0.2 mg/mL were used for the PLQY measurements. The results indicate that core/shell QDs with enhanced optical quality were achieved at higher Zn:S ratios.

Notably, the lifetime of the CIS/ZnS QDs overcoated with S-excess precursor ratios are low, failing to match even the lifetime of the core CIS QDs. Compared to Zn-excess solutions, fewer Zn atoms are provided to diffuse and passivate the shell during growth. Simultaneously, in abrupt T-ramped QDs, the core is stripped of S to provide material for the shell, weakening the core. The excess S in the ZnS solution do not significantly contribute to the shell, and the improvement to QDs is no different than the use of the stoichiometric 1:1 ratio. In Zn-deficient core/shell QDs, blueshifting through core S consumption is more dominant than in other CIS/ZnS configurations.

The improvement in PL intensity and lifetime following Zn-excess overcoating is attributed to zinc passivation, discussed above. The possible formation of a Zn-CIS alloy, discussed above, produce either a Zn-CIS/ZnS core/shell structure or a graded CIS/Zn-CIS/ZnS core/multiple shell structure, both with lower lattice mismatch than the already well-matched CIS/ZnS. However, excess zinc may impede the quality of the core/shell quantum dots by over-passivation. There may be reduced PL intensity through eliminating necessary non-radiative recombination processes for emission [118]. It can be seen that the quantum dots produced using 8:1 Zn:S are lower in PL intensity than QDs with a 4:1 ZnS overcoat. There is a diminishing return on CIS/ZnS QD quality as Zn precursor ratio is increased; the improvement in QD quality from 4:1 to 8:1 Zn:S is not as significant as improvement between 2:1 and 4:1. In fact, over-excess of Zn precursors do not even contribute to the overcoat, and contaminate the QD solution as an unreacted by-product.

Thus, although Zn-excess ZnS overcoats can be considered to improve the optical properties of CIS QDs, oversaturation of Zn is undesirable.

4.2.2 Core QDs Grown with Gradient T-Ramps

Core/shell QDs were synthesized from core CIS QDs with a 1:2 Cu:In ratio, grown using gradient temperature ramping. The slow growth rate and gradual annealing during core growth produced stable core QDs with stronger bonds and more surface passivation sites. Overcoating of gradient T-ramped QDs primarily obtains S from surface DDT ligands, rather than the core (see Fig. 4.4(b)). Therefore, the core is not destabilized by S-extraction during overcoating.

The gradient T-ramped core/shell CIS/ZnS QDs showed strong absorption and PL even when ZnS precursor solutions with lower Zn:S ratios (1:1 or 2:1) were used (Fig. 4.11(a)). With Zn-excess precursors, long-lived emissions were also observed as shown in Fig. 4.11(b). At higher Zn:S molar ratios (8:1) Zn inter-diffuses into the core, replacing Cu or In cations, resulting in ZCIS/ZnS or CIS/ZCIS/ZnS structures with stronger bonds and improved lifetime. With a QD concentration of 0.2 mg/m, PLQY of 18.05%, 17.84%, and 20% were obtained for the CIS/ZnS QDs with Zn:S ratios of 1:1, 2:1, and 8:1, respectively. These relatively similar values indicate that the optical quality of the resulting core/shell CIS/ZnS QDs is high, and less dependent on the Zn:S ratios.

In abrupt T-ramped QDs, excess Zn atoms are required to fill vacancies induced by core S-consumption. The simultaneous surface and core passivation, from the ZnS shell and Zn^{2+} diffusion, respectively, results in improving the PL emission and lifetime of the core/shell QDs. As the cores of gradient T-ramped QDs are not destabilized during overcoating, there is no need for excess Zn. Therefore, strong PL is obtained even with lower Zn:S ratios (1:1 or 2:1) in the overcoat solution (Fig. 4.11(a)). Compared to the abrupt T-ramped QDs, higher excess of zinc do not yield more significant improvements than balanced ratios.

Varying the Zn:S precursor ratio in the ZnS precursor solution has profound effect on core QDs that show defects and nonidealities. High Zn:S ratios result in QDs with improved PL and lifetime, due to the increased contribution of lattice-stabilizing Zn [31]. However, beyond certain concentrations, excess Zn does not contribute to QD improvement, as the QD lattice cannot accommodate more Zn inter-diffusion. The excess Zn simply remains in solution and is wastefully removed during purification. Although overcoating benefits the optical properties of all QDs by eliminating non-radiative pathways, zinc-excess ratios produce fewer benefits for more stable core QDs. Excess elemental S does not notably

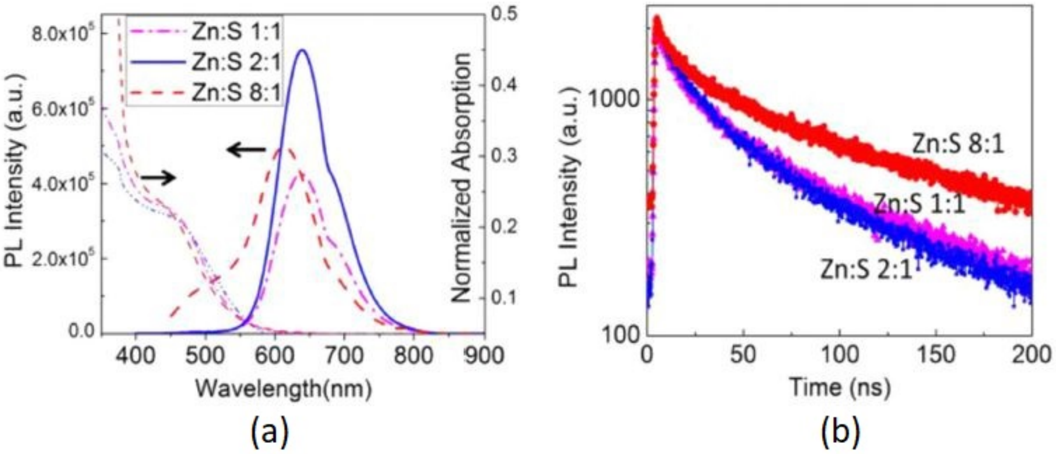

Figure 4.11: (a) Absorption and photoluminescence emission, and (b) PL decay spectra of CIS/ZnS QDs grown with Zn-excess shell overcoat solutions. The core QDs were grown using gradient T-ramp profile.

improve the optical properties of the QD, as it does not serve as a primary source of S for the shell.

4.3 Compositional Analysis of CIS/ZnS QDs

Fig. 4.12(a), top, shows EDS analysis of the synthesized CIS/ZnS QDs, in which Zn was detected in addition to Cu, In, and S. The EDS measurements for the synthesized core CIS quantum dots are also shown for comparison. Elemental mapping (bottom) was also performed on the synthesized CIS/ZnS QDs, detecting the presence of elemental Cu, In, Zn, and S corresponding to the EDS results. Thus, elemental analysis confirmed the incorporation of zinc and production of CIS/ZnS QDs.

TEM and HRTEM were used to observe the structure, crystallinity, dispersity, and size of the synthesized CIS/ZnS quantum dots. The TEM image presented in Fig. 4.12 shows that the synthesized CIS/ZnS quantum dots are spherical in shape and display monodispersity. The top inset shows an HRTEM image of the synthesized CIS/ZnS QDs, which are crystalline, and approximately 2.5 nm in size. The bottom inset shows diffraction patterns, presenting the crystallinity of the QDs. The CIS/ZnS QDs are smaller compared to CIS QDs, corroborating Zn-induced core size decrease.

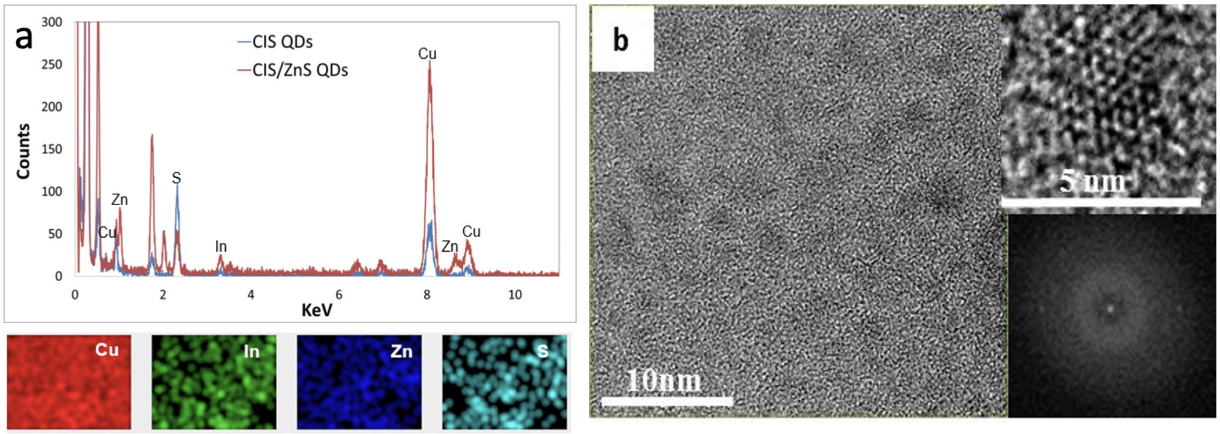

Figure 4.12: Structural/elemental characterization of CIS QDs. (a) Elemental characterization of synthesized CIS/ZnS quantum dots via EDS and elemental mapping. The Cu content of the elemental mapped QDs is high due to the copper TEM substrate. (b) HRTEM image of synthesized CIS/ZnS QDs. Top inset shows close-up of the core/shell QD. Bottom inset shows diffraction patterns.

4.4 Conclusions

In conclusion, CIS/ZnS QDs were produced via ZnS overcoating, resulting in improvements to the PL, PLQY, and lifetime of the original core CIS QDs. CIS/ZnS QDs achieving 20% photoluminescence quantum yield and long-lived emissions in the 85-246 ns range were obtained. The main mechanisms proposed for the observed improvements are elimination of competing non-radiative surface pathways through surface passivation and core stabilization via Zn inter-diffusion. Implementing a drop-wise addition of the ZnS precursor led to prolonged QD extraction that yielded shorter emission wavelengths, allowing more tunability in QD emission compared to core QDs. Several theories were proposed to explain the characteristic blueshifting of CIS QD emission following ZnS overcoating. In differentiating the ZnS growth onto abrupt and gradient T-ramped core QDs, a conceptual mechanism involving S consumption from the core and ligands for the shell formation was presented. Different Zn:S precursor ratios were investigated, and it was found that generally, using higher amounts of $Zn(SA)_2$ produced better QDs due to Zn passivation of the core. A precursor ratio of 4:1 Zn:S produced CIS/ZnS QDs with the best PL, while 8:1 produced abrupt T-ramped QDs with the best lifetime. The use of Zn-excess precursor solutions produced particularly pronounced improvement for QDs synthesized using abrupt T-ramping, as it aided in repairing the more defective lattices. It was determined that over-excess of zinc precursors did not improve QD quality, as the zinc surplus did not contribute to overcoating or passivation. It was found that gradient T-ramped QDs are preferential for use in overcoating, as the formation of the shell does not disrupt the core structure, and off-stoichiometric precursor ratios do not need to be used. Overall, core/shell, Zn-passivated QDs with efficient emission covering a wider range of the visible spectra were produced with good control under the low-T regime. The results of this work are significant for scaled-up, high volume commercial QD production for light emission and management applications. The findings in this chapter were applied to tune and stabilize the optical properties of the as-synthesized core CIS QDs in this work.

Chapter 5

Ligand Functionalization of CIS QDs

Chapter 3 describes the one-pot, low-temperature synthesis of CIS QDs with long, 1-dodecanethiol ligands. The use of DDT is important during the CIS QD synthesis phase, given its multiple roles as solvent, stabilizer, sulfur and ligand precursor, which make it possible to complete the synthesis in a non-injection and one-pot manner. The length of the DDT is key to controlling the dispersion of the QDs in solution. However, while the QDs produced from this process show promising optical characteristics, the DDT ligands pose obstacles to device implementation.

Many QD-based devices utilize metal oxide/QD heterojunctions. Record-achieving QD-based solar cells have primarily been implemented using metal oxide/QD heterojunctions, specifically ZnO/PbS QDs [125]. Unfortunately, the apolarity and length of DDT ligands hinder adhesion to ZnO, making assembly and binding of QD films onto ZnO surfaces difficult. This leads to the production of non-continuous interfaces, causing shorting in large-area devices. Electron transport through DDT-ligated QDs is poor, resulting in subpar device performance. Therefore, DDT is not conducive to forming high-quality QD solids for well-matched metal oxide/QD interfaces in devices. The TOP-ligated core/shell CIS/ZnS QDs present the same issues, as well as additional challenges related to carrier confinement.

Surface treatment and ligand exchange are commonplace for QDs, as the ligand requirements during synthesis and application are vastly different. QD surfaces are riddled with traps and imperfections, leading to mid-gap trap states that promote non-radiative recombination pathways, which compete with radiative recombination [3]. Efficient surface passivation and sufficient ligand attachment is key to removing trap states and improving QDs optical properties. In addition to improving the intrinsic properties of the QD itself, ligand exchange modifies QD surfaces to make them better-suited for film formation. Tailored surface passivation can significantly improve QD arrangements, forming high-quality QD solids. In functionalization of QDs for photovoltaic and photodetector applications, long lifetime and high mobility should be targeted to reduce recombination and improve interfacial transport between layers of the device.

This chapter presents the functionalization of CIS QDs via a solution-based ligand exchange method. The MPA ligand was chosen due to its compatibility with ZnO interface formation and similarity to DDT, which are conducive to a successful ligand transport process. The totality of the ligand exchange and the optical properties of the QDs were studied by FTIR, PL, and absorption analyses. AFM was employed to investigate the quality of CIS QD films. Simple planar diodes with ZnO/CIS QD heterojunctions were fabricated using both DDT-ligated and MPA-exchanged CIS QDs. The resultant I-V characteristics demonstrate the necessity of ligand exchange for devices

5.1 Ligand Contribution to QD Behaviour

For QDs, ligands are typically nucleophilic hydrocarbon species that attach onto an electrophilic metal site [3]. As the surface-to-bulk ratio is so high in QDs, the surface contributes significantly to structural and optical characteristics. The atoms, molecules, and ions present on the QD surface effectively control the electron affinity of the entire structure [3]. Ligands dictate QD interactions with surroundings, stabilize QDs from precipitation, and passivate the dangling bonds and imperfections abundant on QD surfaces [3][104]. Ligands also dictate interfacial properties between QDs and other materials. They are significant to carrier transport, and can even control the effective bandgap of a QD with respect to adjacent materials [5][16].

5.1.1 Interdot Transport

Although some device researchers have moved toward directly growing QDs onto substrates (via CBD, SILAR, etc.), colloidal QDs are advantageous, providing more control over QD properties during synthesis [115][116]. For films formed from colloidal QDs, surface ligands significantly dictate electronic, excitonic, and thermal transport through the QD solid [3]. In addition to directing the QD arrangement, carriers traverse between QDs via their ligands, leading ligands to directly participate in transport. In organic ligands, the mode of carrier transport through QD solids is via tunnelling. Carriers are transported out of each QD and onto the next QD via a series of tunnelling events, “hopping” between QDs. The rate of tunnelling is given as Equation 5.1 [3]:

$$\Gamma \sim exp[(-2m^{*}\Delta E/\hbar^{2})^{1/2}\Delta x] \tag{5.1}$$

Here, m^{*} is effective mass of electrons, $\hbar$ is the reduced Planck’s constant, and ΔE and Δx are the height and width of the tunnel barrier, respectively.

For QD solids, ΔE and Δx are defined by ligands [3][159]. Decreasing width and height through reducing ligand length (and therefore QD separation) increases the rate of tunnelling, resulting in better conduction between adjacent QDs in the film. Long, inorganic ligands provide significant barriers, which block interparticle transport [50]. Notably, the relationship between ligand length (number of hydrocarbon groups) and electron transport is not linear, as longer ligands bend and curl to bring the QDs closer to the substrate surface [160]. However, the unpredictable placement and poor uniformity resulting from these contortions mitigate any small reductions in tunnelling barrier.

Efficient carrier transport is crucial for PV and detector devices, in which electron-hole pairs are generated in the QD film absorber. In QD devices, charge transfer rates improve as distance is decreased, such as in shorter ligands [161]. Additionally, carrier mobility tends to be higher for shorter ligands, increasing transport and collection [5]. The QD/ligand and ZnO/ligand interfaces must also be considered in addition to the ZnO/QD interface [160]. The terminal end groups (-COOH and S for DDT) are chemically attached to the QD and ZnO surfaces they are attached to, leading to strong electronic coupling [160]. The center of the ligand molecule is not bound, and therefore weakly coupled. In shorter ligands, the electronic states of the QD/ligand and ZnO/ligand interfaces strongly overlap, resulting in good coupling throughout the ligand [160]. However, in longer ligands, there is less overlap of the electronic states, causing more resistance to electron flow [160]. Fig. 5.2 illustrates the differences in ligand coupling between long and short ligands.

In the as-synthesized CIS QDs, Cu^{+}, In^{3+} cations interact with the nucleophilic ligands, forming bonds with the S^{2-} anions in the DDT thiol groups [3], while the hydroxyl groups maintain QD stability in non-polar solvents. Thiols are particularly advantageous for ligand utility, as they bind strongly to QDs due to their crystal-bound state, and the sulfur atom incorporates as part of the QD surface [162]. The electronic coupling between the QD surface and the DDT thiol functional group is very strong.

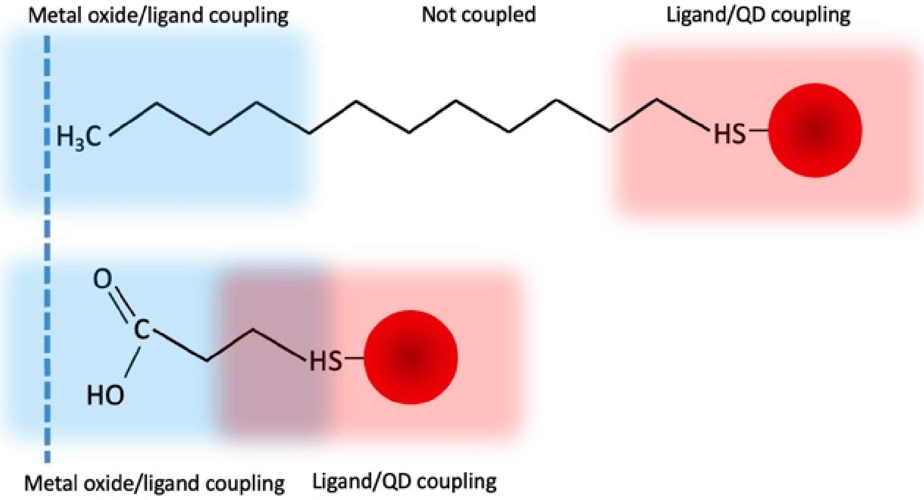

Figure 5.1: Differences in electronic coupling between short and long ligands.

5.1.2 Metal Oxide/QD Interfaces

Metal oxide/QD junctions constitute an important part of many QD-based device structures [163][164]. Due to its good stability, conductivity, transparency, and electron transport, ZnO is a metal oxide that is frequently employed as an electron transport layer in LED and PV devices, especially for devices based on QDs [131][165][166][167][168]. ZnO exhibits compatible band alignment with core/shell CIS QDs [169][170]; dense conformal ZnO films have a wide bandgap that shows good alignment with CIS, which promotes electron transport. The offset of ZnO's CB pairs with the CIS's shallow CB to readily accept electrons, while its VB is located far beneath the VB and acceptor DAP states near the VB of CIS QDs's relatively shallow bandgap, preventing hole transport [11][169][170]. ZnO/QD heterojunctions have formed the majority of record-setting QD-based photovoltaics. Thus, ZnO/CIS QD heterojunctions were utilized in this work. The development of the ZnO thin films will be described later in this thesis.

Due to ZnO's hydrophilicity, long, non-polar DDT ligands hinder electron transport, surface adhesion, and uniform film formation, posing challenges for device integration [162]. The apolarity of DDT ligands result in poor adhesion and wettability to metal oxides, producing discontinuous QD films with agglomeration. Ligand length also significantly affects QD distance and ordered assembly, determining carrier mobility in QD films [18][24][50][162][171]. Although the length of DDT makes it advantageous for stabilizing

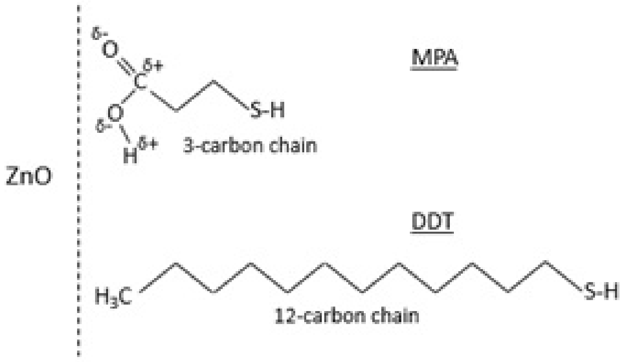

Figure 5.2: Schematic of MPA and DDT at ZnO interface.

QDs and controlling growth during synthesis [172], it provides significant barrier to electron transport. As discussed previously, longer ligands suffer from poor coupling. Hence, the long, 12-carbon chain of the DDT molecule in CIS QDs produce longer electron pathways and weaker coupling throughout its length, resulting in increased electron trapping and recombination compared to shorter molecules. Furthermore, the flexibility of the long DDT ligand make formation of uniform, periodic QD solids nearly impossible. Apolarity and length are the two primary reasons devices cannot be formed from DDT-ligated QDs.

In contrast to DDT, 3-mercaptopropionic acid is a short, hydrophilic ligand with a thiol functional group. The use of these polar, bifunctional ligands were found to improve the binding and interparticle electron transfer between CdSe QDs and ZnO [32][36][48][171][173]. MPA is a suitable replacement ligand for DDT; it possesses a thiol terminal group that bonds to QD surfaces similarly to DDT, but its shorter 3-hydrocarbon chain reduces the barrier to tunnelling. Due to enhanced binding, MPA ligands promote good interparticle electron transfer between QDs and ZnO thin film surfaces [173]. The carboxylic acid functional group in MPA promotes adhesion to ZnO thin film surfaces due to electrostatic repulsion [117], allowing better surface assembly and higher QD loading onto a substrate [56]. Compared to longer ligands, shorter MPA ligands reduce interdot separation, promoting faster band-like charge transport [32] instead of lower-mobility hopping transport [32], resulting in improved carrier conduction [24]. The short, strongly-coupled MPA-ligated QDs pack more closely, leading to higher QD loading [56]. Therefore, a continuous interface with higher density of QDs forms between ZnO films and MPA-ligated CIS QDs. Fig. 5.2 illustrates a comparison of DDT and MPA-ligated QD attachment onto ZnO film.

5.2 Ligand Exchange

The properties of ligands that are advantageous for maintaining QD dispersion are not conducive for film formation. Therefore, the as-synthesized DDT ligands must be expunged. It is possible to partially remove ligands through mechanical methods such as washing, filtering, and sintering, but it is very difficult to completely remove all ligands from a QD [105]. Furthermore, since ligands play an important role in QD passivation and stabilization, total removal is undesirable, creating unwanted dangling bonds and surface traps which lead to QD agglomeration [94], uncontrollable sintering, and instability in solution. These disadvantageous properties lead to formation of poor QD films with insufficient adhesion to ZnO. Complete removal of the ligand also exposes the metalloid cores, leading to leakage and destabilization.

Aqueous QD synthesis, such as in water, have been attempted to imbue as-synthesized QDs with desirable ligands for device application. However, these have produced devices and solar cells with poor performance and low PCE [97]. Long ligands are essential to QD solvent stability during synthesis. Since QD synthesis with MPA ligands requires more complex aqueous environments, it is preferable to synthesize the CIS QDs with DDT ligands, followed by a post-synthesis ligand exchange process prior to device integration.

Ligand attachment is a matter of attraction between electron-deficient cations and electron-rich anions, encouraging bond formation. As-synthesized attached ligands can be removed with the introduction of a molecule with a stronger proclivity for surface binding [3]. In ideal ligand exchange conditions, the new ligand molecule should have stronger binding than the original ligand. Following ligand exchange, it is common to see a reduction in absorption and PL emission intensity. Ligand exchange performs some surface modification, which alters optical properties, as well as producing additional surface non-radiative recombination states. Trap states at the air/solid interface of the QD solid become more abundant, capturing carriers more quickly [50]. Therefore, the benefits of ligand exchange must be considered against the emergence of undesirable properties.

CQD ligand exchange is performed using two methods: liquid-phase or solid-phase. Liquid-phase ligand exchange is accomplished via phase separation of solvents with different polarities. In this process, the QDs are kept in solution, and an additional solution containing the desired replacement is added. If the surface binding of the new ligand is stronger, the old ligand will be removed, with the new ligand attaching to the passivation sites. The old ligand is removed with the supernatant during purification. Solid-phase ligand exchange entails formation of a QD solid, then “ligand dosing” the film (spreading the ligand solution onto the QD solid, or dipping the solid into the ligand) [19]. QDs with the initial ligand are applied as a film onto the substrate, then immersed into a solution containing the desired ligand replacement. The solution containing the new ligand propagates through the QD solid bulk, replacing old ligands and attaching onto the passivation sites. The detached ligands are removed during purification.

The main advantage of liquid-phase ligand exchange is thoroughness, as the entire surface of each QD is accessible during this process. For solid-phase ligand exchange, the QDs have already immobilized onto the substrate, and some facets are not accessible [106]. The solution-based exchange allows better control over surface balance charges, and can access the entire QD to eliminate undesirable midgap states more effectively [106]. However, if it is desirable to limit the ligand reattachment, solid-phase exchange is advantageous as the ligands have less access to the substrate-affixed QDs [174].

As QD solids are difficult or impossible to re-disperse in solution after forming film, the QD film and substrates must be in their final arrangement prior to solid-phase ligand exchange. It is detrimental to device performance if the ligand solution contains solvents that are harmful to any other materials in the device. Furthermore, thicker QD films require longer duration of ligand exchange, and the ligand solution cannot permeate through very thick layers of QDs. This can be circumvented with more steps of QD film formation and solid-phase exchange, which requires more time and interaction [107]. Therefore, liquid-phase ligand exchange is relatively less time consuming. Although QD pellets are readily re-dispersed in solvent, ligand exchange is not performed on QD pellets due to their density, which prevents ligand solution permeation.

Ligand exchange is typically performed to replace long ligands with shorter ligands. As long ligands are better for colloidal stability, the exchange to shorter ligands can cause QD aggregation in solution. This poses some difficulties during subsequent film formation, as the QDs may not be well-stabilized in solvent. In this situation, solid-phase ligand exchange is more advantageous, as it circumvents issues with short-ligand QD colloidal instability [3]. However, solid state exchange is not entirely absolved from poor film formation, as the differences in length between the old and new ligand causes some re-adjustment of the QD positioning, which may result in cracked films during solid-phase ligand exchange. Careful selection of the solvent largely mitigates dispersion issues for QDs that undergo liquid-phase ligand exchange.

Due to the advantages presented above, liquid-phase ligand exchange was selected for this work. As the ligand-exchanged QDs remains stable in (new, polar) solution, film manipulation did not cause issues during device fabrication.

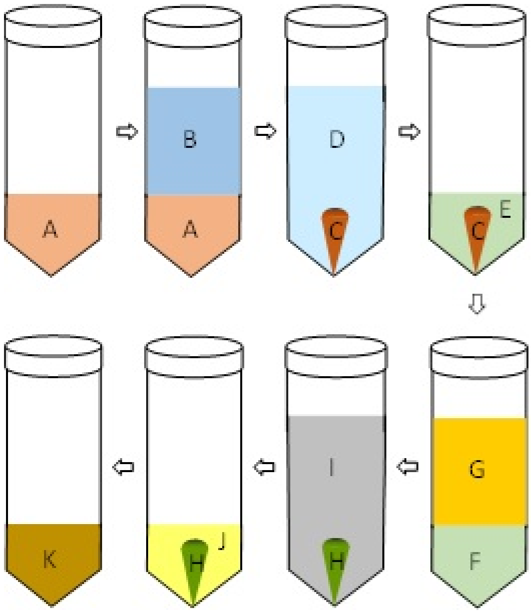

Figure 5.3: Schematic representation of the non-aqueous ligand exchange process. A: as-synthesized DDT-ligated QDs in hexane, B: ethanol (anti-solvent), C: separated QD sediment after centrifuging, D: supernatant to be removed, E: MPA to disperse QDs via sonication, leading to ligand exchange, F: MPA-ligated QDs, G: hexane (anti-solvent), H: separated QD sediment after centrifuging, I: supernatant containing detached DDT ligands and excess MPA to be removed, J: methanol added to dried sediment for re-dispersal, K: MPA-ligated QDs in methanol.

5.3 DDT-to-MPA Ligand Exchange Process

As-synthesized, DDT-ligated CIS QDs in hexane are purified and centrifuged with polar anti-solvent (ethanol) to separate QD sediment from solvent. After disposing of the supernatant and allowing the QD sediment to dry, concentrated 3-mercaptopropionic acid (99%, Sigma Aldrich) is added to the QDs. The QDs-in-MPA mixture is sonicated for over 60 minutes to thoroughly disperse the QD sediment in solution. The QDs must be thoroughly dispersed in the MPA; a small amount of hexane is added to facilitate this. The CIS QDs-in-MPA solution is sealed, then left in a dark environment for ≈3 days to allow the MPA molecules in the solution to displace the DDT ligands and bond to the vacated attachment sites on the QD surface. This process is illustrated in Fig. 5.3.

After this process, the MPA-ligated QDs in the solution are centrifuged using non-

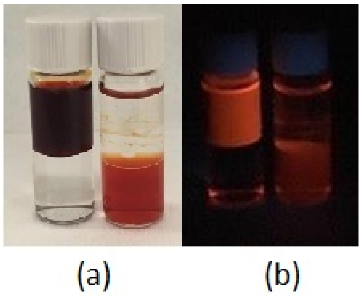

Figure 5.4: DDT-ligated CIS QDs dispersed in hexane and methanol (left), and MPA-ligated CIS QDs dispersed in methanol and hexane, under (a) ambient illumination and (b) UV illumination.

polar antisolvent (hexane). After removing the supernatant containing excess MPA and displaced DDT ligands, the sediment of MPA-ligated QDs are dried, then re-dispersed in a polar solvent. Successful dispersion of the QDs in the polar methanol solvent provides clear indication that ligand exchange is complete. Fig. 5.4 shows DDT- and MPA-ligated CIS QDs, dispersed in hexane and methanol, respectively. The less dense hexane causes the DDT-ligated CIS QDs to form a two-phase solution with the denser methanol; a similar effect is observed with the MPA-ligated CIS QDs in denser methanol with hexane.

5.4 Characterization of MPA-ligated QDs

Chemical and optical analysis were performed to evaluate the properties of the MPA-ligated QDs. FTIR was performed to analyze the bonding species on the MPA-ligated QDs, compared to DDT-ligated QDs, to determine the success of the process. Optical analysis was conducted based on emission and absorption properties of the QDs, to contrast the quality of optical behaviours. Finally, AFM was used to analyze the uniformity of the QD solids formed using QDs before and after ligand exchange. The ligand exchange was successful, and determined to produce QDs with desirable properties for device applications.

5.4.1 Chemical Analysis

The DDT- and MPA-ligated QDs were chemically analyzed using FTIR, performed using a Vertex 70v FTIR spectrometer. Samples for FTIR measurements were prepared

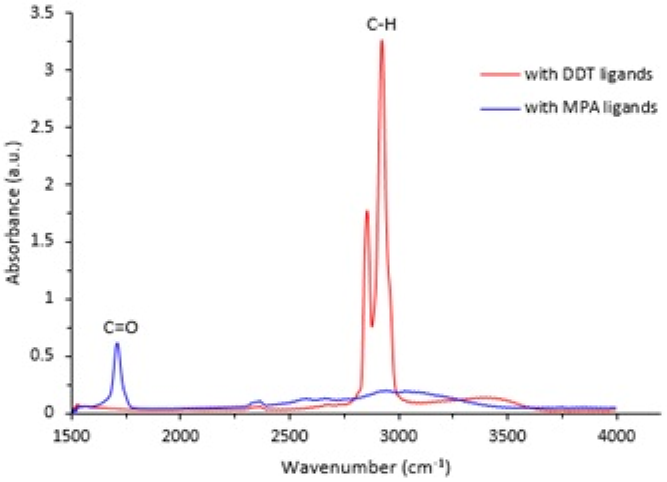

Figure 5.5: FTIR spectra of CIS QDs before and after ligand exchange. The differences in absorption peaks indicates successful DDT-to-MPA ligand exchange.

by drop-casting QDs, diluted to 25 mg/mL, onto acetone and IPA-cleaned 2.2 × 2.2 cm^2 glass substrate via syringe.

The FTIR absorbance measurements of the CIS QDs before and after ligand exchange are shown in Fig. 5.5. Prior to the ligand exchange, there is a large stretch between 3000-2800 cm^{-1}, corresponding to the C-H stretching from alkane groups. This is consistent with the long hydrocarbon chain in the DDT molecule. This peak significantly reduces in size following ligand exchange, in accordance with the much shorter hydrocarbon chain in MPA. Also, a new peak appears at approximately 1700 cm^{-1}. This peak corresponds to a C=O stretch and is consistent with the carboxylic acid group contained in MPA. The results show successful DDT-to-MPA ligand exchange.

Notably, the S-H stretching corresponding to thiol functional groups at 2600-2550 cm^{-1} is absent from both spectra. This is because both DDT and MPA ligands anchor to the CIS surface via their thiol groups, in good agreement with literature [103]. Due to the strong attachment of both ligands to the QD surface, a specific thiol peak cannot be detected.

5.4.2 Optical Analysis

Samples for absorption and PL emission measurements were prepared by spin-casting QDs (25 mg/mL) onto acetone and IPA-cleaned 2.2 × 2.2 cm^2 glass substrate (500 rpm for 10 s, then 1500 rpm for 30 s). Optical characteristics of the CIS QDs were analyzed before

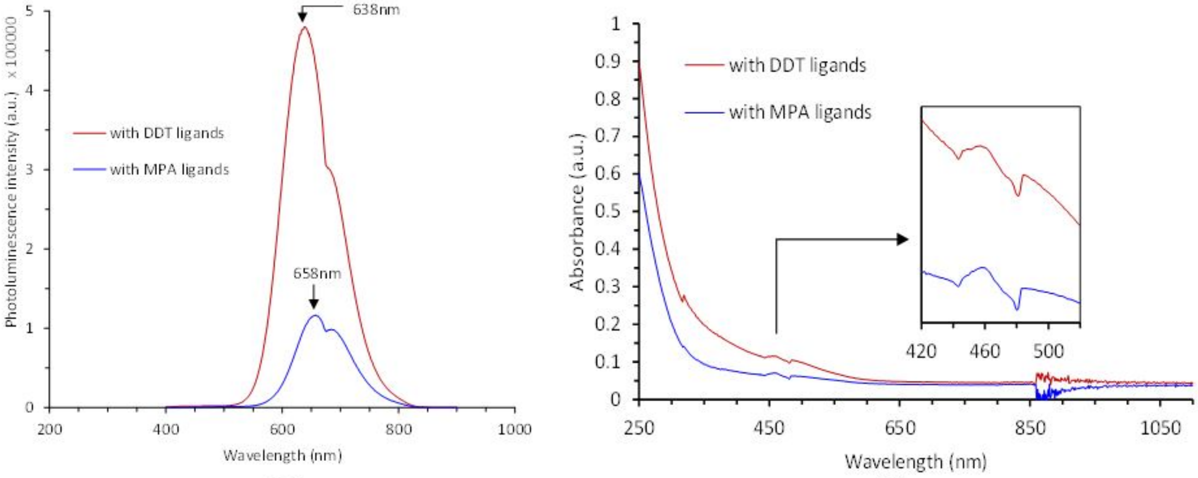

(a) (b)

Figure 5.6: (a) Photoluminescence emission and (b) absorption spectra of quantum dots before and after ligand exchange.

and after ligand exchange. The PL emission spectra of the QDs are shown in Fig. 5.6(a). Both curves show the characteristic broad full width half maximum peak of CIS QDs. The emission peak of the DDT-ligated QDs is stronger than that of the ligand-exchanged QDs (5×10^5 vs 1×10^5 counts).

It appears that the ligand exchange process causes an increase in surface defect states leading to greater non-radiative surface recombination. While one can observe a slight redshift in the peak following the ligand exchange (from 638 to 658 nm), this is insignificant and can also be attributed to slight surface modifications due to ligand exchange. The small secondary peak at 683 nm is a relic of the PL detector in the fluorescence lifetime spectrometer system used in measurements. Fig. 5.6(b) shows the absorption spectra of the CIS QDs, before and after ligand exchange. Similar to the trend in PL emission spectra, the intensity of the absorption peaks decreases after ligand exchange. The absorption peaks are at the same location before and after ligand exchange (≈460 nm; Fig. 5.6(b) inset).

The above results suggest that ligand exchange does not significantly alter the emission and absorption peak positions, and that the CIS QDs retain their properties despite a slight reduction in the PL and absorption characteristics. A reduction in QD PL emission intensity is consistent with literature, as MPA molecules behave like hole scavengers on QD surfaces, reducing recombination [115]. However, these characteristics of the MPA-ligated QDs are still of an acceptable magnitude; the ligand-exchanged QDs show strong

PL emission peak of 1 × 10^5 counts and distinct peaks in the absorption spectra. This slight decrease in optical performance is a worthy compromise for the increased wettability and improved electron transport afforded by the shorter, polar MPA ligands.

5.4.3 Surface Analysis

AFM measurements (Veeco Dimension^{TM} 3100 Atomic Force Microscope in tapping mode) were taken to study the surface morphology of MPA and DDT-ligated CIS QD films. DDT- and MPA-ligated Zn-alloyed CIS QDs were diluted to a concentration of 50 mg/mL, and dip-coated onto spin-cast ZnO on glass substrates. Both substrates were formed under the same conditions (30 mm/min immersion, 60 s submersion, 1 mm/min extraction, 5 cycles). Samples were carefully controlled to ensure transparency without obvious roughness, as the AFM cannot be used to characterize films with a height disparity greater than 6 μm.

Fig. 5.7 presents an AFM scan of the two samples over a 10 μm area. Although some areas of agglomeration are present, the MPA-ligated QDs show better uniformity, with good order and coverage over the surface. There is a small amount of noise arising from nuances in the AFM instrument. In comparison, the DDT-ligated sample surface is visibly agglomerated with significant island formation and an extremely large height variation. Areas of the surface appear to be bare, corresponding to a lack of QD coverage, which negatively impacts device operation.

Fig. 5.8 presents an AFM scan across a smaller, 1 μm area. The MPA-ligated QDs again form a more uniform and ordered morphology with good surface coverage. The DDT-ligated QDs show significant agglomeration and poor adhesion. Root-mean-square (RMS) roughness measurements, which indicate the overall surface roughness of the sample, were measured to be an average of 1.423 nm and 1.139 nm for DDT- and MPA-ligated QDs, respectively, after 1 cycle of dipping. Increasing the thickness of the QDs (5 cycles) significantly increased the RMS roughness of DDT-ligated QDs to 4.817 nm, while the roughness of MPA-ligated QDs remained fairly low, at 1.447 nm. Considering the spin-cast ZnO's existing RMS roughness of 0.869 nm, the MPA-ligated QDs therefore have a very small overall roughness. The significant roughness of DDT-ligated QDs, especially following successive layer build-up, shows that the QD film is clustered and agglomerated, resulting in undesirable films lacking periodicity. Thus, AFM studies confirm the necessity of DDT-to-MPA ligand exchange for device applications.

The studies of QD optical and film formation showed the MPA ligand exchange to be successful. Although the optical properties of the MPA-ligated QDs are slightly dampened,

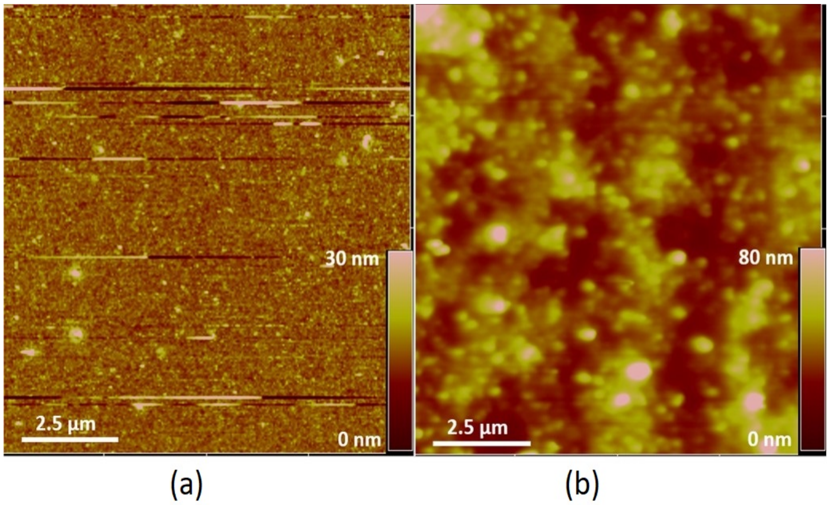

Figure 5.7: AFM images of ZCIS QDs with (a) MPA and (b) DDT ligation, coated under the same dip-coating parameters.

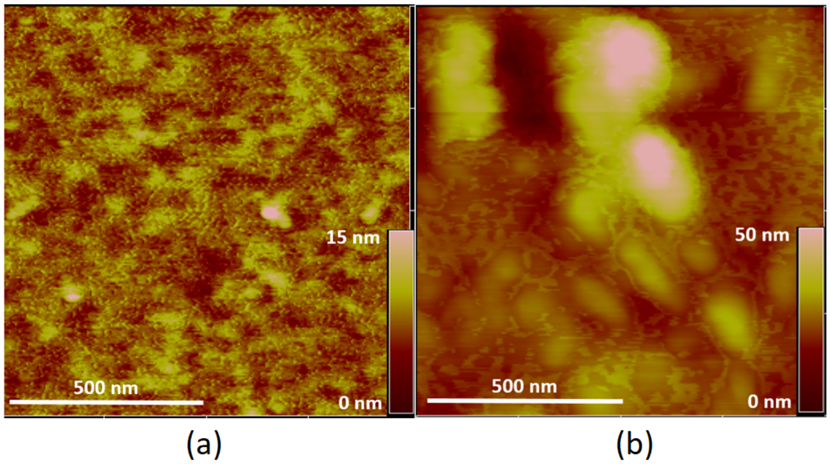

Figure 5.8: AFM images of ZCIS QDs with (a) MPA and (b) DDT ligation, coated under the same dip-coating parameters, on a 1 μm scale.

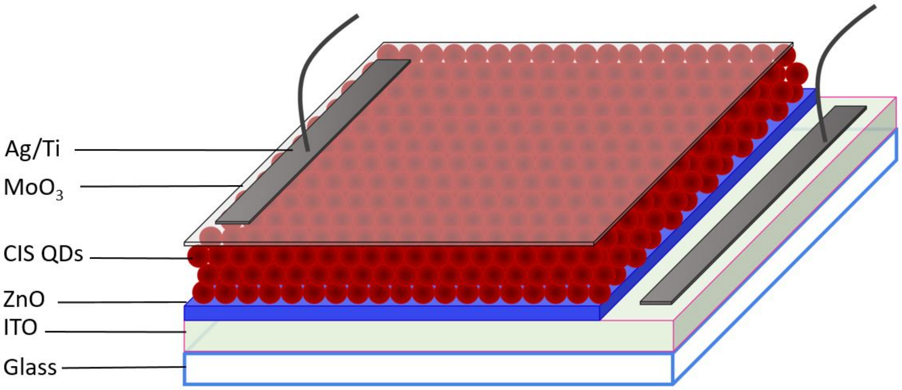

Figure 5.9: Schematic of the planar test structure with CIS QD/ZnO film heterojunction. The QD layer window area on the glass is 20 mm × 16.25 mm.

the absorption and emission intensity is within a reasonable range. The MPA-ligated CIS QDs show stronger adhesion to ZnO, with more uniform film formation.

5.5 Preliminary I-V Characterization of QD Diodes

In order to test the device applicability of the ligand-exchanged CIS QDs, simple planar diode structures were fabricated. Commercial indium tin oxide (ITO)-coated glass substrates of 2.2 × 2.2 cm^2 size were cleaned and a ZnO film was spin-cast from solution as a blanket film. DDT- or MPA-ligated QDs were then spin-cast as a blanket film (500 rpm for 10 s, followed by 1500 rpm for 30 s). For the hole transport layer, MoO_3 was thermally evaporated using a shadow mask. Finally, Ti/Ag top contacts were formed by electron beam evaporation from commercial pellets (Kurt J. Lesker Co.). A schematic of the test structure is shown in Fig. 5.9. The chosen vertical architecture of the devices reduces the carrier traversal distance in the QD layer before collection and allows study of the effectiveness of the ligand exchange process.

An Agilent 4155C Semiconductor Parametric Analyzer connected to a probe station inside of a dark, sealed chamber was used to perform current-voltage measurements on test devices. Fig. 5.10 compares the current-voltage characteristics of the devices fabricated using DDT-ligated and MPA-ligand exchanged samples, measured in the dark. The ligand-exchanged samples show a diode-like characteristic with a turn-on voltage of ≈0.8 V. In contrast, the as-synthesized DDT-ligand samples show resistive behaviour, suggest-

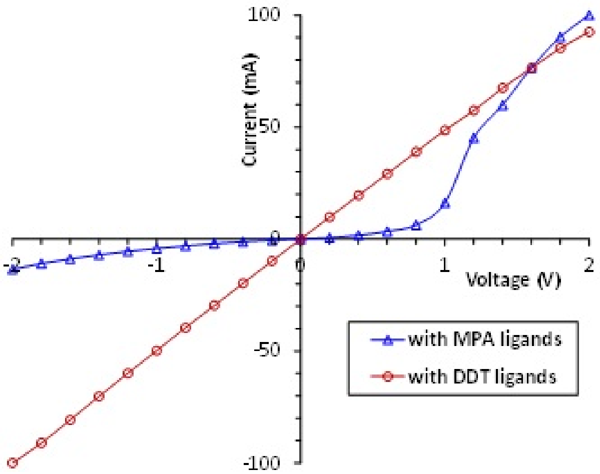

Figure 5.10: I-V characteristic of the CIS/ZnO heterojunction devices comparing the DDT-ligated and MPA-ligated CIS QDs.

ing shorting. This trend was observed in all devices fabricated; as discussed earlier and presented in the AFM images, this is due to the poor adhesion of the apolar DDT ligands to the ZnO film. For instance, when the interface between ZnO and QD film is not continuous and instead contains islands of the QD film, there is increased probability of shorting. Given the large area of this device, any discontinuity in the QD film leads to shorting between the MoO_3 and ZnO films.

The results show that with MPA-ligated CIS QD films, it is possible to achieve good and continuous interfaces with ZnO over large areas. In contrast, long organic ligands tend to reduce inter-particle coupling and disrupt charge transport in QD films [175]. Hence, the ligand exchange is crucial when using core CIS QDs with ZnO films for photovoltaic and photodetector applications.

5.6 Conclusions

Although CIS QD synthesis with DDT ligands is conducive to low-T, one-pot synthesis and maintaining stable colloidal dispersion, such long organic ligands produce poor interfaces that lead to subpar devices. Ligand exchange was implemented on the as-synthesized, DDT-ligated CIS QDs to improve interfacing with ZnO for device implementation. The completeness of the liquid-phase DDT-to-MPA ligand exchange process was verified by

FTIR analysis, and optical measurements showed that the absorption and emission of the ligand-exchanged QDs were only slightly less intense compared to the DDT samples. AFM studies showed MPA-ligated QDs to form films with more desirable morphology than the DDT-ligated QDs. The long and apolar DDT molecules, despite being helpful in the synthesis phase and providing barrier for particle aggregation, hinder device implementation due to poor adhesion to ZnO and impediment of electron transport. Comparison of the I-V behaviour of both DDT-ligated and MPA-ligated QD devices proved the suitability of the latter for formation of high-quality ZnO/QD interfaces, and the importance of the ligand exchange process. The ligand exchange process developed in this chapter is key to the device application of the synthesized CIS QDs.

Chapter 6

Zinc Copper Indium Sulfide QDs

Traditionally, core QDs are implemented in devices to obtain higher electron transfer rates [176]. However, this is problematic in CIS QD-based devices, as the defect-rich structures of unpassivated CIS QDs cause significant carrier trapping. As such, synthesis of CIS core QDs is often accompanied by ZnS overcoating, which are effective in improving the defective lattices of Cu chalcopyrite QDs [35][177]. Disadvantageously, these better-passivated CIS/ZnS core/shell QD structures bring forth issues in carrier confinement, which reduces electron transport in devices. Furthermore, overcoating requires an additional synthesis procedure, necessitating additional purification and characterization of the QDs, reducing overall scalability of the process. Methods of zinc incorporation without carrier confinement are desirable.

Alloying Zn with CIS QDs circumvents issues of core and core/shell CIS QDs. The better structural stability of ZCIS reduces defects, while the absence of a shell prevents carrier confinement. A method was developed to improve the lattice structure of unstable ternary CIS QDs via zinc alloying, leading to quaternary ZCIS QDs. A facile, low-temperature, non-injection, one-pot synthesis process was developed for high-volume production of ZCIS QDs. The variation of cationic stoichiometry was investigated to determine the effects on QD structure and optical behaviour. Furthermore, the impact of ZnS overcoating was explored to analyze the performance of core/shell ZCIS/ZnS structures. The QDs were implemented in a simple planar photodetector. This chapter presents the synthesis and characterization of Zn-alloyed CIS QDs.

6.1 Alternate Strategies for Zinc Incorporation

Reports of zinc-enhanced CIS QDs via are prevalent in literature. For instance, Li et al coated thick ZnS shells over CIS QDs, which resulted in a highly photostable QD (photostability rivalling high-quality CdSe/CdS/ZnS QDs) with higher fluorescence efficiency and significantly lower surface defects than the original core [67]. Nam et al utilized ZnS overcoating in enhancing the QY of core CIS QDs from 5.4% to 50% [75]. Pan et al found that incorporation of zinc into CIS QDs resulted in a 10-fold increase of PLQY, attributed to Zn-induced defect suppression [56]. Chapter 4 of this work also reported the improvement of CIS QD stability and optical properties via ZnS overcoating. In the implementation of CIS/ZnS QD structures, Zn ions inter-diffuse into the CIS core, stabilizing the core to produce QDs with intense photoluminescence emission and long lifetime [31]. Zn-incorporated CIS QDs have been applied towards light-emitting devices [67][68], fluorescent biological labeling and sensing, [67][68], solar cells, lasers, and sensors [68].

ZnS overcoating entails high-temperature addition of a zinc precursor to a crude core CIS solution [31][74], as described in Chapter 4. The zinc precursor combines with the sulfur in the DDT ligands to form a ZnS shell, while simultaneously displacing core cations and forming ZCIS at the interface, reducing the core/shell lattice mismatch of CIS/ZnS. This typically leads to some ionic zinc inter-diffusion, resulting in a graded CIS/ZCIS/ZnS or ZCIS/ZnS structure. Although overcoating provides QDs with greater passivation and improved PLQY and lifetime, it is not desirable in electronic devices, due to issues of carrier confinement that complicate transport dynamics. The most stable core/shell arrangements, including CIS/ZnS, show a Type I arrangement where the larger bandgap of the shell confines carriers inside the core. It is not impossible for carriers to escape the core; carriers have a probability of tunnelling from the core, determined by core thickness (Δx) and the extent of band offset (ΔE). However, due to relative difficulty in controlling the Zn movement and concentration, this is not the best method for Zn incorporation into the QD core. It should also be noted that superficial passivation techniques such as overcoating limit QD enhancements to the surface, and cannot repair defects deep in the CIS QD's bulk [56]. Finally, the necessity of overcoating increases the steps of QD preparation, making it disadvantageous for mass production. Methods for incorporating Zn into the CIS QD structure without overcoating are desirable.

Doping and alloying are efficient methods for manipulating structural, optical, electrical, and other properties in unstable core quantum dots without the use of overcoating. In CIS QDs, Zn alloying provides passivation, reduces trap density, tunes band properties, and improves chemical stability [35] without posing confinement issues. Zn-alloying in ternary chalcopyrite QDs can shift the LUMO, which further improves electron injection when the QDs act as electron donors [35]. Compared to Cu-S and In-S bonds that form ionic CuS^- and InS^+ compounds, Zn^{2+} forms more stable ZnS compounds with S^{2-}. Zn-CIS structures have better fluorescence and more flexible bandgaps, and the addition of Zn to CIS QDs can make the absorption band more homogeneous. Alloyed QDs have better chemical and structural stability, with reduced trap formation [35]. Zn-alloyed CIS quantum dots tend to have a more blueshifted emission in comparison to their zinc-free counterparts. This is attributed to the same mechanism of blueshifting in Cu-deficient CIS QDs, in which reduced Cu contribution results in a larger "bandgap" [78][149]. Based on these advantages, zinc alloying was pursued as a method for CIS QD passivation.

6.2 Synthesis of Stoichiometrically Balanced ZCIS QDs

Zn-CIS quantum dots can be synthesized using a process similar to the recipe presented in Chapter 3, in which precursor complexes of the required metals (Zn, Cu, and In) are added to a solvent, followed by the S precursor, then heated [96]. Alternatively, zinc atoms may also be introduced to pre-existing CIS quantum dots by adding zinc stearate and oleic acid to a crude core CIS QD solution, then heating [118]. In the latter case, controlled Zn-doping is achieved by monitoring parameters such as Zn precursor concentration, temperature, and the maintenance of a contamination-free environment (through application of vacuum and ambient purging). In this work, the former method was chosen due to providing better control over QD properties. This section presents the synthesis and characterization of stoichiometrically balanced ZCIS QDs using a solution-based, bottom-up method.

6.2.1 ZCIS QD Synthesis Procedure

The ZCIS synthesis procedure is based on the synthesis of CIS QDs, described in previous chapters [31][171]. ZCIS quantum dot synthesis is performed using the Schlenk line method, under an inert atmosphere with vacuum and nitrogen, with the aid of a heating/stirring mantle. In synthesizing a stoichiometrically balanced cationic ratio, 1 mmol of CuI, 1 mmol of $In(Ac)_3$, and 1 mmol of $Zn(SA)_2$ are added to a three-neck, round-bottom flask. Different cationic molar ratios will be discussed in subsequent sections. The flask is sealed under vacuum and nitrogen flow, and left for 10 minutes to remove contamination from ambient. 5 mL of DDT is subsequently added to the flask. DDT continues to be critical to this reaction; similar to its function in CIS core QD synthesis, it plays the roles of sulfur precursor, stabilizing ligand, and solvent [31][67][75][171]. The temperature is allowed to gradually reach 80°C over 60 min. Following the complete decomposition of precursors, a clear solution forms, indicating the start of QD nucleation. Then, the temperature is slowly raised to 150°C over a period of 300 min, according to the gradient T-ramping technique. As with CIS QDs, the solution turns from yellow to orange, red, and black over the course of growth, indicating redshifting of emission.

Purification is performed via centrifugation with acetone and ethanol, and the cleaned QD pellet is re-dispersed in hexane. Typically, synthesis is halted at a size corresponding to the optimal emission (approximately 650 nm), although the synthesis can proceed further to a very dark red colour (≈750 nm emission). Unlike the ternary CIS QD, the ZCIS QD cannot reach a size capable of infrared emission. This is due to the addition of Zn in the C-I-S structure, which modifies the stoichiometric CIS chalcopyrite lattice composition, therefore limiting the energy of possible radiative transitions within the core. Over 900 mg of ZCIS QDs are produced per run using this procedure. Compared to Zn inter-diffusion during overcoating, this method of Zn incorporation should produce more uniformly incorporated Zn cations throughout the core, as zinc precursors are included from the start of the core creation process.

6.2.2 Growth Profile of ZCIS QDs

Fig. 6.1 shows the normalized PL and absorption spectra of the ZCIS core QDs, grown over 65 minutes following precursor decomposition and nucleation. Aliquots were extracted every 10 minutes, such that the growth profile and PL shift of the core ZCIS QDs could be studied. As they grew, the QD emission redshifted, with broad emission spectra ranging from 500 nm to 750 nm. The highest peak intensity was achieved for the 650 nm emission, corresponding to a dark red emission colour; this is the optimal size. Growth beyond 750 nm resulted in agglomerated QDs, while halting the synthesis before this point produced a gelatinous QD solution. This correlates with findings from the synthesis of CIS core QDs, in which an optimal size corresponding to maximum surface ligand coverage exists [31]. The characteristic broad PL emission peak, attributed to the DAP recombination mechanism of CIS-based QDs, is also seen in the ZCIS QDs.

6.2.3 Structural and Elemental Characterization of ZCIS QDs

Fig. 6.2 shows the TEM, diffraction, and EDS of the synthesized, stoichiometrically balanced ZCIS QDs. The QDs, marked in red in Fig. 6.2(a), show good monodispersity with a clear spherical shape and crystalline structure. The QDs measure approximately 5

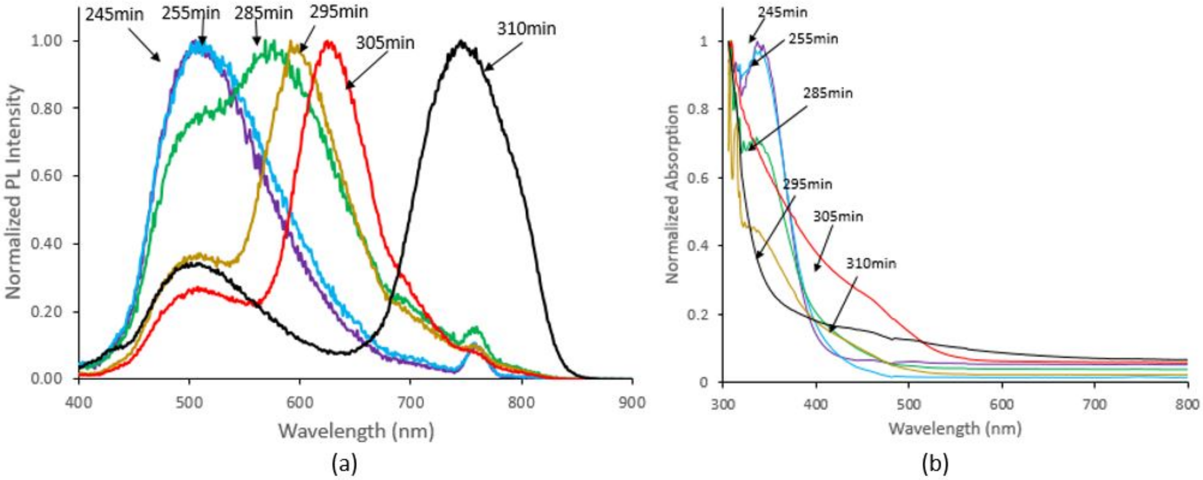

Figure 6.1: (a) PL and (b) absorbance profile of ZCIS core QDs grown over 65 minutes.

nm in size, as apparent from the HRTEM image in Fig. 6.2(a), top inset. The diffraction pattern is strongly visible, affirming the crystallinity of the crystal structure (Fig. 6.2(a), bottom inset). Fig. 6.2(b) shows the EDS analyses, providing the elemental composition of the ZCIS QDs. The EDS spectra shows distinguishing Kα and Lα peaks at 8.630 keV and 1.012 keV, respectively, corresponding to major electron transitions in the Zn atom. EDS identified Zn, Cu, In, and S elements in the QD sample. Cationic variations to the precursor composition produce undefined placement of Zn and In cations into the chalcopyrite lattice. Unlike the defined lattice positions of Cu, In, and S atoms on the chalcopyrite unit cell of stoichiometric CIS QDs, ratios with excess cations result in their random placement into bonding sites. Although bonds are still formed, maintaining the integrity of the CIS QD structure, the unit cell location of each cation is no longer defined as in stoichiometrically balanced Cu:In ratios.

FTIR analysis was carried out in order to verify the presence and stability of the DDT ligands attached to the QDs. As depicted in Fig. 6.3, the strong peaks at ≈2855 cm^{-1} and ≈2924 cm^{-1} correspond to C-H stretching vibrations of the CH$_2$ and CH$_3$ groups, respectively, in the long carbon chains of the QDs' DDT ligands.

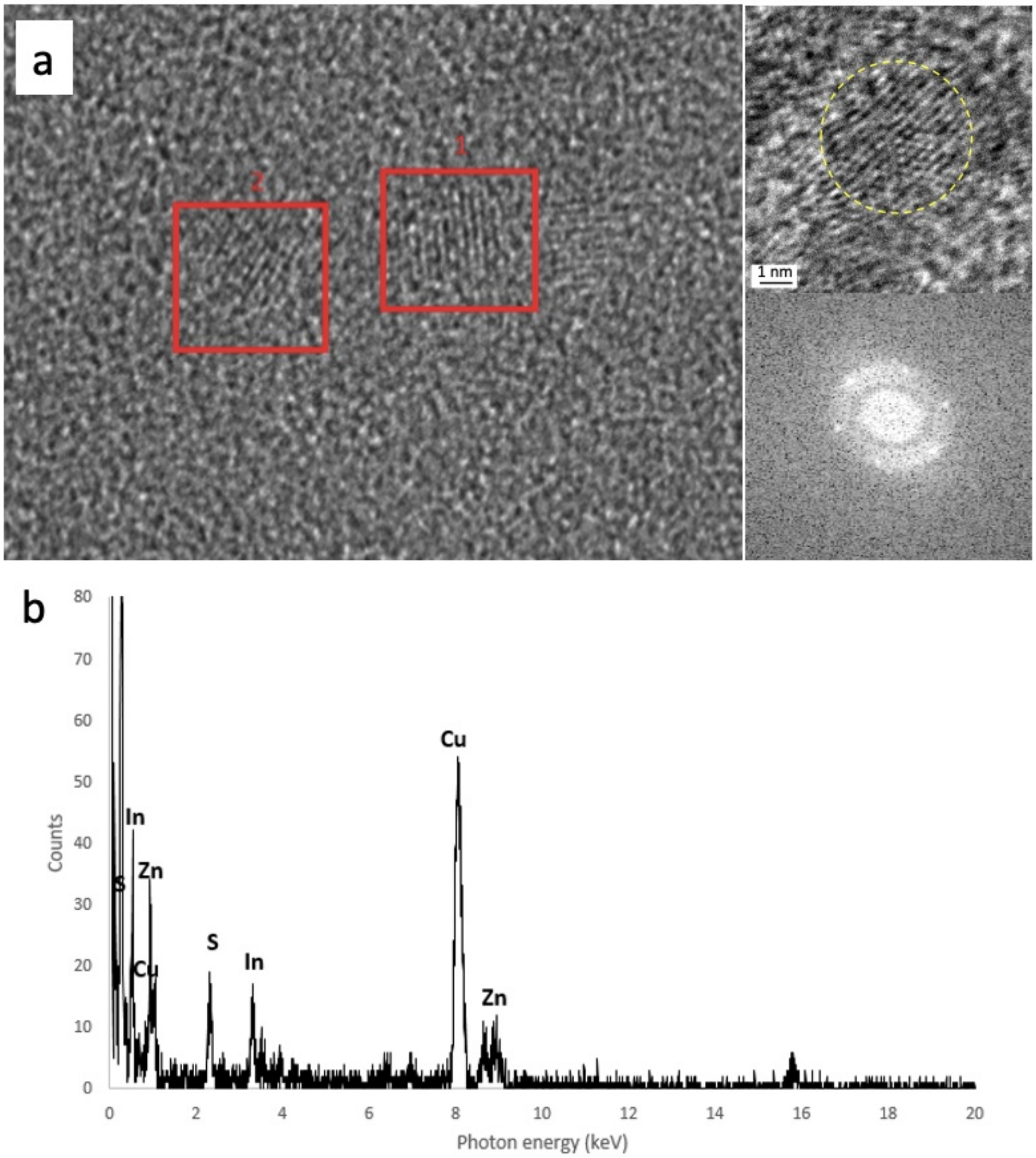

Figure 6.2: (a) TEM, HRTEM (top inset), diffraction (bottom inset) and (b) EDS of 1:1:1 ZCIS QDs.

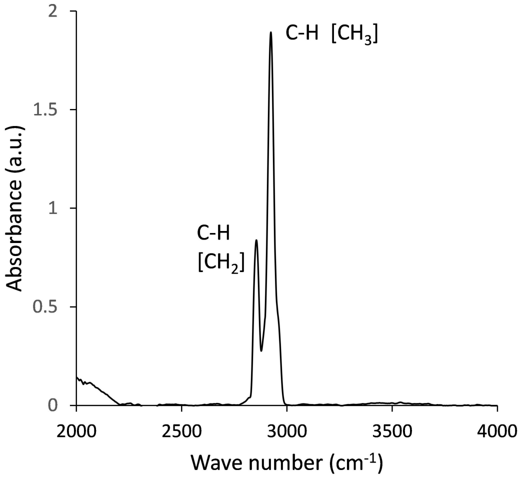

Figure 6.3: FTIR transmission spectra of the synthesized ZCIS QDs showing the C-H stretching vibrations in the DDT ligands [CH_3-$(CH_2)_{11}$-SH].

6.3 Effect of Cationic Stoichiometry on Quaternary QD Lattice

Precursor molar ratio variation affects the growth rate and optical properties of QDs composed of multiple cations [31][146]. This was observed in the synthesis of CIS QDs, where variation of Cu:In ratios produced improvements in PL emission, PLQY, and decay lifetime [31]. Cu or In deficiencies in the CIS QD lattice generate more DAP states, thus dictating the dominant recombination pathways [75]. After successfully establishing the ZCIS QD synthesis process, precursor ratios were varied as a means to produce and study ZCIS QDs with different stoichiometry, generated through variation of Zn:Cu:In precursor ratios. This work is detailed in the following sections.

6.3.1 Optical and Elemental Analysis of ZCIS QDs

To create various stoichiometries, $Zn(SA)_2$, CuI, and $In(Ac)_3$ precursors were used in different molar ratios of 1:1:2, 1:2:1, and 2:1:1. DDT was kept at a constant volume of 5 mL. Fig. 6.4 shows the PL emission and absorption spectra of the ZCIS core QDs synthesized using different Zn:Cu:In molar ratios. Samples for PL, decay, and absorbance characterization were prepared by spin-casting (500 rpm for 10 s, followed by 1500 rpm for 30s) QDs onto a clean 2.2 × 2.2 cm^2 glass substrate.

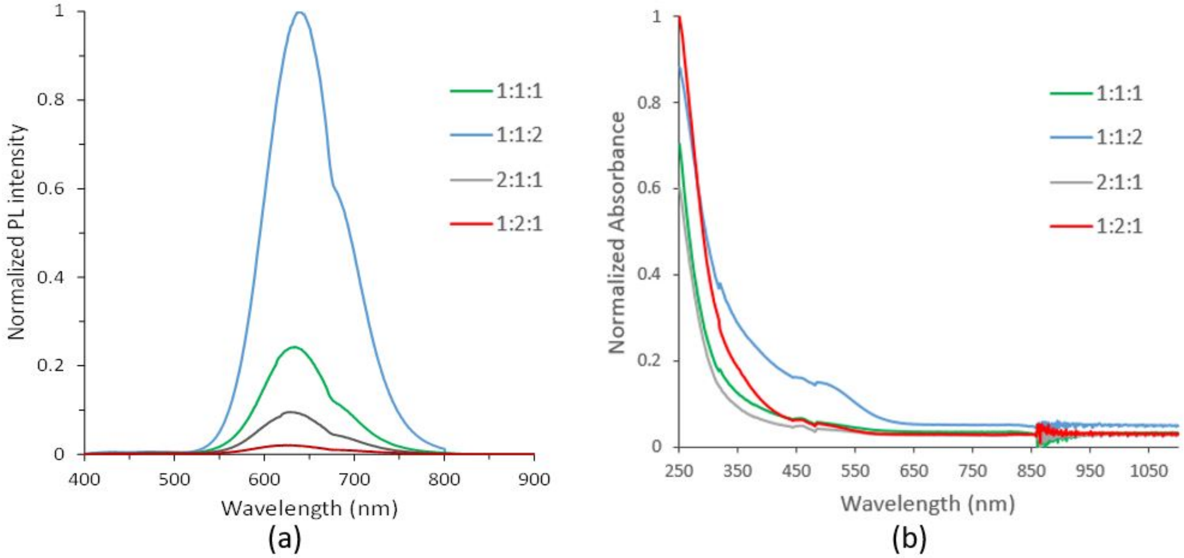

Figure 6.4: (a) Photoluminescence emission and (b) absorption spectra of ZCIS core QDs synthesized using precursors with different Zn:Cu:In ratios.

Fig. 6.4(a) presents PL intensity spectra of the four cationic ratios. The 1:1:2 In-excess ratio showed the strongest emission peak, again affirming In excess to be beneficial to ZCIS QD compositions. The strong emission is attributed to the creation of Cu deficiencies through In excess, promoting radiative DAP recombination via creation of additional In interstitial donor states and Cu vacancy acceptor states [93][149]. The peak displayed by the In-excess ZCIS QDs is comparable to the PL emission intensity of the CIS/ZnS QDs [31]. Interestingly, the other cationic variations show lower PL emission intensity than the stoichiometrically balanced 1:1:1 Zn:Cu:In ratio, which itself is comparable to the core CIS QDs. This is attributed to the simultaneous creation of radiative recombination pathways and suppression of non-radiative surface states in In-excess ZCIS QDs. Implementing In-excess precursor ratios create the Cu vacancies needed for increased radiative recombination, while the presence of Zn promotes QD crystallinity through lattice passivation, reducing the prevalence of surface defects which contribute to non-radiative recombination. This desirable combination is not present in other ratios, resulting in lower emissions that are not comparable to CIS/ZnS QDs.

All QDs show similar absorbance profiles, with a peak at approximately 460 nm (Fig. 6.4(b)). This is congruent with literature, which state CIS QD emission peaks to significantly redshift from absorption peaks [68][75], and is advantageous for avoiding reabsorption. The In-excess precursor ratios show a more pronounced absorption peak, again attributed to the enhanced optical and structural properties produced through Cu deficiency and Zn abundance. The Cu-excess QDs show the poorest optical properties; as Cu-excess ratios are associated with greater strain on the cupric chalcopyrite lattice [149], increased Cu content is attributed to the creation of undesirable surface states and defects.

Fig. 6.5 presents the ICP-MS elemental analysis of the ZCIS QDs of various ratios; this measurement was performed to study the stoichiometric ratio of the ZCIS QDs. The ratio of the detected elements indicated the core structure of the 1:1:1, 1:1:2, 1:2:1, and 2:1:1 Zn:Cu:In QDs to be $Zn_{0.8}CuIn_2S_{0.8}$, $ZnCuIn_3S_{1.5}$, $Zn_{0.4}CuInS_{0.3}$, $Zn_2CuIn_2S_{0.7}$, respectively. In the ratios containing larger amounts of Zn or In precursors, the In content is larger, inducing favourable Cu deficiency. This is in agreement with the higher PL obtained from the In-excess precursor ratio, which is associated with Cu deficiency. However, the Zn-excess ratio shows lower emission than both In-excess and stoichiometrically balanced ZCIS QDs. It can be seen that the In content in the Zn-excess ratios is lower than the In-excess ratios, leading to fewer In_{Cu} defects that contribute to radiative recombination. Zn-excess contributes mainly to repairing the lattice, removing surface state defects and therefore reducing non-radiative recombination pathways. However, the failure of Zn-excess ratios to create additional radiative recombination states leads to lower emission intensity compared to In-excess precursor ratios. The S content of the stoichiometrically balanced ZCIS QDs is slightly higher than Zn-excess ratios, leading to better QD stability and crystallinity, and therefore, more intense emission. Synthesis with Cu-excess precursor ratios create significant Zn and S deficiencies, both of which are undesirable due to the significant roles they play in stabilization of the QD core. This shows that precursor ratios significantly affect ZCIS QD stoichiometry.

6.3.2 Comparison of CIS and ZCIS QDs

Fig. 6.6 presents a comparison of PL emission curves of ZCIS QDs and core CIS QDs. The 1:1:1 ZCIS QD, without off-cationic optimization, shows lower PL emission intensity compared to CIS QDs, whose structural and optical characteristics were optimized through synthesis using a gradient T-ramped, Cu-deficient 1:2 precursor ratio. The emission intensity of the Zn-excess 2:1:1 ZCIS QDs, which have some Cu deficiency, is more comparable with the core CIS QDs, albeit slightly higher. The 1:2:1 ZCIS QDs show significantly lower PL emission intensity than the optimized CIS cores.

The most appropriate comparison can be made between the CIS QDs and the 1:1:2 ZCIS QDs, which both induce Cu deficiency via In-excess precursor ratios. The PL emission

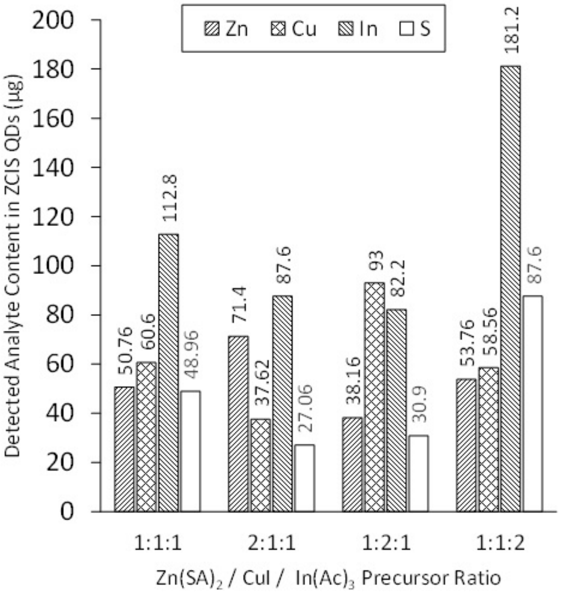

Figure 6.5: ICP-MS analyses of ZCIS QDs synthesized using various precursor ratios.

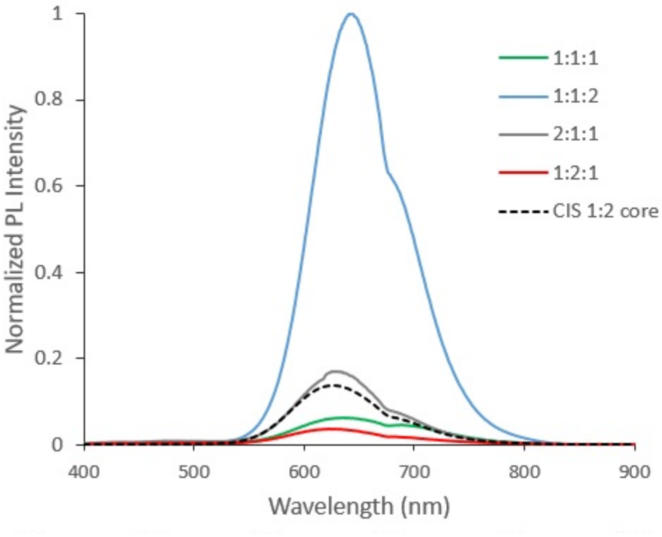

Figure 6.6: PL emission intensity comparison of core CIS QDs with of ZCIS QDs produced using different ratios for the Zn:Cu:In precursor ratios. The QDs were extracted approximately 300 min into the growth.

intensity of the In-excess ZCIS QDs is significantly higher than the emission of the CIS QDs. This enhancement shows the influence of Zn on the ternary CIS structure; although In-excess precursor ratios augment radiative optical pathways on their own, it is clear that the addition of Zn further enhance QD optical properties via lattice passivation. However, as indicated by the comparable performance of the other precursor ratios, simple addition of Zn is not sufficient to enhance ZCIS QDs; the parallel addition of excess Zn and In is vital to improving the quaternary QD effectiveness. Overall, varying the precursor mix ratios provides good control over the stoichiometry of the synthesized QDs.

Indium-Excess ZCIS QD Compositions

In-excess precursor ratios yielded the most optically favourable ZCIS QDs. Fig. 6.7(a) shows TEM images of the In-excess QDs, synthesized using 2 mmol $In(Ac)_3$ and 1 mmol of the other cationic precursors. The QDs are monodisperse, crystalline, spherical, and approximately 4 nm in size. Peaks for Zn, Cu, In, and S were detected by EDS (Fig. 6.7(b)).

Copper-Excess ZCIS QD Compositions

In CIS-based QDs, an abundance of Cu-related defect sites from overly Cu-deficient stoichiometries result in weakened CIS lattices susceptible to thermal instability and quenching [31]. Fig. 6.8 shows the TEM, diffraction, and EDS of the Cu-excess 1:2:1 Zn:Cu:In ZCIS QDs, produced using 2 mmol of CuI while keeping other cationic precursors constant at 1 mmol. During optical analysis, Cu-excess ZCIS QDs consistently showed poorer performance than the other cationic ratios, attributed to lattice distortions produced by implementing the higher Cu molar ratio. HRTEM indicates a spherical, fairly crystalline, monodisperse QD approximately 4 nm in size. However, the QD film appears less crystalline than other ratios, correlating to the Cu-excess QDs' greater lattice deformity. Nevertheless, it should be noted that HRTEM is limited in its capacity of determining structural defect of QDs. EDS detected Zn, Cu, In, and S.

Zinc-Excess ZCIS QD Compositions

Zinc excess was induced by using 2 mmol of the $Zn(SA)_2$ zinc precursor, in addition to 1 mmol each of the In and Cu precursors. Fig. 6.9 shows the TEM, diffraction, and EDS of the QDs synthesized with Zn-excess 2:1:1 Zn:Cu:In precursor ratio. The QDs produced

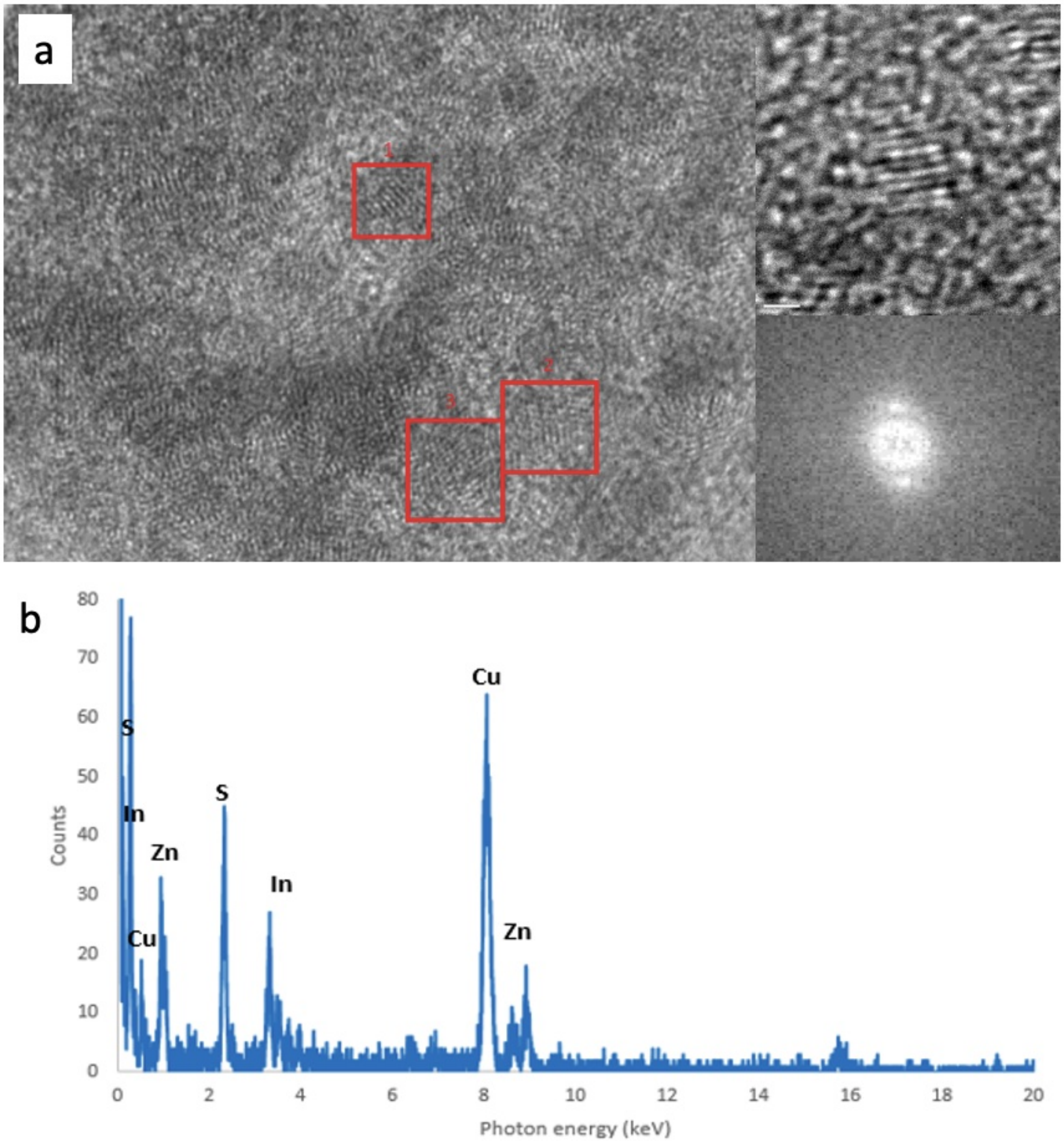

Figure 6.7: (a) TEM, HRTEM (top inset), diffraction (bottom inset) and (b) EDS of 1:1:2 ZCIS QDs.

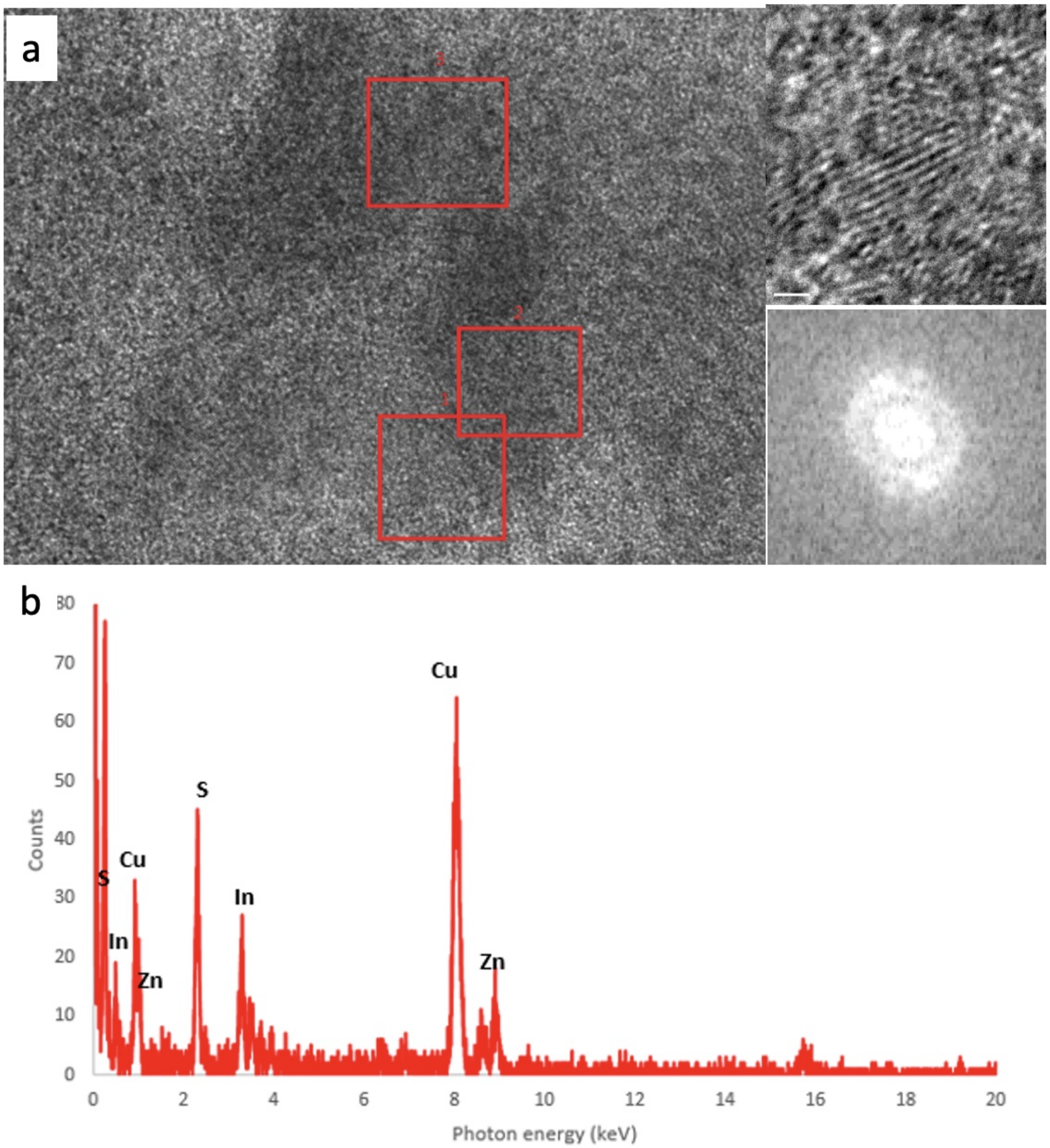

Figure 6.8: (a) TEM, HRTEM (top inset), diffraction (bottom inset) and (b) EDS of 1:2:1 ZCIS QDs.

from the Zn-excess precursor ratio are notably larger, measuring almost 6 nm in diameter. TEM images show that the QDs form a film across the substrate surface; the high loading and packing of the QDs make it appear as a bulk crystalline solid rather than disparate QDs arranged across the surface. The strong crystallinity indicated by the diffraction images show an abundance of QDs. It is known that very monodisperse, crystalline QDs easily arrange into periodic, crystalline solids [17], even when drop-cast (as is the case in preparing TEM samples). This confirms that although the optical performance of Zn-excess ratios do not show advantages over the In-excess ratios, the excess Zn provide improvements in the lattice crystallinity, resulting in greater periodicity of the QD solid configuration. EDS identified the presence of Zn, Cu, In, and S. Although the signal was weaker compared to other ratios, this cannot be taken as a quantitative measurement on the concentration of each element, as the peaks detected are only qualitative affirmation of the presence of the elements under detection.

6.4 ZuCuInS/ZnS Core/Shell Structures

ZnS overcoating significantly improve the optical and structural characteristics of CIS QDs. During the overcoating process, Zn^{2+} ions inter-diffuse into the CIS core, displacing Cu^{+} and In^{3+} ions, reducing structural instability [31]. Furthermore, the surface passivation afforded by overcoating eliminates non-radiative pathways, improving QD optical properties [31]. It has been observed that the PL emission and decay lifetime of CIS/ZnS core/shell structures show strong improvement compared to the original core QDs. ZnS overcoating was implemented on ZCIS core QDs, to determine if similar improvements could be produced. The following sections present the implementation and characterization of ZCIS/ZnS core/shell QDs.

6.4.1 ZCIS/ZnS Overcoating Procedure

The shell growth process is also completed using the same Schlenk line setup, under vacuum and N_2. The overcoating solution is prepared by mixing 0.4 mmol $Zn(SA)_2$ and 0.4 mmol sulfur (i.e., Zn:S molar ratio of 1:1) to 4 mL ODE and 5 mL TOP, followed by sonicating for 90 minutes to thoroughly mix the solution; other ratios will be discussed later. To begin overcoating, 1 mL of purified ZCIS QDs and 4 mL ODE are added to a 3-neck flask and heated to 100°C. Upon reaching this temperature, the ZnS overcoating solution is added drop-wise to the ZCIS QD/ODE solution (≈1 drop/s). As the shell growth commences, the solution blueshifts from the dark red color of the core, towards

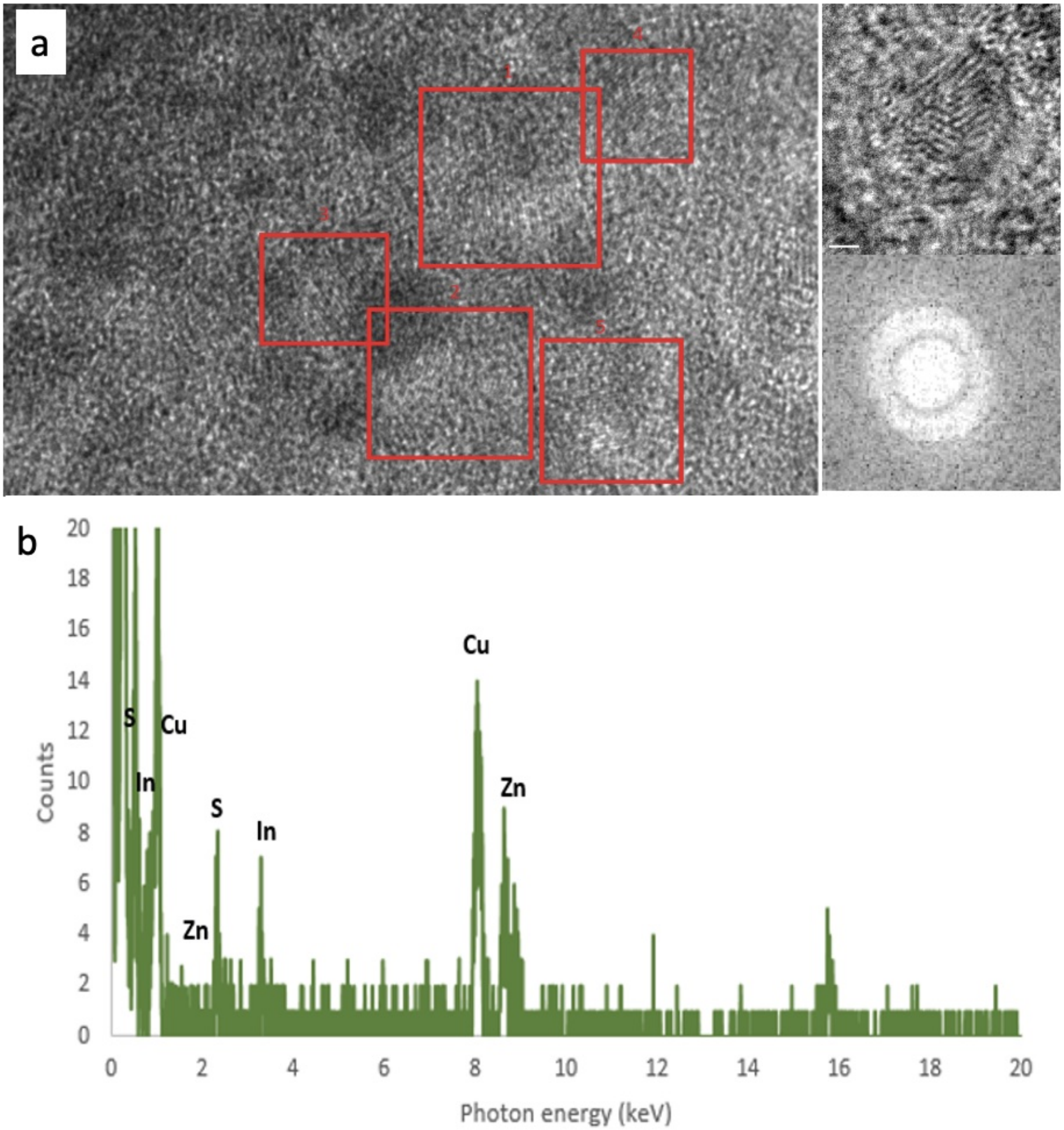

Figure 6.9: (a) TEM, HRTEM (top inset), diffraction (bottom inset) and (b) EDS of 2:1:1 ZCIS QDs.

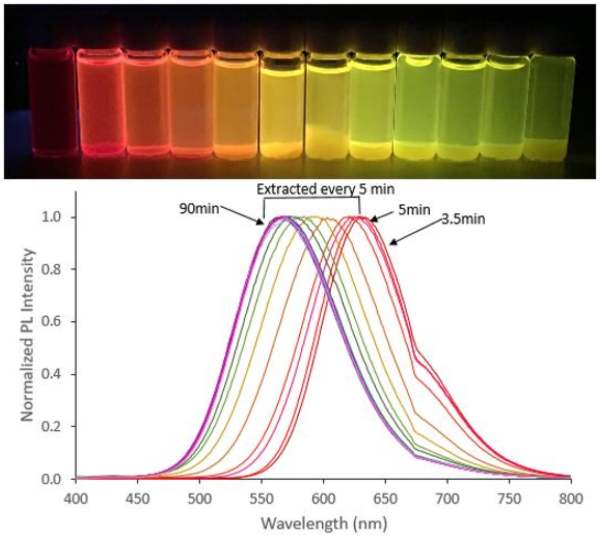

Figure 6.10: Photoluminescence profile of ZCIS/ZnS core/shell QDs grown over 70 minutes of overcoating. The top inset shows select, visually distinct vials of the produced ZCIS QD solutions, arranged in order.

green. The overcoat process can be halted at any point, through fast extraction and immersion in water bath, or injection of hexane. The TOP-ligated ZCIS/ZnS QDs are purified via centrifugation, and subsequently re-dispersed in hexane.

To study the progression of overcoating, aliquots were extracted at 5 minute intervals. Prior to each extraction, a 1 min wait time was observed to allow the overcoat material to incorporate into the solution. The aliquots were extracted using a syringe, into a cooled glass vial sitting in a cold water bath. Fig. 6.10 shows the growth profile of overcoated ZCIS/ZnS QDs, using a 1:1:2 precursor ratio. As with the CIS core QDs, ZnS overcoating produces blueshift of ZCIS QD emission, and a wider range of emission is possible after ZnS overcoating. As the ZCIS core is more stable than CIS, it is more difficult for Zn^{2+} atoms to inter-diffuse, reducing excessive blueshifting during overcoating [118]. However, a flexible range of colours is still possible, with emission as low as 564 nm obtained.

6.4.2 Effect of Overcoat on 1:1:1 ZCIS QDs

The PL emission and decay lifetime of overcoated CIS/ZnS QDs show strong improvement compared to properties of the original core QDs. In Chapter 4, it was found that a ratio of 4:1 (1.6 mmol:0.4 mmol) Zn:S provided the most optimal emission, while a ratio of 8:1 (3.2 mmol:0.4 mmol) providing the longest lifetime [31]. Excessively high Zn content did not contribute to improving the QD structure, and only increased unwanted sedimentation in the QD solution. As S-excess ratios did not significantly contribute to CIS QD improvement, they were not investigated for ZCIS QDs.

Unlike CIS, ZCIS core QDs possess a more stable quaternary lattice with incorporated Zn ions, which are more resistant to replacement by the Zn cations from the overcoat. Thus, the extent of QD improvement aided by ZnS overcoating can be expected to be somewhat limited. ZCIS QDs of various precursor ratios were overcoated with various ratios of ZnS overcoat solutions, then characterized. Fig. 6.11 shows the normalized PL emission and decay spectra of stoichiometrically balanced ZCIS core QDs with a 1:1:1 precursor ratio, overcoated with 1:1 and 4:1 Zn:S overcoats. Normalized spectra are used to emphasize the effects of various Zn:S overcoat ratios on the individual core ZCIS QDs. The PL emission intensity of QDs overcoated with a 4:1 Zn:S ratio is the highest, and overall, the overcoated QDs show more intense emission than the core QDs. However, the decay spectra and lifetime of the core QDs are better than their overcoated counterparts. The stoichiometrically balanced ZCIS QDs show lower Zn content compared to In- and Zn-excess ratios, corresponding to some lattice imperfections. When overcoated, the inter-diffusion of Zn aids in improving the lattice, leading to defect removal and increased radiative recombination. However, for this ratio, the act of overcoating seems to disturb the surface, leading to poorer decay spectra and lifetime.

6.4.3 Effect of Overcoat on In-, Cu-, and Zn-excess ZCIS QDs

Fig. 6.12 shows the PL emission spectra of ZCIS QDs synthesized under various cationic stoichiometries, each overcoated with ZnS shells using 1:1 and 4:1 ratios. Overall, the core/shell formations result in strong PL intensities, especially when the shell is Zn-rich. A Zn:S ratio of 4:1 in the shell seems to yield sharper and narrower PL emissions compared to the core counterparts. In the case of Cu-excess cores (Fig. 6.12(b)) there is a prominent increase in PL intensity, corresponding to higher Zn content in the shell. As discussed earlier, the Zn deficiency prevailing in the initial core seems to have been largely overcome by the Zn-excess shell growth. Interestingly, in the cases of In-excess and Zn-excess cores (Figs. 6.12(a) and 6.12(c)), the improvement induced by increased Zn content in the shell is rather limited. This is due to significant Cu deficiency already existing in those cores.

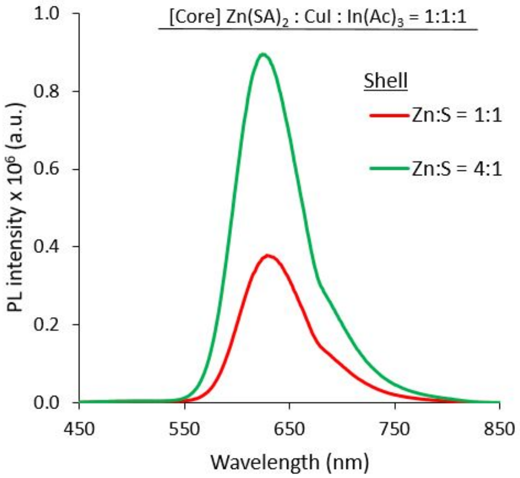

Figure 6.11: Photoluminescence spectra of the ZCIS/ZnS QDs, using 1:1:1 ZCIS cores, with 1:1 and 4:1 ratios in the [$Zn(SA)_2$:S] coating solution.

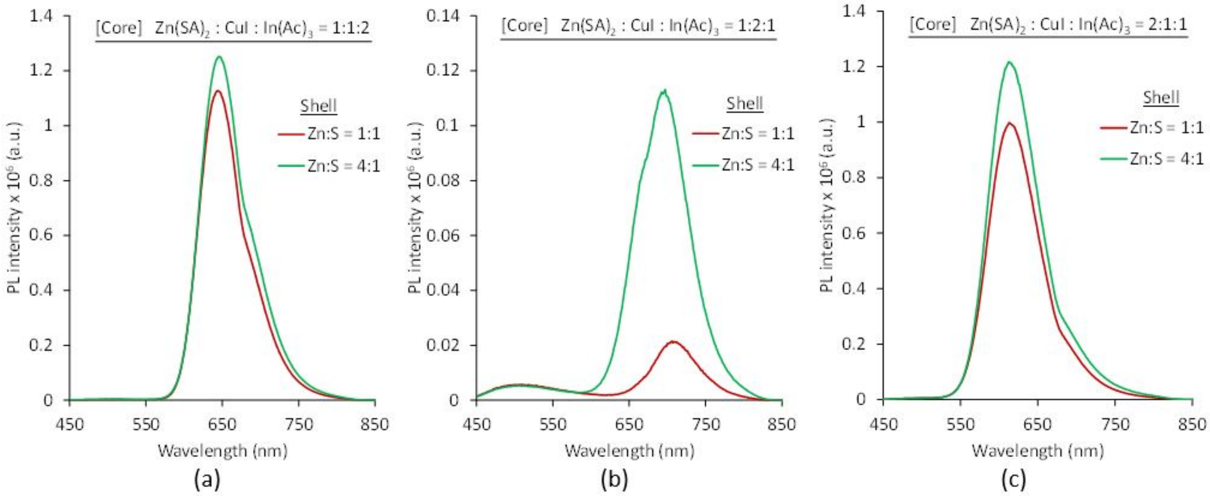

Figure 6.12: Photoluminescence spectra of the ZCIS/ZnS QDs with the cores synthesized with varying $Zn(SA)_2$:CuI:$In(Ac)_3$ precursor ratios of (a) 1:1:2, (b) 1:2:1, and (c) 2:1:1, and with 1:1 and 4:1 ratios in the [$Zn(SA)_2$:S] coating solution.

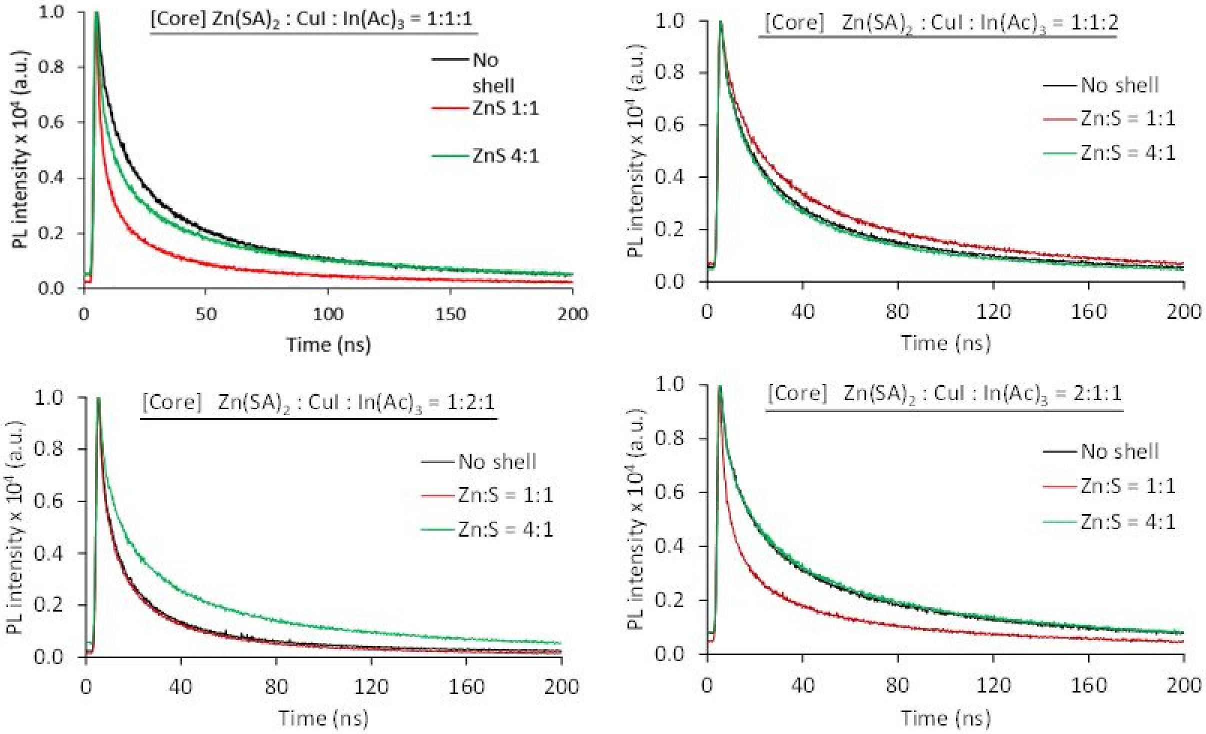

Figure 6.13: Photoluminescence decay curves of the ZCIS/ZnS QDs with the cores synthesized with varying $Zn(SA)_2$:CuI:$In(Ac)_3$ precursor ratios of (a) 1:1:1, (b) 1:1:2, (c) 1:2:1, and (d) 2:1:1, and with different ratios in the shell coating solution.

6.4.4 Decay Lifetime Analysis of ZCIS and ZCIS/ZnS QDs

The measured PL decay curves of the core and core/shell QDs for each of the three precursor ratio groups are shown in Fig. 6.13. The lifetime components are shown in Table 6.1, calculated using multi-exponential tail fitting using the FAST software. For each decay curve, the fit quality factor χ^2 was verified to be < 1.3 to ensure reliability.

Shells Grown on Stoichiometric Cores

The 1:1:1 core ZnS QD shows significantly strong lifetime at over 165 ns, which is comparable to the lifetime of the overcoated CIS/ZnS QDs presented previously. The lifetime is much higher than the 1:2 Cu:In core QDs, indicating this ZCIS to have a more stable,

Table 6.1: Decay lifetime components for synthesized ZCIS and ZCIS/ZnS QDs.

Sample	B_1	τ_1	B_2	τ_2	B_3	τ_3	$\langle\tau\rangle$	χ^2
Stoichiometric								
ZCIS 1:1:1 Core	3376.4	8.752	3847.8	32.696	1546.3	226.177	165.265	1.019
ZnS 1:1	2622.9	5.289	2226.3	17.518	1026.8	76.448	51.439	1.094
ZnS 2:1	3297.9	7.354	3784.1	25.175	1159.2	108.746	66.313	1.075
ZnS 4:1	2693.6	6.812	2621.8	23.203	1871.8	104.176	79.694	0.98
In-excess								
ZCIS 1:1:2 Core	2540	3.424	4297.8	17.458	3042.5	73.066	57.453	1.126
ZnS 1:1	2233.7	3.676	3869.8	18.488	3723.1	78.961	65.731	1.103
ZnS 2:1	2443.7	3.502	353.12	18.654	3438.6	81.44	67.388	1.068
ZnS 4:1	2650.3	3.17	4382.5	16.126	3089.4	68.615	53.981	1.023
Cu-Excess								
ZCIS 1:2:1 Core	3970.9	2.125	4267.1	11.635	1853.6	47.358	32.583	1.126
ZnS 1:1	3654.5	7.075	2884.1	24.48	707.81	114.845	63.275	1.001
ZnS 2:1	3297.9	7.354	3784.1	25.175	1159.2	108.746	66.313	1.075
ZnS 4:1	2706.6	6.016	3597.6	23.845	2114.5	106.851	80.136	1.023
Zn-Excess								
ZCIS 2:1:1 Core	1756.8	6.316	3351.9	18.237	3283	80.102	66.377	1.077
ZnS 1:1	2874.3	6.914	2204.5	25.491	1364.7	120.974	89.326	1.087
ZnS 2:1	2845.5	8.76	3285.4	34.532	2254.6	187.339	148.485	1.075
ZnS 4:1	2651.9	10.741	3420.8	38.144	2152	205.382	159.844	1.023

crystalline lattice with a more passivated surface. However, overcoating significantly reduces the lifetime by less than half of the core lifetime value. This is in stark contrast to previously reported CIS QDs, where overcoating reduced surface traps that produced short-lived non-radiative recombination, allowing radiative recombination to dominate [31]. Based on ICP-MS, use of 1:1:1 precursor ratio does not produce Zn-abundant lattices; ZnS overcoating promotes Zn^{2+} diffusion into the core, thus improving the optical emission. However, during the overcoating, the surface of the QDs is perturbed, creating additional non-radiative surface recombination pathways for overcoated QDs. Therefore, although overcoating improves emission intensity, it also increases the short-lived lifetime components due to surface modifications.

Shells Grown on Indium-Excess Cores

Although the In-excess 1:1:2 ratio showed the highest PL emission intensity compared to the other precursor ratios, its lifetime, while significantly higher than that of Cu-excess core QDs, is comparable to that of Zn-excess core QDs. Also, the shell growth with increasing Zn content does not significantly affect the lifetime, even showing a slight drop for the 4:1 ratio. This suggests that minimal Zn^{2+} inter-diffusion and surface passivation occurs during overcoating. However, the PL emission intensity of all overcoated QDs are of approximately the same magnitude. Overall, for In-excess ZCIS core QDs, increasing Zn in the shell brings little benefit, and excessive Zn in the shell may perturb the surfaces, producing additional pathways which cause faster, short-lived decay.

Shells Grown on Copper-Excess Cores

The Cu-excess ZCIS QD shows particularly low lifetime, which corroborates its lower PL emission intensity compared to the other precursor ratios. Based on PL emission and decay analyses, Cu-excess ZCIS QDs seem to have an abundance of surface defects with dominating non-radiative recombination, making them optically least favorable. ZnS shell growth spectacularly improves the lifetime, making it comparable to the lifetimes of the In- and Zn-excess core QD ratios. This suggests that the Cu-excess ZCIS core lattice is passivated by further alloying via Zn ions, much in the way that the ternary CIS QDs benefit from ZnS overcoating [18][31]. This correlates with the optical and structural behaviour observed using this cationic precursor ratio, which indicates the presence of more serious core and surface defects compared to other ratios. Making the shell more Zn-rich (i.e., 4:1 ratio) further improves the emission intensity.

Shells Grown on Zinc-Excess Cores

The Zn-excess core ZCIS QD shows the highest lifetime out of the three excess-precursor core ZCIS QDs. The lifetime increases after shell formation, reaching a very high value when the shell is Zn-abundant. At the same time, the improvement in PL intensity brought about by shell formation is only moderate. This suggests that a Zn-excess precursor ratio produces core ZCIS QDs with more dominant non-radiative recombination, and continuing to alloy with Zn via overcoating further eliminates surface defects. The addition of Zn ions serves to increase the concentration of internal states associated with longer-lived lifetime, eventually producing lifetimes comparable to CIS/ZnS QDs. Also, the ICP-MS indicate that an excess of Zn precursors during core synthesis produces QDs with the most Zn-abundant stoichiometry ($Zn_2CuIn_2S_{0.7}$). Therefore, although the ZnS shell contributes to passivation of the surface, it does not significantly improve the bulk QD lattice, negating the necessity of Zn-excess overcoating ratios.

Overall, the ZnS shell formation improves, to various degrees, the PL emission intensity in core ZCIS QDs, with a 4:1 Zn:S overcoat ratio producing the highest emission intensity. It is the defective Cu-excessive ZCIS structure that benefits the most, in terms of lifetime and PL intensity, from increasing Zn content in the shell. The In-excess and Zn-excess core ZCIS QDs do not benefit much from high Zn content in the shell. This is in contrast with the ternary CIS QDs, in which Zn-excess shell suppresses non-radiative surface recombination pathways, allowing radiative recombination pathways to dominate. As ZCIS QDs already contain Zn within their cores, incorporation of additional Zn components does not significantly contribute to stability. Most of the improvements in optical properties are attributed to promotion of radiative internal states via Zn inter-diffusion; decay measurements do not indicate significant surface passivation. Compared to overcoating of CIS QDs, overcoating ZCIS QDs does not produce significant improvements in optical and structural properties. In fact, ZCIS/ZnS QDs do not achieve higher lifetimes than CIS/ZnS QDs, attributed to the more complex optical mechanisms in the tri-cation system. However, the PL emission and decay lifetime achieved by core ZCIS QDs are superior to that of unpassivated core CIS; ZCIS QDs are best implemented without overcoating.

6.5 Towards Device Application

Alloyed ZCIS QDs were created to reap the benefits of Zn incorporation in CIS without the disadvantages of carrier transport from shell confinement. A simple planar diode was fabricated based on the In-excess 1:1:2 ZCIS core QDs to study the I-V behaviour of ZnO/ZCIS QD heterojunction devices.

6.5.1 Ligand Exchange of ZCIS QDs

A liquid-phase ligand exchange process was implemented to exchange the long DDT ligands of the In-excess ZCIS QDs for shorter MPA ligands, based on the ligand exchange practiced on the core CIS QDs presented in the previous chapter [171]. Fig. 6.14(a) shows FTIR of 1:1:2 ZCIS QDs, before and after ligand exchange. The characteristic C-H peak at the 2800-3000 cm^{-1} stretch, indicative of a long hydrocarbon, disappears following ligand

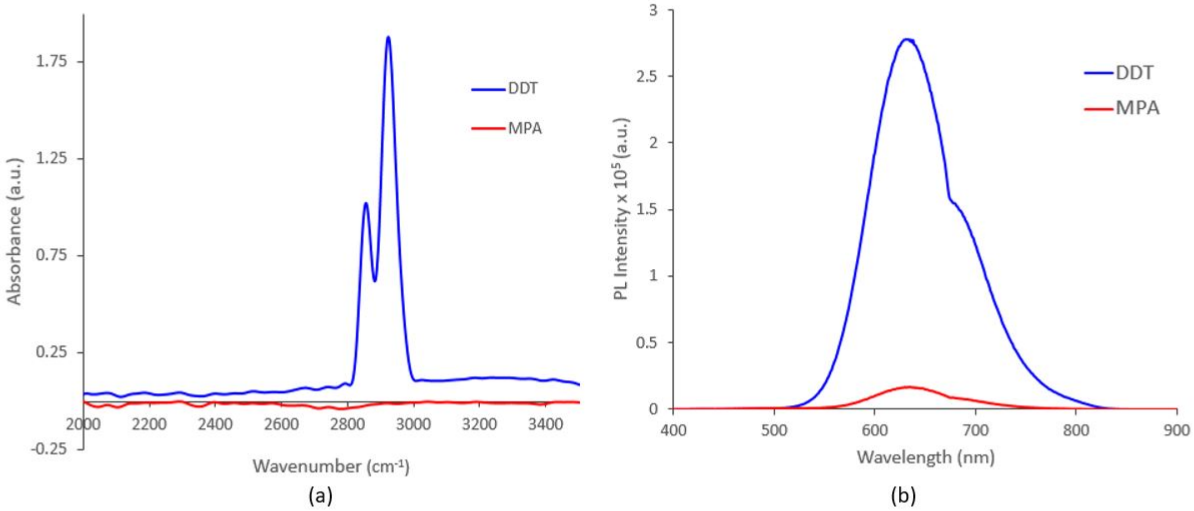

Figure 6.14: (a) FTIR and (b) PL spectra of ZCIS QDs before and after DDT-to-MPA ligand exchange.

exchange. This confirms ligand exchange, as the 12-carbon chain DDT is replaced with the shorter MPA ligand.

Fig. 6.14(b) shows the PL spectra of the ZCIS QDs before and after ligand exchange. The PL emission intensity of the QDs DDT-ligated is nearly 3×10^5 counts. Following ligand exchange, the intensity decreases by one order of magnitude, with the peak measuring approximately 1.6×10^4 counts. Both spectra shows the characteristic wide full width half maximum of CIS-based QDs, and the emission peak is at approximately 640 nm.

6.5.2 Preliminary I-V Characteristics

To investigate the applicability of the ZCIS QDs to devices, a simple, preliminary heterojunction ITO/ZnO/ZCIS QD/MoO_3 diode was fabricated based on the device presented in the previous chapter [171]. I-V curves were obtained for the device under dark and controlled illuminated conditions (Agilent 4155C). Samples were provided inside of a dark, sealed chamber to prevent unwanted ambient illumination. To provide illumination, a fibre optic ring light connected to a JH Technologies EKE light box was mounted over the device under test; the EKE light box generates 1 sun illumination when set to maximum illumination settings and mounted directly over the device. The response of the device was

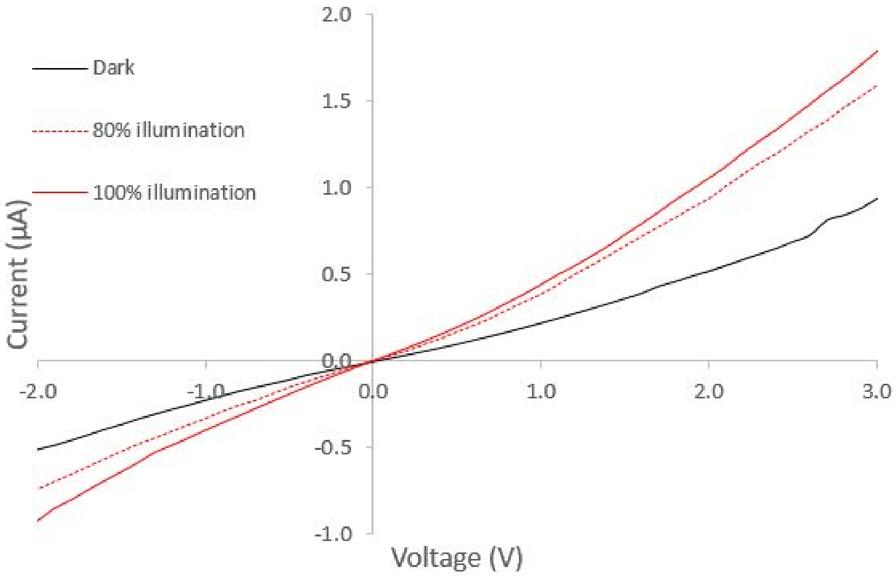

Figure 6.15: I-V curves of photodetector devices made from synthesized, MPA-ligated ZCIS QDs, showing response under illumination.

measured under dark, 80% illumination, and maximum illumination conditions; Fig. 6.15 presents the results.

The device displays a typical diodic I-V curve of a photodetector under dark conditions. Upon illumination at 80% of the light's maximum 1 sun brightness, the device shows a response; this response increases when the device is illuminated more intensely. Turn-on voltage is located at approximately 0.5 V. Thus, the ZCIS-based device shows response to illumination, with expected photodetection behavior, showing the ZCIS QDs to be applicable to devices.

6.6 Conclusions

Zinc copper indium sulfide quantum dots with good optical properties and long lifetimes, were synthesized in a low-temperature, gradient T-ramped, high-throughput process. The ZCIS QDs presented here show strong photoluminescence, good crystallinity, and long lifetime, making them promising in a multitude of applications. The bright photoluminescence emissions of these QDs are tunable in the visible range. Compared to core CIS QDs, the alloying of Zn aided in stabilizing the QD cores and passivating the surfaces, resulting in higher PL emission and longer lifetime. Variation of cationic Zn, Cu, and In precursors were investigated, and found to provide control over the stoichiometric composition of the QD. Inducing excess In or Zn precursors produced desirable Cu deficiency within the lattice, leading to higher PL intensity. QDs containing higher amounts of Zn showed the best lifetime, indicating the passivating nature of Zn incorporation into the core. ZnS overcoating was explored to determine the impact of Zn passivation on the stability and optical properties of ZCIS QDs. Although ZnS overcoating greatly improved the defective lattices of core CIS QDs, it was found to have minimal impact on the PL intensity and lifetime ZCIS QDs, which are more stable and less defective due to the presence of Zn already found within the core. This is with the exception of Cu-excess core ZCIS QDs, which showed the least optically favourable properties due Zn deficiency. ZnS overcoating significantly improved the lifetime of Cu-excess QDs through Zn-passivation. This ZCIS synthesis process is suitable for large-scale, industrial production of stable, less-toxic QDs. The results of this work provide a route for further core QD tunability and functionalization.

Chapter 7

CIS QD solids

Mainstream adaptation to QD technologies strongly depends on the compatibility of uniform film deposition techniques with large-scale, large-area processes. Device quality is contingent on the active QD layer film; non-uniform QD films are highly defective, with cracks and irregular QD arrangements that hinder electron transport. Achieving uniform, ordered QD and nanoparticle arrays produces more cohesive films with better properties [178]. In vertical architectures, the quality of each subsequent material layer is highly dependent on the morphology of previous layers [11].

As QDs are the absorbers in QD-based devices, their position in the device stack significantly influences the formation of other layers of the vertical device. Although solution-processed QDs are preferable for large-scale production, they cannot be deposited using traditional fabrication technologies such as evaporation and sputtering. Solution-based processes such as drop-casting, spin-coating, and dip-coating are most commonly used, especially in research and development (R&D) environments. However, due to the large variation in process control, the use of these techniques pose uncertainty in achieving reliable, high-quality QD films. Self-assembly methodologies that produce ordered, uniform QD solids are sought after in QD device fabrication. The achievement of regular, crystalline QD arrangements is significant to facilitating fast electron transport through the device. This chapter investigates the self-assembly and formation of uniform CIS-based QDs solids for device applications.

7.1 Formation of QD Solids

The formation of QD films from CQDs entails post-synthesis deposition of the QD solution onto the substrate. The solvent evaporates, leaving behind a layer of QDs. The QD surfaces, including ligands, significantly determine their solid arrangement. For instance, the same QD of the same material will form different QD solids if facets of different planes are present on the surface [3]. Polydisperse QDs lead to glassy, amorphous QD films, much as disordered arrangements of atoms produce amorphous bulk materials, while monodisperse, crystalline QDs produce crystalline QD solids with long-range order [3]. QDs occupy the most energetically favourable positions on the surface, forming arrangements that minimize entropy [11]. Therefore, QDs can truly be considered the “atoms” to a QD solid “bulk”. Solvent characteristics are significant to the formation of the QD film; solvents with faster evaporation rates produce poorer QD arrangements, as QDs become immobilized before they are able to traverse to an optimal position [3].

In optimizing the efficiency of the QD absorber, a compromise must be made between loading and carrier transport. In vertical device architectures, the QD absorber must have a sufficient thickness, with a high concentration of QDs for satisfactory light absorption, but cannot be so thick that it hinders transport. Carrier diffusion lengths are fairly short in QD films, and they cannot travel through thick, multi-layered QD films for collection. Overly thick QD layers result in short depletion lengths that increase the likelihood of carrier loss via trapping or recombination, reducing collection [11].

7.1.1 Charge Transport in QD solids

Charge transport within a QD solid is heavily contingent on the arrangement of QDs. In a QD solid, electrons and holes must traverse between orbitals and traps of adjacent QDs via “hopping” (actually multiple tunnelling events; described in Chapter 5). Electronic coupling is one of the major determinants of successful electron transport from one QD to the next QD. Equation 7.1 provides an expression for QD coupling [3], which relies on the rate of tunnelling, Γ (previously defined, and heavily reliant on ligand properties):

$$\beta = h\Gamma \tag{7.1}$$

The availability of orbitals and states determine the success of the transport event. Each transport event brings the probability of losing carriers to trap states or charge recombination. Ligand and QD size contribute significantly to interdot carrier transport in CIS QD solids. In general, QD solids composed of larger QDs are more conducive to efficient electron transport, as less QDs are required per unit area. Therefore, fewer hopping events are needed per unit length to reach the desired location, and there is less probability of carrier loss [179]. QD solids comprised of smaller QDs tend to have lower mobility, corresponding to more frequent loss events, as well as higher amounts of traps in the QDs themselves [141]. In CIS QDs, size correlates to ligand coverage, as established in previous chapters. The presence of too many insulating ligands (such as the under-sized CIS QDs trapped in ligand matrices) hinder charge transport. Conversely, too few ligands (such as in over-sized CIS QDs without sufficient surface ligand coverage) produce cracked, non-uniform films that do not provide pathways to charge transport. Periodic arrangements are preferable, lending to better predictability of charge transport behaviour.

7.1.2 Traps in QD Solids

Trap states are non-uniformly distributed throughout QD solids in large concentrations, making QD transport behaviour difficult to predict. Traps significantly reduce mobility; even if a QD solid shows intrinsically higher mobility, this would only serve to bring carriers to traps more quickly, negating transport [3]. Traps are more concentrated at the solid/air interface, on the topmost layer of QDs (corresponding to the last deposition in this step of fabrication) [45]. As this layer forms an interface in QD-based devices, these solid/air traps provide high probability of retaining carriers within the QD solid before extraction. However, traps that selectively capture electrons or holes are utilized to promote device performance. If a device primarily relies on current from one carrier type, the introduction of traps that preferably capture the other carrier type reduces the probability of recombination, subsequently increasing current.

7.1.3 Core/Shell QD Solids

Type I core/shell structures necessitate tunnelling of carriers through the shell, adding complexity to its transport through the solid. Type I QDs are more common; therefore, in QD device fabrication, core QD solids are preferred over core/shell QD solids. However, the imperfection of unstable core QDs lead to less desirable arrangements and properties for core QD films. The inhomogeneity of core QD states, arising from their defective lattices, may lead to self-quenching or quenching by non-luminescent neighboring QDs. Type I overcoating can reduce such interactions by shielding electron states inside of the core, leading to fewer undesirable quenching events [3].

The formation of QD solids from Type II core/shell configurations provide some advantages through selective confinement of one carrier type. The shell should be arranged in a manner that confines the minority carriers. Similar to carrier-selective traps, carrier-selective confinement is beneficial for devices that rely on current from one type of carrier [143]. Although the advantages of core/shell QD solids were considered, core CIS QDs were primarily utilized in the device implementation of this work, to obtain higher electron transfer rates [176] and completely avoid carrier confinement issues [171].

7.2 QD Film Formation Methodologies

Film formation methodologies are significant in determining the quality of the QD film. The processes employed in various film formation methodologies strongly affect solvent evaporation and QD arrangement, which are significant in determining the crystallinity of the QD solid. This section explores the common methods of QD film formation, and analyzes their applicability in this work.

Drop-Casting

Drop-casting is the simplest and most economical method of QD film deposition; the colloidal QD solution is simply drizzled onto the substrate and the solvent is evaporated, leaving a film [11]. However, difficulties in controlling the film thickness and profile using this imprecise technique results in non-uniform films [11]. The structure of the QD solid heavily relies on QD and solvent properties, with assembly dependent on the interactions between the charged particles [180]. Difficulty in controlling solvent evaporation frequently produces non-uniform, flawed films with thicker edges [3][11]. To exert greater control over film properties, drop-casting is used with strategies to promote film formation, such as controlled solvent evaporation or containing QD coverage within a defined area.

Although imprecise, the low cost and simplicity of drop-casting cultivates its status as the most common method of QD film formation. Drop-casting is best performed with QDs that have proclivity towards self-assembly. Very monodisperse, crystalline QDs will arrange themselves into regular, periodic monolayers [17], while polydisperse QDs will form amorphous QD solids. Due to their intrinsically defective dual-cationic lattices, ordered monolayers are difficult to obtain in CIS QDs, and there is great risk for formation of QD “islands” that leave significant portions of the substrate bare.

Spin-Coating

Spin-coating, or spin-casting is a procedure in which the QD solution is deposited over the substrate, then rotated at a high speed to coat the substrate and evaporate the solvent. Compared to drop-casting, spin-coating allows better control over uniformity and thickness, via rotational speed and solvent concentration [11]. However, this method comes with the caveat of significant material waste (over 90% of the precious, expensive solution initially deposited [11]), and a risk of undesirable cracks [113][181]. Spin-coating is one of the most common methods of QD film formation, and can be applied industrially.

Dip-Coating

Dip-coating is a more complicated method of film formation, in which the substrate is precisely immersed and withdrawn vertically from the QD solution, producing crack-free, uniform films with minimal solution waste. Excess QD solution drains back into the vessel, and a film forms when the solvent evaporates. The precision of dip-coating allows significantly more control over the final film properties, such as film thickness and morphology [181]. Four main categories of factors determine the results of dip-coating: functionalization of substrate surface, functionalization of solution, dipping parameters, and environmental conditions. The substrate should be clean and free from contamination; furthermore, the substrate surface can be functionalized to improve film adhesion. Meanwhile, the solution composition, concentration, viscosity, and temperature strongly determine film adhesion and morphology. The dipping parameters most significant in affecting the final form morphology include submersion time, withdrawal speed, and number of dipping cycles. Finally, environmental factors such as temperature and humidity affect film quality and should be carefully monitored [182][183]. Dip-coating is easily scaled up for roll-to-roll process industrial processes [11]. Dip-coating of CIS QD films is further discussed later in this chapter.

Langmuir-Blodgett

In the Langmuir-Blodgett method, the QD solution is placed onto a liquid/gas interface in a bath, then transferred onto the substrate. Similar to dip-coating, the substrate is placed vertically into the solution, and entraining forces are utilized to draw a monolayer of QD film onto its surface. The surface pressure within the Langmuir-Blodgett bath is strictly controlled in this delicate process [11]. As the liquid employed in the bath is water, QDs that are moisture-sensitive are not compatible with this process. The fastidiousness of this process makes it less popular than the other methods in R&D. Due to the sensitivity of QDs to humidity and ambient, as well as significant issues of QD aerosolization and exposure during the process, the use of Langmuir-Blodgett is questionable for safety-conscious QD film formation. For reasons related to safety and QD and facility contamination, Langmuir-Blodgett was not utilized in any part of this work.

Doctor Blading

The methods presented previously are mainly relegated to small-area QD film formation, practiced in research laboratories and R&D facilities. Doctor blading is employed for coating large-area substrates, and can be applied towards QD film formation. In doctor blading, the QD solution is deposited, and drawn across the substrate using a bladed apparatus. A small gap is maintained between the blade and the substrate, through which the solution passes to produce a uniform coating. Doctor blading is attractive for industrial processes, as it allows for roll-to-roll processing over large areas. Using an appropriately smaller blade size, doctor blading can be scaled down for small-area devices.

Spray-Coating

Spray-coating is mainly utilized for large-area substrates, and entails aerosolization of a solution and its high velocity projection onto a substrate. The movement of the spray across the substrate controls uniformity and thickness. Spray-coating may be performed with QDs, but additional parameters must be considered to avoid production of rough, cracked films [184]. The size of the droplets must be controlled ($\approx$20 μm) to ensure that the solvent evaporates rapidly and uniformly. Controlling solvent evaporation is particularly significant to ensure achievement of uniform films [184]. However, the aerosolization and exposure concerns posed by spray-coating make it a less acceptable method of QD film formation. Thus, spray-coating was not considered for any part of this work.

Inkjet Printing

Inkjet methods may be utilized for formation of CQD solids on both large- and small-area substrates. In inkjet printing, QDs are loaded into a syringe and injected through a needle bevel. The volume of injection is determined by the pressure exerted on the plunger, as well as duration of pressure; this is typically managed by a program. QD solution volatility, viscosity, surface tension, concentration, and other parameters must be carefully controlled to produce high-quality prints [19]. Nozzle blockage is a significant concern. Furthermore, as the solvent evaporates, QDs tend to accumulate at the edges of the film, following the path of evaporation; producing "coffee-fringe" effects [11][185]. This is undesirable due to production of non-uniformities, and largely avoided by solvent selection and manipulation [11][185]. For example, tailoring the solvent to create gradient surface tension and high contact angle droplets resolve issues in QD accumulation at droplet edges when drying. Overall, the use of inkjet techniques fully realize the use of CQDs as "inks". Similar to drop-casting, the inkjet method utilizes only the required volume of CQDs, resulting in minimal waste [11]. However, a more complex equipment setup is required for true inkjet printing; the sophistication of this method precludes its use in most R&D environments.

7.3 Analysis of Common QD Deposition Methods

AFM was used to analyze the morphologies of CIS-based QD solids formed with the common drop-casting, spin-casting, and dip-coating methods. ZCIS QDs were synthesized according to the recipe presented in Chapter 6, then diluted to 25 mg/mL in hexane, and deposited onto RCA-cleaned 2.2 × 2.2 cm^2 glass substrates via spin-casting, drop-casting, and dip-coating. Further dilutions were performed as required for each film formation method. Fig. 7.1 presents AFM images of the ZCIS QDs deposited using the various methods. Fig. 7.1(a) shows an AFM image of spin-cast ZCIS QD film; the irregularity of the film is clearly visible, corresponding to its high RMS roughness. Fig. 7.1(b) shows a portion of an AFM image of drop-cast ZCIS QD film. The resultant film is extremely uneven and defective, even to the unaided eye. Although the scan was performed in a locally smooth area, the noise from the roughness of the film precluded completion of the scan; only a portion of the scan is shown. Surface profilometry (Veeco DekTak 150) reveals the film surface to have significantly higher height variation than the RMS roughness determined from AFM.

Fig. 7.1(c) presents an AFM image of dip-coated ZCIS QD film, dipped for 5 cycles with an immersion rate of 30 mm/min, submersion time of 60 s, and withdrawal time of 5 mm/min each cycle. Although areas of QD agglomeration are present, analysis reveals it is smoother than the other films. The QD formation shown in the AFM images is more structured than the other deposition methods, providing evidence of self-assembly. Overall, dip-coated films have significantly lower roughness and better film morphology than spin-cast and drop-cast films, although there is some QD agglomeration.

Table 7.1 presents the roughness analysis of films formed using each method. Areas of

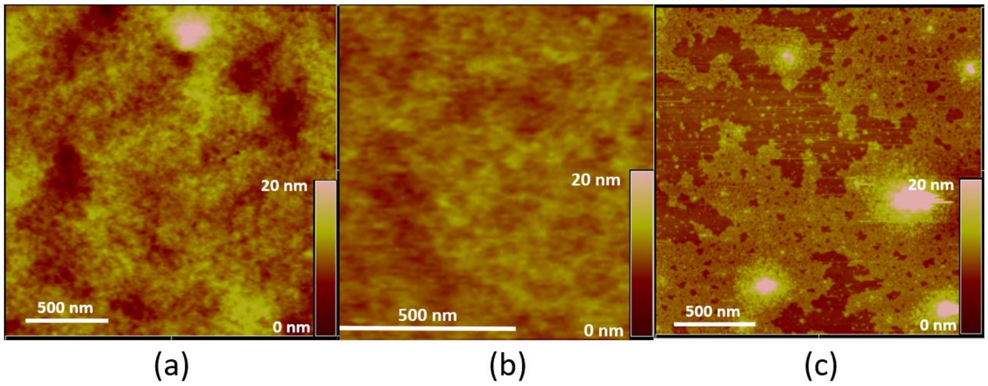

Figure 7.1: AFM image of ZCIS QD film deposited via (a) spin-casting, (b) drop-casting, and (c) dip-coating.

significant roughness, such as agglomerated QDs, were excluded from analysis. The dip-coated films show the lowest roughness. For the drop-cast sample (which shows lower RMS roughness than the spin-cast sample), roughness analysis was made on a locally smooth area; measurements could not be obtained from other areas due to roughness from the film. The data obtained is fairly congruent with the AFM images in Fig. 7.1.

Table 7.1: AFM analysis of drop-cast, spin-cast, and dip-coated QD films.

Film Formation Method	**RMS roughness**
Spin-casting	1.535 nm
Drop-casting	1.057 nm
Dip-coating	0.991 nm

7.4 Dip-coated QD Films

Due to the significantly smoother films obtained using dip-coating, as well as the evidence of self-assembly present in the AFM analysis, dip-coated QD films were further investigated. As dip-coating allows finer mastery over the film morphology than the common drop- and spin-casting methods, control of various dip-coating parameters were studied to create thick, ordered CIS-based QD films conducive to efficient photovoltaic and photodetection operation. This work is presented in the following sections.

7.4.1 Control of Dip-Coating Parameters

Dip-coated samples were formed using the schematic setup presented in Fig. 7.2(a). The dip-coat system (KSV NIMA) consists of a vertically-moving robotic dipping arm connected to a DC motor, and an adjustable stage where the QD-containing vessel is placed. The substrate is affixed to the end of the arm. The linear movement of the arm, including position and speed, are controlled via the KSV NIMA software. The system includes a shield to prevent solvent evaporation and QD spread, and a vibration-cancelling base. To eliminate undesirable ambient effects and contain QD spread, the system is housed in a glove box under nitrogen.

Two categories of forces act on the vertically held substrate during dip-coating: entraining forces which draw the fluid up onto the substrate (hydrostatic and capillary), and draining forces which pull the fluid back into the vessel (gravity). At the stagnation point, the entraining and draining forces are balanced, and the local velocity of fluids is zero. Final film thickness is dictated by the forces exerted on the stagnation point. Fig. 7.2(b) illustrates this concept for dip-coating: here, the stagnation point exists on the vertical surface of the substrate placed into the flow field, in contact with the QD solution. Thicker films are formed with faster withdrawal speeds, as the rate and volume of fluid drawn onto the substrate surface is greater than the rate of fluid flowing back into the vessel [182]. Meanwhile, slower withdrawal speeds provide QDs with the opportunity to traverse to more favourable positions on the substrate surface, affording the possibility of crystalline, monolayer QD film arrangements [182]. The viscosity and density of the QD solution, as well as surface tension, are significant parameters that determine the rate of fluid withdrawal vs return to vessel [182]. The number of dipping cycles, corresponding to number of QD layers, is significant in determining film morphology. In most cases, a single cycle does not produce sufficient substrate coverage. However, each additional cycle risks disturbing and removing previous layers.

The Landau-Levich equation, Eq. 7.2, provides a model for the thickness (or height) of dip-coated films [11]:

$$h = c\frac{(\eta U)^{2/3}}{\gamma^{1/6}(\rho g)^{1/2}} \tag{7.2}$$

Here, η is liquid viscosity (kg/ms), which relates to the QD solution concentration, U is withdrawal speed (m/s), γ is liquid-vapour surface tension (kg/s^2), ρ is solution density (kg/m^3), g is gravitational acceleration (9.8 m/s^2 on Earth), and c is a constant (0.944 for

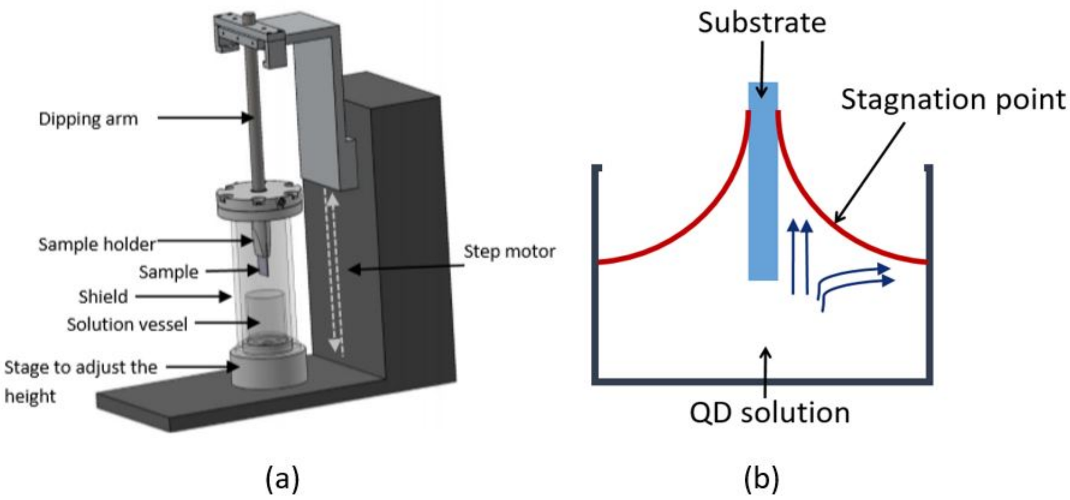

Figure 7.2: (a) Schematic of dip-coater setup. (b) The dip-coating process; film thickness depends on the balance of forces exerted on the substrate.

Newtonian fluids) [11]. Of these properties, QD concentration (leading to viscosity) and withdrawal speed are the most readily controlled during operation.

The dip-coating process can be divided into three major actions: immersion of the substrate into the solution, submersion of the substrate under the solution, and withdrawal of substrate from the solution. The rate of insertion and withdrawal are significant in the first and last step, while length of submersion in the second step contributes to film morphology. Based on Eq. 7.2, withdrawal is the process that impacts film formation most significantly. Therefore, studies were conducted to explore the dip-coating film formation of CIS-based QDs, presented in the following sections. The QD solution concentration was kept constant, so that withdrawal conditions could be primarily investigated.

7.4.2 Dip-Coated ZCIS QDs for Device Applications

In QD film formation with dip-coating, slower rates of withdrawal correspond to higher-quality QD solids, with atoms arranged in energetically favourable positions [182]. To ensure uniformity, a slow rate of 5 mm/min was initially used to study the film formation of MPA-ligated ZCIS QDs onto ZnO [183]. ZCIS QDs were synthesized, and ligand exchange was performed based on the process in Chapter 5. To observe the layer formation over increased cycles, samples were fabricated after 1, 5, and 10 cycles of dipping; AFM images

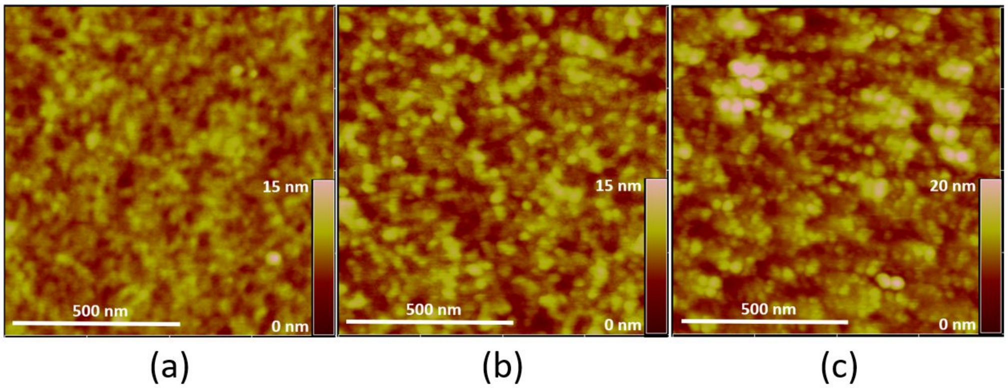

Figure 7.3: AFM images of MPA-ligated ZCIS QD films formed on ZnO thin film, using a withdrawal rate of 5 mm/min, for (a) 1 (b) 5, and (c) 10 cycles.

shown in Fig. 7.3. Although formation of QD layers is evident, a withdrawal rate of 5 mm/min produces somewhat agglomerated QD arrangements.

The RMS roughness analysis of these samples, presented in Table 7.2 show that the overall roughness increases as more QD layers are added (all roughness values were taken as an average of five measurements). This corroborates with the observation of decreased uniformity from the AFM images, and a slower withdrawal rate was investigated.

Table 7.2: AFM analysis of dip-coated ZCIS QD Films on ZnO

Sample	**Dipping Cycles**	**RMS roughness (nm)**
ZnO thin film	N/A	0.869
QDs, withdrawn at 5 mm/min		
	1	1.139
	5	1.458
	10	1.810
QDs, withdrawn at 1 mm/min		
	1	1.662
	5	1.447
	10	1.082

The decreased uniformity is attributed to films being disturbed by subsequent dipping. Fast withdrawal does not provide the QDs with sufficient time to navigate across the substrate surface to favourable positions that are conducive to crystalline monolayer

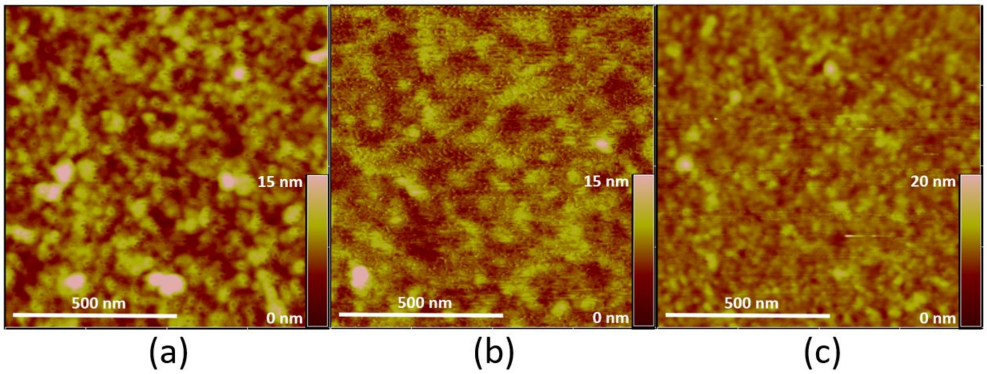

Figure 7.4: AFM images of MPA-ligated ZCIS QD films formed on ZnO thin film, using a withdrawal rate of 1 mm/min, for (a) 1 (b) 5, and (c) 10 cycles.

film formation. Therefore, dip-coated QD film samples were fabricated using a slower withdrawal rate of 1 mm/min; Fig. 7.4 presents the AFM results.

As more layers are coated, the QD arrangement appeared more ordered and uniform. This was corroborated by the decrease in roughness with increased dipping cycles. Therefore, slower withdrawal promotes better film uniformity for ZnO/QD interfaces. PL studies were also performed to investigate the effect of dipping cycles on film integrity. Fig. 7.5 presents the PL emission measurements of all samples.

The PL emission of the samples withdrawn at 1 mm/min increases over progressive dipping cycles, indicating that successive layers are built with each dipping cycle, without disturbing previous layers. In contrast, the PL of the 5 mm/min rate samples diminishes between 5 and 10 layers, indicating progressive film damage. Therefore, ordered formation of QD films onto ZnO requires slow withdrawal rates to promote QD uniformity and prevent film destruction. With the use of slow withdrawal rates, it is possible to form thicker QD layers with increased substrate coverage.

Although 10 cycles were coated without significant perturbation to film loading, the films remained fairly thin, as evidenced by the low PL emission intensity. Simple diodes with dip-coated QD/ZnO heterojunctions were made based on the structure presented in Chapters 5 and 6. However, the resultant devices did not show diodic I-V behaviour, but were instead, ohmic, as shown in Fig. 7.6. Even with up to 60 layers of dip-coated ZCIS QDs, the linear I-V behaviour persisted, indicating the surface to contain QD islands and bare areas of substrate, allowing shorting between the top and bottom contacts. It is evident that continued dip-coating results in removal of subsequent films, although this effect is not observed for fewer layers of QDs. Therefore, although uniform, ordered QD

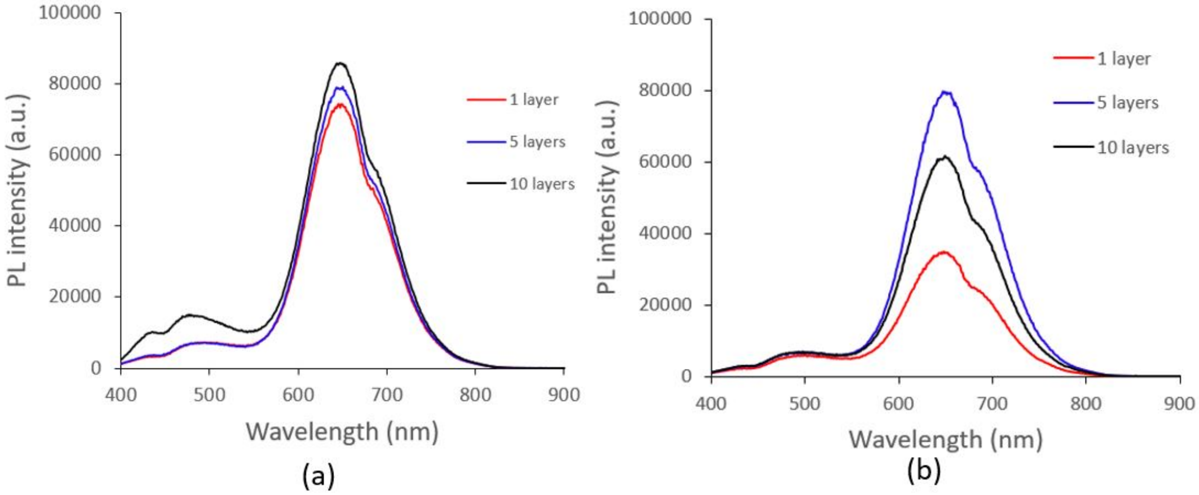

Figure 7.5: PL emission spectra of MPA-ligated ZCIS QDs on ZnO, withdrawn at (a) 1 mm/min and (b) 5 mm/min over progressive dipping cycles.

films are achievable via dip-coating, this method does not provide sufficiently thick QD solids for device applications.

7.5 Annealing Dip-Coated QD Films

As MPA itself is an insulating compound, it is not the most conducive ligand for carrier transport. Annealing and other ligand-removing post-treatments are practiced to limit the amount of insulating MPA (at temperatures as high as 280°C [180]). Ligand removal for QD solids is not as problematic as removal in the liquid state, as the QDs have already affixed onto a substrate, removing any questions of colloidal stability. Furthermore, annealing is frequently practiced for improving QD film uniformity and morphology. In addition to sintering excess ligands, annealing provides energy to QDs to traverse to optimal positions across the surface, maximizing energetic favourability. Therefore, annealing was investigated to determine the effect on CIS QD film morphology.

PL intensity of the MPA-ligated QD films dip-coated at 5 mm/min decreased significantly after 5 layers. Therefore, after 5 coats of QDs were applied, the sample was annealed at 50°C for 30 min. This lower temperature was chosen to prevent damage to the delicate QDs. Fig. 7.7 compares the PL emission spectra of the annealed, dip-coated samples with

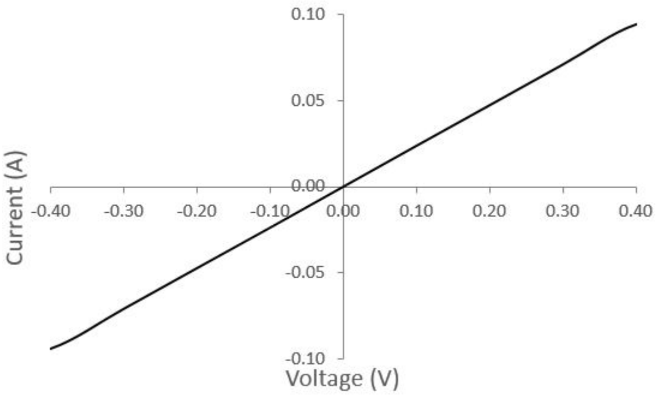

Figure 7.6: I-V curve of device fabricated with 60 layers of dip-coated ZCIS QDs. There is shorting due to insufficient QD coverage.

non-annealed QD film. Previously, the PL emission intensity of the 10-layer sample was shown to be lower than the 5-layer sample, indicating film removal. The PL of the annealed 5-layer sample is one order of magnitude higher than the non-annealed sample, and there is no decreased PL intensity associated with additional cycles of coating, suggesting that the film is not removed. Therefore, annealing aids in stabilizing the film adhesion, preventing removal with subsequent cycles of dip-coating. Even annealing at a low temperature such as 50°C mitigates of film destruction for up to 10 cycles of dipping. This improved QD loading leads to superior absorption and optical characteristics of the QD solid, and should be further investigated for thicker QD films.

7.6 Conclusions

This chapter explores the formation of QD solids for QD-based device applications. Common techniques of drop-casting, spin-casting, and dip-coating were investigated to compare the morphology of the resultant films. As dip-coating was found to produce the most uniform QD films with evidence of self-assembly, parameters of withdrawal rate and cycle number were investigated to produce ordered, multi-layered ZCIS QD films on ZnO. With a controlled withdrawal rate that promote QD adhesion, successive cycles of dip-coating using slow withdrawal rates produced smoother films with higher substrate coverage. However, it was not possible to achieve the thick film thickness required for QD absorbers. Many cycles of dip-coating resulted in some QD removal, leaving areas of bare substrate that caused device shorting. Annealing was found to be effective at mitigating

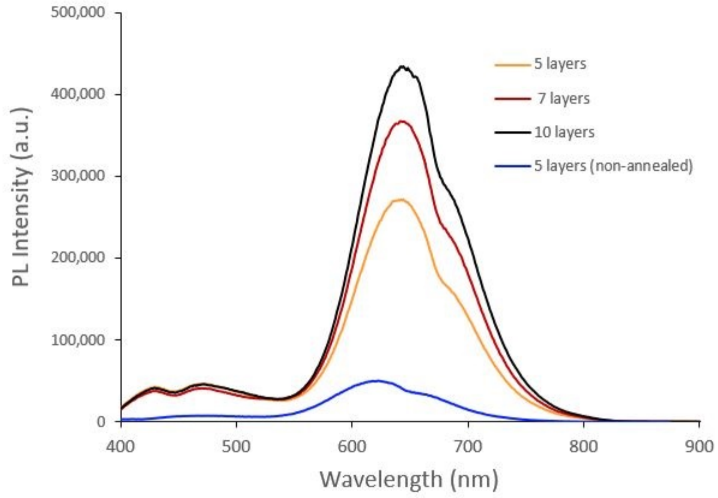

Figure 7.7: PL emission spectra of MPA-ligated ZCIS QDs on ZnO, with and without annealing.

film removal for up to 10 cycles of dipping. Overall, despite its drawbacks, drop-casting continues to be a critical method for CIS-based QD film formation in this thesis, due to its ability to achieve thick QD films. Nevertheless, dip-coating is viable for achieving uniform, periodic, albeit thin QD solids. The knowledge gained in studying QD film formation, presented in this chapter, are significant for subsequent work in QD/metal oxide interfaces and QD-based device development.

Chapter 8

Process Development for CIS QD Photodetector Fabrication

Although metal oxide/QD heterojunction devices have shown good performance, the majority of photovoltaic and photodetector architectures implementing CIS-based QDs utilize a QDSSC configuration. The realization of metal oxide/CIS QD heterojunction structures avoids disadvantages posed by the liquid junctions in QD-sensitized devices. This chapter presents the fabrication of a planar photodetector based on a ZnO/CIS QD heterojunction. This device was used to study the behaviour and illumination response of ZnO/CIS-based QD heterojunctions, especially the dynamics of carrier separation and transport. The device was fabricated using simple microfabrication and solution-casting techniques amenable to VLSI. The individual materials and interfaces comprising the device were studied to better understand its operation. Electrical characterization methods were used to study the behaviour of carriers at interfaces and throughout the device bulk. The results obtained from this simple, preliminary device are significant in understanding the constitution of a metal oxide/QD heterojunction device, allowing the successful pursuit of more complex architectures.

8.1 Zinc Oxide Thin Films

In heterojunction devices, the incorporation of materials and structures that promote charge separation improves device operation [33][44]. As explored in previous chapters, metal oxide/QD junctions are a significant component of many QD-based devices

[163][164]; the quality of these metal oxide films are essential to device performance. In previous chapters, simple device structures of CIS-based QDs were fabricated with ZnO/CIS QD heterojunctions; ZnO was selected due to the compatible band alignment between ZnO and CIS or ZCIS structures [169][170][186]. ZnO's wide bandgap (3.2 eV [187]) and low CB and VB positioning make it ideal for electron transport. ZnO's CB is located at -4.19 eV relative to vacuum level [187]; this is below CIS's CB of -4.06 eV [187], thus facilitating electron transport from CIS donor states (located slightly below CIS CB) to ZnO. ZnO's VB is located at -7.39 eV relative to vacuum level [187], while the bulk CIS VB is at -5.56 eV [187], preventing the unwanted transport of holes from CIS acceptor states (located slightly above CIS VB) to ZnO. Therefore, a ZnO/CIS QD heterojunction is conducive to the operation of the device intended in this work. This section presents the development of planar ZnO films.

Procedure for Sol-Gel ZnO Film

A ZnO solution is created by combining 0.194 g zinc acetate dehydrate ($\geq$98%), 54 μL ethanolamine ($\geq$99.5%), and 6 mL ethanol (90%), purchased from Sigma Aldrich, in a vial and stirring at 45°C for 2 hours [28]. The clear, viscous solution is subsequently spin-cast onto the substrate at 800 rpm for 60 s. The ZnO films are then annealed at 180°C for 30-60 min to stabilize the film and optimize ZnO molecules' surface positioning [28]. Surface profilometry measurements established the films to be approximately 40 nm in thickness on glass and ITO-coated glass. The thickness is varied by controlling the speed of rotation: faster rotation results in thinner films. The same rotation speed may produce different thickness on different substrates.

Procedure for Sputtered ZnO Film

ZnO films are sputtered using an RF magnetron sputtering system (Intlvac - Nanochrome I) with a ZnO target (Angstrom Sciences) and shadow mask. Based on a process established in the facility [188], 40 nm of ZnO film is achieved after 8 min of sputtering at room temperature, with an RF power of 150 W, Ar flow rate of 50 sccm, and pressure of 4.8 mTorr. The target is subject to a 5 min pre-sputtering period in the chamber to stabilize plasma conditions, and a substrate rotation of 50 rpm is maintained to promote film uniformity. After the process completes, the films are annealed at 350°C for 20 minutes to improve conductivity.

Both methods are repeatable and amenable to large-scale fabrication. Sol-gel methods of ZnO preparation are popular due to its inexpensiveness and simplicity [131]. However, these ZnO films result in imperfections and dangling bonds that contribute to trapping and recombination [131]. In contrast, sputtered ZnO requires more extensive equipment, but provides better of control, with less ambient interference. Table 8.1 summarizes the thickness, deposition rate, sheet resistance (R_{SH}), and resistivity (ρ) of films formed using the methods and parameters presented above, obtained from an average of several measurements made on several samples. Sheet resistance and resistivity measurements are not included for the ZnO films on ITO, as the measured values more accurately reflect the very high conductivity of the ITO films.

Table 8.1: Properties of ZnO thin film deposited under various conditions

Type	Thickness (nm)	Rate (nm/min)	$\mathrm{R_{SH}}$ (Ω/sq)	ρ (Ω·cm)
Spin-cast on glass	60.2		10.08	6.07×10^{-5}
Spin-cast on ITO	37.68			
Sputtered on glass	37.26	4.66	68.45	2.58×10^{-4}
Sputtered on ITO	42.62	5.33		

The sol-gel ZnO films are easier to fabricate and present higher conductivity (lower resistivity) by one order of magnitude; it was used more prominently in earlier portions of the ZnO/CIS heterojunction development in this work. However, the greater repeatability of the sputtered ZnO films afford some advantage. Thus, both sol-gel and sputtered ZnO were utilized in this work. The thickness of the ZnO is kept to 40 nm to ensure that efficient vertical electron transport is achieved from QDs to ITO, without insulation from overly thick ZnO [28]. Overly thin spin-cast ZnO films do not cover the ITO films completely, leading to leakage, while extremely thick ZnO films show significant roughness due to the surface morphology changing from nanoparticulate to rippled [189]. RMS roughness of ZnO-on-ITO is minimal between 20-40 nm; this is the thickness range in which spin-cast ZnO films are the most optimal in morphological quality [189]. Fig. 8.1 shows AFM images of spin-cast sol-gel and sputtered ZnO films on glass. The spin-cast ZnO film has an RMS roughness of 0.869 nm, while the sputtered ZnO displays a slightly lower RMS roughness of 0.743 nm. The variation in roughness between the two methods of ZnO film deposition can provide some indication of film porosity, which affects the quality of ZnO/QD interfaces.

8.2 Molybdenum Oxide Thin Films

Molybdenum trioxide, MoO_3, is a wide-bandgapped oxide that is commonly employed as a hole extraction material [190][191] due to its proclivity for hole transport, ability to

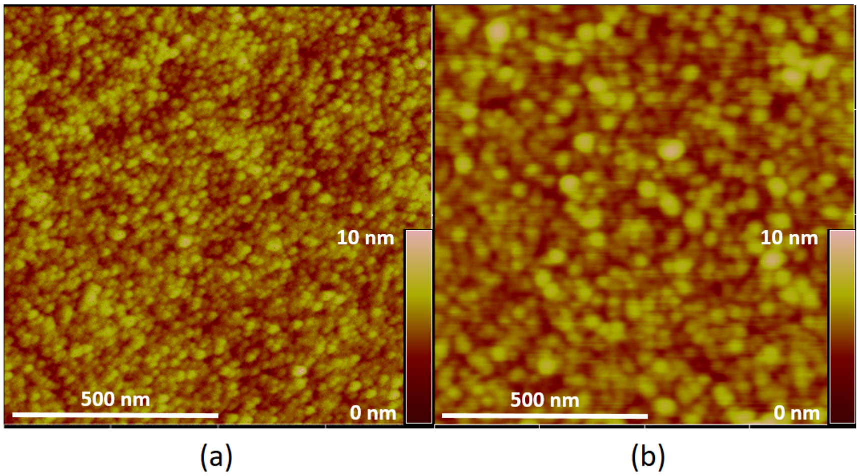

Figure 8.1: AFM microscope images of (a) sol-gel and (b) sputtered ZnO film.

improve device stability [192], and compatibility with straightforward vacuum deposition [192]. MoO_3 shows advantages over the more established poly(3,4-ethylenedioxythiophene) polystyrene sulfonate (PEDOT:PSS) for hole extraction. PEDOT:PSS is susceptible to device degradation and electrical inhomogeneity, and its acidity degrades the underlying ITO, compromising the integrity of the device [192][193]. MoO_3 is utilized as the hole transport layer in the devices presented in this thesis. MoO_3's bandgap is reported in the 3-3.1 eV range[190][194]; its HOMO is located at -5.3 eV [194], placing it slightly above CIS VB of -5.56 eV [187], promoting hole transport from CIS to MoO_3. Meanwhile, electrons are prevented from travelling into MoO_3 due to its higher LUMO of -2.3 eV [194] compared to the CIS CB of -4.06 eV [187].

Molybdenum oxide pellets (99.95%) were purchased from Angstrom Sciences and used as precursors for MoO_3 films. The films in this work are thermally evaporated with a shadow mask and substrate rotation at 100 rpm to maintain uniform deposition. As MoO_3 is an insulating material, its thickness must be limited to avoid impacting conduction and carrier transport. However, deposition of extremely thin MoO_3 layers (below 1 nm) form islands which do not adequately cover the surface of the substrate area [194]. An ideal thickness of 5 nm [28][192][194] is used in this work. As MoO_3 shows extreme ambient sensitivity, and its band properties are significantly affected upon exposure to oxygen and humidity [16], deposition is performed under a base vacuum of approximately 1×10^{-6} mbar. A 5 nm-thick layer of MoO_3 is evaporated onto the device at a rate of 0.3 Å/s; this slow deposition rate is used to avoid unwanted variations in film properties [192].

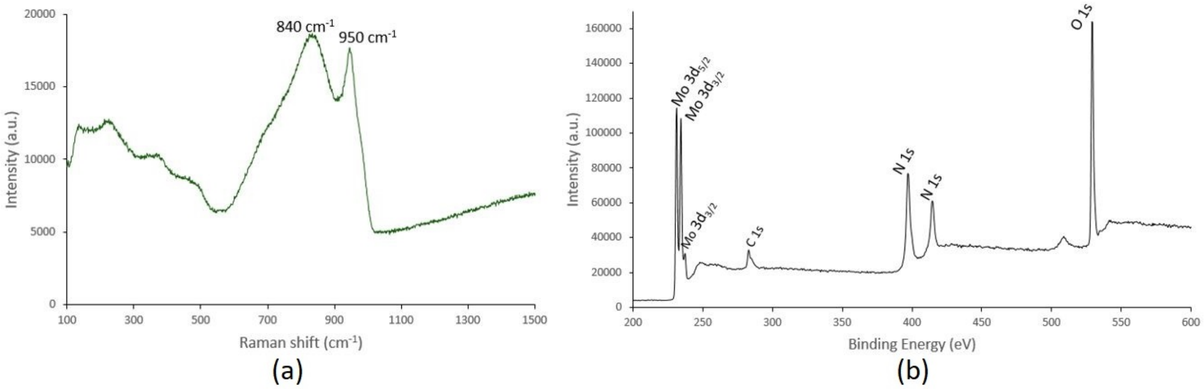

Figure 8.2: (a) Raman and (b) XPS spectra of MoO_3.

8.2.1 MoO_3 Characterization

MoO_3 films were thermally evaporated onto RCA-cleaned glass to study the effect of deposition rate on film quality. Films of 5, 50 nm, and 565 nm thickness were deposited at 0.3 Å/s and 1.5 Å/s to observe the effect of thickness and deposition rate on film performance and uniformity. It was found that, for deposition of MoO_3 on glass, the deposition rate did not particularly affect film morphology. However, slower deposition rates were used in device fabrication to ensure uniformity. The MoO_3 films were characterized using Raman and X-ray photoelectron spectroscopy (XPS), and AFM.

Raman spectroscopy (Renishaw Ramascope Dual-wavelength micro-Raman spectrometer, 623 nm laser excitation source) of the films were measured to observe the structure of the bonds. Fig. 8.2(a) shows the Raman spectrum taken from the measurements of 565 nm-thick MoO_3 film deposited via thermal evaporation at a rate of 1.5 Å/s. In the spectrum, a distinct peak can be identified at approximately 840 cm^{-1}, corresponding to tetrahedrally coordinated surface molybdates [195], while a broad peak is found at approximately 950 cm^{-1}, corresponding to ν(Mo-O) stretching in octahedral surface molybdates [195][196]. These are in agreement with Raman bands associated with MoO_3 [196][197][198]. MoO_3 is susceptible to oxidation, evolving to MoO_2; however, the absence of Raman bands at wavenumbers associated with MoO_2 [197][198] affirms the deposited thin film maintain the desirable MoO_3 structure.

X-ray photoelectron spectroscopy (Thermo-VG Scientific ESCALab 250 Microprobe equipped with a monochromatic Al Kα X-ray source at 148.6 eV) was performed on MoO_3 film (Fig. 8.2(b)) to investigate the chemical composition. Fig. 8.3 displays the Mo and O

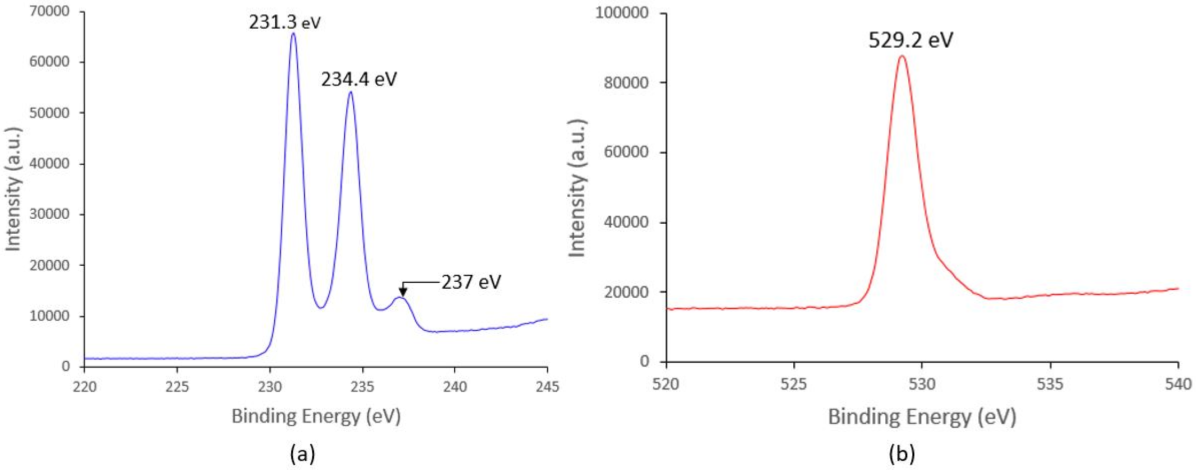

Figure 8.3: XPS spectra of MoO_3, with focus on (a) Mo and (b) O to more clearly show binding energy values.

portions of the graph more clearly. The spectra displays a characteristic Mo $3d_{5/2}$ binding energy at 231.3 eV and Mo $3d_{3/2}$ binding energy at 234.4 eV, with a small shoulder at 237 eV also corresponding to Mo $3d_{3/2}$ state (Fig. 8.3(a)). The spectra also shows an O *1s* binding energy of 529.2 eV (Fig. 8.3(b)). The shape of the spectra is typical for MoO_3 thin films [199], with a recognizable $3d_{5/2}$-$3d_{3/2}$ doublet [196][200]. The distinct resolution of the doublet, as well as the narrow peaks, indicate the absence of different molybdenum(VI) oxo-species and a small range of binding energies; the measured film contained only MoO_3 [200][201]. A peak at 485 eV, corresponding to carbon *1s*, is present in the spectra, attributed exposure of the samples to ambient [199]. The peaks at 400 eV and 415 eV are attributed to N *1s*, again due to ambient exposure of the samples.

AFM topography images of the 5 nm MoO_3 film, evaporated at 0.3 Å/s, were taken to observe the film uniformity, presented in Fig. 8.4(a). The films are extremely uniform and smooth, with little variation in film height. The RMS roughness is approximately 0.27 nm, showing good uniformity. Fig. 8.4(b) presents the height profile of the imaged area. Cursors are placed at two points with the largest height difference; the vertical distance is only 1.169 nm between these points, confirming low height variation in this film.

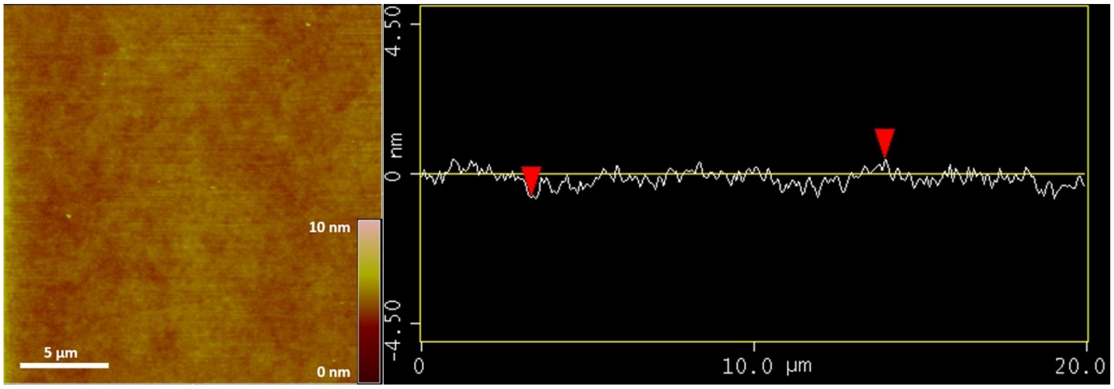

(a) (b)

Figure 8.4: AFM (a) topography image and (b) height profile of 5 nm MoO_3 film thermally evaporated at a rate of 0.3 Å/s.

8.3 QD Absorbers in Heterojunction Devices

In QD-based photodetectors and photovoltaics, QDs are applied as absorbers, capable of absorbing incident photons that have energies larger than their bandgaps [3][21][88][104]. This process generates an electron-hole pair, or an exciton [18], which is separated and removed from the QD layer. The efficiency of device operation depends on efficient charge separation and transport to appropriate electrodes for collection. The absorption onset energy of QDs can be tuned to the photons of interest, as QDs are able to absorb all photons with energies higher than their bandgaps. Like emission, absorption of QDs correspond to their sizes; smaller QDs cannot absorb as wide of a range as larger QDs with smaller bandgaps [179]. Unlike bulk semiconductors, QDs can efficiently utilize the absorption of high-energy photons via MEG. Instead of losing the excess energy via thermalization, excitons can create additional excitons, thus making it theoretically possible for one photon to generate multiple excitons [3]. Due to these advantageous properties, QDs are very efficient at photon absorption and electron-hole generation [20]. Electron-hole pairs are loosely bound in bulk materials, as they possess high dielectric constants that correspond to a small Coulomb binding energy. However, nanomaterials such as QDs have strong quantum and dielectric confinement that lead to strongly bound electron-hole pairs. The rules of allowed optical transition are strict in QDs, and electrons are only allowed to promote or relax to specific, discrete electronic states following absorption or recombination [3]. For this reason, electron-hole pairs in QD solids are typically termed “excitons”, to emphasize the distinction of their behaviour and binding compared to bulk solids.

For direct bandgap semiconductors, recombination is a radiative band-to-band transition. However, as previous established, radiative recombination in CIS-based QDs primarily occurs via DAP processes. Non-radiative pathways, typically arising from surface trap states, compete with radiative recombination. Furthermore, Auger processes, in which the energy of electron-hole recombination is transferred to a third electron to inject it to a remote, high-energy state, may also compete with radiative recombination. Auger processes are efficient in QDs, and may work with traps to interfere with radiative recombination pathways, injecting the "hot" carriers into trap states [3]. Although these "hot" carriers tend to non-radiatively relax to band-edge states, the energy they lose during descent can be utilized to separate other electron-hole pairs [3]. QD solids formed from polydisperse CQDs show random packing and QD aggregation, which results in inhomogeneous energy landscapes, where the electronic states at band edges are broad and varied. These solids also possess localized energy states directly below and above the CB and VB, respectively, which provide an abundance of undesirable thermalization sites for photoexcited carriers [132]. Formation of crystalline, ordered QD solids from QDs with few defects produce films with more advantageous optical properties.

8.3.1 Charge Separation

In heterojunction photodetectors and photovoltaics, electron-hole pairs must be separated at the heterojunctions and collected at their respective electrodes [18]. The metal oxide/QD interface is key to charge carrier separation. QDs, including CIS QDs, are considered to behave more as a p-type material, while the metal oxide (ZnO) behaves in an n-type manner. A depletion region forms at the ZnO/CIS QD interface, while the remainder of the QD solid, far away from the junction, is quasi-neutral [18]. The CBs and DAP states of ZnO and QDs, respectively, are staggered such that the ZnO CB is below the QDs, and the built-in field at the junction removes electrons from the QDs into the ZnO. Meanwhile, the ZnO VB is far below the VB and DAP states of the QD, presenting a high barrier which prevents holes from injection into ZnO. Therefore, the charges are separated. An additional hole transport/electron blocking layer (here, MoO_3) with appropriately aligned band levels may also be added to transport the holes to the opposite contact. The QD size is significant, as it determines the energies the DAP states, which in turn affects the junction formation [11].

The quality of the interfaces strongly determine the effectiveness of carrier separation and transport. If the QDs do not show good adhesion to the n-type material, the quality of the contact is poor, and charge separation is limited. QD aggregates also negatively impact transport, causing the QDs to cluster and transport carriers amongst themselves rather than towards the interfaces [116]. The interfaces may present issues, such as trap sites, which reduce carrier lifetime and promote recombination, decreasing device gain and speed [3][116][126]. The distribution of states at interfaces causes interstitial scattering, resulting in decreased transport. Therefore, ligand functionalization and surface treatments, which remove mobility-hindering traps and improve QD adhesion, are significant in the realization of high-quality interfaces conducive to charge separation [3]. Strategies such as thermal treatment and Zn-alloying, which suppress charge recombination and optimize QD solid configuration [35][36], are also effective in improving device performance.

The mechanism of charge separation in ZnO/CIS QD heterojunctions is as follows:

$$\begin{aligned} &\mathrm{CuInS_2} + h\nu \longrightarrow \mathrm{CuInS_2}(e+h) \\ &\mathrm{CuInS_2}(e+h) \longrightarrow \mathrm{CuInS_2}(e_t+h_t) \\ &\mathrm{CuInS_2}(e_t+h_t) + \mathrm{MoO_3} \longrightarrow \mathrm{CuInS_2}(e_t) + \mathrm{MoO_3}(h) \\ &\mathrm{CuInS_2}(e_t) + \mathrm{ZnO} \longrightarrow \mathrm{CuInS_2} + \mathrm{ZnO(e)} \end{aligned} \tag{8.1}$$

Upon absorbance of photons, excitons are generated in the CIS QD solid. Electrons are promoted to donor DAP states near the CB, while holes remain in the lower energy acceptor DAP states near the VB. Through interdot transport, electrons traverse through the CB DAP states to the ZnO/QD interface, upon which they are extracted from the CIS QD solid into the ZnO's conduction band. Simultaneously, holes traverse toward the QD/MoO_3 interface, and exit the CIS QD solid via the MoO_3 HOMO. Due to the complexity of the multiple hopping, de-trapping, and transport involved in this process, the conduction and valence bands of ZnO and MoO_3 must be correctly aligned to the QD solid's DAP states.

8.4 Planar Heterojunction Device Architecture

Planar photodetectors were fabricated to evaluate the I-V characteristics of the ZnO/CIS QDs/MoO_3 junctions with ITO bottom contacts and Ti/Ag top contacts. The schematic of the device is shown in Fig. 8.5. A Focused Ion Beam (FIB) Scanning Electron Microscope (Zeiss Auriga) was used to obtain a cross-section of the device; HRTEM images of the MoO_3/CIS QDs and CIS QDs/ZnO/ITO interfaces are inset. A Pt layer was deposited for the FIB extraction process, visible in the TEM image of the MoO_3/CIS QDs interface; this is not present in the device during operation.

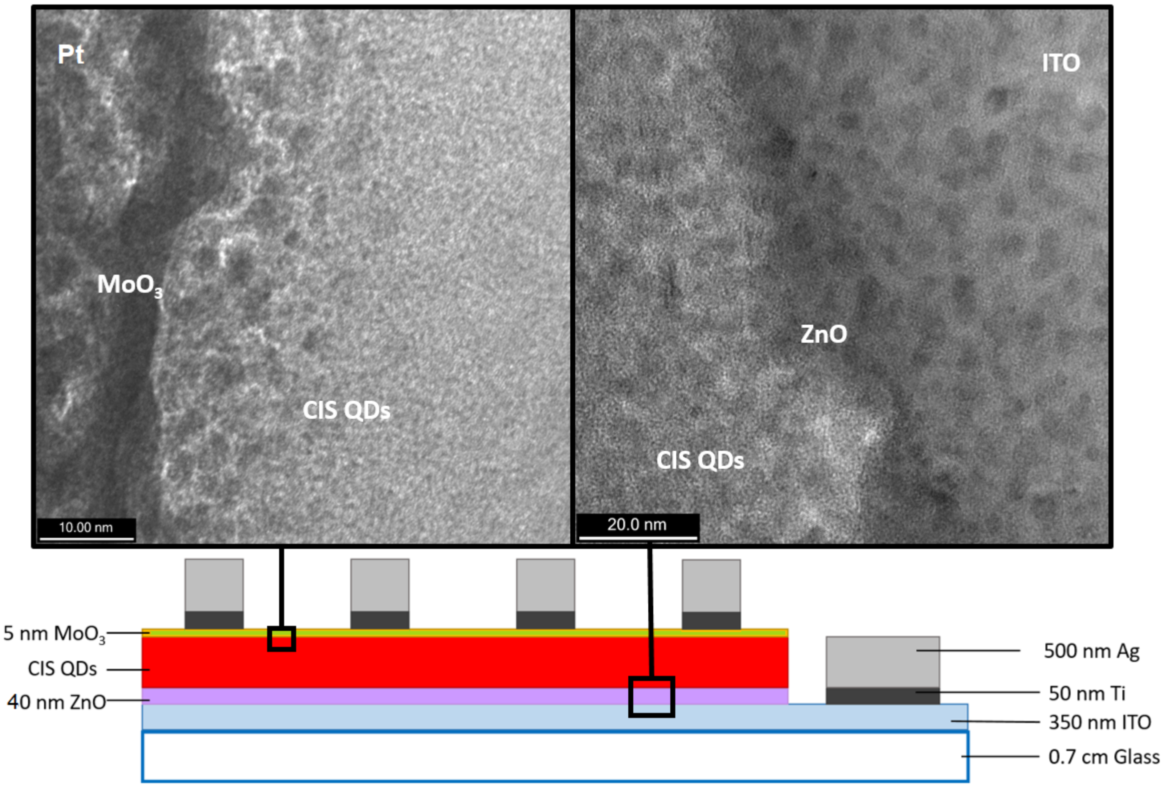

Figure 8.5: Device schematic. Inset: HRTEM images of the MoO$_3$/CIS QDs and CIS QDs/ZnO/ITO interfaces. The layer to the left of MoO$_3$ shows deposited Pt thin film, obtained from the preparation process of the cross-sectional sample.

ITO was selected as an electrode due to its work function [202], transparency [191][202], conductivity [192], transmittance [203], and overall established reliability [191]. ITO's high work function, generally reported to be between 4.4-4.5 eV [202][204][205][206], is advantageous for electron extraction (or hole injection) from ZnO's CB. The ITO-coated glass is cleaned with oxygen plasma, then rinsed with solvent prior to ZnO deposition. Wet and dry surface contamination removal treatments have been shown to increase the work function [204][205][206], advantageous in this application. Sugiyama et al found that surface contamination removal thorough UV-ozone treatment increased the work function to as much as 4.75 eV [204]. In Ding et al's work, oxygen plasma exposure increased the work function to as much as 5.2 eV [206]. Schlaf et al's measurements showed the work function of ITO-coated glass, cleaned by sonication in acetone, IPA, and other solvents, to be 4.78 eV [202], in good agreement with typical values measured in literature [202]. All proposed ITO work function values, including untreated ITO, are lower than ZnO's CB position, allowing for electrons to easily transport from ZnO to ITO.

Notably, there are reports that direct contact between ITO and ZnO can lead to non-uniform resistance and Schottky barrier creation, resulting in unideal device function [203]. Additionally, subjecting ITO to high temperatures (above 100-170°C) has been reported to disrupt its crystalline lattice [203] and decrease conductivity [189]. This indicates that the ZnO thin film annealing processes, for both spin-cast and sputtered ZnO, may somewhat disrupt structural integrity of ITO. However, as no significant defects were observed during device characterization, this issue was not further pursued in this work.

Fig. 8.6 shows the band diagram of the device; as discussed previously, the band alignment is conducive to electron-hole separation and improved conduction. The CIS QDs active layer absorbs photons and generates electron-hole pairs; electrons move towards the ZnO layer, where they are conducted towards ITO, and extracted. However, holes cannot traverse by this pathway, and travel from CIS to MoO_3, where they are subsequently extracted through the Ti/Ag electrodes, which possess appropriate work functions to accept holes from MoO_3 [207]. Electrons are blocked from entering MoO_3 from CIS QDs. Thus, the bandgap alignment promotes removal of photoexcited carriers from the QD layer, and prevents electron-hole recombination. In this work, both Al and Ag were used to metallize the bottom ITO contact and improve electron extraction. The band diagram in Fig. 8.6 only shows Al, but both metals are acceptable, as they display similar work functions compatible with ITO.

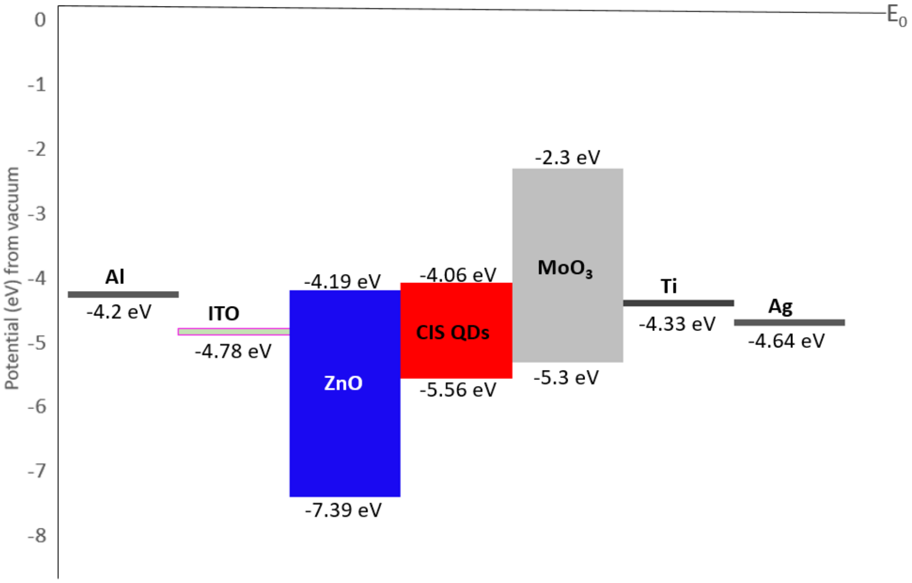

Figure 8.6: Band diagram of photodetector device.

8.4.1 Procedure for Device Fabrication

ITO-coated glass substrates (2.2 × 2.2 cm^2, 5 Ω/□), purchased from LumTec Inc., are cleaned via reactive ion etching with O_2 (30 sccm, 50 mTorr, ICP 200 W, DC 200 W, for 3 min), washed with acetone and isopropyl alcohol in sequence, then dehydrated at 110°C for 5 minutes to prepare the surface. Kapton tape or photoresist is used to isolate a section of the ITO film from subsequent fabrication steps, so that it can be metallized as the bottom contact. 40 nm of ZnO is then spin-cast from solution, as described above.

MPA-ligated core CIS QDs, with emission peaks ranging from 650-750 nm, were synthesized as outlined in previous chapters, or purchased from NN Labs (680 nm emission). To prevent unwanted shorting between the top and bottom contacts of the device, it is critical for the QD film sufficiently cover the device surface [33]. Thus, for simplicity and to achieve maximum thickness, CIS QDs are drop-cast onto the glass/ITO/ZnO stack, using Kapton tape to define the device area. Various concentrations and layer thicknesses are implemented to determine the effect on device performance. Effort is taken to maximize QD uniformity and coverage, but it is not possible to thoroughly detect discontinuities in the QD film over the large substrate area. For devices with multiple QD layers, previous layers are allowed to dry, then subsequent layers are drop-cast, building the absorber thick-

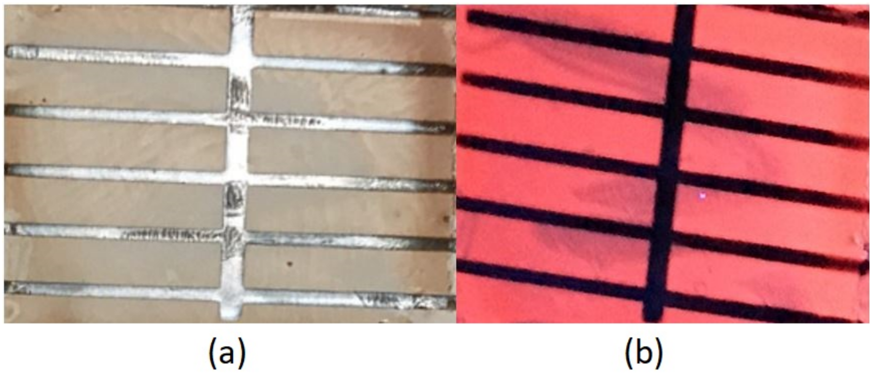
(a) (b)

Figure 8.7: Images of the device in (a) ambient lighting and (b) illuminated under UV.

ness. Some QD films are subject to a 50°C, 15 min annealing step to improve uniformity, further discussed in later sections. Up to this step, all of the fabrication is completed in an N_2-filled glove box or under vacuum, to avoid ambient interference, which is detrimental to arrangement of QD states [113].

After depositing the QD absorber layer, a 5 nm layer of MoO_3 is thermally evaporated onto the partially completed photodetector, as described previously (0.3 Å/s). Finally, top and bottom metallization is performed via electron beam deposition with shadow mask. An initial 50 nm titanium adhesion layer is deposited (at a rate of 3 Å/s) to allow good adhesion between MoO_3 and the Ag electrode. Then, Ag is deposited at a rate of 2-3 Å/s, to a thickness of 500-1000 nm. Some devices possess an Al bottom contact, deposited at a rate of 5 Å/s. MoO_3, Ti, Ag, and Al are deposited using a Sigma Technologies Evaporator system, under a base pressure of 1×10^{-6} Torr, with the substrates rotated at 100 rpm to maintain even deposition. The active area of the device is defined to be 2 cm × 1.525 cm (3.05 cm^2). The vertical structure of this device reduces the travel distance of photoexcited carriers, thus promoting conduction [33]. Fig. 8.7 shows images of the device under ambient and UV illumination. Under ambient light conditions, the device is fairly transparent, with the thick CIS QD layer hardly visible (Fig. 8.7(a)). The quantum dots are highly fluorescent when the device is illuminated under UV light (Fig. 8.7(b)).

8.4.2 Structural Analysis

The structure of the device under test was investigated using transmission electron microscopy. Using FIB, a cross-section of the device was lifted, and observed under TEM (Fig. 8.8(a)); EDS was used to identify the elements. Each individual layer of the device is

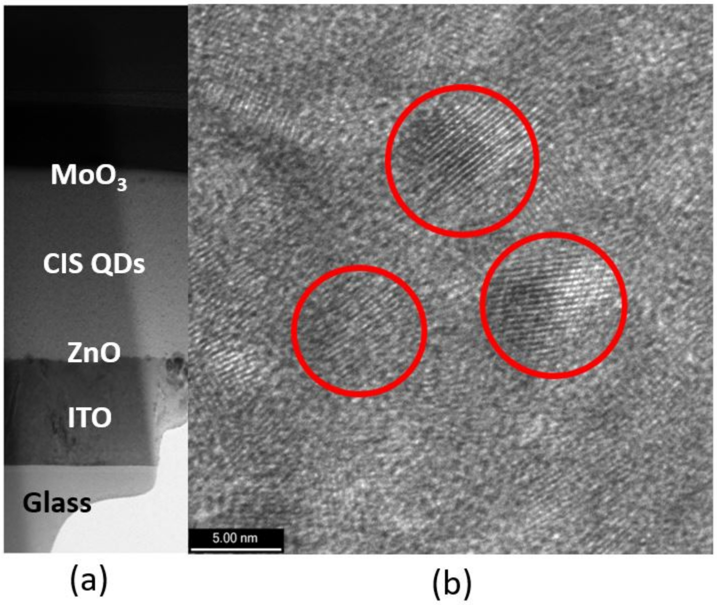

Figure 8.8: (a) TEM of device cross-section. (b) HRTEM of CIS QDs in the device.

visible, and clear interfaces between each layer can be noted. Fig. 8.8(b) shows a HRTEM image of the CIS QDs absorber in the device. The QDs are crystalline and approximately 5 nm in diameter; individual QDs can be distinctly observed in the HRTEM image.

8.5 Preliminary Photodetection Characteristics

To analyze the I-V behaviour of the devices and determine their response to illumination, I-V curves under dark and controlled illuminated conditions were obtained, based on the measurement setup in Chapter 6. For UV illuminated I-V measurements, a Cole Parmer 4-Watt UV lamp with dual 365 nm wavelength tubes was mounted over the device under test, and illuminated at full intensity. A commercial integrated chip (IC)-controlled flash-set, LED lamp (Nova-Strobe BBL) was used as the illumination source in photoconductivity measurements, while an Agilent E3620 A power supply was used to apply a bias to the device. Photoconductivity measurements were made using an Agilent Technologies DSO5012A 5000 series oscilloscope.

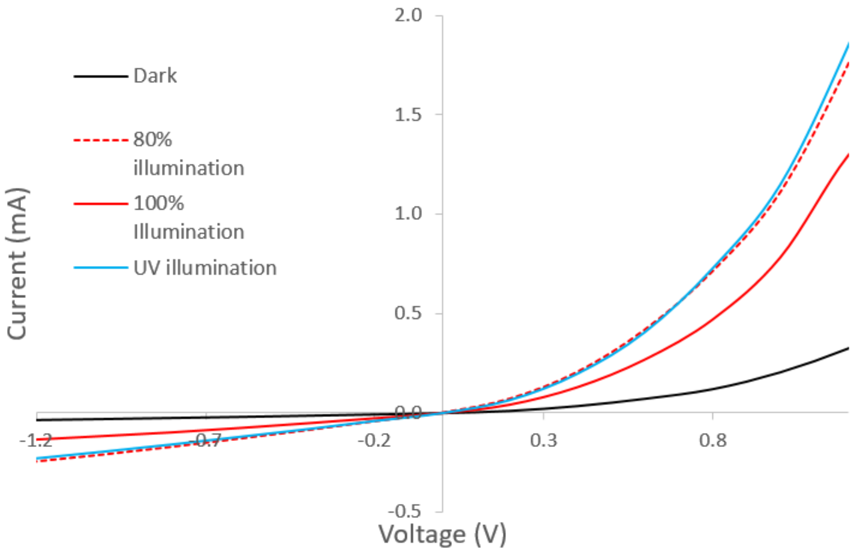

Figure 8.9: I-V measurements of the device under dark, illuminated, and UV-illuminated conditions.

8.5.1 I-V Response to Visible Illumination

Fig. 8.9 shows the result of I-V measurements taken on a planar heterojunction device. Under dark conditions, the device shows a typical diodic I-V curve. Upon illumination at 80% of the maximum capable 1 sun intensity, the device shows a strong response via production of photocurrent; turn-on voltage is located at approximately 0.8 V. A similar photocurrent is produced upon illumination of the device with the UV lamp.

Interestingly, illumination at 100% intensity produces a weaker photocurrent than 80% intensity. Several explanations are proposed for this phenomenon. First, the high illumination intensity results in device degradation, leading to weaker photocurrent. Alternatively, charge traps in the active QD layer may capture carriers more significantly at the stronger light intensity, resulting in reduced responsivity and lack of linear correlation between photointensity and photocurrent [135]. Finally, as photocurrent is attributed to the majority carrier [3][18][174], higher photointensity leads to increased minority carrier generation, which increases recombination and degrades majority carrier lifetime; this is discussed further in the next chapter. This I-V behaviour was not seen in all devices, due to difficulty achieving reliable fabrication and control over QD deposition in this large-area device. A more repeatable device architecture, with clearly defined QD active areas, is required to achieve more predictable device response.

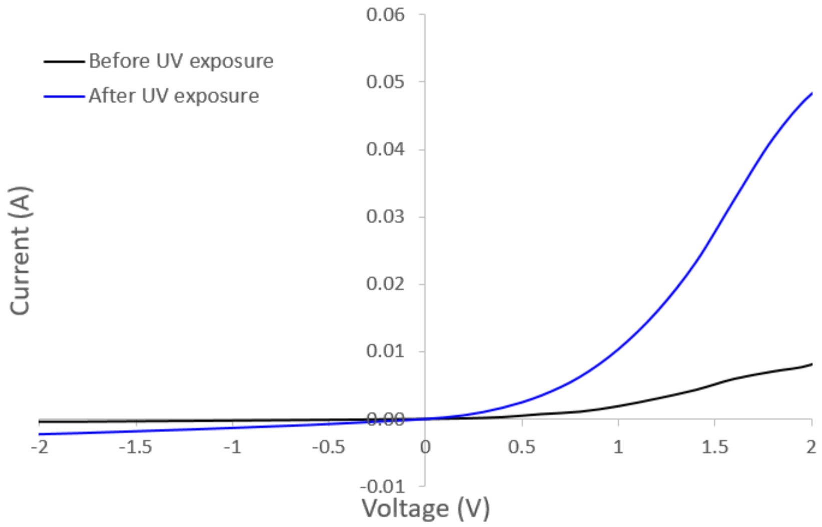

Figure 8.10: Dark I-V measurements taken before and after extended UV exposure.

8.5.2 I-V Response to UV Exposure

It was observed that the dark I-V curves of subsequent measurements changed after illuminating the device with the UV lamp, with higher dark current obtained than previous measurements. To observe the impact of UV exposure on the device under test, the device was subject to extended UV illumination. The UV lamp was mounted over the device, and the chamber was sealed to avoid ambient light. The UV lamp was switched on, and the device was illuminated under the UV lamp for 10 minutes. Then, the UV lamp was removed, and dark I-V measurements were performed. Fig. 8.10 presents the results of dark I-V measurements taken prior to and following extended UV illumination.

Despite the absence of any illumination during the measurement, the current of the device is significantly higher after extended UV exposure. Several explanations can be proposed for this change in the device's response. It has been reported that exposure to UV can reduce the work function of ITO [202], which results in easier electron transport from the active quantum dot layer to the ITO contact, after passing the ZnO/QD junction. The UV exposure's impact on ITO work function effectively modifies the device band alignment, resulting in improved conduction. Alternatively, the UV exposure may provide an annealing effect to the quantum dot film, which improves film quality, ligand structure, and interdot spacing. This subsequently leads to overall improved conduction in the device. However, this is contradictory to findings in previous studies, in which extended UV exposure degraded CdSe QDs [66][208]. Conversely, the improved stability of the CIS QDs compared to heavy metal-containing CdSe QDs, and the shorter duration of UV exposure (10 min compared to 1 hour), perhaps induces only positive changes without producing lattice disruptions to the CIS QDs. Another probable cause of the prolonged photocurrent is attributed to long-living traps, which capture and release carriers after an extended period of time, allowing prolonged recombination and creating secondary photocurrents that can continue for days [1].

8.5.3 Effect of Annealing on Device

The formation of smooth, uniform QD films is critical to device fabrication. The smoothness of the MoO_3 HTL and Ti/Ag top contacts, and therefore efficiency of hole transport across the CIS QDs/MoO_3 interface, strongly depends on the quality of the CIS QD film they sit on. Although drop-casting is the most economical method of film deposition, it results in undesirable, non-uniform films with a risk of areas without QD coverage. However, methods that promote greater film uniformity and periodicity, such as dip-coating, do not produce the sufficient thickness required in QD absorbers.

In the investigation of CIS QD solids, it was found that annealing QD films at low temperatures improved QD adhesion and loading. When dip-coated CIS QD films were annealed at 50°C for 30 minutes, thicker QD films could be achieved, as subsequent cycles of dip-coating did not disturb and remove previous films. It is known that annealing improves QD solid morphology and loading by providing QDs with sufficient energy to traverse to energetically favourable sites. The improved periodicity results in consistent interdot separations, which is advantageous for carrier transport and photoconduction.

Annealing was performed to improve the uniformity and quality of the drop-cast CIS QD film for devices. Devices were built without QD annealing, and with annealing performed using the same parameters (50°C, 15 min; a shorter annealing duration was used out of consideration for the other films in the device architecture), before and after MoO_3 deposition; all other fabrication steps were identical. Fig. 8.11 presents the I-V curves obtained from these devices, with the I-V curve of the annealed device, presented above, again inserted for comparison. In the absence of proper annealing, the device I-V curves do not display diodic characteristics.

Shorting is observed in both the non-annealed device and the device with annealing is performed after MoO_3 deposition. Without annealing, QDs are not ideally distributed across the substrate surface, leading to discontinuity and island formation. Annealing also adjusts ligand arrangement, producing shorter paths to improve conduction. When

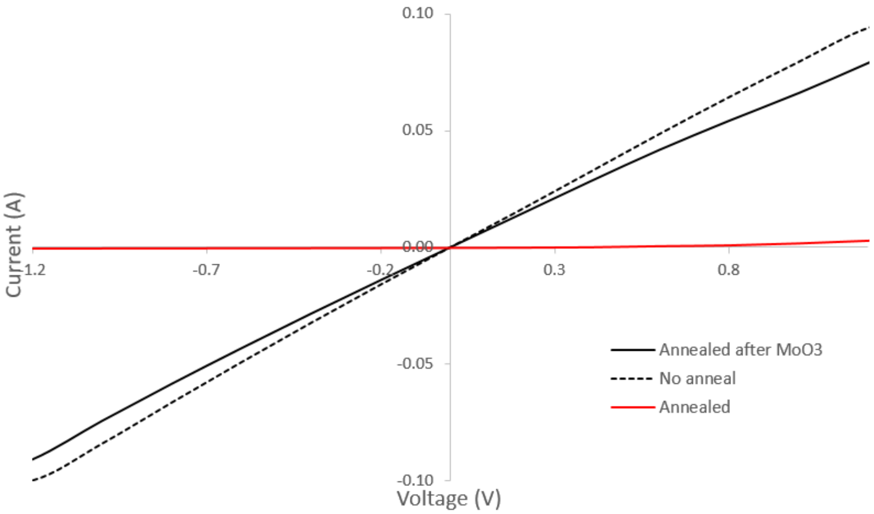

Figure 8.11: I-V measurements of devices with and without QD annealing, and with annealing performed after MoO_3 deposition.

annealing is not performed in a timely manner, such as after MoO_3 deposition, the QDs are also not able to distribute themselves in an energetically favourable manner across the substrate, again forming discontinuities that lead to shorting. The additional complexity of the MoO_3 also impede QD distribution. For optimal QDs coverage of substrates, QDs must be annealed after drop-casting, prior to MoO_3 deposition.

8.5.4 Photoconductivity Response

The transient photoconductivity decay method was used to measure the device's response to illumination. Fig. 8.12(a) shows the schematic of the setup used for measurements. A 10 V bias was applied to the device, which was connected in series to a 5 kΩ resistor, to produce a current of 2 mA. An LED stroboscope was mounted directly and perpendicularly above the device to provide excitation. An amplifier set to 40 dB was used to increase the strength of the signal, monitored using the oscilloscope.

The device was illuminated by the pulsed LED stroboscope. Fig. 8.12(b) shows the photoconductivity of the device. The device shows a strong periodic response to the illumination, with an exponential rise in photoconductivity, followed by steady-state as conductivity reaches maximum, then concluding with an exponential decay following removal of the excitation source. Therefore, the device shows response to pulsed illumination.

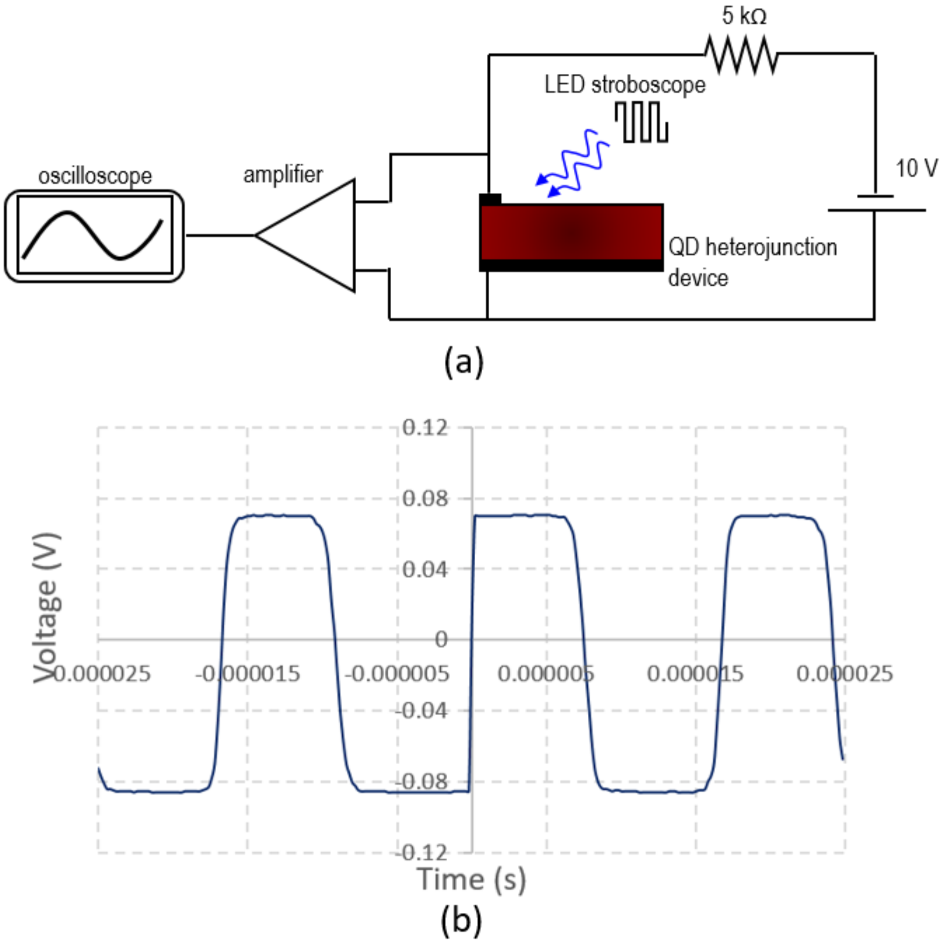

Figure 8.12: (a) Circuit utilized to monitor device photoconductivity response. (b) Amplified photoconductivity response of a device under illumination.

However, as with I-V behaviour, this response was not repeatable across multiple devices, due to difficulty in controlling device fabrication, especially the arrangement of QDs in the large active area.

8.6 Conclusions

A simple planar photodetector was fabricated based on optimized processes for ZnO, CIS QD, and MoO_3 films, forming a ZnO/CIS QD heterojunction with MoO_3 HTL. The structure and behaviour of the photodetector based on this heterojunction was studied. The photodetector showed sensitivity to visible and ultraviolet illumination. Devices with annealed QDs showed better performance, with a visibly more uniform film, and better response to illumination. The preliminary response shown in this work demonstrates the applicability of ZnO/CIS QD heterojunctions for photodetector devices. However, the large area of the device lead to poor fabrication repeatability, especially in control of the QD absorber, necessitating optimization to device architecture. The processes developed and results obtained for the simple planar heterojunction device presented in this chapter are utilized in the realization of more sophisticated ZnO/CIS QD devices in this thesis.

Chapter 9

Fabrication of Micrometer-Scale QD Heterojunction Photodetectors

As novel QD-based photodetector and light management devices continue to be heavily investigated among the research community, it is critical that reliable processes are implemented in device fabrication. The use of novel materials pose many uncertainties and challenges; questions regarding fabrication should be eliminated via the development of reliable, repeatable processes and device architectures. The previous chapter presented the fabrication and characterization of a ZnO/CIS QD heterojunction device that showed strong response to visible and UV illumination. However, the drop-casting method used to implement QDs over the large, centimeter-scale active area (2.0×1.525 cm^2) resulted in non-uniform, imperfect QD films. Due to the lack of repeatability in device fabrication, particularly for QD film formation, more optimized device architectures are required. The crystallinity of a QD solid significantly determines electron transport through the device, and therefore, its performance. Large-area QD devices are problematic, as they show a proclivity for unwanted lateral carrier transport and trapping. Due to lack of control over the fabrication process, the large-area device presented in the previous chapter did not show reliable performance.

Smaller-area QD-based devices, in the scale of micrometers or hundreds of nanometers, are desirable in avoiding issues of large-area QD trapping. However, the use of smaller substrates complicate the fabrication process, as they present challenges for device manipulation and are incompatible with standardized fabrication equipment, which are designed for cm-scale substrates. This chapter presents the development of a process for fabricating small, micron-scale heterojunction QD devices onto standard centimeter-scale substrates.

Patterning was used to define QDs with 19.63 μm^2 active areas onto 2.2 × 2.2 cm^2 substrates compatible with industry fabrication. Each layer of the device, including the QD film layer, was defined through the use of photo and shadow masks. The repeatability afforded by this processes allowed exclusion of device architecture as a factor contributing to device performance. I-V measurements of the photodetector devices showed promising performance, and higher process reliability was achieved.

9.1 Conduction in Photodetectors

Photodetector photocurrent primarily relies on majority carrier mobility. Therefore, it is advantageous to reduce recombination by hindering the transport of minority carrier [3][18][174]. In QDs, the holes are typically considered majority carriers, making them p-type materials. Recombination can be reduced by confining minority carriers within a trap state, such as QD shells (preferably in a Type II configuration that allows selective carrier confinement), or internal defects. Defect states that selectively trap the minority carrier allow the majority carrier to traverse to collection without recombination. Ligand exchange can be leveraged to accomplish the desirable selective trapping, as some ligands produce interface states closer to the QD's CB to capture electrons. Trapped minority carriers are eventually released, which can lead to residual minority carrier mobility after initial photogeneration ceases [94].

ON-OFF ratio, which describes the strength of the photodetector's photocurrent compared to dark current, is a significant figure of merit in evaluating a photodetector's performance and sensitivity. It is desirable for photodetectors to have minimal dark current, strong photocurrent, and defined turn-on at a specific photocarrier density [3]. Dark current is affected by the p-n junction, and can be minimized through tailoring higher barriers to prevent significant injection at low-light conditions. Photocurrent is maximized by increasing majority carrier mobility and effective minority carrier trapping [50].

9.1.1 Photointensity and Photocurrent

The photocurrent at low-light conditions may be larger than at higher intensities. This was observed in the large-area device presented in the previous chapter, and it is attributed to minority carrier traps. The number of traps present in QD solids are finite. At low optical intensities, they are only partially filled, easily trapping any generated minority carriers and minimizing recombination. However, high intensities generate many more electron-hole pairs, causing traps to fill quickly [141]. At a high photointensity, free minority electrons are abundant in the QD solid, posing as recombination obstacles to majority holes, resulting in decreased majority carrier lifetime. Equation 9.1 describes the relationship between photocurrent and light intensity, I_v, in CIS QDs [141][209]:

$$I \propto {I_v}^b \tag{9.1}$$

The parameter b describes the response of photocurrent to light intensity, and takes a value between $0.5 < \mathrm{b} < 1$. The non-linear nature of this relationship arises from the complex interactions between generation, recombination, and trapping of carriers within QD solids [141][209]. At a lower photointensity, the density of trapped minority carriers is greater than free minority carriers, leading to less recombination. However, after traps are filled, minority carriers freely recombine with majority carriers, resulting in reduced current [48][50][174]. Higher temperatures simultaneously contribute to, and detract from photocurrent: although majority carrier mobility increases with temperature, thermal energy also de-traps minority carriers, simultaneously increasing recombination [210].

9.2 Device Architecture

The device architecture is presented in Fig. 9.1. The device composition is similar to the planar device, but the 2.2 × 2.2 cm^2 substrate is divided into ten sections, each holding a single device. The negative, epoxy-based photoresist, SU-8, is implemented as insulator to confine the conductive area to a single 5 μm-diameter well, effectively reducing the effective device area to the micron-scale. The standard size of the substrate allows the use of existing fabrication equipment and facilities. The use of SU-8 in this architecture required adjustments to the process presented in the previous chapter; this is further discussed in subsequent sections. Two configurations are utilized: ZnO under SU-8 (ZnO/SU-8) and SU-8 under ZnO (SU-8/ZnO).

Fig. 9.2 shows the top-view of the device layout, depicting the ten individual devices on the 2.2 × 2.2 cm^2 substrate. The mask is designed using LayoutEditor software. The 5 μm-diameter device well is located underneath the top contacts, and is too small to view in this image. An additional contact is placed onto the SU-8, midway between the top and bottom contacts. This contact is utilized to test the mechanical and electrical stability of the SU-8, verifying its insulation effectiveness. Further details on the dimensions of the substrate and features, as well as individual images of the patterns used in each layer, are found in Appendix A.

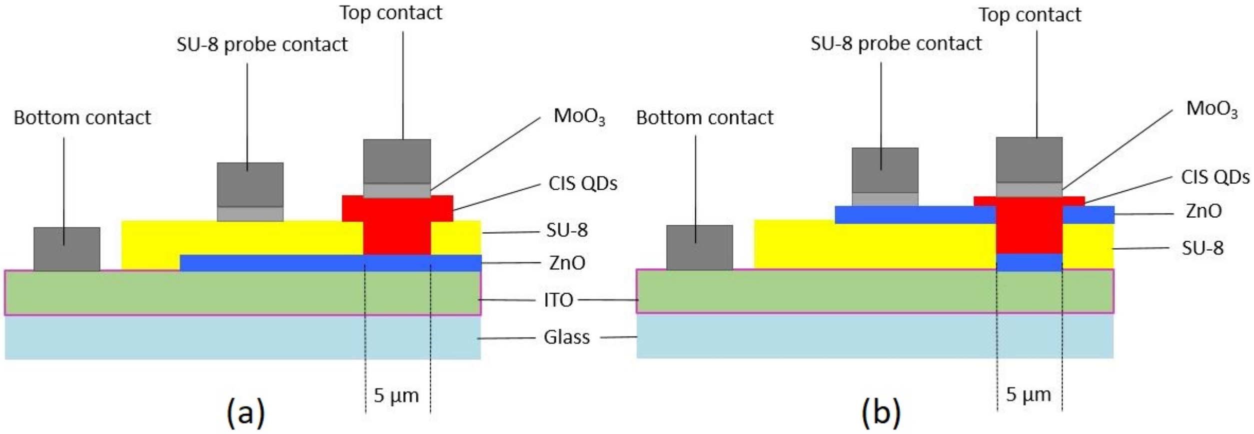

Figure 9.1: Cross-section device diagrams of the small-area device, with (a) ZnO under SU-8 (ZnO/SU-8) and (b) ZnO over SU-8 (SU-8/ZnO) configurations.

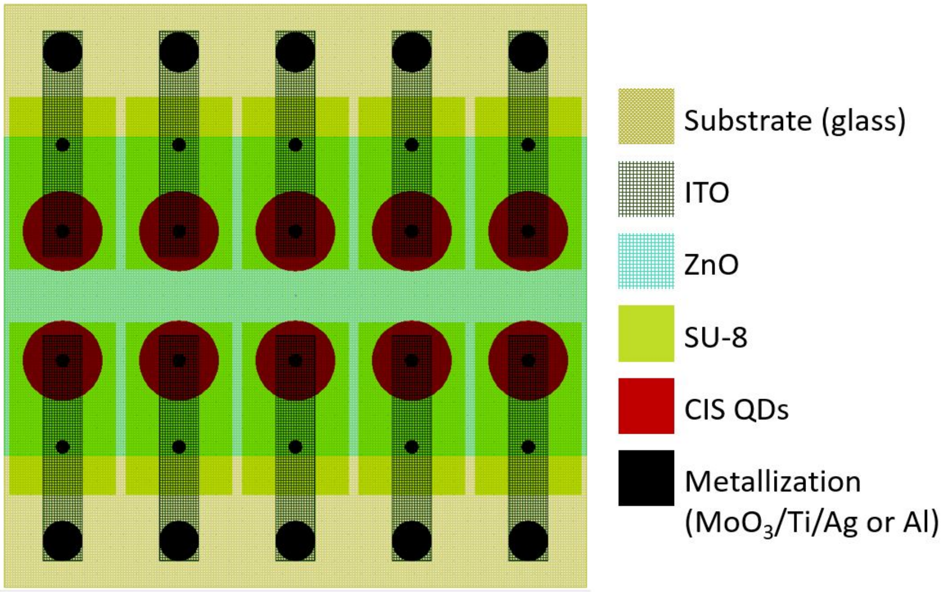

Figure 9.2: Layout of the patterned small-area device.

9.3 Process for Fabrication of Patterned Device

Metallization, and ITO, ZnO, and MoO_3 deposition are completed according to Section 8.4.1. CIS QDs are deposited into the device well using a QD injection system; this is presented in detail in the next section. All layers of the device are the same as the planar device, save for the addition of insulating SU-8.

To pattern the layers of the device, AZ 3312 positive photoresist is spin-cast onto the cleaned substrates at 3000 rpm for 1 min; the AZ 3312-coated substrate is then baked at 90°C for 1 minute, according to manufacturer specifications. The AZ 3312 is exposed using UV lithography, with patterns defined by photomasks or maskless aligner (MLA; Heidelberg Instruments MLA150; 450 mJ/cm^2, defocus -6). The substrates are exposed and patterned according to the mask found in Appendix A, subject to a post-exposure bake (PEB) at 90°C for 1 minute, then developed for 60 s in AZ MIF 300 developer, followed by hard bake at 90°C for 3 minutes. The ITO is etched in $HCl{:}HNO_3{:}H_2O$ (10:1:10 ratio) [211]; 350 nm of ITO is completely removed after approximately 20 minutes. ZnO is etched using 2% HCl; 40 nm of ZnO is completely removed after 30 s of etching. AZ 3312 is removed by rinsing with acetone, IPA, and DI water in sequence.

SU-8 photoresist is prepared by diluting SU-8 2025 with SU-8 thinner to achieve SU-8 2001.5. Meanwhile, the substrate is dehydrated at 110°C for 5 min to enhance SU-8 adhesion. SU-8 2001.5 is spin-cast onto the substrate at 3000 rpm for 1 minute, resulting in a 1.2-1.5 μm-thick layer. The SU-8 is baked at 90°C for 1 minute. The SU-8 is exposed using a mask aligner or MLA, then subject to PEB. The exposure and PEB conditions were tuned based on the conditions of the substrate (ITO or ZnO), and are further discussed in subsequent sections. Following PEB, the SU-8 is developed in SU-8 developer for 1 min, followed by a 10 s rinse with fresh SU-8 developer, and then a 10 s rinse with IPA, according to manufacturer specifications. Finally, the developed SU-8 is subject to a hard bake at 150°C for 10 min.

9.4 QD Injection

In optimizing the thickness of QD absorbers, there is trade-off between absorption and conduction. Thicker QD absorbers correlate to higher QD loading, in which more QDs are present within the active area to absorb more photons, creating more excitons. However, overly thick QD films reduces transport, leading to lower current density. Carriers must complete more hopping events and traverse through a longer path to reach the desired interface, giving rise to higher probability of unwanted trapping. Thicker films are achieved through the deposition of multiple QD layers, which leads to greater formation of imperfections and QD aggregates that negatively impact electron transport [20]. Furthermore, QD film aggregates and impurities can result in the production of light-emitting species, which may capture photons and down-convert their emission [3]. Strategies such as cross-linking or annealing decreases thickness while maintaining equivalent QD loading, by forcing the QD layers to pack more densely. As well, annealing partially removes some insulating ligands to eliminate barriers to carrier transport. This in turn improves QD adhesion onto substrates, leading to better interfaces.

Overall, thicker QD films are desirable in vertical device architectures. Lower energy, long-wavelength photons are absorbed deeper in the device; in devices with thin QD absorbers, long-wavelength photons may be lost to non-absorbing layers of the device. The QD film thickness should be tailored to absorb photons with the longest wavelength of interest, as more energetic photons are easily absorbed near the surface. The QD should have a thickness of α^{-1}, in which $\alpha = \frac{1}{\delta}$, where δ is the absorption depth at which 63% of the longest-wavelength photons are absorbed.

The work presented up to this chapter has predominantly employed drop-casting, which is more compatible with achieving thicker films over larger areas. However, as the rate of solvent evaporation varies over such larger surfaces, and can be volatile, it is difficult to maintain uniformity throughout the QD solid. Ligand and surface functionalization mitigates, but does not entirely prevent formation of clusters, cracks, and bare areas. The ease and low-waste of drop-casting is extremely advantageous, but the lack of control over deposition is detrimental to film formation. The inelegant, large-area QD deposition methods presented in the previous chapters are not amenable to the small-area device architecture. The lack of control and film uniformity in drop-casting may not even deposit QDs within the small 5 μm-diameter device well.

Therefore, a hybrid QD injection mechanism was implemented to combine the ease of drop-casting with the control of inkjet printing. A shadow mask was designed with openings to expose only the areas around the device wells for QD film formation. O-rings were placed around the openings to ensure QD confinement; when the substrate is placed into the mask, the O-rings are pressed tightly against it, preventing QDs seeping across the surface. The QD area is defined by the 3 mm inner diameter of the O-rings, indicated red circles in Fig. 9.2. The actual QD area is smaller, as the O-rings' inner diameter decreases when pressed tightly against the substrate. A fine-tipped syringe is used in conjunction with an Eppendorf injection system to release QD solution into the mask openings under a set pressure and time. The device is kept in the shadow mask until the QDs dry. Unlike many other QD film formation methods, this method ensures that each injection releases an identical volume of QDs into a defined area, making it reliable and repeatable. Although

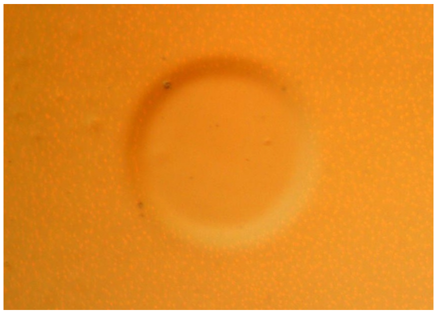

Figure 9.3: High-magnification microscope image of the QDs filling the 5 μm-diameter device hole after injection.

the inner diameter of the O-rings, and therefore the QD film area, is larger than the device well (3 mm vs 5 μm), this process produces significantly fewer variations in QD uniformity and morphology than larger-area methodologies. This QD injection method retains the simplicity and low-waste of drop-casting, while bringing benefits of inkjet printing without the need for expensive, complicated equipment. The design of the injection system is found in Appendix B.

Fig. 9.3 shows a microscope image of QDs injected into the 5 μm-diameter device well. Unlike drop-casting, confinement provided by the O-rings prevents lateral movement during solvent evaporation, ensuring QDs have good contact with the base of the well.

Fig. 9.4(a) shows cross-sectional SEM images of injected QDs in a device well. The apparent roughness is due to the proclivity of QDs to form clusters; although it seems significant at this scale, the QD film is much more uniform than the QD films formed by drop-casting. Fig. 9.4(b) shows an undesirable void formed in the QD absorber within the device well. Such voids and discontinuities, which frequently form during drop-casting, are undesirable because they hinder carrier collection. They can be mitigated through tailoring injection conditions.

Thicker QD layers are achieved through the use of more concentrated CQD solutions or increasing the number of injections. It is preferable to optimize the QD concentration, such that the desired film thickness is achieved with just one injection. More injections create multiple QD interfaces within the film, leading to problematic carrier transport. However, overly concentrated QD solutions hinder performance, as the abundance of ligands decreases transport through the film. In this work, the QD injection is kept constant at a pump pressure of 1 psi with a 0.6 s injection duration. When used with CIS CQDs in ethanol, these parameters produce low-mobility droplets with a high contact angle, leading to good QD film formation. The best QD devices were achieved through one pump of

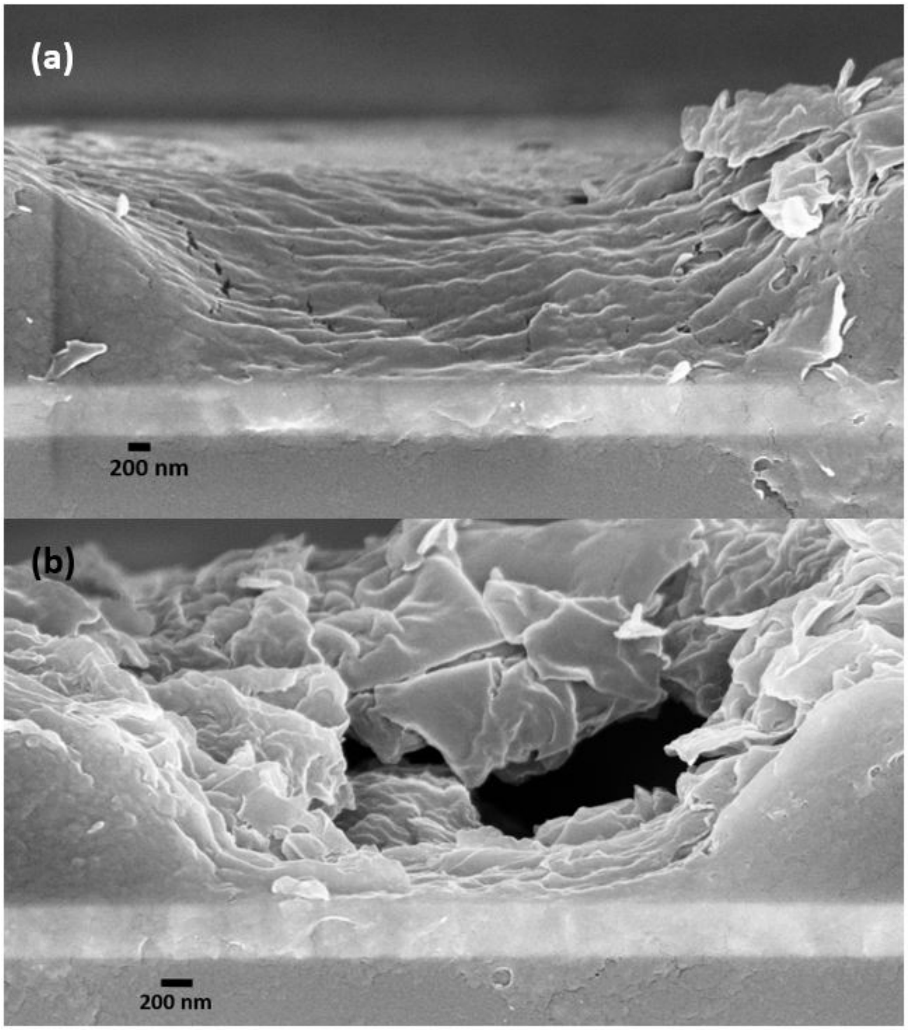

Figure 9.4: SEM cross-section image of (a) QDs in device well using injection system, (b) and formation of QD voids in the well.

less-concentrated CQD solutions; this is discussed further in later sections.

9.5 Development of SU-8 and ZnO

Although the device maintains the heterojunction architecture of the planar device in Chapter 8, the incorporation of SU-8 and adjustment of the active device area required modification of the ZnO formation. The following sections present the development of SU-8 and adjustment of ZnO to accommodate SU-8 incorporation in the small-area device.

9.5.1 Development of SU-8 Layer

As SU-8 was purchased commercially, the manufacturer's guide was primarily referenced for its implementation. Maskless photolithography was used to expose this negative photoresist, and dose/defocus tests were performed to determine the best exposure conditions to use for the desired substrate. The MLA system uses a 375 nm laser and digital micromirror device (DMD) to scan the design onto the substrate, thus rendering a physical photomask unnecessary. In the MLA, the dose parameter indicates the intensity of exposure (given in mJ/cm^2), while defocus describes the depth at which the laser is focused (on a scale from -10 to 10, in increments of 2). Dose/defocus tests entail arraying the substrate with a pattern containing features on the scale of the smallest feature on the device (in this case, the 5 μm-diameter device well). Each position in the array is exposed under different dose and defocus conditions, to determine the best combination to use for the photoresist and substrate. The dose/defocus conditions given for AZ 3312 on ITO and ZnO, earlier in this chapter, were determined using dose/defocus tests.

As SU-8 is a permanent component of the device, its exposure conditions are much more significant than AZ 3312, which is removed after etching. Fig. 9.5 shows images of SU-8 on ITO, exposed under four different dose/defocus conditions. The pattern for the dose test is provided by Quantum-Nano Fabrication and Characterization Facilities at the University of Waterloo. In Fig. 9.5(a), the correct exposure conditions of 800 mJ/cm^2 and -4 for dose and defocus, respectively, are used. The 2.5 and 3-wide μm trenches are crisp, without the presence of residual photoresist.

Fig. 9.5(b) shows a sample exposed with the correct dose (800 mJ/cm^2), but an incorrect, shallow defocus (0). The features are not as clear compared to development using the correct conditions. Fig. 9.5(c) and (d) show samples that are exposed using doses that are too low (750 mJ/cm^2) and too high (1000 mJ/cm^2), respectively. In the underexposed

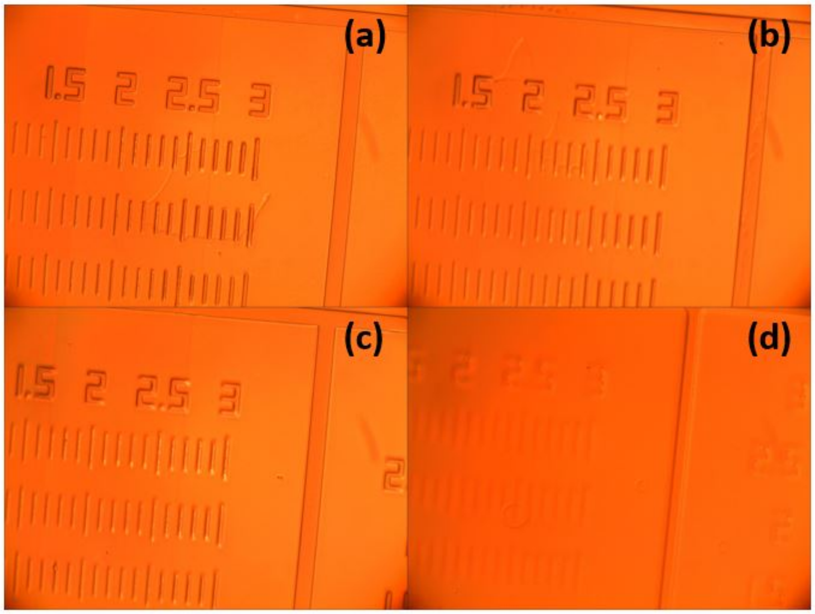

Figure 9.5: Microscope images of dose test for SU-8 exposed with (a) the correct exposure conditions (800 mJ/cm^2/-4), (b) incorrect defocus (800 mJ/cm^2/0), and at doses that are (c) too low (750 mJ/cm^2/0) and (d) too high (1000 mJ/cm^2/0).

sample, the photoresist is underdeveloped, leading to blurry features. The features are hardly present in the overexposed sample. The 1.5 and 2-wide μm are not well-defined for any of the exposure conditions, including the correct exposure in Fig. 9.5(a). This indicates that SU-8 is not capable of achieving such fine features on ITO; such limitations must be considered in device design. This limit is not a concern in this device, where the smallest feature is 5 μm.

As shown in Fig. 9.1, two architectures were implemented, with the SU-8 deposited on ITO (SU-8/ZnO) and on ZnO (ZnO/SU-8). Two types of ZnO: sol-gel and drop-cast, were utilized. Therefore, the dose/defocus test was performed for three substrates. Table 9.1 shows the dose and defocus determined for substrate, as well as PEB conditions.

Fig. 9.6 demonstrates the importance of performing dose/defocus tests for each combination of photoresist and substrate. The sample in the image depicts SU-8 on sol-gel ZnO, exposed using the dose/defocus conditions perfected for ITO (800 mJ/cm^2/-4). Although these values are appropriate for ITO, the SU-8 is underexposed on the ZnO, and appears to peel instead of adhering to the substrate. The SU-8 forms undesirable undercut trenches, which may result in problematic lift-off of subsequent layers (QDs and top contacts).

Table 9.1: Exposure and PEB conditions of SU-8 on various substrates

Substrate	Dose (mJ/cm^2)	Defocus	PEB Temperature (°C)	PEB time (min)
ITO	800	-4	100	3
Sol-gel ZnO	1300	8	100	22.5
Sputtered ZnO	1100	0	100	22.5

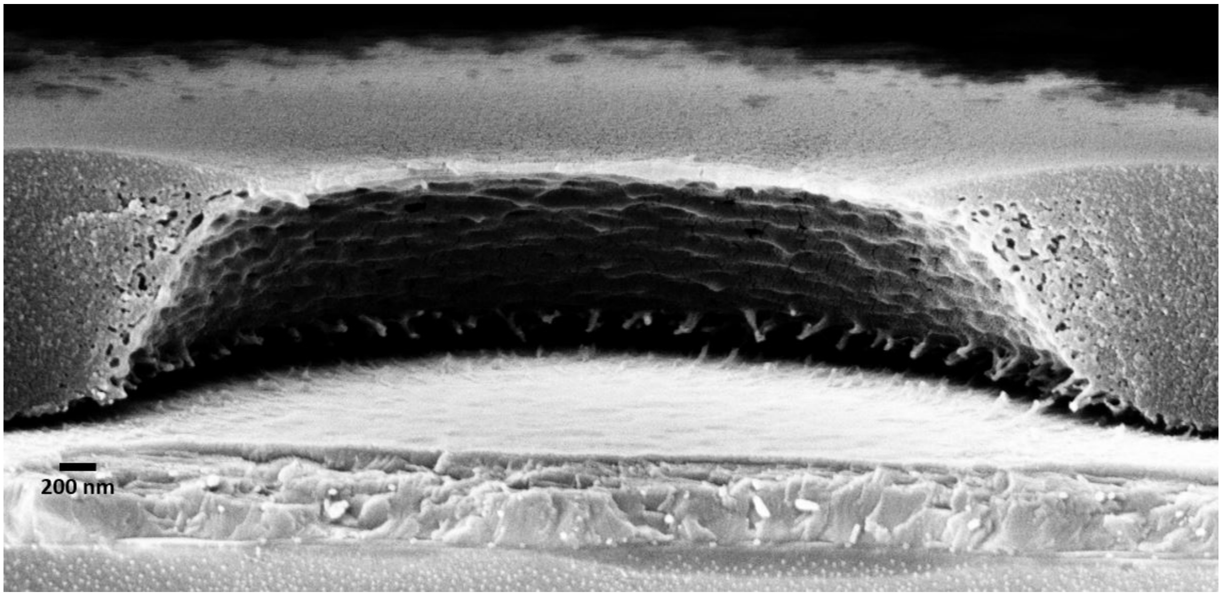

Figure 9.6: SEM cross-section of insufficiently exposed SU-8 on ZnO.

Compared to ITO, significantly higher exposure intensity is required for SU-8 on ZnO. However, higher exposure intensities are problematic, weakening the integrity of the SU-8 structure and posing challenge to its role as insulator. Fig. 9.7 shows the I-V curves of the SU-8. In Fig. 9.7(a), the SU-8 exposed at the intensity required for ZnO (1100 mJ/cm^2) breaks down when subject to a fairly low voltage of 5 V. Fig. 9.7(b) shows the expected breakdown behaviour at 5 V. SU-8 breakdown leads to shorting in regions outside of the active device area, depreciating device performance. It should be noted that breakdown does not occur at the operation range of the device (-1 to 1 V), but breakdown at such low voltages affirms the reduced stability of the SU-8 subject to higher-intensity exposure.

It is crucial that the substrate is well-cleaned prior to SU-8 film implementation, as the SU-8 is highly sensitive to impurities and moisture. Fig. 9.8 show microscope images of SU-8 issues that arise on poorly cleaned substrates. Bubbles and peeling (Fig. 9.8(a))

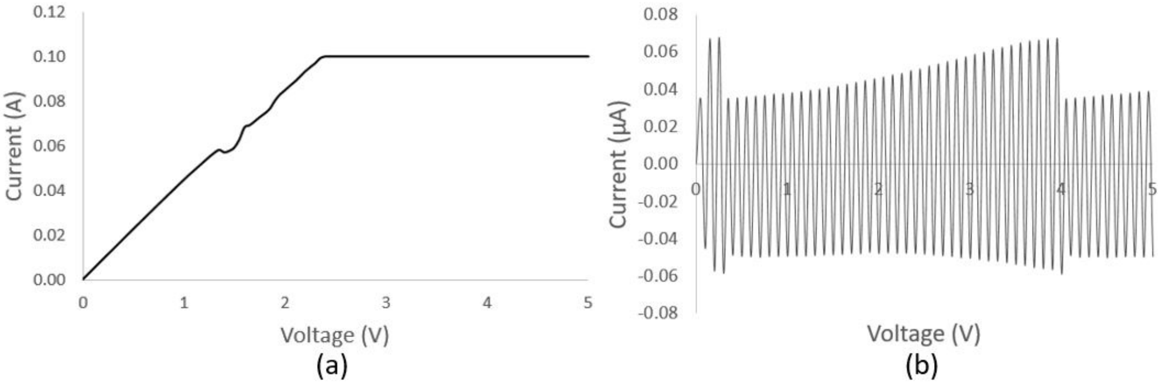

Figure 9.7: I-V curves of SU-8. (a) Overexposed SU-8 breaks down at low voltages. (b) Structurally sound SU-8 does not suffer breakdown at the same voltages.

correlate to unstable SU-8, which lead to device performance issues. Fig. 9.8(c) depicts SU-8 patterned onto a clean substrate; the vertical grooves across the sample is an artifact of the DMD's operation, and does not affect the SU-8's structural integrity.

To study the ITO/SU-8/ZnO interfaces inside of the 5 μm-diameter device well, the design shown in Fig. 9.9 was created to more easily observe the device cross-section under SEM. Briefly, the device well in the actual device layout presented in Fig. 9.2 is too small to efficiently cleave, compounded by the amorphous nature of the glass substrate. Therefore, 5 μm-diameter circles representing the device well were patterned over the entire substrate. The wells are displaced 12.5 μm vertically and 15 μm horizontally, with individual wells in each row offset 2.5 μm vertically. This pattern ensures that, when cleaved from the x-direction, there is a high probability that the cross-section of several wells will be obtained, regardless of glass amorphousness. The array presented in Fig. 9.2(a) measures 260 × 117 μm^2, and is repeated across the surface of the 2.2 × 2.2 cm^2 substrate many times. Fig. 9.2(b) shows an angled SEM image of a sample patterned with this design. Several cleaved wells can be seen at the edge, making them appropriate for evaluation of the ZnO/ITO interface. One substrate can be cleaved several times to obtain multiple wells for evaluation. This method was employed to evaluate the device interfaces in the subsequent sections. Note that, as cleaving does not exactly divide the wells across the center, the well widths in the analyzed samples are not necessarily 5 μm.

(a) (b) (c)

Figure 9.8: Microscope images of imperfections in SU-8 spun onto unclean substrates, including (a) bubbles and (b) poor adhesion, compared to (c) clean substrates.

9.5.2 Adjustment of Spin-cast ZnO to Accommodate SU-8

As organic materials such as photoresist are not allowed to enter the high-purity sputtering equipment, sol-gel ZnO must be used for devices with the SU-8/ZnO configuration. Initially, ZnO was spin-cast at 800 rpm onto the SU-8, based on the recipe for 40 nm sol-gel ZnO presented in the previous chapter. However, inside the confines of the device well, this speed produced thick ZnO films of almost 100 nm, as shown in Fig. 9.10(a). As a result, the ZnO showed insulating characteristics, which hindered device performance. Higher speeds were investigated in effort to produce thinner ZnO films within the device well. The ZnO solution and films were prepared (stirred 45°C, 2 hours) and annealed (180°C for 30-60 min) using the same parameters. Fig. 9.10(b) shows the cross-section for ZnO spun at 2000 rpm. Although the profile of the ZnO film inside of the well is no longer flat, the film covering the largest area in the middle of the well is at the acceptable 40 nm thickness (the sides are approximately 100 nm). Therefore, 2000 rpm was used for devices using sol-gel ZnO, in the SU-8/ZnO configuration. Spin speeds beyond 2000 rpm formed bumpy, uniform ZnO films, and were not considered.

Sol-gel ZnO can also be implemented for the ZnO/SU-8 configuration. As this ZnO is deposited as a blanket layer onto ITO, the original 800 rpm speed can be used. However, the highest SU-8 exposure intensity of 1300 mJ/cm^2 is required for sol-gel ZnO, which weakens the mechanical integrity of the SU-8, resulting in breakdown. Successful devices were not achieved from architectures employing spin-cast ZnO under SU-8.

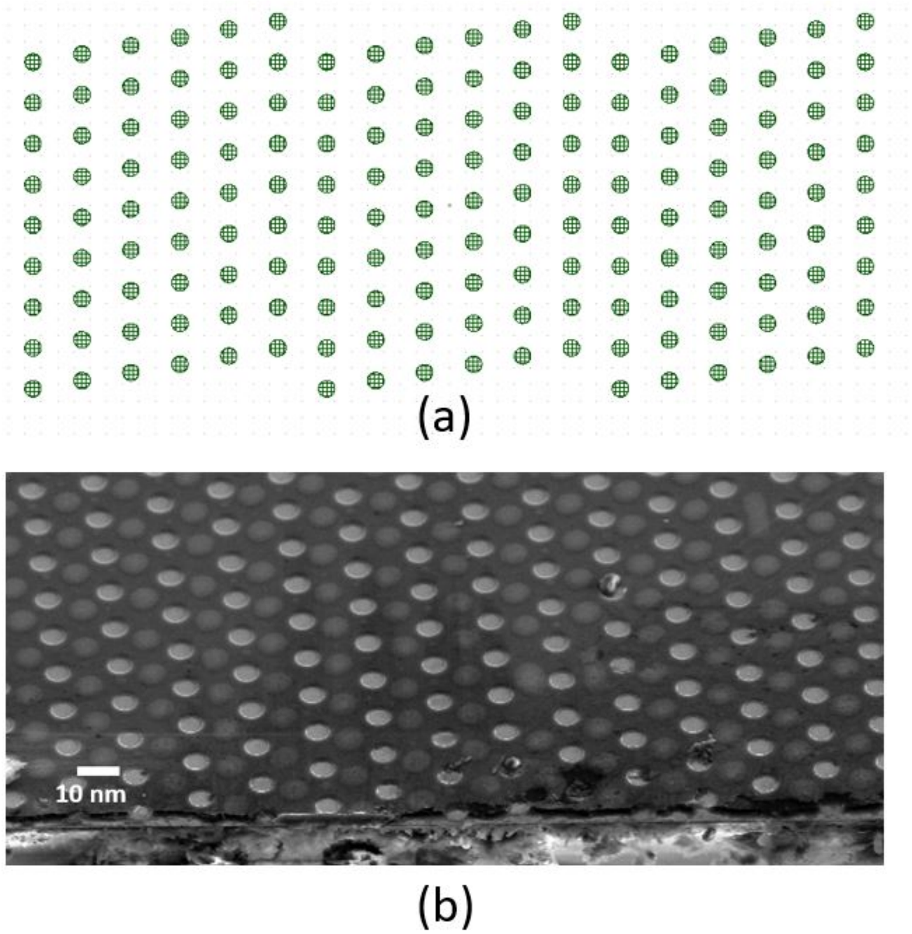

Figure 9.9: (a) Design of SEM test pattern and (b) angled SEM image of ZnO on SU-8, patterned with the test pattern.

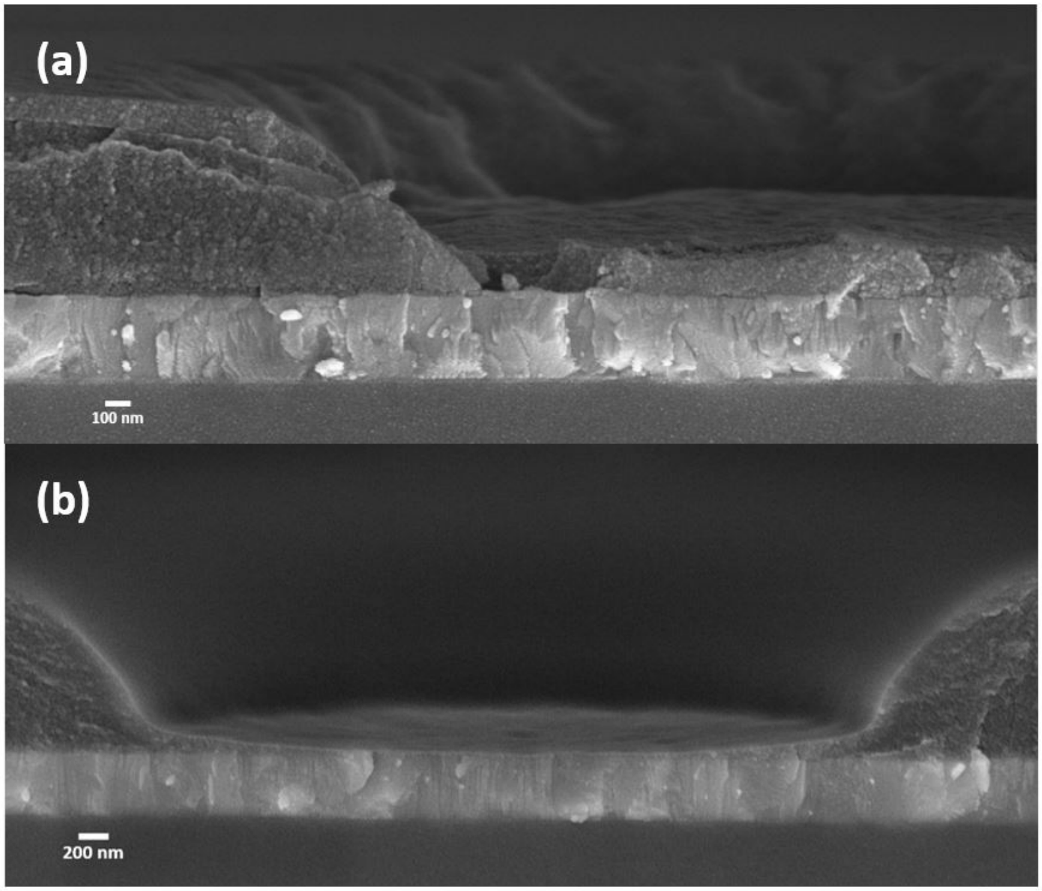

Figure 9.10: SEM image of device well cross-section for ZnO spin-cast at (a) 800 rpm and (b) 2000 rpm.

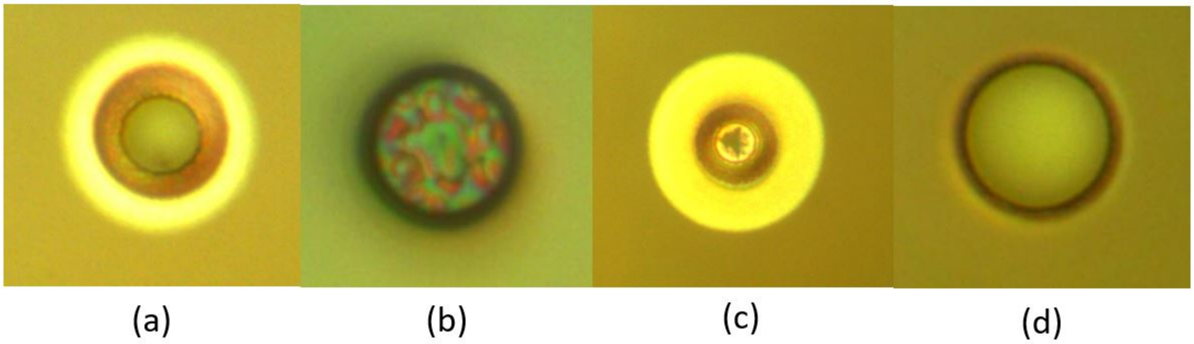

Figure 9.11: Microscope images of the developed SU-8 on sputtered ZnO, showing (a) poor adhesion to the substrate and (b) total and (c) partial adhesion to the device well. (d) Correct exposure conditions produce defined trenches with clean device wells.

9.5.3 Adjustment of Sputtered ZnO to Accommodate SU-8

Due to the issues of SU-8 adhesion onto sol-gel ZnO, devices were fabricated using sputtered ZnO, following the ZnO/SU-8 architecture in Fig. 9.1(b). Sputtered ZnO was also preferred due to the compatibility of the sputtering process with industrial fabrication. As indicated in Table 9.1, a dose/defocus condition of 1100 mJ/cm^2/0 is required exposure of SU-8 onto sputtered ZnO.

SU-8 photoresist on sputtered ZnO is particularly susceptible to the effects of overexposure. The microscope images in Fig. 9.11(a)-(c) show some issues associated with overexposure (all samples exposed at 1200 mJ/cm^2). Multiple rings are visible around the device well in Fig. 9.11(a), indicating poor substrate adhesion and lifting. Simultaneous to adhesion issues, the SU-8 inside of the well may fully (Fig. 9.11(b)) or partially (Fig. 9.11(c)) remain after development, insulation the device. Fig. 9.11(d) shows a clean, well-developed device well of a sample exposed using the correct conditions. Due to the design of the Heidelberg MLA150's DMD, the devices on the edges of the substrate tend to always be overexposed, suffering from the issues shown in Fig. 9.11(a)-(c).

Fig. 9.12(a) shows a cross-sectional SEM of the adhesion issue suffered in Fig. 9.11(a) and (c). The multiple rings visible in the microscope images correspond to multiple levels of thickness on the SU-8, caused by lifting and peeling. This is very undesirable, as it causes the QDs and metallization resting in the well to become discontinuous with the area sitting on the SU-8, severing device contact. Fig. 9.12(b) shows an SEM cross-section image of the phenomenon depicted in Fig. 9.11(b) and (c), in which the SU-8 is not entirely removed from the device well during development. The devices with the best performance

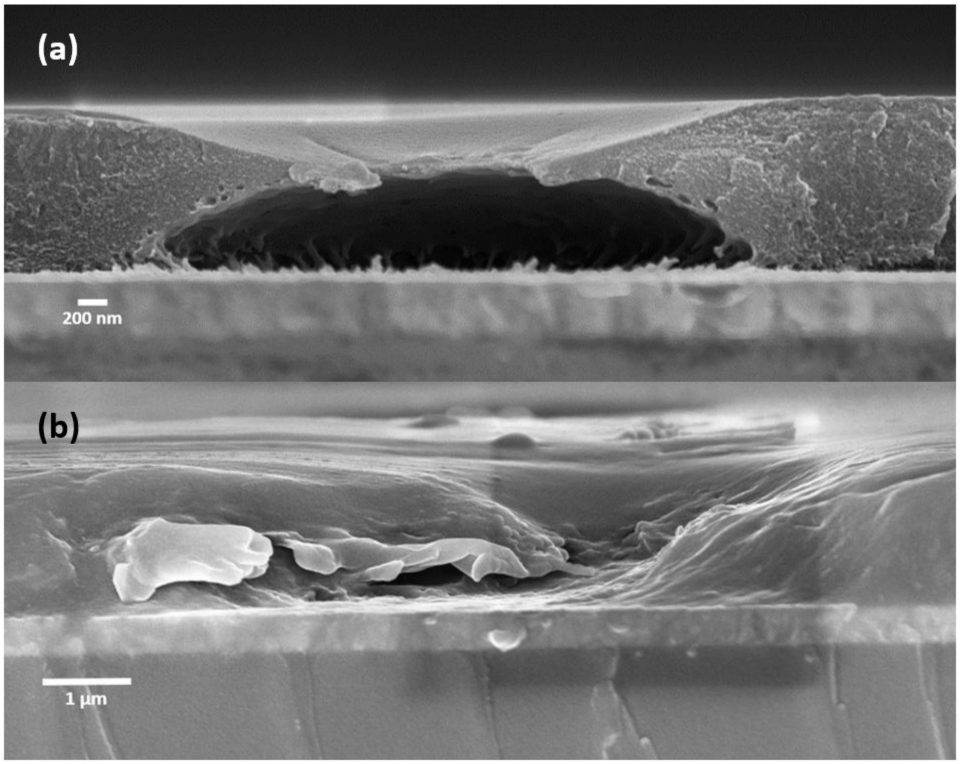

Figure 9.12: SEM cross-section of (a) SU-8 with poor adhesion to sputtered ZnO and (b) not totally removed after developing.

were achieved with sputtered ZnO, using the optimized exposure conditions.

9.5.4 Aluminum Shielding

Although the effective device area is 19.63 μm^2 (as defined by the 5 μm-diameter device well), the QDs occupy a larger area of up to 7.07 mm^2 (as defined by the 3 mm inner diameter of the O-rings in the injection setup). Furthermore, ITO and ZnO display response to illumination. To eliminate the effects of light excitation in non-active device areas, a thin layer of Al was deposited in areas of the device outside of the device well. Fig. 9.13 shows the cross-sectional structure of the device.

To implement the Al shielding, a 40 nm layer of Al was evaporated via electron beam following ZnO deposition and patterning. The SU-8 was then spun, exposed (300 mJ/cm^2/-4), and developed (PEB of 6 min at 95°C). The SU-8 was utilized as a mask to etch Al

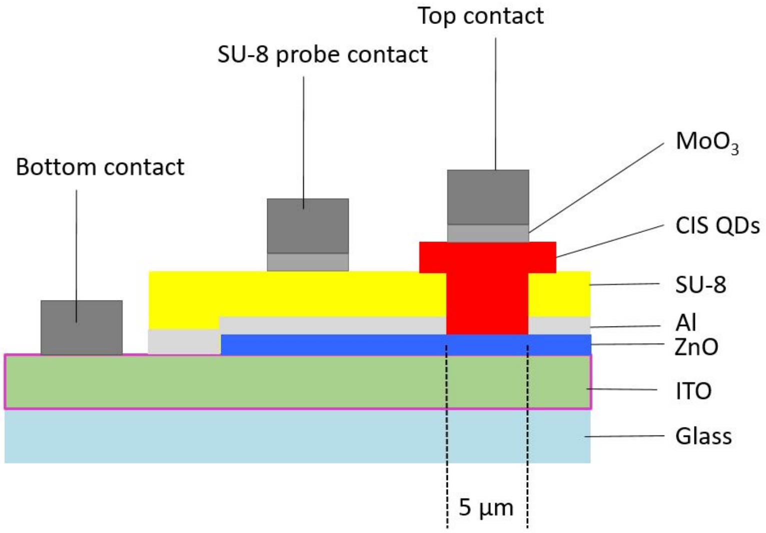

Figure 9.13: Structure of device incorporating Al shielding.

from the active device area. As ZnO is sensitive to acidic etching via HCl and nitric acid, traditional acid-based wet etching was not compatible. 2% NaOH was utilized, which was found to etch 40 nm of Al in 45 s. 2% NaOH slightly etches ZnO (12.5 nm/min), but significant ZnO etching was largely mitigated with swift removal of the substrate from the etchant when Al etching was complete. SU-8 was not etched by 2% NaOH.

It was found that Al redeposited onto ZnO and ITO during etching. Although Al redeposition onto ITO is only an aesthetic issue, Al redeposition onto ZnO is highly problematic for device performance. Fig. 9.14(a) and (b) show microscope images of uniform and non-uniform deposition of Al into the device well, in contrast to a device well where Al is completely removed (Fig. 9.14(c)). Redeposition was random, although device wells with partial SU-8 adhesion tended to attract more Al (Fig. 9.14(b)). Such device wells are completely unusable; Al blocks illumination and prevents formation of ZnO/QD interfaces. In a typical substrate holding 10 devices, over half were lost to Al redeposition.

Fig. 9.15 shows a cross-sectional SEM image of Al redeposition within the device well. Al shows proclivity for hillock formation at high temperatures, which it is exposed to during SU-8 annealing and MoO$_3$ and top contact deposition. When performing SU-8 verification, some I-V curves were conductive, indicating Al spiking through the SU-8 and making contact with the top metal; the low exposure of SU-8 on Al eliminated the

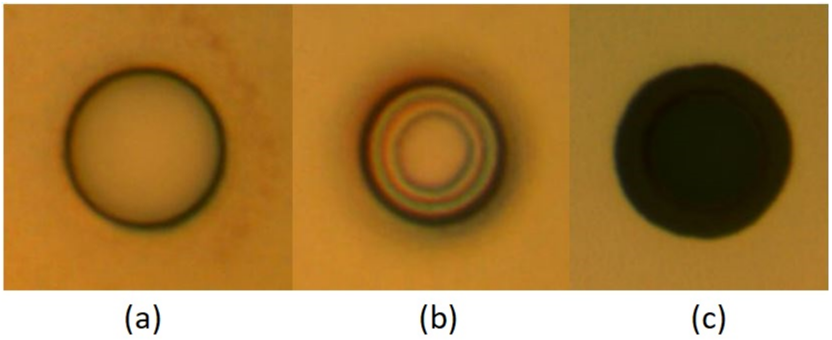

Figure 9.14: Microscope images of devices wells where Al is redeposited (a) uniformly and (b) non-uniformly (likely onto partially unremoved SU-8), (c) in contrast to a clear hole without Al re-deposition.

possibility of SU-8 breakdown due to overexposure. The Al likely spikes through several areas of the SU-8, creating paths that redirect current from the device well. This is detrimental to device performance.

Fig. 9.16 shows the best performance achieved from a device employing Al shielding. The CIS QD absorber was implemented through 1 pump of an MPA-ligated CIS CQD solution (NN Labs, 680 nm) diluted to 5 mg/mL. The device was annealed at 100°C for 15 min following QD deposition. The device displays evident response to illumination, but does not show better performance than devices without Al shielding (discussed later). The poor repeatability of this device, and issues of Al shunting, precluded the use of Al shielding as an established part this device fabrication process.

9.6 I-V Characteristics of CIS QD Photodetectors

Current-voltage characteristics of the QD photodetectors were investigated under dark and illumination. As the structure of the device requires light to enter from the bottom, an underlit setup was designed and built. White LEDs were fitted into the chuck to provide illumination. Fig. 9.17 depicts photographs of the setup utilized in measurement.

Fig. 9.18 shows the I-V response of a SU-8/ZnO device, with ZnO spin-cast at a speed of 2000 rpm. The QD absorber was formed by a 1-pump injection of a 5 mg/mL solution, and was not annealed. All other layers of the device were formed as described in the previous sections. This device shows the highest photocurrent of the small-area QD

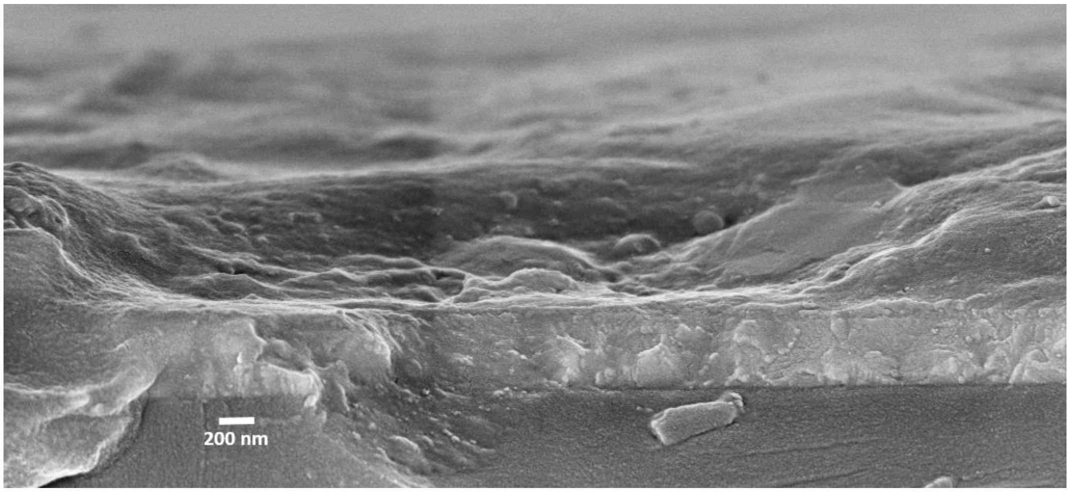

Figure 9.15: SEM cross-section image of Al adhesion in device well.

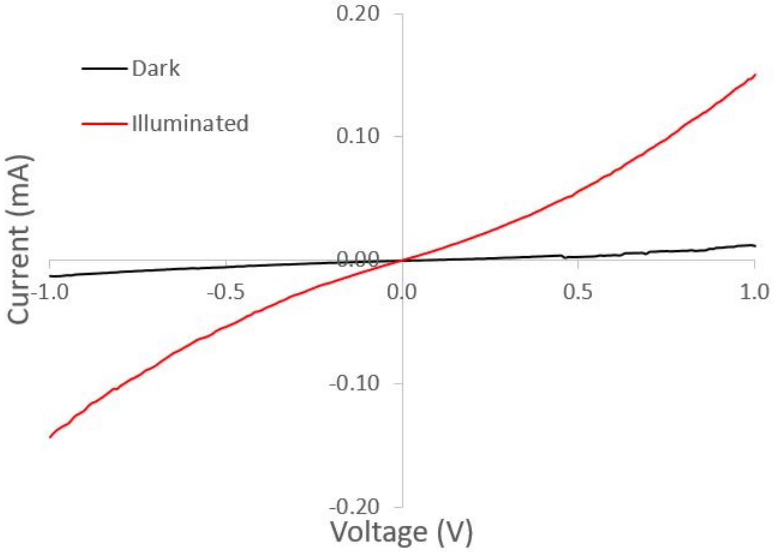

Figure 9.16: I-V curve of device with Al shielding.

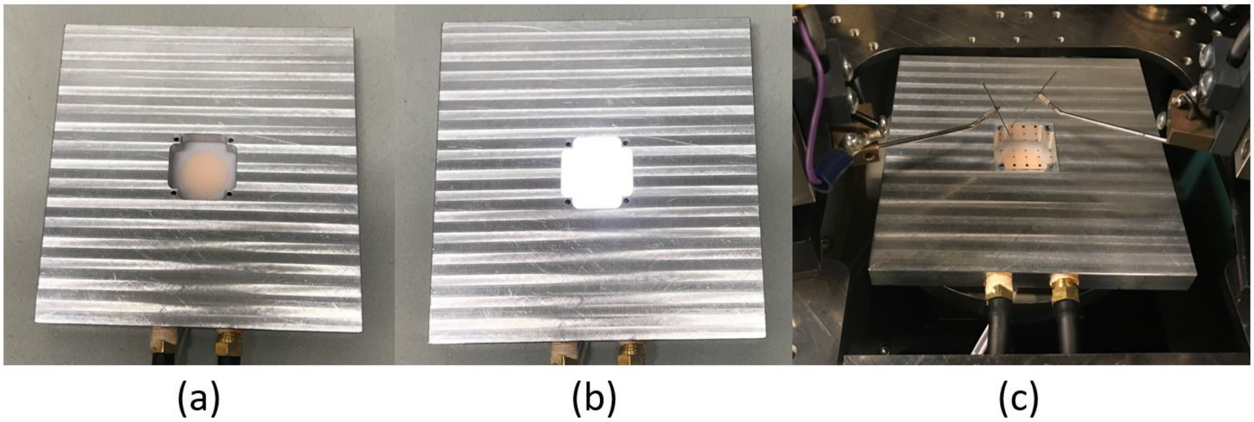
(a) (b) (c)

Figure 9.17: (a) Underlit measurement setup fitted with white LEDs, used for small-area photodetector measurement. (b) Setup with LEDs turned on. (c) Configuration of device and setup during I-V measurement.

photodetectors, in the mA range. However, the dark current is also fairly high, indicating ZnO/QD interface optimization is required.

Fig. 9.19(a) shows the I-V response of a device fabricated using sputtered ZnO, in a ZnO/SU-8 configuration. 40 nm of ZnO was sputtered using the recipe described in the previous chapter, and SU-8 was spun, exposed, and developed according to the conditions in Table 9.1. The QD absorber was formed by a 1-pump injection of a 1.25 mg/mL solution, and was not annealed. The device shows a clear turn-on voltage of 0.5 V. Although the photocurrent displayed is one order of magnitude lower than the device with spin-cast ZnO, this device displays the highest ON-OFF ratio (10.36% at 0.5 V, 17.91% at 1 V) of any photodetector fabricated up to this point. Although difficult to see in the compiled image, the dark I-V curve is also diodic in shape (Fig. 9.19(b)).

In the development of CIS QD solids, it was found that annealing CIS QDs improves adhesion to ZnO. Therefore, a device was fabricated using the same conditions as the device shown in Fig. 9.19, with the addition of QD annealing at 50°C for 15 min. Fig. 9.20 shows the I-V response of the device. There is response to illumination, but the device shows poorer photocurrent and higher dark current compared to the non-annealed counterpart. It is likely that within the well defining the smaller device area, the unannealed QDs present a more advantageous arrangement of DAP states carrier-selective traps, which reduce recombination and improve photocurrent. Thus, the need for annealing is negated, and implementing annealing may have disturbed the arrangement of transoirt states within the well, while increasing defect states that contribute to dark current.

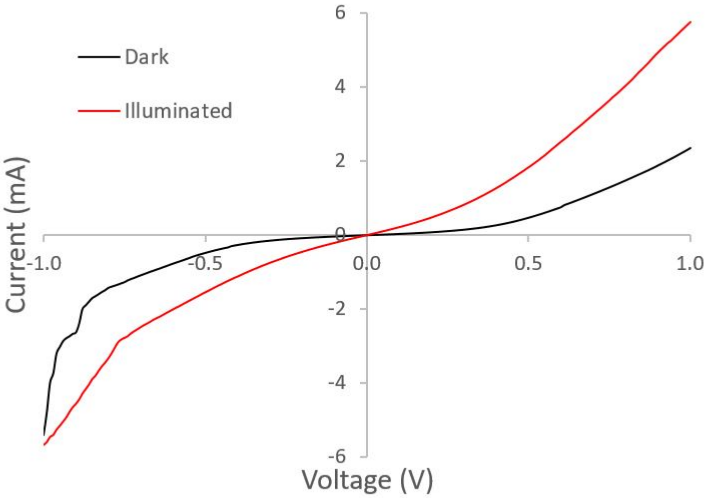

Figure 9.18: I-V response of a device with SU-8/ZnO configuration, with sol-gel ZnO.

9.7 Conclusions

In this chapter, a process was developed for fabricating small-area heterojunction QD devices onto standard 2.2 × 2.2 cm^2 substrates. The architecture presented in this chapter allowed the active area of the device to be confined to a small, 5 μm-diameter well, while maintaining the mechanical stability and ease of manipulation of the large cm-scale glass substrate. The dimensions of the device was controlled via substrate patterning using typical photolithography and shadow masks. The optimized architecture and standardized process allowed for systematic examination of ZnO/QD heterojunction parameters, to determine the impact on device performance. ZnO/CIS QD heterojunction devices were reliably fabricated using this process.

SU-8 was systematically developed as part of the photodetector, confining the device active areas to 19.63 μm^2 within the 2.2 × 2.2 cm^2 substrate. A QD injection system was developed to control the QDs within a 7.07 mm^2 area around the active device area, rather than forming a non-uniform blanket film across the entire substrate. Light-responsive devices were formed based on sputtered and sol-gel ZnO/CIS QD heterojunctions. The highest photocurrent was achieved using a sol-gel ZnO/CIS QD heterojunction. However, the device formed using sputtered ZnO/CIS QDs showed the best I-V behaviour and highest ON-OFF ratio. Further improvements to the QD quality will result in higher photocurrents and superior performance.

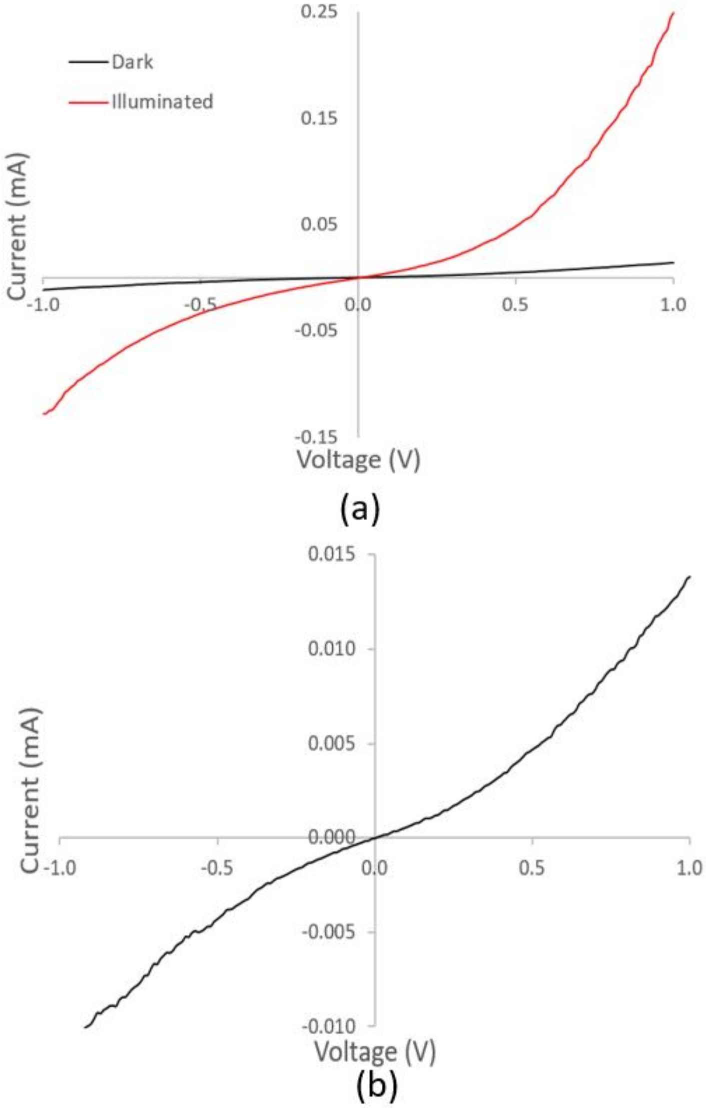

Figure 9.19: (a) I-V response of a device with ZnO/SU-8 configuration, with sputtered ZnO, (b) The dark I-V of the device is also diodic.

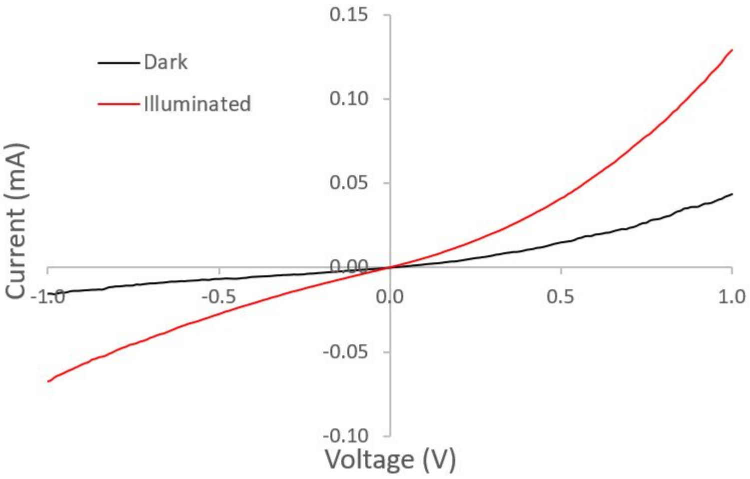

Figure 9.20: I-V response of a device with ZnO/SU-8 configuration, with sputtered ZnO and annealed CIS QDs.

The results presented in this chapter show the significance of process standardization for R&D of QD devices. The methodical processes used in the design and fabrication of these CIS QD-based photodetectors were key to their performance. The repeatability of fabrication allowed focus on investigating parameters that contribute to device performance, as it eliminated irrelevant questions regarding device architecture and fabrication. The processes developed in this chapter will continue to be implemented for the effective development of future devices based on QDs and other nanomaterials.

Chapter 10

Toxicity Analysis of QD Synthesis, Development, and Processing

The application of nanotechnology is found in every field of scientific research, from device engineering to medicine. With the prevalence of nanomaterials across multiple and disparate fields of research, the presence of a nanotechnological future is certain [137]. Although nanomaterials have moved beyond the realm of research into the consumer market, knowledge regarding the impact of their exposure is inadequate. Strong regulations must be enacted over nanomaterials used as therapeutic, diagnostic, and imaging tools [212][213][214]. As well, nanomaterials applied towards electronics should not be precluded from regulations. Although consumer nano-electronics are not intended for ingestion, they nevertheless pose exposure risk during manufacturing, deployment, and end-of-cycle disposal. Currently, there is a lack of impactful study on the toxicity effects of QD exposure to workers and researchers that handle QDs for non-biomedical purposes.

This chapter presents methods and studies for practising safety and mitigating exposure at every level of nanomaterials R&D, from materials selection to engineering. Strategies for mitigating exposure were applied to the research taken in this work, from synthesis of QDs, to QD film formation, towards device fabrication. The following sections detail the design and execution of studies on the toxicity effects of quantum dots in device processing and fabrication environments. Studies were performed to investigate risk of exposure and potential cytotoxicity effects associated with heavy metal and less-toxic QDs used in research environments. Optical spectroscopy was used to study QD exposure during QD processing and testing. Cell viability studies were performed on HeLa and CHSE to study the potential cytotoxicity effects of QDs [66][215]. The safety analysis conducted here is useful for developing strategies for handling large-scale production of QD-based materials and devices. The findings of this chapter were utilized to guide the remainder of the QD material and device development in this work.

10.1 The Role of QDs as Workplace Hazards

Due to their size-tunable fluorescence and ease of functionalization, QDs are considered a good candidate for optical and bioimaging applications. Material selection is an important aspect of mitigating safety risk. Heavy metal ions, which are found in some common QDs, pose significant health hazards if released into the workplace. Due to official sanctions on the use of Cd, Pb-containing semiconducting compounds in devices [216], there has been a shift towards development of less-toxic QDs for employment in commercially-viable devices. CIS-based QDs have particularly gained attention because of their biological stability and optically advantageous properties [98][99]. However, due to their nanoscale size and non-classical behaviour, less-toxic QD materials are not precluded from imparting biological toxicity.

Aerosolized QDs and other nanoparticles represent a significant safety hazard in the development of large-scale manufacturing processes that utilize nanomaterials [66]. Population studies have determined direct correlation between relative death rate and the prevalence of fine particles ($PM_{2.5}$) [217][218] and particulate pollution in urban areas [219]. In addition to producing inflammation and acute phase response, inhaled NPs can circulate within the bloodstream, producing arterial build-up leading to cardiovascular disease [138]. The safety issues posed by nanoparticles are of special concern over other particulates; due to their small sizes, large surface area, and various enhancements that modify their behaviour, NPs and QDs display toxicological properties that are not found in the bulk [137][138]. Uncertainties regarding the consequences to their exposure limit work even at the research and prototyping stage, and nanomaterials safety practices are exercised in academic research. It is the responsibility of academic researchers to consider the ramifications of nanomaterials toxicity and spread beyond the research laboratory, on workers in nanomaterial manufacturing industries and among consumers of products containing nanomaterials. It is necessary to perform nanotoxicological research and develop risk assessment protocols and safe handling guidelines for legislation [220][221][222].

Although studies of QD application to pharmacology and medicine are abundant, there is a lack of understanding on the toxicity risks of nanotechnology intended for other applications. Since such QDs are being accelerated in incorporation into scaled-up PV processing platforms for production of high-efficiency devices, studies are needed to develop a rapid and sensitive method for detection of toxic element and aerosolized QDs. Therefore, better comprehension of toxicity and safety for non-medical quantum dot applications is needed to develop relevant, regulated safety protocols. Based on the fast rate of projected quantum dot growth and dominance within the next decade [8][9], it is critical to gain insight into quantum dot toxicity and health risks before they become commonplace.

10.2 Development of a Safety Controls Model

The small size of nanomaterials and QDs make them particularly effective in aerosolizing [66][83] and eliciting biological response [83][84][122]. In addition to intentional exposure in medical treatment, humans are inadvertently exposed to nanomaterials, nanoparticles, and QDs via inhalation, ingestion, or skin absorption [82][138]. Of these, inhalation is the most prevalent path of exposure for workers. This is of concern, as NPs and ultrafine particles (UFPs) can evoke inflammation and other undesirable biological responses due to difficulty of natural removal compared to other unwanted particles in the human body. Hougaard et al found prolonged inhalation of TiO_2 NPs in mice produced lung inflammation and altered offspring behaviour[137]. In Jackson et al's study, extended nano-carbon black exposure to mice was also found to produce lung inflammation [223]. In addition to having small sizes and large surface areas that elicit undesirable physical response, QDs are subject to specific functionalization and chemical treatments that further alter their interaction with biological organisms [138]. Thus, due to the relatively poor understanding of nanomaterials compared to bulks, current response, treatment, and removal of nano-contamination is guesswork, at best. Given the risk posed by nanoparticles and ultrafine particles, there should be a clear hierarchy of safety controls to minimize nanomaterial exposure, which must be implemented in the research phase prior to large-scale manufacturing [85].

Handling Safety at the Source

The first and foremost strategy of exposure prevention should aim to eliminate exposure at the source by substituting hazardous substances with non-toxic or less-toxic substances [224]. QD toxicity is dictated by a variety of factors aside from material composition; size, charge, coatings, and functionalization significantly contribute to toxicity [39][208]. Notably, ligands govern QDs' interactions with their surrounding materials based on lipophilicity/hydrophilicity. Therefore, ligand/host pairings can be employed to reduce toxicity risks, minimize biological accumulation, and prevent aerosolization. If exposure occurs, the attachment of certain ligands minimizes biological toxicity by blocking ion leakage from QD cores and reducing QD interaction within the human body [225][226].

Process and Engineering Design to Minimize Spread

When material substitutions are not possible, engineering considerations must be employed to minimize exposure [224]. First, nanoparticle quantity and phase significantly determine the hazard of nanomaterial exposure. Dosage impacts toxicity [39]; lowering the quantity of "toxic" materials can effectively prevent the most devastating effects of exposure. Therefore, risky exposure is mitigated through selection of low-concentration QDs in configurations that do not easily aerosolize. Second, the quality of the work environment, such as ventilation and cleanliness, have profound effect on exposure. It is advisable to isolate all nanomaterials-related research in a facility to specific "nanoparticle containment rooms", in which traditional High Efficiency Particulate Air (HEPA) filters with 99.97% efficiency or Ultra Low Penetration Air (ULPA) filters with 99.99% efficiency are used [224]. Local Exhaust Ventilation (LEV) systems should be placed as close to the source as possible to control hazardous exposure. At minimum, nanoparticles and QDs should be handled only in well-ventilated containment modules, such as fume hoods and gloveboxes that are dedicated for their use [224]. Finally, the duration of the task is significant; as exposure to nanomaterials and particulates are prolonged, the consequence of toxicity is multiplied [218][224]. Researchers can ease exposure through choosing shorter processes and implementing regular breaks. Therefore, if a substitution for a less-toxic QD cannot be made, the design of equipment and processes alleviates potential toxicity by decreasing the potency of QD exposure. Researchers should take care to isolate QD handling in dedicated areas and choose fabrication techniques with less risk of aerosolization.

Evaluation

After safety considerations are made, exposure risk should be practically evaluated at the research and prototyping stage, while experiments are performed on a relatively small scale. In all environments performing QD coating, quantitative evaluation tools should be implemented to determine particle levels at both the source of QD exposure and the worker station, immediately outside of the nanoparticle containment enclosure. This is to establish that the precautions in place, such as fume hoods and enclosures, are operating as required. The volume and type of particles detected at the worker station should be significantly lower than the source of exposure inside of the enclosure; processes should be reconsidered and redesigned based on the outcome of the analysis. If the design does not pass evaluation for non-fatal levels, it is mandatory that the first two steps (handling at source and process design) are revisited and adjusted, until satisfactory levels are reached.

Administrative Protocols

Finally, mitigation at the administrative level is critical in promoting nanomaterials safety [224]. Developing strict workplace safety standards for employees allows the observation of safe nanomaterials practices to become intrinsic. There should be adequate training and proper monitoring to ensure that workers are complying with safety regulations. Workers should keep their work areas clean, wear proper personal protective equipment (PPE), and follow all procedures when procuring, handling, and disposing materials. Significantly, PPE should be the last line of defence against NP and QD exposure; all other safety controls should be strictly enforced to a degree that does not force workers to rely solely on PPE. To mitigate exposure incidents among workers and members of the public, it is critical that processes are evaluated based on source toxicity and exposure risks posed by the process. Through better knowledge of risks, a more complete understanding can be achieved and communicated, allowing workplace monitoring programs to become more widespread [227]. Only when the risks are well understood, can researchers take steps and develop protocols with considerations for public health and safety.

Fig. 10.1 summarizes the strategies suggested for preventing nanomaterial exposure. When designing technology that is meant for mass production and utility, it is a researcher's duty to consider impact on workers and public health. Thus, careful observation of this safety control hierarchal process is recommended during research and development, prior to developing prototypes intended for large-scale production.

10.3 Evaluation of Toxicity at the Source

Health risks are primarily mitigated by material selection; substituting the common, toxic Cd- and Pb-based QDs for less-toxic materials ensures minimal harm even if exposure occurs [39][63][66]. QD toxicity is mainly related to properties such as physiochemical, oxidative, photolytic properties, mechanical stability, and bioactivity. QD shape, size, concentration, surface area, surface coating, and aggregation state [208][228][229][230][231] are the key parameters that affect QDs' abilities to impart toxicity.

The core composition, particularly for heavy metal-containing QDs, is a primary and obvious source of toxicity. It has been suggested that the Cd core of QDs drives the observed toxicity due to leakage of Cd ions (Cd^{2+}) [61][213]. Cadmium mainly targets the body's cardiovascular, renal, gastrointestinal, neurological, reproductive and respiratory systems [208]. Lead is known for its detrimental effects to the central nervous and renal systems [136]. The concerns of these materials' toxicity in bulk have transferred to their

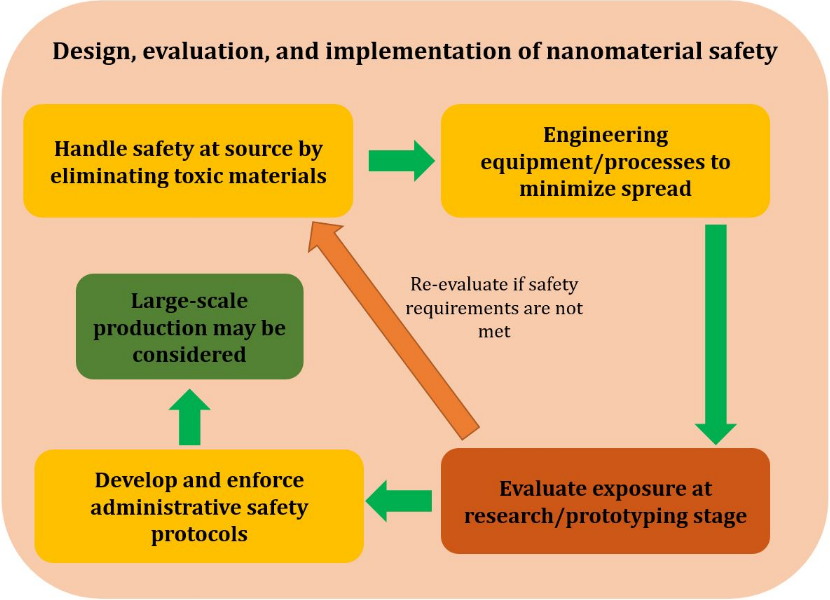

Figure 10.1: Evaluation flow diagram for evaluating NP/QD containment effectiveness.

nanoscale counterparts. Although nanomaterials contain smaller amounts of the heavy metal of concern, their small size and aerosolization allow easy entrance to and difficult expulsion from the body.

As the primary mechanism of QD toxicity is leakage of ionized material into the body, overcoating and ligand selection help shield source toxicity [225]. However, poor selection of shell and ligand materials may escalate toxicity, by either improving QD uptake in the body, or themselves posing as the source of toxicity. The effect of various surface chemistries (organic, carboxyl [COOH], amino [NH_2], etc.) and core/shell materials on cell viabilities have been reported in literature; these studies can better elucidate the origin of QD toxicity [232]. Surfaces have significant impact on QD toxicity; strong cytotoxicity has been reported for QDs with organic ligands even at low particle concentrations. Reduced cell viability was also detected as a result of exposure to higher concentration of COOH and [NH_2]-ligated QDs. These investigations concluded that among QD core, core/shell and surface coating, surface coating contributes most substantially to QD toxicity. Surface modification of QDs has been reported as the main method to control QD interaction with the human body, reducing health risk [233][234].

Core, shell, and ligand materials all contribute to QD toxicity, and each parameter should be considered when evaluating toxicity of the source QD material. The following sections present simple *in vitro* cell studies tests performed on QDs of various composition, size, ligands, and overcoats. The materials evaluated are well-known core, shell, and ligands utilized in QD research, and the investigation was conducted with effort to better understand the impact of these materials on cell cultures. The findings from this research provide elucidation on the impact of QDs on human biology.

10.4 *In Vitro* Modeling Using HeLa Cell Lines

The potential cytotoxic effects of quantum dots in mammalian cells were examined via cell culture viability tests using HeLa and CHSE cells as *in vitro* models. Healthy HeLa cells were exposed to QDs of varying sizes, ligands, and coatings, and their response was observed. The cells were exposed to various CdSe- and CIS-based quantum dots, such that the effects of heavy metal QDs could be compared to exposure to less-toxic quantum dots. CdSe-based quantum dots dispersed in toluene were purchased from NN Labs [66][215], while CIS and CIS/ZnS quantum dots were synthesized in-house. Solvents used for QD dispersion (toluene, hexane) were obtained from Sigma-Aldrich.

The typically non-polar solvents used to disperse QDs are toxic to HeLa cells, and incompatible with the polar media used to grow and store HeLa cells. Therefore, this study was designed to remove the effect of solvent by evaporation prior to contact with HeLa. Before QD exposure, HeLa cells were maintained as a monolayer and routinely subcultivated every three to four days in a nutritious growth medium (Dulbecco's Minimum Essential Medium (DMEM) supplemented with 10% Fetal Bovine Serum (FBS) and 1% penicillin/streptomycin (PS)). Each well was seeded with approximately 2×10^5 cells in a total of 0.5 mL media. The cells were incubated at 37°C in an atmosphere of 5% CO_2-95% air. Three replicate cultures were used for each treatment. All reagents used in this study were of analytical grade. The cells were seeded in a 24-well plate, at 0.2×10^6 cells per well with 0.5 mL of the growth medium. After 24 hours of incubation, the cells were washed once with Dulbecco's Phosphate Buffered Saline (DPBS), and the medium was exchanged with fresh medium containing various concentrations of QDs in toluene [66].

10.4.1 Toxicity Evaluation of CdSe QDs in Solvent

Despite their bulk phase toxicity, CdSe-based materials are popular in QD device research due to their intense fluorescence across the visible spectrum [4]. The cytotoxicity effects of CdSe-based QDs were investigated to determine if they share the toxic properties

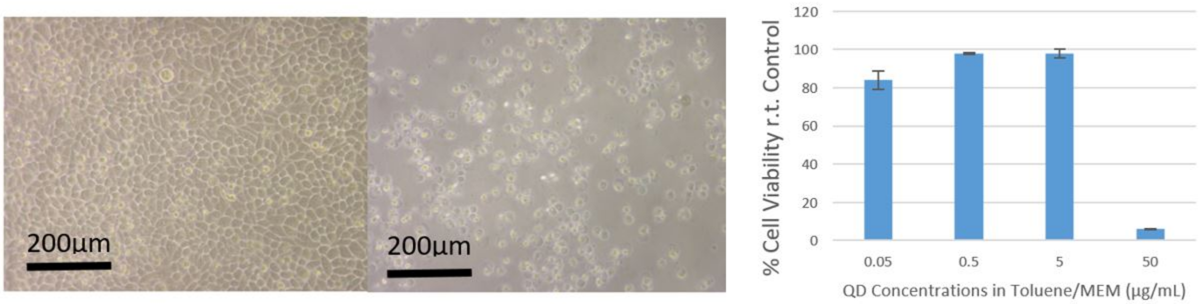

(a) (b) (c)

Figure 10.2: Microscopy images of (a) control and (b) HeLa exposed to 50 μg/mL of 540 nm CdSe/ZnS QDs. (c) Resazurin metabolic activity assay to assess relative viability of HeLa exposed to 540 nm CdSe/ZnS QDs. At 0.5 mL of QDs in media per well, this equates to 0.025, 0.25, 2.5, and 25 μg of QDs per corresponding well.

of their bulk counterparts. The CdSe QDs were kept in organic toluene solvent to maintain their colloidal dispersion during testing. As toluene is deadly to HeLa, a preliminary test with different dilutions of toluene in DMEM was conducted to determine the non-lethal concentrations. A 1% v/v concentration of toluene was determined to be the highest acceptable concentration that did not cause HeLa cell death. This concentration was kept constant in subsequent studies.

Various concentrations of CdSe/ZnS QDs with a wavelength of 540 nm in toluene and MEM were prepared. The QDs were diluted ten-fold into toluene from a stock solution with a concentration of 5 mg/mL in toluene. The diluted solutions were further diluted in DMEM to ensure a constant 1% v/v concentration of toluene in DMEM. The final concentrations of the QDs were: 50 μg/mL, 5 μg/mL, 0.5 μg/mL, and 0.05 μg/mL.

Each well was treated with 0.5 mL of QD/toluene/MEM solution. The cells were incubated with the QD solutions for 24 hours, at 37°C, with 5% CO_2-95% air-95% air, similar to the initial incubation in MEM. Following incubation, cells were viewed under optical microscope to visually determine the results of QD exposure. Fig. 10.2(a) and (b) show optical images of living HeLa cells in the control solution, and dead HeLa cells incubated with 50 μg/mL of 540 nm CdSe/ZnS QDs, at 100× magnification, respectively. Living and dead cells were visually distinguishable: healthy HeLa cells maintained a uniform monolayer in the well bottom, while dead cells became floating cell debris. From visual inspection, it was found that the highest concentration (50 μg/mL) killed nearly all of the exposed cells. However, the lower concentrations showed either low or negligible cell death.

Resazurin metabolic activity assay was used to precisely and quantitatively investigate the effects of QD exposure on HeLa viability. HeLa cells were exposed to a solution containing resazurin dye (Alamar Blue), and incubated for approximately 45 to 90 minutes. During incubation, living cells reduce resazurin to resorufin, a strongly fluorescent dye that can be measured by a fluorescent plate reader (Cytofluor) [66]. Dead cells cannot complete this reduction process, and thus, do not produce a fluorescence. The viability of QD-treated cells can thus be determined by measuring their fluorescent emission after exposure to resazurin relative to control cells [215]. Fig. 10.2(c) shows the results of the resazurin metabolic activity assay for exposure to the CdSe/ZnS QDs, which supports the results from optical microscopy (5.96% relative viability).

10.4.2 Toxicity Evaluation of CdSe QD Solids

The initial exposure tests followed a more traditional method of cytotoxicity testing, in which the toxin under investigation was delivered to the cells via the DMEM solution. However, the incompatibility between the non-polar QDs-in-toluene and polar DMEM necessitated constant agitation to prevent two-phase formation. QD functionalization to induce polarity was not feasible, as it would not allow study of the QD ligands. Furthermore, to prevent bacterial growth, it was necessary to filter the QD/toluene/MEM solution prior to testing. Although the larger pores of the 0.2 μm filters Supor membrane filters would not theoretically catch the smaller QDs (approximately 7 nm in diameter), the unstable polar/nonpolar solution resulted in formation of ligand/MEM networks that trapped QDs and increased their effective size. As a result, the actual QD concentration the cells were exposed to was lower. To avoid the ambiguities posed by toluene, a technique was devised to directly expose HeLa cells to QDs.

CQDs in toluene were drop-cast onto circular glass microscope slide covers, then dried for approximately 75 minutes for solvent evaporation. The QD film-on-glass slides (1.5 cm diameter) were inserted QD-side-up into the wells of the 24-well plate (1.53 cm diameter), and HeLa cells were added [63]. Ten-fold concentrations were used for the CdSe QD film-on-glass exposures, at 0.0025, 0.25, 2.5, and 25 μg per slide. To confirm that residual toluene did not interfere with the study, one set of control slides were always prepared with evaporated solvent (toluene) as control. For consistency, blank were also inserted for media control and calibrating blanks; the schematic is shown in Fig. 10.3.

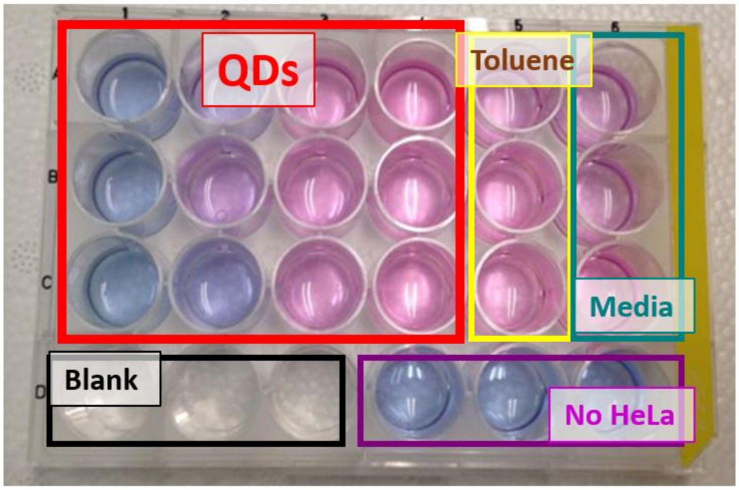

Figure 10.3: Layout of a 24-well plate used in QD toxicity studies.

10.4.2.1 Cytotoxicity Effects of Core and Core/Shell CdSe QDs

The effects of core and core/shell QDs were investigated with CdSe-based QDs. Oleic acid-ligated, 540 nm emission CdSe/ZnS QDs and comparatively-sized CdSe core, OA-ligated, 520 nm emission QDs were used to model the effects of core and core/shell for similarly sized QDs. The QDs were significantly and negatively impacted by exposure to both QDs. Figure 10.4 presents images of HeLa cells with and without exposure to the CdSe/ZnS QDs; there was nearly total cell fatality when exposed to a QD dosage of 25 μg/slide. Notably, this yielded the same result as CdSe/ZnS QDs in solution, where 50 μg/mL CdSe/ZnS QDs in 0.5 mL solution (25 μg per well dosage) produced fatality. Therefore, QDs exposure using the QD-film-on-glass method was deemed an effective alternative to the method using the QD/toluene/DMEM solution, although the resolution of the microscope images slightly decreased due to the reflection from the glass slides at the bottom of the well.

Core CdSe QDs began causing significant cell death at only 0.25 μg/slide (Fig. 10.4(a); 19.53 % relative viability), and with almost total cell death at 2.5 μg/slide (4.75% viability). In contrast, CdSe/ZnS only caused cell death at a ten-fold lower dosage of 25 μg/slide (Fig. 10.4(b); 8.78% relative viability), with lower dosages showing negligible cell death. It can be concluded that the presence of the passivating, less-toxic ZnS shell mitigates significant cell death compared to core QDs.

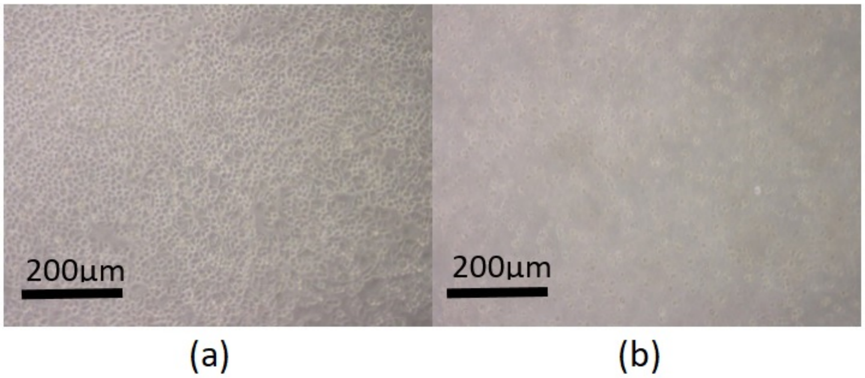

Figure 10.4: Optical images of HeLa cells grown in (a) nutrient media without QDs and (b) 25 μg/slide of CdSe/ZnS QDs.

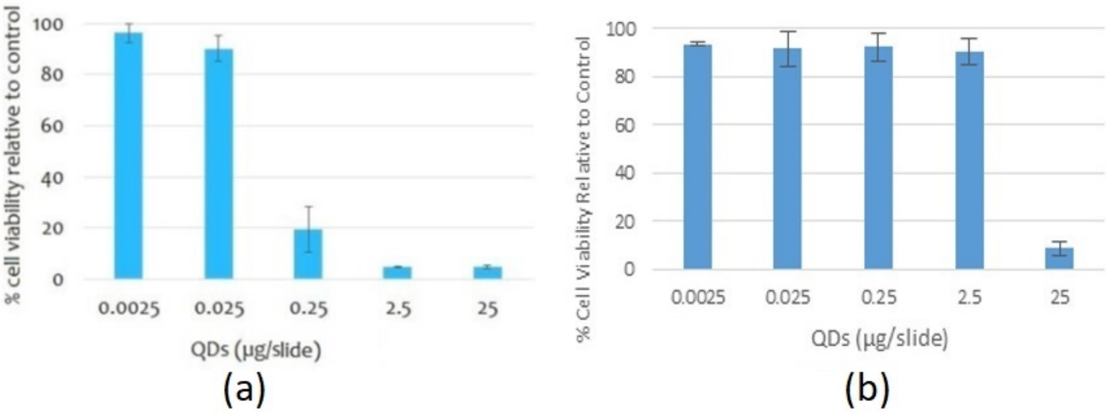

Figure 10.5: Relative viability of HeLa cells exposed to (a) CdSe QDs with 520 nm emission, and (b) CdSe/ZnS QDs with 540 nm emission.

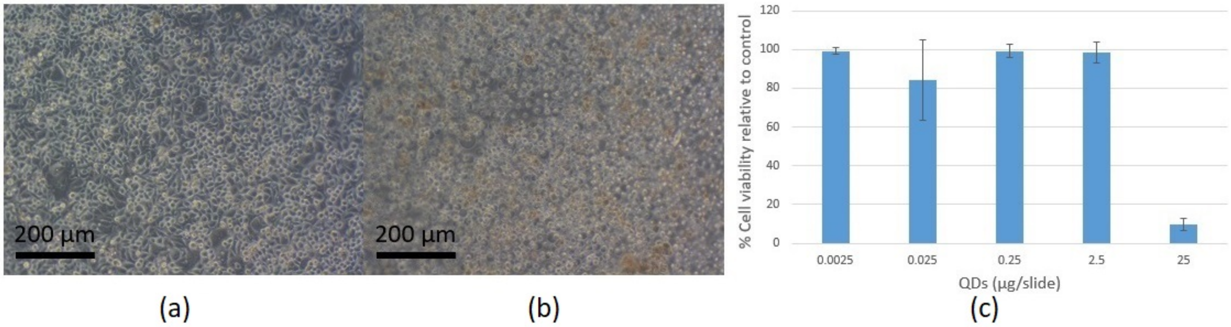

Figure 10.6: Microscopy images of (a) control and (b) HeLa exposed to 25 μg/slide of ODA-ligated CdSe/ZnS/Silica QDs. (c) Relative viability of HeLa exposed to ODA-ligated CdSe/ZnS/Silica QDs.

10.4.2.2 Cytoxicity Mitigation Using Silica Overcoating

From the core and core/shell studies, it was established that core CdSe QDs showed significant toxicity, and the extent of toxicity was somewhat mitigated through a protective overcoat. ZnS is commonly used to overcoat CdSe due to lattice compatibility, not out of consideration for biotoxicity. As ZnS overcoats provided some mitigation of toxicity, it was reasoned that passivation with a known biologically benign material could further alleviate toxicity effects. Thus, the effects of silica overcoating on QD toxicity were studied.

HeLa was exposed to 10-fold dilutions of silica-overcoated, 550 nm-emitting CdSe/ZnS QDs, with octadecylamine (ODA) and trioctylphosphine oxide (TOPO) ligands. The optical microscope images for ODA-ligated, silica-coated QDs are shown in Fig. 10.6(a) and (b). The images appear darker due to the thickness of the silica shells, which significantly increase overall QD size (although the core is comparable to the previously studied QDs). Cytofluor fluorescent plate reading results are shown in Fig. 10.6(c). Significant cell death appeared between 25 μg/slide and 2.5 μg/slide, and the relation between dose and viability was largely the same as CdSe/ZnS QDs. Thus, the additional silica overcoating did not significantly mitigate toxicity. It is possible that, due to the greater biological compatibility of the benign silica shell material, there was greater biological interaction compared with just the ZnS shell, leading to increased cell/QD interactions.

Fig. 10.7(a) and (b) show the microscope images of HeLa exposed to TOPO-ligated, silica-coated CdSe/ZnS QDs. Cytofluor results are shown in Fig. 10.7(c). The effect of the 25 μg/slide CdSe/ZnS/silica on HeLa toxicity was less fatal than the lethal dose of 25 μg/slide for the ODA-ligated QDs. The viability decreased to 43.92%, compared to 9.76%

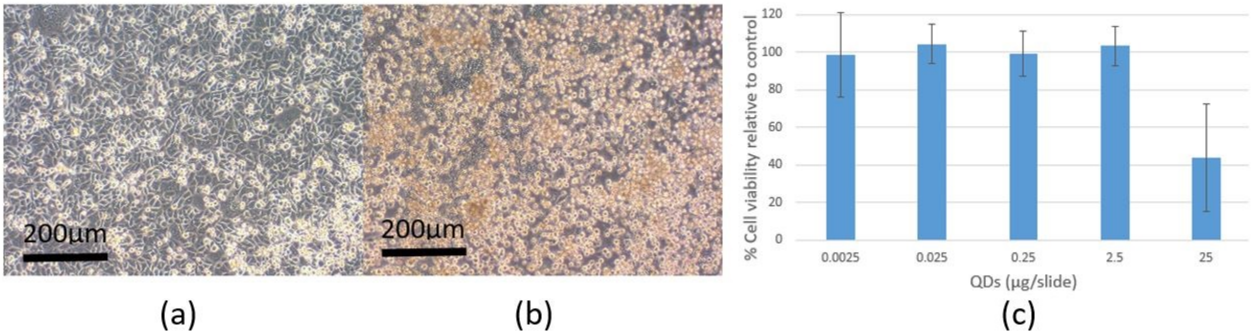

Figure 10.7: Microscopy images of (a) control and (b) HeLa exposed to 25 μg/slide of TOPO-ligated CdSe/ZnS/Silica QDs. (c) Relative viability of HeLa exposed to TOPO-ligated CdSe/ZnS/Silica QDs.

viability for ODA-ligated QDs at 25 μg/slide. This effect cannot be solely attributed to the silica passivation, but is related to both the overcoat and ligand.

10.4.2.3 Cytotoxicity Effects of QD Ligand and Size

Ligands and surface treatments are significant in shielding the potentially toxic effects of the metalloid core; uncoated QDs easily produce reactive oxygen species that cause strong damage to cells [235]. The study of silica-coated QDs in the previous section showed the impact of ligands on cytotoxicity. Ligands are key to the interaction of QDs with biological organisms; the lipophilicity and hydrophilicity of organic ligands make them more miscible among the fats and tissues that comprise the biological organism. Therefore, cytotoxicity effects of ligands were further investigated with core, 520 nm-emitting, organic/inorganic chalcogenide-ligated CdSe QDs, for comparison with the results in Section 10.4.2.1. The relative viability of the chalcogenide-ligated, 520 nm-emitting CdSe core QDs is presented in Fig. 10.8. Significant cell death appeared at 25 μg/slide (14.53% relative cell viability) compared to oleic acid-ligated QDs of the same size and composition (cytotoxicity effects appear at 0.25 μg/slide; Fig. 10.5(a)); higher doses of chalcogenide-ligated QDs were needed to induce cell death (i.e., the OA-ligated QDs are more lethal). Among the ligands studied on CdSe QDs (OA, TOPO, chalcogenide), oleic acid imparted the most toxicity. As oleic acid is a staple of the human diet, it is reasonable to conclude that it has better miscibility among biological structures. This leads to greater cell uptake of OA-ligated QDs, which, in the case of Cd-based QDs, results in inducing greater cell toxicity.

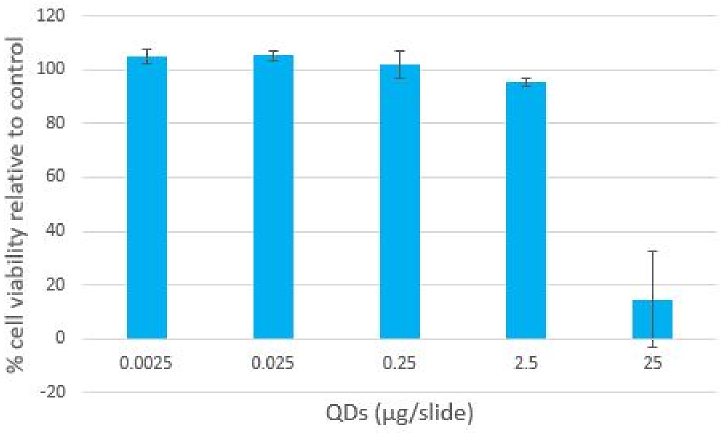

Figure 10.8: Relative viability of HeLa cells exposed to chalcogenide-ligated CdSe QDs.

Size effects were investigated by comparing chalcogenide-ligated quantum dots with increasing emission wavelengths, correlated with increasing QD size (480 nm and 560 nm emission; increased emission wavelength corresponds with larger core size), and the results of their effects on HeLa were compared to the results of the 520 nm-emitting CdSe chalcogenide-ligated QDs (Fig. 10.9). All QD exposures caused cell death between 2.5 μg/slide and 25 μg/slide (with approximately 5% relative cell viability at 25 μg/slide for both). Although further tests were performed to more accurately determine the fatal dosage, the results of exposures for concentrations between 2.5 μg/slide and 25 μg/slide did not follow a clean trend. This is attributed to the 2.5 μg/substrate-25 μg/substrate range causing marginal cytotoxicity, resulting in the death of some, but not all cells across the entire exposure range. Although the chalcogenide-ligated QDs do not possess an overcoat, they are less lethal to the cells than the uncoated OA-ligated QDs, attributed to decreased cellular interaction.

The data obtained from CdSe QD cytotoxicity studies indicate that ligands mainly contribute to toxicity, while overcoats slightly mitigate core toxicity. QD size did not have any effect on toxicity. TOPO-ligated, silica-overcoated CdSe/ZnS QDs were the least toxic QDs among the CdSe QDs investigated. Toxicity primarily stems from the Cd-containing cores; the relative lack of impact from the TOPO-ligated, silica-coated QDs is attributed to the shielding from the thicker ZnS/silica shells, and decreased cell interactions as a result of the less biologically compatible TOPO ligands.

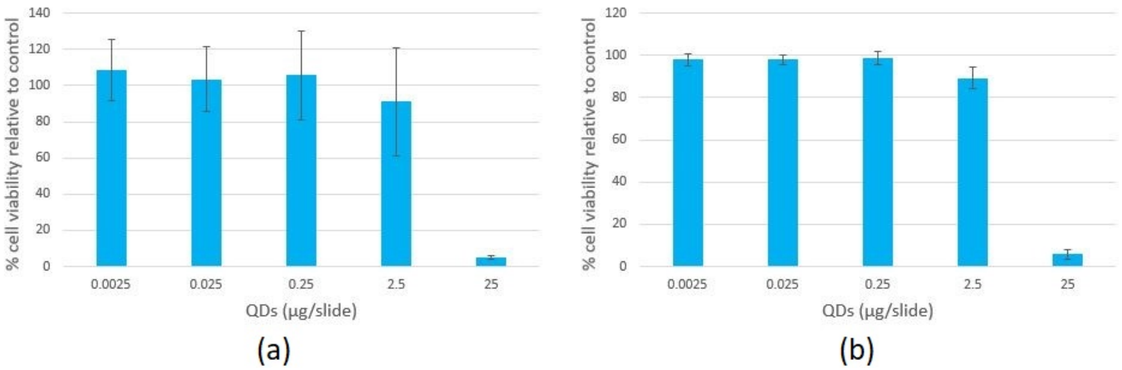

Figure 10.9: Relative viability of HeLa cells exposed to (a) CdSe QDs with 480 nm emission, and (b) CdSe QDs with 560 nm emission.

10.4.3 CIS QD Toxicity

HeLa cells were exposed to CIS QDs using the QD-film-on-glass methodology. The ten-fold concentrations used for the CIS exposures were 0.025, 0.25, 2.5, 25 (same as the CdSe QD exposures), and 250 μg/slide. The synthesized CIS QDs at the highest dosage of 250 μg/slide (three orders of magnitude higher than the death-inducing dosage of 0.25 μg/slide for core CdSe QDs) only invoked a slight negative response from the HeLa. At a CIS QD exposure of 20 μg/slide, the cell viability was 75.92%, almost two times higher than cell viability at the same dose of the "least toxic" TOPO-ligated, silica-coated CdSe/ZnS QDs. Fig. 10.10(a) and (b) show the results of CIS QD exposure at 250 μg/substrate; the cells expressed some stress but maintained a uniform cell monolayer inside the well, indicating the presence of living HeLa similar to the unexposed, healthy HeLa cells. The relative viability was 61.31%, determined by resazurin metabolic activity assay (Fig. 10.10(c)).

Fig. 10.11 shows the results of optical microscopy and resazurin metabolic activity assay for HeLa exposure to synthesized CIS/ZnS QDs. Although up to 250 μg/substrate of core CIS QDs did not provoke significant cell death, CIS/ZnS exposure at 250 μg/substrate was shown to cause cytotoxicity (10.05% relative viability). As the above experiments showed ZnS shell material to not have a significant impact on cell viability, this difference is attributed to the ligands; while the CIS QDs were ligated with long DDT molecules, the CIS/ZnS QDs were covered by trioctylphosphine ligands, which can be concluded to produce more cytotoxic effects, either through the ligand itself, or by increasing cell interaction. A CIS/ZnS QD dosage of 25 μg/slide, the lethal exposure for CdSe QDs, did not result in HeLa death.

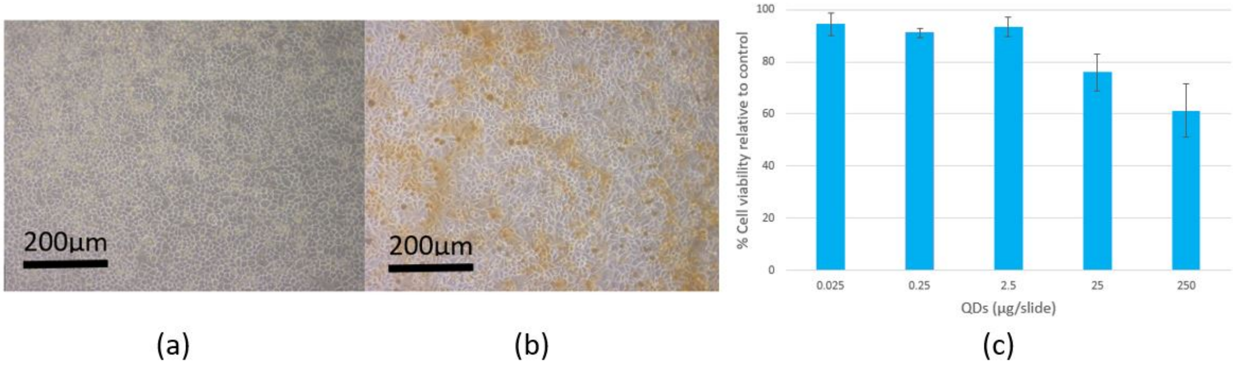

Figure 10.10: Microscopy images of (a) control and (b) HeLa exposed to 250 μg/substrate of synthesized CIS QDs. (c) Relative viability of HeLa exposed to CIS QDs.

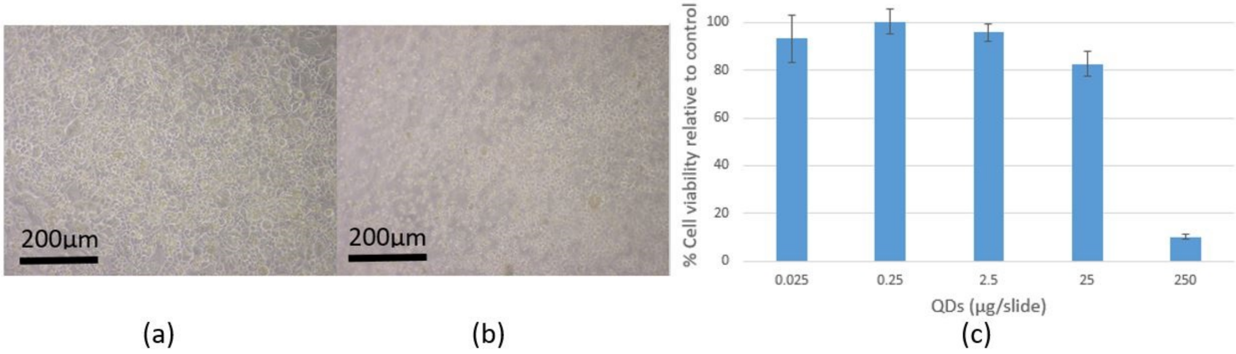

Figure 10.11: Microscopy images of (a) control and (b) HeLa exposed to 250 μg/substrate synthesized CIS/ZnS QDs. (c) Relative viability of HeLa exposed to CIS/ZnS QDs.

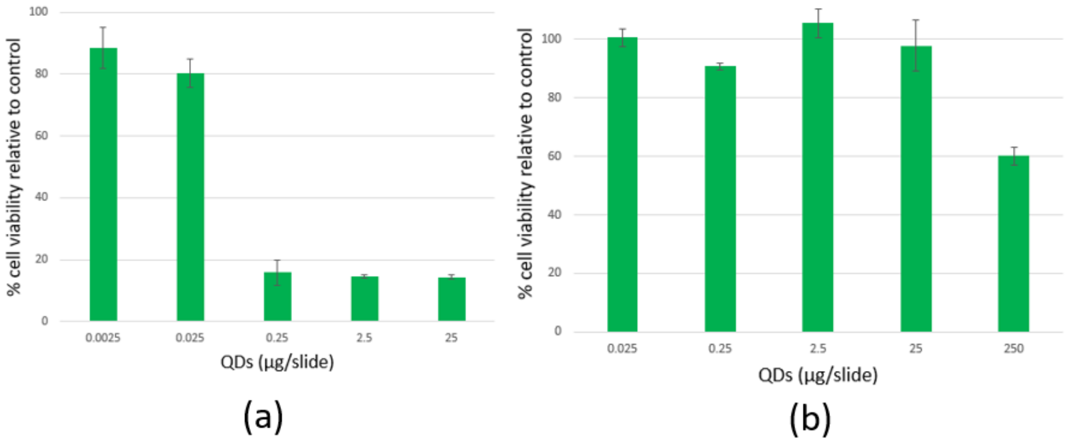

Figure 10.12: Relative viability of CHSE cells exposed to (a) CdSe QDs and (b) CIS QDs.

In the CdSe QD experiments on HeLa, the dosage that typically induced cell death was between 0.25 to 25 μg/slide. When HeLa cells were exposed to CIS QDs at higher concentrations, relative cell viability did not significantly decrease compared to the results of CdSe exposure. Overall, the HeLa cells exposed to CIS QDs remained more viable than those exposed to CdSe QDs. CIS QDs can be concluded to be less biologically toxic compared to CdSe QDs.

10.4.4 QD Cytotoxicity Mechanisms

To explore the effects of QD cytotoxicity on other cell lines, the *in vitro* viability of fish cells (CHSE line) were exposed to ODA-ligated CdSe and DDT-ligated CIS QDs using the method described above. The results from Cytofluor fluorescent plate reading presented in Fig. 10.12 demonstrated that the CHSE cells are slightly more sensitive than Hela cells when exposed to QDs, resulting in overall higher cell death at lower dosage. The response of the CHSE cells were fairly consistent with HeLa; less significant CHSE cell death observed when CIS QDs were used (15.86% relative viability at 0.25 μg/slide for CdSe QDs, 47.77% viability for CIS QDs).

Confocal microscopy was employed to optically examine the interaction between CHSE cells and QDs. CHSE cells were stained with 4',6-diamidino-2-phenylindole (DAPI), a membrane-permeable fluorescent dye that emits a wavelength of 460 nm, then exposed to QDs. CdSe/ZnS QDs with a 560 nm emission, and CIS QDs with 650 nm emission, at

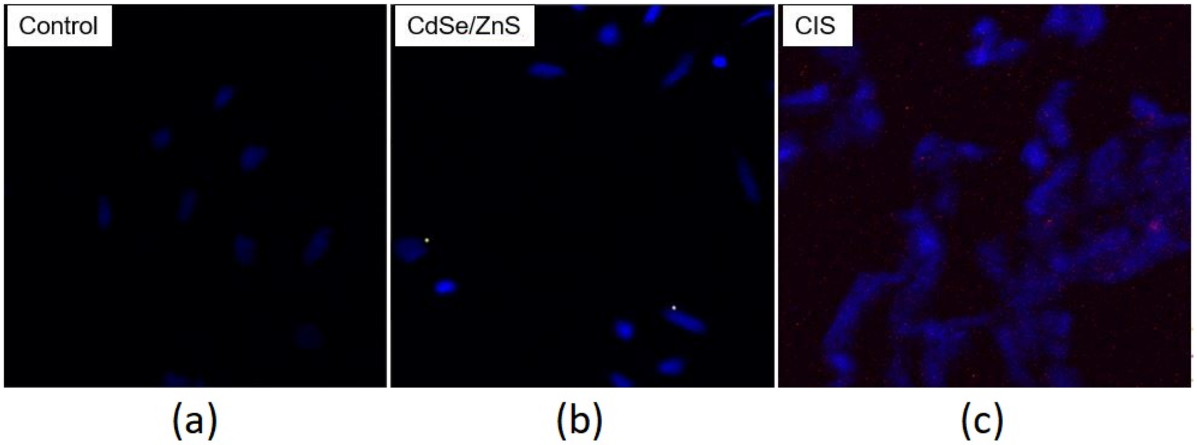

Figure 10.13: Confocal microscope images of (a) CHSE cells stained with DAPI (b) exposed to Cdse/ZnS QDs with 560 nm emission and (c) CIS QDs with 650 nm emission.

a 10^4 dilution in toluene in media, were used. QD emissions were selected to be visually distinct from DAPI, so that the interaction between QDs and cells could be observed. Fig. 10.13 presents the microscope images of the cells with and without QD exposure, excited with a 358 nm light source.

The blue emission stems from the dye-stained CHSE cells, while yellow and red mark the CdSe/ZnS QD and CIS QD locations, respectively. In exposed samples, QDs fluorescence can be seen inside of the cells, suggesting cell uptake of the QDs. This postulates the method of cell toxicity. It is notable that CHSE cells take up CIS QDs as readily as CdSe QDs. This suggests that the lower levels of toxicity obtained from Cytofluor readings for CIS QDs is not a matter of decreased uptake, but lesser toxicity of the core material itself. Therefore, CIS is a safer, less-toxic QD material than CdSe. Further studies of interaction between cells and QDs are required to determine more definitive causes for toxicity; this is beyond the scope of this thesis.

This evaluation of QD materials assisted in elucidating the toxicity of CIS QDs in comparison to widely used CdSe QDs. In conclusion, it was found that the composition of the quantum dot core and ligand was more significant in contributing to cytotoxicity than overcoat and size. The presence of a less-toxic overcoat, such as ZnS or silica, somewhat mitigated the effects of cytotoxicity. From these results, it was concluded that CIS QDs produced less cytotoxic effects on HeLa cells than CdSe QDs at the same concentrations. Therefore, they can be a considered non-toxic, safer material than CdSe for high-throughput synthesis and application to large-area, large-scale processes. This study justifies the pursuit of CIS QDs for this PhD research.

10.5 Detection of QD Degradation and Spread

The toxicity posed by various QD materials were investigated using HeLa and CHSE cell lines, presented in the previous section. However, as the primary objective of this thesis does not concern the biological applications of QDs, *in vitro* cytotoxicity studies cannot be the sole mode of investigation for interaction between workers and QDs in a device fabrication environment. Therefore, the risks of exposure and aerosolization in a QD processing facility must be understood.

Au NPs are useful as adsorbent sensitive materials in sensing technology [66]. The high surface area and adjustable surface modification chemistry of Au NPs allows the formation of a high-affinity material. As a result, Au NPs have been used as colorimetric sensors using the appropriate functional group that can react specifically with heavy metal cations. The optical changes associated with nanoparticle aggregation, and/or local refractive index change, have been exploited as optical sensing methods for the detection of toxins, heavy metals and other environmental pollutants [236]. Au NPs are also used as chemical probes, in which the shift in the surface plasmon resonance (SPR) peak of Au NPs is monitored to detect the presence of specific chemical species [237].

In this study, the detection of aerosolized QDs was experimentally studied by trapping loose QDs using a plasmonic film composed of adsorbent, amine-functionalized gold NPs. Sensor fabrication was simple: the Au NPs in water were drop-cast onto a glass substrate and the solvent was evaporated to form a thin film. A number of QDs varying in composition, structure, size and surface coating were investigated. The Au sensors were placed in environments utilized during QD synthesis, processing, and testing. After a period of exposure, this simple sensor was subject to spectroscopic measurements. As QDs display specific optical characteristics that the Au adsorbents do not share, these properties, as well as plasmon resonant shift and PL quenching from the interaction between QDs and Au NPs, were used to identify their presence on the Au sensors and physiochemical changes when exposed under various degradation conditions, illustrated in Fig. 10.14.

QD processing is typically conducted under carefully controlled environments with little ambient and light exposure, which cause degradation. However, it is inevitable that QDs are exposed to air and light during transport and handling, especially in larger manufacturing environments. Solution-stabilized CdSe QDs have been found to release Cd ions upon oxidation from air or exposure to UV [208]. QD samples were left in ambient atmosphere for up to 3 weeks and exposed to UV for 1 hour, to escalate degradation

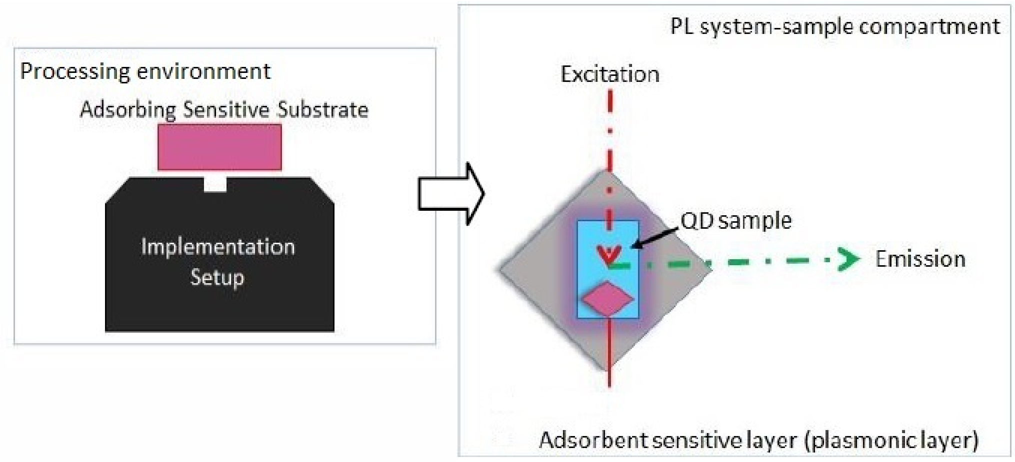

Figure 10.14: Adsorbent sensitive layer following spectroscopic measurement.

and promote aerosolization of heavy metal atoms comprising the QD's structure. Preliminary PL and absorption spectroscopy were performed on CdSe QDs and CdSe QD/Au NP samples to observe the interaction of the QDs and Au NPs [66]. Fig. 10.15 shows the normalized absorption and PL spectra of core CdSe QDs with QA ligands and 600 nm emission peak. Measurements were obtained before and after QDs were exposed to air and UV. The blueshift in absorption and emission peak of the QDs following exposure is indicative of decreased QD size, which corresponds to QD deterioration caused by oxidation. Evident blueshift occurred even after just 45 min of UV exposure. The resonant peak of the gold NPs (inset the Fig. 10.15(a)) red-shifted, indicating nanoscale materials were released from the QDs during exposure. Shifts in SPR peak of Au NPs indicated absorption of toxic elements.

Fig. 10.16(a) shows PL spectra of Au NP samples known to contain CdSe QDs. After exposure to the QDs, the samples were subject to various deterioration conditions. Broad and slightly redshifted peaks corresponding to the QDs' emission wavelength were observed in the PL spectra of the gold layer after QD exposure to ambient and UV illumination.

Fig. 10.16(b) presents the FTIR transmission spectra of Au NPs after QD exposure. Traces of organic ligands (C-H bonds) were detected in FTIR spectra in the 2800-3000 cm^{-1} range, corresponding to the C-H bonds of the OA ligand in the CdSe QDs. From these optical studies, it is apparent that QDs show degradation under ambient and UV exposure. Additionally, exposure of Au NPs to QDs presents a visible change in PL emission, absorption, and FTIR spectra. Therefore, Au NPs are applicable for simple detection of QDs around processes and activities performed around a research lab.

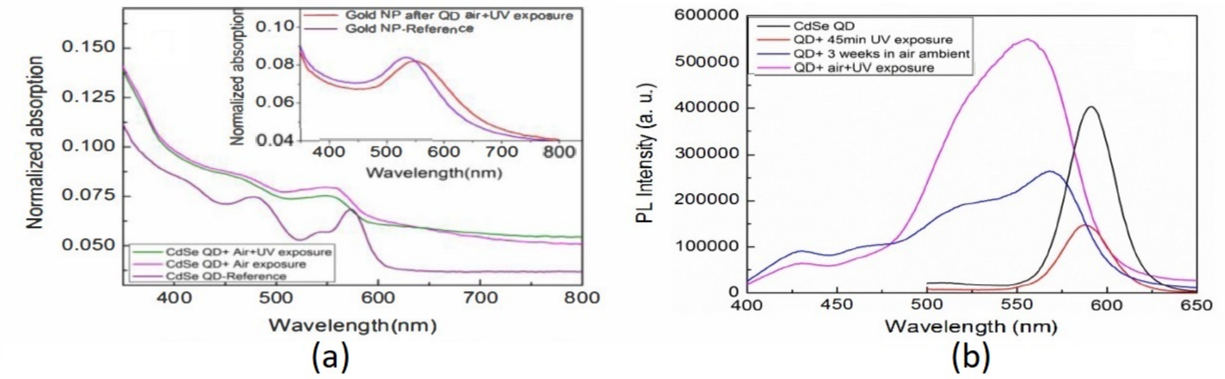

Figure 10.15: (a) Normalized absorption and (b) PL spectra of the core CdSe QDs with OA ligand after ambient and UV exposures. Inset of (a) is the resonant peak of gold NPs after QD exposure.

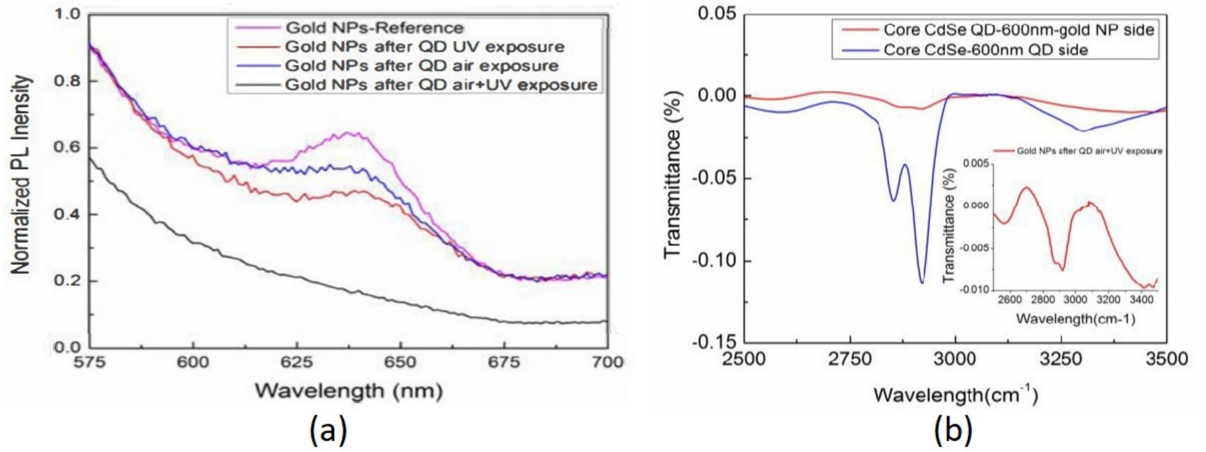

Figure 10.16: (a) PL spectra of adsorbent gold NPs after core QD exposure to ambient and UV illumination. (b) FTIR transmittance spectra of the gold NPs (red) after QD exposure. The Au NPs display the C-H peaks found in the spectra for the reference CdSe QDs, shown in blue.

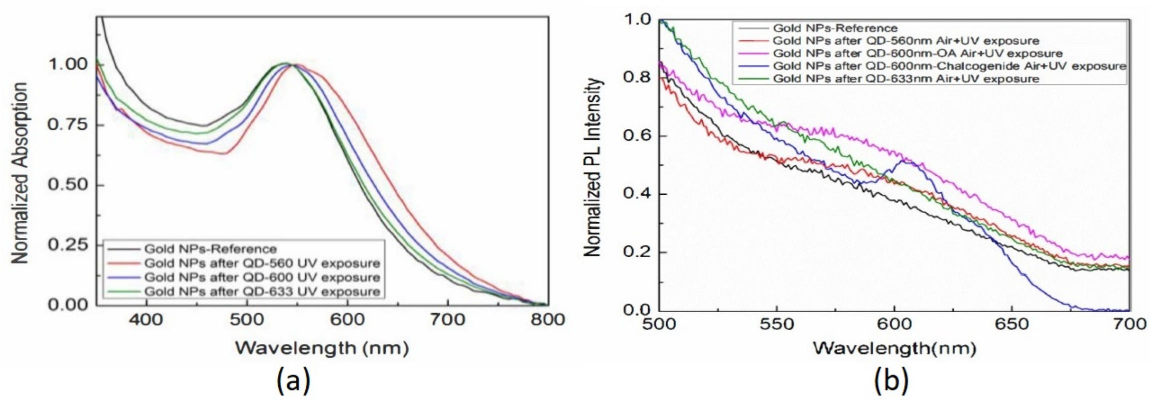

Figure 10.17: (a) Absorption and (b) PL peaks of gold NPs for different sizes core QDs exposed to UV for 30 min.

10.5.1 Effect of QD Size and Ligand on Degradation and Spread

Using the adsorbent Au sensors, the correlation between QD size and exposure were studied. Absorption measurements obtained from various QD sizes are shown in Figure 10.17(a). After QD exposure and degradation, there was a redshift in the gold NPs' absorption peaks, consistent with release of material from QDs. Larger shifts occurred for the smaller size QDs, indicating more material released from the QDs. This suggests that smaller QDs (corresponding to lower wavelength emission) deteriorate more significantly from light degradation, thus causing greater concern of heavy metal exposure.

Fig. 10.17(b) shows the normalized PL spectra obtained on Au NPs after exposure to various QD sizes and degradation conditions. All samples exhibit broad peaks at the QDs' emission wavelengths, distinct from the PL emission spectra of the Au NP reference sample. This corresponds to the redshift in the absorption spectra, verifying its origin to be from QD exposure.

Fig. 10.18 show the PL results obtained for QDs with two different types of ligands: chalcogenide and OA. The pronounced PL quenching of QDs with chalcogenide ligands indicate less stability than OA-stabilized QDs. The PL emission spectra of Au NPs with and without QD exposure are also included in the insets, showing both types of QDs to cause changes in the Au NP's spectra. The additional QD emission peak was more pronounced in the chalcogenide-ligated sample. Notably, in the cell studies, chalcogenide-ligated QDs were found to be comparatively less toxic than OA-ligated QDs. However, the observation of the QDs' effect on the Au NPs indicate a breakdown of the QD structure

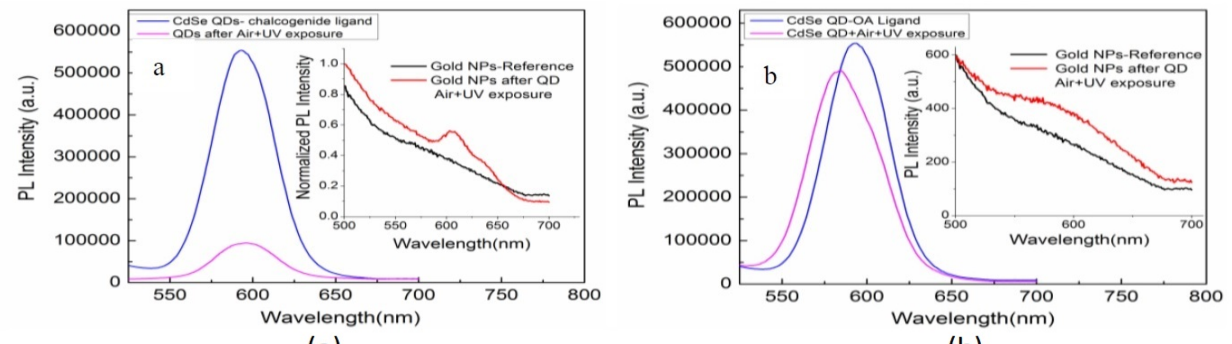

(a) (b)

Figure 10.18: PL spectra of (a) Chalcogenide- and (b) OA-ligated core QDs after ambient and UV exposure. Insets are the absorption peaks of gold NPs after QD exposures.

into its toxic heavy metal components, which eliminated the relative protection afforded by the ligands encasing the whole QD structure.

10.5.2 Core/Shell QD Degradation and Potential Spread

The degradation of core/shell CdSe/ZnS QD were investigated. The core/shell structures were generally stable when they are fresh; no trace of QDs was detected after short-period exposure to UV and air. However, after 10 days of exposure in air, traces of QDs were observed on the Au NPs when subject to the similar spectroscopic investigation presented in the previous subsection.

Au NPs were exposed to ODA- and OA-ligated core/shell CdSe/ZnS QDs, then degraded with air and UV. The ODA-ligated core/shell QDs were not detected on Au NPs after 3 weeks of air exposure and 1 hour of UV exposure, indicating it to be fairly stable, as it either evaded capture by the Au sensor, or did not release material from its lattice. However, absorption (Fig. 10.19(a)) and PL (see Fig. 10.19(b)) measurements of the OA-ligated core/shell QD samples showed changes in the Au NPs' spectra, 10 days of ambient exposure, indicating QD degradation and release of material. Various QD sizes were explored, with smaller QDs causing larger shifts in absorption. Thus, similar to core QDs, ligand and size affects degradation and spread in core/shell QDs, albeit with better stability provided by the shells.

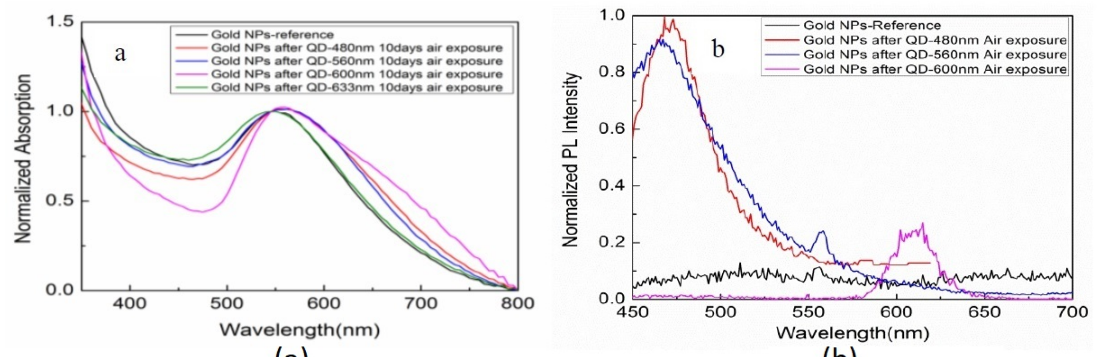

(a) (b)

Figure 10.19: (a) Absorption and (b) PL peaks of gold NPs deposited in vicinity of QD layer after OA-ligated core/shell QDs with different sizes exposed to ambient for 10 days.

10.6 Exposure in QD Processing Environments

Since their inception, QDs have been envisioned for a variety of industrial applications, in which their production and handling reaches a volume far exceeding the scale implemented in research lab environments. Even if the source material does not pose strong toxicity concerns, efforts must be made to minimize QD exposure and spread. As nanoparticles are difficult to remove from the human body due to their size and physiology, the methodologies and equipment utilized in QD processing and handling must be carefully evaluated to minimize exposure.

Previous sections explored the biological toxicity and ease of spread of various QDs. It was determined that CIS QDs are relatively less toxic than CdSe-based QDs, and that ligand and shell plays a role in imparting toxicity. Additionally, it was found that the size, ligand, and coating of QDs affect the ease of degradation, which influences the release and spread of the core heavy metal components of toxic CdSe QDs. However, regardless of a QDs' toxicity and proclivity for spread, exposure-reducing processes and setups should be implemented when possible. QDs and NPs are fairly difficult to quantitatively detect, as their small sizes (typically 2-20 nm) preclude them from detection using typical particle counting methods. Using the Au NP sensor presented previously, this section presents simple strategies for detection of QDs in processing environments, which can be implemented as preliminary tests to indicate the presence of airborne QDs and effectiveness of containment. The simple toxicity investigations proposed here focuses on three main areas of QD processing: synthesis, implementation, and characterization.

10.6.1 Detection of Spread During QD Film Processing

As discussed in earlier portions of this thesis, drop-casting, spin-coating, and drop-casting are the most methods for forming QD films from CQD in solvent in laboratory environments. Drop-casting is simple: QD solution is deposited onto a flat substrate, and the solvent is dried, leaving a layer of QDs. The main risk of exposure arises during evaporation, in which QDs may be carried with the evaporating solvent. Worker exposure is mitigated through the use of containment modules, such as glove box or fume hood. Spin-casting uses centripetal force and angular momentum; QD solution is deposited onto a flat substrate, which is quickly rotated to create uniform, reproducible films [11]. There is significant spread and exposure due to flinging of the QD solution; this can be diminished through the use of spin-coating systems with better containment (coverings and high side walls around the spinning chuck). Dip-coating entails speed-controlled withdrawal of a substrate from a solution; this method poses the least risk of exposure. Although there is some concern of spread via solution evaporation, this can be prevented with good containment of the QD-containing components. QD aerosolization during spin-casting, drop-casting, and dip-coating were investigated.

A Larell Technologies Corporation spin-coating system with Model WS-400B-6NPP-Lite Processor controller was utilized for spin-coating of QD samples. Due to having a fitted covering and deep side walls, this spin-coater prevents spread compared to typical spin-coating setups. A glass substrate was placed over a small opening on the cover, then CdSe QDs with 610 nm emission was spin-cast onto a separate substrate using the system. Fig. 10.20(a) presents the PL of the detector after 10 coats of spin-cast QDs. There is an apparent peak at 610 nm, corresponding with the emission of the spin-cast QDs, thus indicating aerosolization of QDs and exposure even outside of the containment area.

To prevent QD exposure to ambient conditions, QD processing is typically performed under contained environments such as glove boxes. In particular, drop-casting is completed under such containment, to prevent spread and QD degradation from ambient. Samples of glass and Au NP sensors were situated as QD indicators under a fume hood used for QD synthesis and sample preparation, for a month. PL measurements, shown in Fig. 10.20(b), indicate QDs traces, thus confirming aerosolization of QDs. QDs were only detected on samples with gold NPs, which the QDs adhere to more readily than glass.

To investigate QD aerosolization during dip-coating, a glass sample was placed vertically on top of a dip coater vessel (KSV NIMA) containing CdSe QDs in hexane. The distance between the bottom of the sample and top of the vessel was maintained at 2 cm. The setup was left overnight in this position to allow adsorption of aerosolized QDs from the vessel. The PL spectra indicate presence of QDs on this sample (Fig. 10.20(c)). QDs were

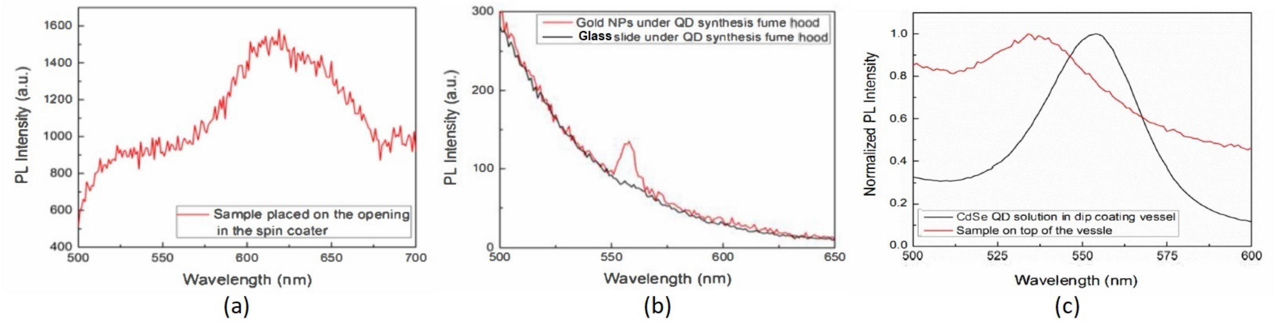

Figure 10.20: PL spectra of (a) glass after 10 rounds of spin coating CdSe QDs, (b) glass and gold NPs samples placed in synthesis fume hood for 30 days, (c) glass samples placed in vicinity of dip-coater for 24 h.

detected on all sensor samples, indicating all three common QD film formation methods to provide some degree of aerosolization and exposure risk. Thus, greater containment protocols must be implemented when completing these QD processes.

Results from PL show that when placed in proximity of adsorbent Au NPs, some traces of aerosolized QD adsorbed onto Au NPs are detected during QD film formation. Therefore, aerosolization of QDs is a concern for workers that handle QDs, or work in environments for QD synthesis, processing, and testing.

10.7 Conclusions

The work presented in this chapter emphasizes the need for safety considerations in nanomaterials processing and proposes a pathway to safely scale up nanomaterials manufacturing and integration during the research and development phase. Creating rigorous and quantitative approaches to handling QD and nanomaterial exposure risks in a research setting ensures the safety of researchers and provides groundwork for establishing safe manufacturing practices at the industrial scale. *In vitro* viability was examined with HeLa cell cultures, showing CdSe-containing QDs to impart some biological toxicity regardless of overcoating, size, and ligand. The results indicate that QD material and their surface functionalizations are important factors in determining cytotoxicity effects. It was also demonstrated that CIS QDs have less cytotoxic effects than CdSe QDs, and may be considered less-toxic in comparison, justifying their use in this research. Process studies were conducted to investigate the risk of environment exposure to toxic QDs in device processing. Evidence on the detection of aerosolized nanoparticles was experimentally verified using gold NP adsorbent, followed by spectroscopic and elemental detection. This study qualitatively showed the presence of small traces of aerosolized QDs components adsorbed onto Au NPs using absorption and PL spectroscopy. As QDs aerosolization was determined to have occurred during spin-coating, drop-casting, and dip-coating, further containment strategies must be implemented going forward. These studies highlight the necessity of carefully considering actions and designs to mitigate potential exposure, both at the research and prototyping level. The results presented in this chapter were pivotal to the development and evaluation of the synthesis and fabrication techniques utilized in this thesis, with consideration towards future large-sale QD device production.

Chapter 11

Conclusions and Outlook

11.1 Conclusions

This doctoral work presented a methodology for facile, high-throughput synthesis for less-toxic CIS and ZCIS QDs, and the development of reliable, standardized processes for fabrication of photodetector and photovoltaic devices based on these QDs. First, core CIS CQDs were synthesized using a one-pot method in a low-temperature regime. The processes yielded QDs with a wide range of tunability in the visible-to-IR spectrum, along with intense PL and long-lived emission. As much as 800 mg of QDs were obtained through this scalable, solution-based process, circumventing typical QD synthesis issues such as hot-injection and insufficient production. The CIS QDs were overcoated in a controlled, solution-based process to create CIS/ZnS core/shell QDs with intense PL and long lifetimes. Overcoating achieved better stability and more flexibility in QD emission and absorption properties.

The effect of precursor composition on core and core/shell QDs growth were systematically investigated. Various molar ratios of Cu:In and Zn:S were employed to control the structure and optical properties of the resultant QDs. For core CIS QDs, it was observed that inducing a cationic Cu^+ deficiency resulted in improved optical properties, attributed to the creation of additional radiative recombination pathways. In core/shell QDs, it was found that the use of precursor ratios with excess Zn^{2+} produced enhanced PL emission and lifetime. The best QDs were obtained with a 1:2 Cu:In ratio. Further Cu deficiencies were found to be disadvantageous to QD properties, attributed to weakening of the lattice structure. A Zn-rich Zn:S ratio of 8:1 was determined to have the best effect on QD lifetimes, while 4:1 produced the most intense PL. ZnS overcoating of CIS cores incorporated Zn^{2+} cations within the core, stabilizing the lattice and blueshifting emission. Furthermore, surface passivation reduced non-radiative recombination pathways, leading to enhanced emission. These results demonstrated that reactant composition contribute to QD bandgap and optical characteristics as significantly as QD size. The elucidation of enhanced radiative recombination in Cu-deficient core QDs and Zn inter-diffusion and lattice passivation were the most significant results obtained in these studies.

The effect of synthesis temperature and temperature ramping on QD properties were also studied. It was found that a gradual increase of reaction temperature was significant to producing the best results, as it provided sufficient energy and time to allow atoms to traverse to the most favourable positions within the QD lattice. Gradient T-ramps not only resulted in core CIS QDs with more ligand coverage and fewer defects, but also made it possible to produce high-quality CIS/ZnS QDs even with lower Zn:S molar ratios in the precursor. Gradual, dropwise incorporation and prolonging the overcoating process were also significant in maintaining monodispersity within the core/shell QD solution. A PLQY of 10% was achieved for 1:2 CIS core QDs grown with gradient temperature ramp. Core/shell CIS/ZnS QDs with PLQY of 20% was obtained at an overcoating temperature of 160°C. The long-lived emission achieved in these CIS-based QDs made them promising for device applications. The low-T regime processes, lower toxicity, and tunability of these CIS QDs made them compatible with large-area, scaled-up fabrication.

The formation of CIS QD solids was investigated for the purpose of device fabrication. Ligand exchange was successfully carried out, replacing the as-synthesized DDT ligands with short, bifunctional MPA ligands. Although the as-synthesized ligands were vital to the one-pot synthesis, their long, apolar nature hindered QD film formation and carrier transport. Both DDT- and MPA-ligated CIS QDs were applied to a ZnO/CIS QD heterojunction diodes. Comparison of the I-V behaviour of both DDT-ligated and MPA-ligated QD devices proved the suitability of the latter for device implementation and the importance of the ligand exchange process. While the device based on MPA-ligated QDs showed desirable diodic I-V behaviour, the DDT-ligated QD device suffered from shorting, attributed to the non-uniform, agglomerated films that lacked substrate coverage.

Inspired by the development of CIS and CIS/ZnS QDs, a low-temperature, high-throughput, scalable synthesis process was developed for Zn-alloyed CIS QDs, or ZCIS QDs. This process was developed to reap the benefits of Zn incorporation in stabilizing and enhancing CIS QDs, without introducing issues of carrier confinement and transport. Over 900 mg of brightly photoluminescent ZCIS QDs were produced using the synthesis process, which allowed for flexible tunability in the visible range. Variation of cationic stoichiometry was also studied, and similar to CIS, it was found that induction of Cu deficiency through In or Zn-excess precursor ratios was most effective in enhancing optical properties. The QDs were further functionalized via ZnS overcoating, although this was found to produce less improvement than overcoating of ternary CIS QDs.

MPA-ligated CIS QDs were applied towards investigation of various QD solid formation methodologies, including spin-casting, dip-coating, and drop-casting. It was determined that QD absorber films require a trade-off between uniformity and layer thickness; with the former being significant for promoting effective carrier transport, and the latter critical for photon absorption and carrier creation. Compared to other techniques, dip-coating was found to result in the most uniform QD films with the least defects, and was used to further develop the formation of regular, self-assembled CIS QD films. Drop-casting was found to result in the best QD loading. The results of this study were applied towards the fabrication of a preliminary, large-area, ZnO/CIS QD heterojunction photodetector devices. The photodetector showed sensitivity to visible and ultraviolet illumination, beyond the capability of silicon-based photodetectors.

As the many dubious procedures employed in the fabrication of novel, nanomaterials-based research devices pose significant questions regarding the validity of their performance, a reliable, repeatable fabrication procedure was developed for small-area CIS QD devices on standard cm-scale substrates. Photolithography and shadow masks were employed to define the area and architecture of the device. The fabrication procedures were designed to be compatible with standard, industry fabrication technology, streamlining the transition from research to production. A QD injection system was also designed to define the QD area and conformation in a repeatable manner. Developing the QD photodetector design through standardized fabrication processes allowed focus on enhancing significant parameters of photodetector performance, without lingering on questionable aspects of the fabrication procedure. ZnO/CIS QD heterojunction photodetectors with strong response to illumination, and high ON-OFF ratios were reliably produced. Finally, assessments of the *in vitro* toxicity and QD uptake probability were made. Risks of QD aerosolization and worker exposure in research and production facilities were evaluated, and the findings were applied to analyze the design of equipment and processes in this research. This work highlighted the necessity of standardizing design to mitigate process ambiguity, even at the research and prototyping level. The creation of rigorous and repeatable processes from materials synthesis to device assembly, with a focus on minimizing exposure, provides a pathway to compatibility with VLSI manufacturing processes used for commercial production. Consideration of up-scaling and production at the research and prototyping of novel technology is critical in ensuring a safe nanotechnological future.

11.2 Outlook and Future Work

This section presents recommendations for continued expansion of the work presented in this thesis. Through investigation of these areas, the material quality, film quality, process applicability, and ultimately, device performance will be improved.

SU-8 Enhancement

In this work, significant effort was put forth in developing the SU-8 insulator, which is a critical aspect of the device architecture. In particular, SU-8 encountered notable challenges in adhesion onto ZnO. Exposure at higher dosages aided in adhesion, but resulted in some weakening of the SU-8 structure. Exploration of appropriate linkers and adhesion promoters, such that lower dose exposure can be used, is worthy in improving the SU-8 stability, and subsequently, device performance. Linkers must be carefully selected to avoid interfering with device performance.

Bulk Heterojunction and Increased QD Loading

This work presented a planar, solid-state ZnO/CIS QD heterojunction device. The development of a bulk heterojunction device may enhance device performance through increased charge separation and QD loading. One method of achieving this is the incorporation of the CQD solution with the ZnO sol-gel solution. Inducing porosity onto sputtered ZnO is another avenue to accomplish the possibility of bulk heterojunction formation and increased QD loading. Although ZnO nanoparticles were not used in this work, their incorporation into the device, whether as a planar or bulk heterojunction architecture, is also a promising path of future development.

QD Size Optimization

In device development, the use of large QDs is desirable, as fewer QDs must be arranged to cover a unit area. Furthermore, larger QDs show more sensitivity to infrared illumination. In this work, visible and UV-detection were primarily investigated. The synthesis and application of larger CIS-based QDs is valuable for development of CIS-based IR QD photodetectors. The use of ZCIS QDs in achieving the device architecture is also worthy of investigation.

Surface and Ligand Optimization

This work utilized MPA to replace DDT and facilitate QD film formation and ZnO/QD interface creation. MPA was chosen due to sharing a thiol terminal group with DDT, allowing anchoring to the QD, while possessing a polar carboxylic terminal group to anchor onto ZnO. Other ligands, such as thioglycolic acid, thioacetic acid, or the biologically benign mercaptoacetic acid, show the same properties, but are shorter in length(one- to-two-hydrocarbon chain rather than three-hydrocarbon chain). This may be more advantageous for device formation, as the barrier to carrier transport is reduced.

CIS/ZnS QDs were produced in this work, but their Type I alignment was deemed unfit for device formation, due to concerns with carrier transport. Although Type II core/shell configurations are advantageous in selective carrier confinement for photodetector applications, the lack of a readily available CIS-based Type II core/shell QD precluded their utility in this work. Therefore, the development of Type II CIS-based core/shell QDs are a worthy area of investigation.

Alternative Metal Oxides

ZnO/QD heterojunctions are significant in photodetector and photovoltaic devices, as they have been employed successfully in high-performance planar QD device architectures. However, investigation of metal oxides such as aluminum zinc oxide and TiO_2, which show higher conductivity and allow for increased QD loading, may enhance device performance.

Device Architectures

The devices presented in this work utilized ZnO/CIS QD metal oxide/QD heterojunctions. A p-i-n structure, in which an intrinsic material is placed between the n-type ZnO and p-type CIS QDs, could result in faster device response, better carrier transport, and enhanced performance. Furthermore, other works have reported the use of QD/QD heterojunctions, in which interfaces are formed from the same type of QD, with variation in doping, induced mainly by surface optimization. The reduced layer incompatibility and enhanced carrier transport from such architectures are also worthy of investigation.

Metallic Shielding

The use of Al shielding in the 5 μm-diameter device was employed, with effort to concentrate illumination onto the active device area, and reduce excitation in other parts of the device. The incompatibility of Al with the developed fabrication process precluded its inclusion as a part of the established fabrication process. Systematic investigation of other metals and metallic alloys, to determine a compatible material, is a worthy undertaking. The implementation of light focusing and metallic shielding would significantly enhance the reliability of the fabrication process.

Novel Cupric Chalcopyrite QDs

This work focuses on CIS, ZCIS, CIS/ZnS, and ZCIS/ZnS QDs, with the former primarily employed in device architectures. Within the world of cupric chalcopyrite QDs, copper indium selenide QDs have also been successfully employed in high-performance photodetectors and photovoltaics. However, the toxicity of selenium creates significant concerns in use of CISe QDs. Although CIS- and ZCIS-based QDs are toxicologically benign, the use of In is increasingly problematic, due to its high cost and low availability, with its supply already exacerbated by the use of ITO in industry. Copper zinc tellurium (CZT) QDs are a promising alternative that displays the advantageous tunability and optical properties of cupric chalcopyrites. Notably, tellurium is mildly toxic, and further toxicity studies must be undertaken before its implementation. CZT QDs have so far not been significantly investigated, and are a novel, intriguing material of study. The development of alternative CIGS and other related compositions, to simultaneously optimize performance and sustainability, would be significantly beneficial to the future of consumer nanodevices.

References

[1] D. V. Talapin, J.-S. Lee, M. V. Kovalenko, and E. V. Shevchenko, “Prospects of colloidal nanocrystals for electronic and optoelectronic applications,” *Chemical reviews*, vol. 110, no. 1, pp. 389–458, 2009.

[2] L. Li, A. Pandey, D. J. Werder, B. P. Khanal, J. M. Pietryga, and V. I. Klimov, “Efficient synthesis of highly luminescent copper indium sulfide-based core/shell nanocrystals with surprisingly long-lived emission,” *Journal of the American Chemical Society*, vol. 133, no. 5, pp. 1176–1179, 2011.

[3] C. R. Kagan, E. Lifshitz, E. H. Sargent, and D. V. Talapin, “Building devices from colloidal quantum dots,” *Science*, vol. 353, no. 6302, p. aac5523, 2016.

[4] D. Bera, L. Qian, T.-K. Tseng, and P. H. Holloway, “Quantum dots and their multimodal applications: a review,” *Materials*, vol. 3, no. 4, pp. 2260–2345, 2010.

[5] P. R. Brown, D. Kim, R. R. Lunt, N. Zhao, M. G. Bawendi, J. C. Grossman, and V. Bulovic, “Energy level modification in lead sulfide quantum dot thin films through ligand exchange,” *ACS nano*, vol. 8, no. 6, pp. 5863–5872, 2014.

[6] C. B. Murray, a. C. Kagan, and M. Bawendi, “Synthesis and characterization of monodisperse nanocrystals and close-packed nanocrystal assemblies,” *Annual review of materials science*, vol. 30, no. 1, pp. 545–610, 2000.

[7] S. A. Ivanov, A. Piryatinski, J. Nanda, S. Tretiak, K. R. Zavadil, W. O. Wallace, D. Werder, and V. I. Klimov, “Type-ii core/shell Cds/Znse nanocrystals: Synthesis, electronic structures, and spectroscopic properties,” *Journal of the American Chemical Society*, vol. 129, no. 38, pp. 11708–11719, 2007.

[8] K. Ghaffarzadeh, “Quantum dot materials and technologies 2020–2030: Trends, markets, players,” 2020.

[9] T. Research, “Global quantum dots market,” 2019.

[10] C.-C. Lin, “Hybrid optoelectronic devices with colloidal quantum dots,” in *Quantum Dot Solar Cells*, pp. 67–90, Springer, 2014.

[11] J. Yang, M. K. Choi, D.-H. Kim, and T. Hyeon, “Designed assembly and integration of colloidal nanocrystals for device applications,” *Advanced materials*, vol. 28, no. 6, pp. 1176–1207, 2016.

[12] J. Duan, H. Zhang, Q. Tang, B. He, and L. Yu, “Recent advances in critical materials for quantum dot-sensitized solar cells: a review,” *Journal of Materials Chemistry A*, vol. 3, no. 34, pp. 17497–17510, 2015.

[13] S.-W. Baek, S. Jun, B. Kim, A. H. Proppe, O. Ouellette, O. Voznyy, C. Kim, J. Kim, G. Walters, J. H. Song, *et al.*, “Efficient hybrid colloidal quantum dot/organic solar cells mediated by near–infrared sensitizing small molecules,” *Nature Energy*, vol. 4, no. 11, pp. 969–976, 2019.

[14] M. Hao, Y. Bai, S. Zeiske, L. Ren, J. Liu, Y. Yuan, N. Zarrabi, N. Cheng, M. Ghasemi, P. Chen, *et al.*, “Ligand-assisted cation-exchange engineering for high-efficiency colloidal $\mathrm{Cs_{1-x}FA_xPbI_3}$ quantum dot solar cells with reduced phase segregation,” *Nature Energy*, vol. 5, no. 1, pp. 79–88, 2020.

[15] E. M. Sanehira, A. R. Marshall, J. A. Christians, S. P. Harvey, P. N. Ciesielski, L. M. Wheeler, P. Schulz, L. Y. Lin, M. C. Beard, and J. M. Luther, “Enhanced mobility $\mathrm{CsPbI_3}$ quantum dot arrays for record-efficiency, high-voltage photovoltaic cells,” *Science advances*, vol. 3, no. 10, p. eaao4204, 2017.

[16] C.-H. M. Chuang, P. R. Brown, V. Bulović, and M. G. Bawendi, “Improved performance and stability in quantum dot solar cells through band alignment engineering,” *Nature materials*, vol. 13, no. 8, p. 796, 2014.

[17] D. C. Reifsnyder, X. Ye, T. R. Gordon, C. Song, and C. B. Murray, “Three–dimensional self–assembly of chalcopyrite copper indium diselenide nanocrystals into oriented films,” *ACS nano*, vol. 7, no. 5, pp. 4307–4315, 2013.

[18] J. P. Clifford, G. Konstantatos, K. W. Johnston, S. Hoogland, L. Levina, and E. H. Sargent, “Fast, sensitive and spectrally tuneable colloidal-quantum-dot photodetectors,” *Nature nanotechnology*, vol. 4, no. 1, pp. 40–44, 2009.

[19] R. Sliz, M. Lejay, J. Z. Fan, M.-J. Choi, S. Kinge, S. Hoogland, T. Fabritius, F. P. García de Arquer, and E. H. Sargent, "Stable colloidal quantum dot inks enable inkjet–printed high-sensitivity infrared photodetectors," *ACS nano*, vol. 13, no. 10, pp. 11988–11995, 2019.

[20] D. Qi, M. Fischbein, M. Drndić, and S. Šelmić, "Efficient polymer-nanocrystal quantum-dot photodetectors," *Applied Physics Letters*, vol. 86, no. 9, p. 093103, 2005.

[21] S. McDonald, P. Cyr, L. Levina, and E. Sargent, "Photoconductivity from PbS-nanocrystal/semiconducting polymer composites for solution-processible, quantum-size tunableinfrared photodetectors," *Applied physics letters*, vol. 85, no. 11, pp. 2089–2091, 2004.

[22] I. Zharikov, R. Davydov, V. Lyapishev, V. Y. Rud, Y. V. Rud, and A. Glynushkin, "Features of the induced photopleochroism oscillations in a photosensitive structures based on $CuInSe_2$," in *Journal of Physics: Conference Series*, vol. 917, p. 052011, IOP Publishing, 2017.

[23] I. E. Agency, "Technology roadmap: Solar photovoltaic energy," 2014.

[24] G. Konstantatos and E. H. Sargent, "Solution–processed quantum dot photodetectors," *Proceedings of the IEEE*, vol. 97, no. 10, pp. 1666–1683, 2009.

[25] A. Nozik, "Nanoscience and nanostructures for photovoltaics and solar fuels," *Renew. Sustainable Energy Rev.*, vol. 10, no. 8, pp. 2735–2741, 2010.

[26] A. Berbezier and F. Michelin, "Modeling of quantum dot junction for third generation solar cell," *Thin Solid Films*, vol. 543, pp. 16–18, 2013.

[27] P. V. Kamat, "Quantum dot solar cells. the next big thing in photovoltaics," *The journal of physical chemistry letters*, vol. 4, no. 6, pp. 908–918, 2013.

[28] H. Zamani Siboni, B. Sadeghimakki, S. Sivoththaman, and H. Aziz, "Very high brightness quantum dot light-emitting devices via enhanced energy transfer from a phosphorescent sensitizer," *ACS applied materials & interfaces*, vol. 7, no. 46, pp. 25828–25834, 2015.

[29] A. Litvin, I. Martynenko, F. Purcell-Milton, A. Baranov, A. Fedorov, and Y. Gun'Ko, "Colloidal quantum dots for optoelectronics," *Journal of Materials Chemistry A*, vol. 5, no. 26, pp. 13252–13275, 2017.

[30] K. Qiao, H. Deng, X. Yang, D. Dong, M. Li, L. Hu, H. Liu, H. Song, and J. Tang, "Spectra–selective PbS quantum dot infrared photodetectors," *Nanoscale*, vol. 8, no. 13, pp. 7137–7143, 2016.

[31] B. Sadeghimakki, Y. Zheng, N. M. Jahed, and S. Sivoththaman, "Synthesis of CIS quantum dots in low-temperature regime: Effects of precursor composition and temperature ramps," *IEEE Transactions on Nanotechnology*, vol. 16, no. 4, pp. 659–666, 2017.

[32] C. R. Kagan and C. B. Murray, "Charge transport in strongly coupled quantum dot solids," *Nature nanotechnology*, vol. 10, no. 12, p. 1013, 2015.

[33] A. R. Izadpour, H. D. Jahromi, and M. H. Sheikhi, "Plasmonic enhancement of colloidal quantum dot infrared photodetector photosensitivity," *IEEE Journal of Quantum Electronics*, vol. 54, no. 3, pp. 1–7, 2018.

[34] A. J. Labelle, S. M. Thon, S. Masala, M. M. Adachi, H. Dong, M. Farahani, A. H. Ip, A. Fratalocchi, and E. H. Sargent, "Colloidal quantum dot solar cells exploiting hierarchical structuring," *Nano letters*, vol. 15, no. 2, pp. 1101–1108, 2015.

[35] J. Du, Z. Du, J.-S. Hu, Z. Pan, Q. Shen, J. Sun, D. Long, H. Dong, L. Sun, X. Zhong, *et al.*, "Zn–Cu–In–Se quantum dot solar cells with a certified power conversion efficiency of 11.6%," *Journal of the American Chemical Society*, vol. 138, no. 12, pp. 4201–4209, 2016.

[36] R. Guo, T. Shen, and J. Tian, "Broadband hybrid organic/$CuInS_2$ quantum dot photodetectors," *Journal of Materials Chemistry C*, vol. 6, no. 10, pp. 2573–2579, 2018.

[37] A. M. Smith, A. M. Mohs, and S. Nie, "Tuning the optical and electronic properties of colloidal nanocrystals by lattice strain," *Nature nanotechnology*, vol. 4, no. 1, p. 56, 2009.

[38] A. M. Smith and S. Nie, "Semiconductor nanocrystals: structure, properties, and band gap engineering," *Accounts of chemical research*, vol. 43, no. 2, pp. 190–200, 2009.

[39] Y. Chong, Y. Ma, H. Shen, X. Tu, X. Zhou, J. Xu, J. Dai, S. Fan, and Z. Zhang, "The in vitro and in vivo toxicity of graphene quantum dots," *Biomaterials*, vol. 35, no. 19, pp. 5041–5048, 2014.

[40] R. Smith and T. Giorgio, "Quantitative measurement of multifunctional quantum dot binding to cellular targets using flow cytometry," *Cytometry Part A: The Journal of the International Society for Advancement of Cytometry*, vol. 75, no. 5, pp. 465–474, 2009.

[41] B. Sadeghimakki, N. M. Jahed, and S. Sivoththaman, "Spectrally resolved dynamics of synthesized CdSe/Zns quantum dot/silica nanocrystals for photonic down-shifting applications," *IEEE Transactions on Nanotechnology*, vol. 13, no. 4, pp. 825–834, 2014.

[42] S. Jun, J. Lee, and E. Jang, "Highly luminescent and photostable quantum dot–silica monolith and its application to light-emitting diodes," *Acs Nano*, vol. 7, no. 2, pp. 1472–1477, 2013.

[43] B. Pejova, "Optical absorption of semiconductor quantum dot solids," *Semiconductor Science and Technology*, vol. 29, no. 4, p. 045007, 2014.

[44] J. Luo, H. Wei, Q. Huang, X. Hu, H. Zhao, R. Yu, D. Li, Y. Luo, and Q. Meng, "Highly efficient core–shell $CuInS_2$–Mn doped CdS quantum dot sensitized solar cells," *Chemical Communications*, vol. 49, no. 37, pp. 3881–3883, 2013.

[45] V. Sukhovatkin, S. Hinds, L. Brzozowski, and E. H. Sargent, "Colloidal quantum–dot photodetectors exploiting multiexciton generation," *Science*, vol. 324, no. 5934, pp. 1542–1544, 2009.

[46] A. J. Nozik, "Multiple exciton generation in semiconductor quantum dots," *Chemical Physics Letters*, vol. 457, no. 1-3, pp. 3–11, 2008.

[47] Z. Ren, J. Sun, H. Li, P. Mao, Y. Wei, X. Zhong, J. Hu, S. Yang, and J. Wang, "Bilayer PbS quantum dots for high–performance photodetectors," *Advanced materials*, vol. 29, no. 33, p. 1702055, 2017.

[48] S. L. Diedenhofen, D. Kufer, T. Lasanta, and G. Konstantatos, "Integrated colloidal quantum dot photodetectors with color-tunable plasmonic nanofocusing lenses," *Light: Science & Applications*, vol. 4, no. 1, p. e234, 2015.

[49] S. E. Keuleyan, P. Guyot-Sionnest, C. Delerue, and G. Allan, "Mercury telluride colloidal quantum dots: Electronic structure, size-dependent spectra, and photocurrent detection up to 12 μm," *ACS nano*, vol. 8, no. 8, pp. 8676–8682, 2014.

[50] S. Yakunin, D. N. Dirin, L. Protesescu, M. Sytnyk, S. Tollabimazraehno, M. Humer, F. Hackl, T. Fromherz, M. I. Bodnarchuk, M. V. Kovalenko, *et al.*, "High infrared photoconductivity in films of arsenic–sulfide–encapsulated lead–sulfide nanocrystals," *ACS nano*, vol. 8, no. 12, pp. 12883–12894, 2014.

[51] M. Yuan, M. Liu, and E. H. Sargent, "Colloidal quantum dot solids for solution-processed solar cells," *Nature Energy*, vol. 1, no. 3, p. 16016, 2016.

[52] K. Zhao, Z. Pan, and X. Zhong, "Charge recombination control for high efficiency quantum dot sensitized solar cells," *The journal of physical chemistry letters*, vol. 7, no. 3, pp. 406–417, 2016.

[53] C. Steinhagen, M. G. Panthani, V. Akhavan, B. Goodfellow, B. Koo, and B. A. Korgel, "Synthesis of Cu_2ZnSnS_4 nanocrystals for use in low-cost photovoltaics," *Journal of the American Chemical Society*, vol. 131, no. 35, pp. 12554–12555, 2009.

[54] M. Bruchez, M. Moronne, P. Gin, S. Weiss, and A. P. Alivisatos, "Semiconductor nanocrystals as fluorescent biological labels," *science*, vol. 281, no. 5385, pp. 2013–2016, 1998.

[55] T. Jiang, J. Song, H. Wang, X. Ye, H. Wang, W. Zhang, M. Yang, R. Xia, L. Zhu, and X. Xu, "Aqueous synthesis of color tunable Cu doped Zn–In–S/ZnS nanoparticles in the whole visible region for cellular imaging," *Journal of Materials Chemistry B*, vol. 3, no. 11, pp. 2402–2410, 2015.

[56] Z. Pan *et al.*, "High-efficiency green quantum dot solar cells," *Journal of the American Chemical Society*, vol. 136, no. 25, pp. 9203–9210, 2014.

[57] S. Baskoutas and A. F. Terzis, "Size-dependent band gap of colloidal quantum dots," *Journal of applied physics*, vol. 99, no. 1, p. 013708, 2006.

[58] Y. Huang, X. Zhan, K. Xu, L. Yin, Z. Cheng, C. Jiang, Z. Wang, and J. He, "Highly sensitive photodetectors based on hybrid 2D-0D SnS_2-copper indium sulfide quantum dots," *Applied Physics Letters*, vol. 108, no. 1, p. 013101, 2016.

[59] S. V. Kershaw, M. Harrison, A. L. Rogach, and A. Kornowski, "Development of IR–emitting colloidal II–VI quantum-dot materials," *IEEE Journal of Selected Topics in Quantum Electronics*, vol. 6, no. 3, pp. 534–543, 2000.

[60] G. Zaiats, D. Yanover, R. Vaxenburg, J. Tilchin, A. Sashchiuk, and E. Lifshitz, "PbSe-based colloidal core/shell heterostructures for optoelectronic applications," *Materials*, vol. 7, no. 11, pp. 7243–7275, 2014.

[61] A. M. Derfus, W. C. Chan, and S. N. Bhatia, "Probing the cytotoxicity of semiconductor quantum dots," *Nano letters*, vol. 4, no. 1, pp. 11–18, 2004.

[62] Y. Pu, F. Cai, D. Wang, J.-X. Wang, and J.-F. Chen, "Colloidal synthesis of semiconductor quantum dots toward large-scale production: a review," *Industrial & Engineering Chemistry Research*, vol. 57, no. 6, pp. 1790–1802, 2018.

[63] B. Sadeghimakki, Y. Zheng, N. M. Jahed, R. S. Tarighat, P. H. Pham, J. J. Kim, N. C. Bols, and S. Sivoththaman, "Toxicity and safety study of Cd-based and Cd-free quantum dots in third-gen PV and scaled-up processing platforms," in *2016 IEEE 43rd Photovoltaic Specialists Conference (PVSC)*, pp. 3593–3597, IEEE, 2016.

[64] R. Hardman, "A toxicologic review of quantum dots: toxicity depends on physicochemical and environmental factors," *Environmental health perspectives*, vol. 114, no. 2, pp. 165–172, 2005.

[65] D.-E. Nam, W.-S. Song, and H. Yang, "Facile, air-insensitive solvothermal synthesis of emission-tunable $CuInS_2$/zns quantum dots with high quantum yields," *Journal of Materials Chemistry*, vol. 21, no. 45, pp. 18220–18226, 2011.

[66] B. Sadeghimakki, Y. Zheng, N. M. Jahed, P. H. Pham, A. Babujee, N. C. Bols, and S. Sivoththaman, "Toxicity and safety aspects of nanoparticle spread in third generation photovoltaic device processing environments," in *2015 IEEE 42nd Photovoltaic Specialist Conference (PVSC)*, pp. 1–6, IEEE, 2015.

[67] L. Li, T. J. Daou, I. Texier, T. T. Kim Chi, N. Q. Liem, and P. Reiss, "Highly luminescent $CuInS_2$/ZnS core/shell nanocrystals: cadmium-free quantum dots for in vivo imaging," *Chemistry of Materials*, vol. 21, no. 12, pp. 2422–2429, 2009.

[68] J. Lee and C.-S. Han, "Large-scale synthesis of highly emissive and photostable $CuInS_2$/ZnS nanocrystals through hybrid flow reactor," *Nanoscale research letters*, vol. 9, no. 1, p. 78, 2014.

[69] M. Booth, R. Peel, R. Partanen, N. Hondow, V. Vasilca, L. J. Jeuken, and K. Critchley, "Amphipol-encapsulated $CuInS_2$/ZnS quantum dots with excellent colloidal stability," *RSC Advances*, vol. 3, no. 43, pp. 20559–20566, 2013.

[70] T. Kameyama, "Advances in colloidal $I--III--VI_2$–based semiconductor quantum dots toward tailorable photofunctional materials," *Electrochemistry*, pp. 18–6, 2018.

[71] L. Wu, S.-Y. Chen, F.-J. Fan, T.-T. Zhuang, C.-M. Dai, and S.-H. Yu, "Polytypic nanocrystals of Cu-based ternary chalcogenides: colloidal synthesis and photoelectrochemical properties," *Journal of the American Chemical Society*, vol. 138, no. 17, pp. 5576–5584, 2016.

[72] T. Pons, E. Pic, N. Lequeux, E. Cassette, L. Bezdetnaya, F. Guillemin, F. Marchal, and B. Dubertret, "Cadmium-free $CuInS_2$/zns quantum dots for sentinel lymph node imaging with reduced toxicity," *ACS nano*, vol. 4, no. 5, pp. 2531–2538, 2010.

[73] V. K. Komarala, C. Xie, Y. Wang, J. Xu, and M. Xiao, "Time-resolved photoluminescence properties of $CuInS_2$/ZnS nanocrystals: Influence of intrinsic defects and external impurities," *Journal of Applied Physics*, vol. 111, no. 12, p. 124314, 2012.

[74] M. Fu, W. Luan, S.-T. Tu, and L. Mleczko, "Green synthesis of $CuInS_2$/ZnS nanocrystals with high photoluminescence and stability," *Journal of Nanomaterials*, vol. 16, no. 1, p. 401, 2015.

[75] D.-E. Nam, W.-S. Song, and H. Yang, "Noninjection, one–pot synthesis of Cu-deficient $CuInS_2$/ZnS core/shell quantum dots and their fluorescent properties," *Journal of colloid and interface science*, vol. 361, no. 2, pp. 491–496, 2011.

[76] A. D. Leach and J. E. Macdonald, "Optoelectronic properties of $CuInS_2$ nanocrystals and their origin," *The journal of physical chemistry letters*, vol. 7, no. 3, pp. 572–583, 2016.

[77] C. Xia, W. Wu, T. Yu, X. Xie, C. Van Oversteeg, H. C. Gerritsen, and C. de Mello Donega, "Size-dependent band-gap and molar absorption coefficients of colloidal $CuInS_2$ quantum dots," *ACS nano*, vol. 12, no. 8, pp. 8350–8361, 2018.

[78] P.-H. Chuang, C. C. Lin, and R.-S. Liu, "Emission-tunable $CuInS_2$ /ZnS quantum dots: structure, optical properties, and application in white light-emitting diodes with high color rendering index," *ACS applied materials & interfaces*, vol. 6, no. 17, pp. 15379–15387, 2014.

[79] J. van Embden, A. S. Chesman, and J. J. Jasieniak, "The heat-up synthesis of colloidal nanocrystals," *Chemistry of Materials*, vol. 27, no. 7, pp. 2246–2285, 2015.

[80] J. Chang and E. R. Waclawik, "Colloidal semiconductor nanocrystals: controlled synthesis and surface chemistry in organic media," *RSC Advances*, vol. 4, no. 45, pp. 23505–23527, 2014.

[81] N. Guijarro, E. Guillén, T. Lana-Villarreal, and R. Gómez, "Quantum dot–sensitized solar cells based on directly adsorbed zinc copper indium sulfide colloids," *Physical Chemistry Chemical Physics*, vol. 16, no. 19, pp. 9115–9122, 2014.

[82] S. F. Hansen, C. V. Howard, M. Martuzzi, and M. Depledge, "Nanotechnology and human health: Scientific evidence and risk governance: Report of the WHO expert meeting 10–11 December 2012, Bonn, Germany," 2013.

[83] L. E. Hopkins, E. S. Patchin, P.-L. Chiu, C. Brandenberger, S. Smiley-Jewell, and K. E. Pinkerton, "Nose-to-brain transport of aerosolised quantum dots following acute exposure," *Nanotoxicology*, vol. 8, no. 8, pp. 885–893, 2014.

[84] G. Oberdörster, A. Maynard, K. Donaldson, V. Castranova, J. Fitzpatrick, K. Ausman, J. Carter, B. Karn, W. Kreyling, D. Lai, *et al.*, "Principles for characterizing the potential human health effects from exposure to nanomaterials: elements of a screening strategy," *Particle and fibre toxicology*, vol. 2, no. 1, p. 8, 2005.

[85] M. Debia, C. Beaudry, S. Weichenthal, R. Tardif, and A. Dufresne, "Characterization and control of occupational exposure to nanoparticles and ultrafine particles," *André Studies and Research Projects/Report R-777, Montréal, IRSST*, 2013.

[86] O. Okoturo-Evans, A. Dybowska, E. Valsami-Jones, J. Cupitt, M. Gierula, A. R. Boobis, and R. J. Edwards, "Elucidation of toxicity pathways in lung epithelial cells induced by silicon dioxide nanoparticles," *PloS one*, vol. 8, no. 9, p. e72363, 2013.

[87] N. Science and T. C. (US), *National Nanotechnology Initiative: Environmental, Health, Safety Research Strategy.* National Science and Technology Council, Committee on Technology, 2011.

[88] G. Konstantatos, I. Howard, A. Fischer, S. Hoogland, J. Clifford, E. Klem, L. Levina, and E. H. Sargent, "Ultrasensitive solution–cast quantum dot photodetectors," *Nature*, vol. 442, no. 7099, p. 180, 2006.

[89] Z. H. *et al.*, "Low temperature synthesis of ZnS and CdZnS shells on CdSe quantum dotss," *Angew. Chem.*, vol. 21, pp. 1–10, 2010.

[90] Z. Ning, O. Voznyy, J. Pan, S. Hoogland, V. Adinolfi, J. Xu, M. Li, A. R. Kirmani, J.-P. Sun, J. Minor, *et al.*, "Air-stable n-type colloidal quantum dot solids," *Nature materials*, vol. 13, no. 8, p. 822, 2014.

[91] K.-T. Kuo, D.-M. Liu, S.-Y. Chen, and C.-C. Lin, "Core-shell $CuInS_2$/ZnS quantum dots assembled on short ZnO nanowires with enhanced photo-conversion efficiency," *Journal of Materials Chemistry*, vol. 19, no. 37, pp. 6780–6788, 2009.

[92] D. Mocatta, G. Cohen, J. Schattner, O. Millo, E. Rabani, and U. Banin, "Heavily doped semiconductor nanocrystal quantum dots," *Science*, vol. 332, no. 6025, pp. 77–81, 2011.

[93] M. Uehara, K. Watanabe, Y. Tajiri, H. Nakamura, and H. Maeda, "Synthesis of $CuInS_2$ fluorescent nanocrystals and enhancement of fluorescence by controlling crystal defect," *The Journal of chemical physics*, vol. 129, no. 13, p. 134709, 2008.

[94] W. Liu, J.-S. Lee, and D. V. Talapin, "III–V nanocrystals capped with molecular metal chalcogenide ligands: high electron mobility and ambipolar photoresponse," *Journal of the American Chemical Society*, vol. 135, no. 4, pp. 1349–1357, 2013.

[95] W. Zhang and X. Zhong, "Facile synthesis of ZnS- $CuInS_2$ -alloyed nanocrystals for a color-tunable fluorchrome and photocatalyst," *Inorganic chemistry*, vol. 50, no. 9, pp. 4065–4072, 2011.

[96] W. Guo, W. Yang, Y. Wang, X. Sun, Z. Liu, B. Zhang, J. Chang, and X. Chen, "Color-tunable Gd-Zn-Cu-In-S/ZnS quantum dots for dual modality magnetic resonance and fluorescence imaging," *Nano research*, vol. 7, no. 11, pp. 1581–1591, 2014.

[97] S. Higashimoto, T. Nakase, S. Mukai, and M. Takahashi, "Copper–indium–sulfide colloids on quantum dot sensitized TiO_2 solar cell: Effects of capping with mercapto-acid linker molecules," *Journal of colloid and interface science*, vol. 535, pp. 176–181, 2019.

[98] C.-W. Chen, D.-Y. Wu, Y.-C. Chan, C. C. Lin, P.-H. Chung, M. Hsiao, and R.-S. Liu, "Evaluations of the chemical stability and cytotoxicity of $CuInS_2$ and $CuInS_2$/ZnS core/shell quantum dots," *The Journal of Physical Chemistry C*, vol. 119, no. 5, pp. 2852–2860, 2015.

[99] W.-W. Xiong, G.-H. Yang, X.-C. Wu, and J.-J. Zhu, "Aqueous synthesis of color-tunable $CuInS_2$/ZnS nanocrystals for the detection of human interleukin 6," *ACS applied materials & interfaces*, vol. 5, no. 16, pp. 8210–8216, 2013.

[100] O. Chen, J. Zhao, V. P. Chauhan, J. Cui, C. Wong, D. K. Harris, H. Wei, H.-S. Han, D. Fukumura, R. K. Jain, *et al.*, "Compact high-quality CdSe–CdS core–shell nanocrystals with narrow emission linewidths and suppressed blinking," *Nature materials*, vol. 12, no. 5, p. 445, 2013.

[101] Y. Chen, J. Vela, H. Htoon, J. L. Casson, D. J. Werder, D. A. Bussian, V. I. Klimov, and J. A. Hollingsworth, "giant multishell cdse nanocrystal quantum dots with suppressed blinking," *Journal of the American Chemical Society*, vol. 130, no. 15, pp. 5026–5027, 2008.

[102] I. Coropceanu and M. G. Bawendi, "Core/shell quantum dot based luminescent solar concentrators with reduced reabsorption and enhanced efficiency," *Nano letters*, vol. 14, no. 7, pp. 4097–4101, 2014.

[103] M. Green, "The nature of quantum dot capping ligands," *Journal of Materials Chemistry*, vol. 20, no. 28, pp. 5797–5809, 2010.

[104] V. T. Chebrolu and H.-J. Kim, "Recent progress in quantum dot sensitized solar cells: an inclusive review of photoanode, sensitizer, electrolyte, and the counter electrode," *Journal of Materials Chemistry C*, vol. 7, no. 17, pp. 4911–4933, 2019.

[105] R. A. Sperling and W. J. Parak, "Surface modification, functionalization and bioconjugation of colloidal inorganic nanoparticles," *Philosophical Transactions of the Royal Society A: Mathematical, Physical and Engineering Sciences*, vol. 368, no. 1915, pp. 1333–1383, 2010.

[106] A. H. Ip, S. M. Thon, S. Hoogland, O. Voznyy, D. Zhitomirsky, R. Debnath, L. Levina, L. R. Rollny, G. H. Carey, A. Fischer, *et al.*, "Hybrid passivated colloidal quantum dot solids," *Nature nanotechnology*, vol. 7, no. 9, p. 577, 2012.

[107] A. R. Kirmani, G. H. Carey, M. Abdelsamie, B. Yan, D. Cha, L. R. Rollny, X. Cui, E. H. Sargent, and A. Amassian, "Effect of solvent environment on colloidal–quantum–dot solar-c-ell manufacturability and performance," *Advanced Materials*, vol. 26, no. 27, pp. 4717–4723, 2014.

[108] M. Soreni-Harari, N. Yaacobi-Gross, D. Steiner, A. Aharoni, U. Banin, O. Millo, and N. Tessler, "Tuning energetic levels in nanocrystal quantum dots through surface manipulations," *Nano letters*, vol. 8, no. 2, pp. 678–684, 2008.

[109] V. Celibert, E. Tranvouez, G. Guillot, C. Bru-Chevallier, L. Grenouillet, P. Duvaut, P. Gilet, P. Ballet, and A. Million, "MBE growth optimization and optical spectroscopy of inas/gaas quantum dots emitting at 1.3 μm in single and stacked layers," *Journal of crystal growth*, vol. 275, no. 1-2, pp. e2313–e2319, 2005.

[110] S. Sivoththaman, "Fabrication of nanostructures." Lecture slides for ECE 433- Fabrication Technologies for Micro and Nano Devices., 2015.

[111] R. M. Sankaran, D. Holunga, R. C. Flagan, and K. P. Giapis, “Synthesis of blue luminescent Si nanoparticles using atmospheric-pressure microdischarges,” *Nano letters*, vol. 5, no. 3, pp. 537–541, 2005.

[112] L. Mangolini, E. Thimsen, and U. Kortshagen, “High-yield plasma synthesis of luminescent silicon nanocrystals,” *Nano letters*, vol. 5, no. 4, pp. 655–659, 2005.

[113] A. R. Kirmani, A. D. Sheikh, M. R. Niazi, M. A. Haque, M. Liu, F. P. G. de Arquer, J. Xu, B. Sun, O. Voznyy, N. Gasparini, *et al.*, “Overcoming the ambient manufacturability–scalability–performance bottleneck in colloidal quantum dot photovoltaics,” *Advanced Materials*, vol. 30, no. 35, p. 1801661, 2018.

[114] P. K. Santra, P. V. Nair, K. George Thomas, and P. V. Kamat, “$CuInS_2$-sensitized quantum dot solar cell. Electrophoretic deposition, excited-state dynamics, and photovoltaic performance,” *The journal of physical chemistry letters*, vol. 4, no. 5, pp. 722–729, 2013.

[115] Z. Pan, H. Zhang, K. Cheng, Y. Hou, J. Hua, and X. Zhong, “Highly efficient inverted type-I CdS/CdSe core/shell structure QD-sensitized solar cells,” *ACS nano*, vol. 6, no. 5, pp. 3982–3991, 2012.

[116] Z. Zhou, S. Yuan, J. Fan, Z. Hou, W. Zhou, Z. Du, and S. Wu, “$CuInS_2$ quantum dot-sensitized TiO_2 nanorod array photoelectrodes: synthesis and performance optimization,” *Nanoscale research letters*, vol. 7, no. 1, p. 652, 2012.

[117] W. Wang, L. Zhao, Y. Wang, W. Xue, F. He, Y. Xie, and Y. Li, “Facile secondary deposition for improving quantum dot loading in fabricating quantum dot solar cells,” *Journal of the American Chemical Society*, vol. 141, no. 10, pp. 4300–4307, 2019.

[118] W. Guo *et al.*, “Synthesis of Zn-Cu-In-S/ZnS core/shell quantum dots with inhibited blue-shift photoluminescence and applications for tumor targeted bioimaging,” *Theranostics*, vol. 3, no. 2, p. 99, 2013.

[119] Z. Zhang, D. Liu, D. Li, K. Huang, Y. Zhang, Z. Shi, R. Xie, M.-Y. Han, Y. Wang, and W. Yang, “Dual emissive Cu: InP/ZnS/InP/ZnS nanocrystals: single-source greener emitters with flexibly tunable emission from visible to near-infrared and their application in white light-emitting diodes,” *Chemistry of Materials*, vol. 27, no. 4, pp. 1405–1411, 2015.

[120] L. Peng, D. Li, Z. Zhang, K. Huang, Y. Zhang, Z. Shi, R. Xie, and W. Yang, "Large-scale synthesis of single-source, thermally stable, and dual-emissive Mn-doped Zn–Cu–In–S nanocrystals for bright white light-emitting diodes," *Nano Research*, vol. 8, no. 10, pp. 3316–3331, 2015.

[121] S. H. Park, A. Hong, J.-H. Kim, H. Yang, K. Lee, and H. S. Jang, "Highly bright yellow–green–emitting $CuInS_2$ colloidal quantum dots with core/shell/shell architecture for white light–emitting diodes," *ACS applied materials & interfaces*, vol. 7, no. 12, pp. 6764–6771, 2015.

[122] B. Sadeghimakki, Z. Gao, and S. Sivoththaman, "Proof of down-conversion by CdSe/ZnS quantum dots on silicon solar cells," in *2014 IEEE 40th Photovoltaic Specialist Conference (PVSC)*, pp. 2262–2266, IEEE, 2014.

[123] Z. Ning, X. Gong, R. Comin, G. Walters, F. Fan, O. Voznyy, E. Yassitepe, A. Buin, S. Hoogland, and E. H. Sargent, "Quantum-dot-in-perovskite solids," *Nature*, vol. 523, no. 7560, p. 324, 2015.

[124] Y. Takeda, "Requisites for highly efficient hot-carrier solar cells," in *Quantum Dot Solar Cells*, pp. 187–232, Springer, 2014.

[125] N. R. E. Laboratories, "Best research-cell efficiency chart," 2021.

[126] L. Zhang, H. Rao, Z. Pan, and X. Zhong, "ZnS_xSe_{1--x} alloy passivation layer for high-efficiency quantum-dot-sensitized solar cells," *ACS Applied Materials & Interfaces*, vol. 11, no. 44, pp. 41415–41423, 2019.

[127] X. Lan, O. Voznyy, A. Kiani, F. P. García de Arquer, A. S. Abbas, G.-H. Kim, M. Liu, Z. Yang, G. Walters, J. Xu, *et al.*, "Passivation using molecular halides increases quantum dot solar cell performance," *Advanced Materials*, vol. 28, no. 2, pp. 299–304, 2016.

[128] X. Lan, O. Voznyy, F. P. García de Arquer, M. Liu, J. Xu, A. H. Proppe, G. Walters, F. Fan, H. Tan, M. Liu, *et al.*, "10.6% certified colloidal quantum dot solar cells via solvent–polarity–engineered halide passivation," *Nano letters*, vol. 16, no. 7, pp. 4630–4634, 2016.

[129] Y. Kim, F. Che, J. W. Jo, J. Choi, F. P. García de Arquer, O. Voznyy, B. Sun, J. Kim, M.-J. Choi, R. Quintero-Bermudez, *et al.*, "A facet–specific quantum dot passivation strategy for colloid management and efficient infrared photovoltaics," *Advanced Materials*, vol. 31, no. 17, p. 1805580, 2019.

[130] G.-H. Kim, F. P. García de Arquer, Y. J. Yoon, X. Lan, M. Liu, O. Voznyy, Z. Yang, F. Fan, A. H. Ip, P. Kanjanaboos, *et al.*, "High–efficiency colloidal quantum dot photovoltaics via robust self–assembled monolayers," *Nano letters*, vol. 15, no. 11, pp. 7691–7696, 2015.

[131] X. Yang, L. Hu, H. Deng, K. Qiao, C. Hu, Z. Liu, S. Yuan, J. Khan, D. Li, J. Tang, *et al.*, "Improving the performance of PbS quantum dot solar cells by optimizing ZnO window layer," *Nano-micro letters*, vol. 9, no. 2, p. 24, 2017.

[132] M. Liu, O. Voznyy, R. Sabatini, F. P. G. de Arquer, R. Munir, A. H. Balawi, X. Lan, F. Fan, G. Walters, A. R. Kirmani, *et al.*, "Hybrid organic–inorganic inks flatten the energy landscape in colloidal quantum dot solids," *Nature materials*, vol. 16, no. 2, pp. 258–263, 2017.

[133] A. D. Stiff-Roberts, "Quantum-dot infrared photodetectors: a review," *Journal of Nanophotonics*, vol. 3, no. 1, p. 031607, 2009.

[134] J. Ramade, J. Qu, A. Chu, C. Gréboval, C. Livache, N. Goubet, B. Martinez, G. Vincent, and E. Lhuillier, "Potential of colloidal quantum dot based solar cells for near–infrared active detection," *ACS photonics*, vol. 7, no. 1, pp. 272–278, 2019.

[135] M. Ahmadi, T. Wu, and B. Hu, "A review on organic–inorganic halide perovskite photodetectors: device engineering and fundamental physics," *Advanced Materials*, vol. 29, no. 41, p. 1605242, 2017.

[136] A. Ara, J. A. Usmani, *et al.*, "Lead toxicity: a review," *Interdisciplinary toxicology*, vol. 8, no. 2, pp. 55–64, 2015.

[137] K. S. Hougaard, P. Jackson, K. A. Jensen, J. J. Sloth, K. Löschner, E. H. Larsen, R. K. Birkedal, A. Vibenholt, A.-M. Z. Boisen, H. Wallin, *et al.*, "Effects of prenatal exposure to surface–coated nanosized titanium dioxide (UV-Titan). a study in mice," *Particle and fibre toxicology*, vol. 7, no. 1, p. 16, 2010.

[138] U. Vogel, "Health effects of inhaled nanomaterials & ultrafine particles," 2019.

[139] D. Scheunemann, S. Wilken, J. Parisi, and H. Borchert, "Investigation of the spatially dependent charge collection probability in $CuInS_2$/ZnO colloidal nanocrystal solar cells," *Acs Photonics*, vol. 2, no. 7, pp. 864–875, 2015.

[140] J. E. Halpert, F. S. Morgenstern, B. Ehrler, Y. Vaynzof, D. Credgington, and N. C. Greenham, "Charge dynamics in solution–processed nanocrystalline $CuInS_2$ solar cells," *ACS nano*, vol. 9, no. 6, pp. 5857–5867, 2015.

[141] D. So and G. Konstantatos, "Thiol–free synthesized copper indium sulfide nanocrystals as optoelectronic quantum dot solids," *Chemistry of Materials*, vol. 27, no. 24, pp. 8424–8432, 2015.

[142] A.-R. Hong, J. Kim, S. Y. Kim, S.-I. Kim, K. Lee, and H. S. Jang, "Core/shell-structured upconversion nanophosphor and cadmium-free quantum-dot bilayer-based near-infrared photodetectors," *Optics letters*, vol. 40, no. 21, pp. 4959–4962, 2015.

[143] M.-L. Lu, C.-W. Lai, H.-J. Pan, C.-T. Chen, P.-T. Chou, and Y.-F. Chen, "A facile integration of zero-(I–III–VI quantum dots) and one-(single SnO_2 nanowire) dimensional nanomaterials: fabrication of a nanocomposite photodetector with ultrahigh gain and wide spectral response," *Nano letters*, vol. 13, no. 5, pp. 1920–1927, 2013.

[144] R. Pan and J. Wang, "Ultra-high responsivity graphene-cis/zns qds hybrid photodetector," in *9th International Symposium on Advanced Optical Manufacturing and Testing Technologies: Optoelectronic Materials and Devices for Sensing and Imaging*, vol. 10843, p. 108431B, International Society for Optics and Photonics, 2019.

[145] R. Xu, S. Ruan, D. Zhang, Z. Li, B. Yin, K. Li, J. Zhou, Y. Chen, and C. Li, "Enhanced performance of ultraviolet photodetector modified by quantum dots with high responsivity and narrow detection region," *Journal of Alloys and Compounds*, vol. 751, pp. 117–123, 2018.

[146] B. Zhang, Y. Wang, C. Yang, S. Hu, Y. Gao, Y. Zhang, Y. Wang, H. V. Demir, L. Liu, and K.-T. Yong, "The composition effect on the optical properties of aqueous synthesized Cu–In–S and Zn–Cu–In–S quantum dot nanocrystals," *Physical Chemistry Chemical Physics*, vol. 17, no. 38, pp. 25133–25141, 2015.

[147] R. Zhang, P. Yang, and Y. Wang, "Facile synthesis of $CuInS_2$/ZnS quantum dots with highly near-infrared photoluminescence via phosphor–free process," *Journal of nanoparticle research*, vol. 15, no. 9, p. 1910, 2013.

[148] S.-C. Shei, W.-J. Chiang, and S.-J. Chang, "Synthesis of $CuInS_2$ quantum dots using polyetheramine as solvent," *Nanoscale research letters*, vol. 10, no. 1, p. 122, 2015.

[149] B. Chen, H. Zhong, W. Zhang, Z. Tan, Y. Li, C. Yu, T. Zhai, Y. Bando, S. Yang, and B. Zou, "Highly emissive and color–tunable $CuInS_2$-based colloidal semiconductor nanocrystals: off-stoichiometry effects and improved electroluminescence performance," *Advanced Functional Materials*, vol. 22, no. 10, pp. 2081–2088, 2012.

[150] L. Zhang, Z. Pan, W. Wang, J. Du, Z. Ren, Q. Shen, and X. Zhong, "Copper deficient Zn–Cu–In–Se quantum dot sensitized solar cells for high efficiency," *Journal of Materials Chemistry A*, vol. 5, no. 40, pp. 21442–21451, 2017.

[151] J. Sun, M. Ikezawa, X. Wang, P. Jing, H. Li, J. Zhao, and Y. Masumoto, "Photocarrier recombination dynamics in ternary chalcogenide $CuInS_2$ quantum dots," *Physical Chemistry Chemical Physics*, vol. 17, no. 18, pp. 11981–11989, 2015.

[152] J. Park and S.-W. Kim, "$CuInS_2$/zns core/shell quantum dots by cation exchange and their blue-shifted photoluminescence," *Journal of Materials Chemistry*, vol. 21, no. 11, pp. 3745–3750, 2011.

[153] W. J. Baumgardner, Z. Quan, J. Fang, and T. Hanrath, "Timing matters: the underappreciated role of temperature ramp rate for shape control and reproducibility of quantum dot synthesis," *Nanoscale*, vol. 4, no. 12, pp. 3625–3628, 2012.

[154] O. Yarema, M. Yarema, D. Bozyigit, W. M. Lin, and V. Wood, "Independent composition and size control for highly luminescent indium–rich silver indium selenide nanocrystals," *ACS nano*, vol. 9, no. 11, pp. 11134–11142, 2015.

[155] J.-Y. Chang, S. C. Chang, S.-H. Tzing, and C.-H. Li, "Development of nonstoichiometric $CuInS_2$ as a light-harvesting photoanode and catalytic photocathode in a sensitized solar cell," *ACS applied materials & interfaces*, vol. 6, no. 24, pp. 22272–22281, 2014.

[156] Y. Zheng, B. Sadeghimakki, N. M. Jahed, and S. Sivoththaman, "Scalable non-injection synthesis of Cd-free copper indium sulfide/zinc sulfide quantum dots for third-gen photovoltaic application," *MRS Advances*, vol. 1, no. 30, pp. 2193–2198, 2016.

[157] A. Zhang, C. Dong, L. Li, J. Yin, H. Liu, X. Huang, and J. Ren, "Non-blinking (Zn)CuInS/ZnS quantum dots prepared by in situ interfacial alloying approach," *Scientific reports*, vol. 5, p. 15227, 2015.

[158] T. J. Macdonald, Y. J. Mange, M. Dewi, A. McFadden, W. M. Skinner, and T. Nann, "Cation exchange of aqueous $CuInS_2$ quantum dots," *CrystEngComm*, vol. 16, no. 40, pp. 9455–9460, 2014.

[159] F. Xu, L. Gerlein, X. Ma, C. Haughn, M. Doty, and S. Cloutier, "Impact of different surface ligands on the optical properties of PbS quantum dot solids," *Materials*, vol. 8, no. 4, pp. 1858–1870, 2015.

[160] D. A. Hines, R. P. Forrest, S. A. Corcelli, and P. V. Kamat, "Predicting the rate constant of electron tunneling reactions at the CdSe–TiO_2 interface," *The Journal of Physical Chemistry B*, vol. 119, no. 24, pp. 7439–7446, 2015.

[161] S. K. Goswami, T. S. Kim, E. Oh, K. K. Challa, and E.-T. Kim, "Optical properties and effect of carrier tunnelling in CdSe colloidal quantum dots: A comparative study with different ligands," *AIP Advances*, vol. 2, no. 3, p. 032132, 2012.

[162] J. Choi, W. Choi, and D. Y. Jeon, "Ligand–exchange–ready $CuInS_2$/ZnS quantum dots via surface–ligand composition control for film-type display devices," *ACS Applied Nano Materials*, vol. 2, no. 9, pp. 5504–5511, 2019.

[163] K. Tvrdy, P. A. Frantsuzov, and P. V. Kamat, "Photoinduced electron transfer from semiconductor quantum dots to metal oxide nanoparticles," *Proceedings of the National Academy of Sciences*, vol. 108, no. 1, pp. 29–34, 2011.

[164] H.-M. Kim, D. Geng, J. Kim, E. Hwang, and J. Jang, "Metal–oxide stacked electron transport layer for highly efficient inverted quantum–dot light emitting diodes," *ACS applied materials & interfaces*, vol. 8, no. 42, pp. 28727–28736, 2016.

[165] Y. Lee, B. G. Jeong, H. Roh, J. Roh, J. Han, D. C. Lee, W. K. Bae, J.-Y. Kim, and C. Lee, "Enhanced lifetime and efficiency of red quantum dot light-emitting diodes with Y–doped ZnO sol–gel electron-transport layers by reducing excess electron injection," *Advanced Quantum Technologies*, vol. 1, no. 1, p. 1700006, 2018.

[166] S. Wang, Y. Guo, D. Feng, L. Chen, Y. Fang, H. Shen, and Z. Du, "Bandgap tunable $\mathrm{Zn_{1-x}Mg_x o}$ thin films as electron transport layers for high performance quantum dot light-emitting diodes," *Journal of Materials Chemistry C*, vol. 5, no. 19, pp. 4724–4730, 2017.

[167] S. Zang, Y. Wang, M. Li, W. Su, H. Zhu, X. Zhang, and Y. Liu, "Fabrication of efficient PbS colloidal quantum dot solar cell with low temperature sputter–deposited ZnO electron transport layer," *Solar Energy Materials and Solar Cells*, vol. 169, pp. 264–269, 2017.

[168] H.-M. Kim, S. Cho, J. Kim, H. Shin, and J. Jang, "Li and Mg co-doped zinc oxide electron transporting layer for highly efficient quantum dot light–emitting diodes," *ACS applied materials & interfaces*, vol. 10, no. 28, pp. 24028–24036, 2018.

[169] H. Chen, P. Chao, D. Han, H. Wang, J. Miao, H. Zhong, H. Meng, and F. He, "Hydroxyl-terminated $CuInS_2$-based quantum dots: potential cathode interfacial

modifiers for efficient inverted polymer solar cells," *ACS applied materials & interfaces*, vol. 9, no. 8, pp. 7362–7367, 2017.

[170] Y.-C. Chen, H.-H. Chang, and Y.-K. Hsu, "Synthesis of $CuInS_2$ quantum dots/In_2S_3/ZnO nanowire arrays with high photoelectrochemical activity," *ACS Sustainable Chemistry & Engineering*, vol. 6, no. 8, pp. 10861–10868, 2018.

[171] Y. Zheng, B. Sadeghimakki, J. A. Brunning, and S. Sivoththaman, "Ligand exchange functionalization of CIS quantum dots for CIS/ZnO film heterojunctions," *IEEE Transactions on Nanotechnology*, vol. 18, pp. 728–733, 2019.

[172] M. He, D. Kou, W. Zhou, Z. Zhou, Y. Meng, and S. Wu, "Se-assisted performance enhancement of $Cu_2ZnSn\,(S, Se)_4$ quantum-dot sensitized solar cells via a simple yet versatile synthesis," *Inorganic chemistry*, vol. 58, no. 19, pp. 13285–13292, 2019.

[173] A. Kharkwal, S. N. Sharma, S. Chand, and A. Singh, "Effect of linker on the photosensitization of ZnO layers with CdSe quantum dots," *Colloid and Polymer Science*, vol. 290, no. 1, pp. 49–61, 2012.

[174] G. Konstantatos, J. Clifford, L. Levina, and E. H. Sargent, "Sensitive solution–processed visible–wavelength photodetectors," *Nature photonics*, vol. 1, no. 9, pp. 531–534, 2007.

[175] L. Korala, Z. Wang, Y. Liu, S. Maldonado, and S. L. Brock, "Uniform thin films of CdSe and CdSe (ZnS) core (shell) quantum dots by sol–gel assembly: enabling photoelectrochemical characterization and electronic applications," *Acs Nano*, vol. 7, no. 2, pp. 1215–1223, 2013.

[176] J. Sun, J. Zhao, and Y. Masumoto, "Shell–thickness–dependent photoinduced electron transfer from $CuInS_2$/ZnS quantum dots to TiO_2 films," *Applied physics letters*, vol. 102, no. 5, p. 053119, 2013.

[177] J.-Y. Kim, J. Yang, J. H. Yu, W. Baek, C.-H. Lee, H. J. Son, T. Hyeon, and M. J. Ko, "Highly efficient copper–indium–selenide quantum dot solar cells: suppression of carrier recombination by controlled ZnS overlayers," *ACS nano*, vol. 9, no. 11, pp. 11286–11295, 2015.

[178] E. V. Shevchenko, D. V. Talapin, C. B. Murray, and S. O'Brien, "Structural characterization of self–assembled multifunctional binary nanoparticle superlattices," *Journal of the American Chemical Society*, vol. 128, no. 11, pp. 3620–3637, 2006.

[179] W. Ma, S. L. Swisher, T. Ewers, J. Engel, V. E. Ferry, H. A. Atwater, and A. P. Alivisatos, "Photovoltaic performance of ultrasmall PbSe quantum dots," *ACS nano*, vol. 5, no. 10, pp. 8140–8147, 2011.

[180] X. Hu, Q. Zhang, X. Huang, D. Li, Y. Luo, and Q. Meng, "Aqueous colloidal $\mathrm{CuInS_2}$ for quantum dot sensitized solar cells," *Journal of Materials Chemistry*, vol. 21, no. 40, pp. 15903–15905, 2011.

[181] J. M. Luther, M. Law, Q. Song, C. L. Perkins, M. C. Beard, and A. J. Nozik, "Structural, optical, and electrical properties of self-assembled films of PbSe nanocrystals treated with 1, 2-ethanedithiol," *ACS nano*, vol. 2, no. 2, pp. 271–280, 2008.

[182] S. Dashmiz, "Quantum dots for intermediate band in solar cells," Master's thesis, University of Waterloo, 2013.

[183] Y. Zheng, B. Sadeghimakki, E. Piano, and S. Sivoththaman, "A method for uniform embedment and self-assembly of cis-based qds for formation of ordered qd thin films in pv devices," in *2019 IEEE 46th Photovoltaic Specialists Conference (PVSC)*, pp. 1806–1812, IEEE, 2019.

[184] I. J. Kramer, J. C. Minor, G. Moreno-Bautista, L. Rollny, P. Kanjanaboos, D. Kopilovic, S. M. Thon, G. H. Carey, K. W. Chou, D. Zhitomirsky, *et al.*, "Efficient spray–coated colloidal quantum dot solar cells," *Advanced materials*, vol. 27, no. 1, pp. 116–121, 2015.

[185] M. Böberl, M. V. Kovalenko, S. Gamerith, E. J. List, and W. Heiss, "Inkjet–printed nanocrystal photodetectors operating up to 3 μm wavelengths," *Advanced Materials*, vol. 19, no. 21, pp. 3574–3578, 2007.

[186] F. Donat, S. Corbel, H. Alem, S. Pontvianne, L. Balan, G. Medjahdi, and R. Schneider, "ZnO nanoparticles sensitized by $\mathrm{CuInZn_xS_{2+x}}$ quantum dots as highly efficient solar light driven photocatalysts," *Beilstein Journal of Nanotechnology*, vol. 8, no. 1, pp. 1080–1093, 2017.

[187] Y. Xu and M. A. Schoonen, "The absolute energy positions of conduction and valence bands of selected semiconducting minerals," *American Mineralogist*, vol. 85, no. 3-4, pp. 543–556, 2000.

[188] *Heterojunction Quantum Dot Solar Cells.* PhD thesis, University of Waterloo.

[189] L. K. Jagadamma, M. Abdelsamie, A. El Labban, E. Aresu, G. O. N. Ndjawa, D. H. Anjum, D. Cha, P. M. Beaujuge, and A. Amassian, “Efficient inverted bulk–heterojunction solar cells from low-temperature processing of amorphous ZnO buffer layers,” *Journal of Materials Chemistry A*, vol. 2, no. 33, pp. 13321–13331, 2014.

[190] K. Kanai, K. Koizumi, S. Ouchi, Y. Tsukamoto, K. Sakanoue, Y. Ouchi, and K. Seki, “Electronic structure of anode interface with molybdenum oxide buffer layer,” *Organic Electronics*, vol. 11, no. 2, pp. 188–194, 2010.

[191] *The Impacts of Solvents, Heat Treatments and Hole Injection Layers on the Electroluminescent Lifetime of Organic Light-Emitting Devices.* PhD thesis, University of Waterloo.

[192] I. Hancox, P. Sullivan, K. Chauhan, N. Beaumont, L. Rochford, R. Hatton, and T. Jones, “The effect of a MoO_x hole-extracting layer on the performance of organic photovoltaic cells based on small molecule planar heterojunctions,” *Organic Electronics*, vol. 11, no. 12, pp. 2019–2025, 2010.

[193] E. Salsberg and H. Aziz, “Degradation of PEDOT:PSS hole injection layers by electrons in organic light emitting devices,” *Organic Electronics*, vol. 69, pp. 313–319, 2019.

[194] V. Shrotriya, G. Li, Y. Yao, C.-W. Chu, and Y. Yang, “Transition metal oxides as the buffer layer for polymer photovoltaic cells,” *Applied Physics Letters*, vol. 88, no. 7, p. 073508, 2006.

[195] C. C. Williams, J. G. Ekerdt, J. M. Jehng, F. D. Hardcastle, A. M. Turek, and I. E. Wachs, “A raman and ultraviolet diffuse reflectance spectroscopic investigation of silica–supported molybdenum oxide,” *The Journal of Physical Chemistry*, vol. 95, no. 22, pp. 8781–8791, 1991.

[196] P. A. Spevack and N. McIntyre, “A raman and XPS investigation of supported molybdenum oxide thin films. 1. Calcination and reduction studies,” *The Journal of Physical Chemistry*, vol. 97, no. 42, pp. 11020–11030, 1993.

[197] M. Dieterle and G. Mestl, “Raman spectroscopy of molybdenum oxides. Part ii. Resonance Raman spectroscopic characterization of the molybdenum oxides Mo_4O_11 and MoO_2,” *Physical Chemistry Chemical Physics*, vol. 4, no. 5, pp. 822–826, 2002.

[198] J. S. Cross and G. L. Schrader, "Low pressure chemical vapor deposition of molybdenum oxides from molybdenum hexacarbonyl and oxygen," *Thin Solid Films*, vol. 259, no. 1, pp. 5–13, 1995.

[199] R. Senthilkumar, G. Anandhababu, T. Mahalingam, and G. Ravi, "Photoelectrochemical study of MoO_3 assorted morphology films formed by thermal evaporation," *Journal of energy chemistry*, vol. 25, no. 5, pp. 798–804, 2016.

[200] Y. V. Plyuto, I. Babich, I. Plyuto, A. Van Langeveld, and J. Moulijn, "XPS studies of MoO_3/Al_2O_3 and MoO_3/SiO_2 systems," *Applied surface science*, vol. 119, no. 1-2, pp. 11–18, 1997.

[201] C. Girotto, E. Voroshazi, D. Cheyns, P. Heremans, and B. P. Rand, "Solution-processed MoO_3 thin films as a hole-injection layer for organic solar cells," *ACS applied materials & interfaces*, vol. 3, no. 9, pp. 3244–3247, 2011.

[202] R. Schlaf, H. Murata, and Z. Kafafi, "Work function measurements on indium tin oxide films," *Journal of Electron Spectroscopy and Related Phenomena*, vol. 120, no. 1-3, pp. 149–154, 2001.

[203] T.-Y. Yun, S.-R. Park, J.-Y. Baek, H.-J. Han, and C.-W. Jeon, "Comparison of aluminum zinc oxide and indium tin oxide for transparent conductive oxide layer in $\mathrm{Cu(In, Ga)Se_2}$ solar cell," *Molecular Crystals and Liquid Crystals*, vol. 586, no. 1, pp. 82–87, 2013.

[204] K. Sugiyama, H. Ishii, Y. Ouchi, and K. Seki, "Dependence of indium–tin–oxide work function on surface cleaning method as studied by ultraviolet and x-ray photoemission spectroscopies," *Journal of Applied Physics*, vol. 87, no. 1, pp. 295–298, 2000.

[205] Y. Park, V. Choong, Y. Gao, B. Hsieh, and C. Tang, "Work function of indium tin oxide transparent conductor measured by photoelectron spectroscopy," *Applied Physics Letters*, vol. 68, no. 19, pp. 2699–2701, 1996.

[206] X. Ding, L. Hung, L. Cheng, Z. Deng, X. Hou, C. Lee, and S. Lee, "Modification of the hole injection barrier in organic light–emitting devices studied by ultraviolet photoelectron spectroscopy," *Applied Physics Letters*, vol. 76, no. 19, pp. 2704–2706, 2000.

[207] W. Haynes, *Electron Work Function of the Elements*, ch. 12. CRC Press, 2013.

[208] K. M. Tsoi, Q. Dai, B. A. Alman, and W. C. Chan, “Are quantum dots toxic? exploring the discrepancy between cell culture and animal studies,” *Accounts of chemical research*, vol. 46, no. 3, pp. 662–671, 2013.

[209] L. Li, E. Auer, M. Liao, X. Fang, T. Zhai, U. K. Gautam, A. Lugstein, Y. Koide, Y. Bando, and D. Golberg, “Deep–ultraviolet solar-blind photoconductivity of individual gallium oxide nanobelts,” *Nanoscale*, vol. 3, no. 3, pp. 1120–1126, 2011.

[210] M. Chen, H. Yu, S. V. Kershaw, H. Xu, S. Gupta, F. Hetsch, A. L. Rogach, and N. Zhao, “Fast, air–stable infrared photodetectors based on spray-deposited aqueous HgTe quantum dots,” *Advanced Functional Materials*, vol. 24, no. 1, pp. 53–59, 2014.

[211] Y. Zhang and H. Aziz, “Very high efficiency phosphorescent organic light–emitting devices by using rough indium tin oxide,” *Applied Physics Letters*, vol. 105, no. 1, p. 102_1, 2014.

[212] A. Hoshino, K. Fujioka, T. Oku, M. Suga, Y. F. Sasaki, T. Ohta, M. Yasuhara, K. Suzuki, and K. Yamamoto, “Physicochemical properties and cellular toxicity of nanocrystal quantum dots depend on their surface modification,” *Nano Letters*, vol. 4, no. 11, pp. 2163–2169, 2004.

[213] A. Shiohara, A. Hoshino, K.-i. Hanaki, K. Suzuki, and K. Yamamoto, “On the cyto–toxicity caused by quantum dots,” *Microbiology and immunology*, vol. 48, no. 9, pp. 669–675, 2004.

[214] H. M. Azzazy, M. M. Mansour, and S. C. Kazmierczak, “Nanodiagnostics: a new frontier for clinical laboratory medicine,” *Clinical chemistry*, vol. 52, no. 7, pp. 1238–1246, 2006.

[215] P. H. Pham, J. Jung, and N. C. Bols, “Using 96–well tissue culture polystyrene plates and a fluorescence plate reader as tools to study the survival and inactivation of viruses on surfaces,” *Cytotechnology*, vol. 63, no. 4, pp. 385–397, 2011.

[216] J. H. Shim, J. H. Jung, M. H. Lee, T. W. Kim, D. I. Son, A. N. Han, and S. W. Kim, “Memory mechanisms of nonvolatile organic bistable devices based on colloidal $CuInS_2/ZnS$ core–shell quantum dot–poly (N-vinylcarbazole) nanocomposites,” *Organic Electronics*, vol. 12, no. 9, pp. 1566–1570, 2011.

[217] D. W. Dockery, C. A. Pope, X. Xu, J. D. Spengler, J. H. Ware, M. E. Fay, B. G. Ferris Jr, and F. E. Speizer, “An association between air pollution and mortality in

six US cities," *New England journal of medicine*, vol. 329, no. 24, pp. 1753–1759, 1993.

[218] C. A. Pope Iii, R. T. Burnett, M. J. Thun, E. E. Calle, D. Krewski, K. Ito, and G. D. Thurston, "Lung cancer, cardiopulmonary mortality, and long-term exposure to fine particulate air pollution," *Jama*, vol. 287, no. 9, pp. 1132–1141, 2002.

[219] L. Clancy, P. Goodman, H. Sinclair, and D. W. Dockery, "Effect of air–pollution control on death rates in Dublin, Ireland: an intervention study," *The lancet*, vol. 360, no. 9341, pp. 1210–1214, 2002.

[220] N. I. for Occupational Safety and Health, "Approaches to safe nanotechnology: An information exchange with NIOSH," 2006.

[221] N. N. Initiative, "Environmental, health, and safety research needs for engineered nanoscale materials; national nanotechnology initiative.," 2006.

[222] U. N. E. Programme, "Global environmental outlook yearbook 2007," 2007.

[223] P. Jackson, K. S. Hougaard, A. M. Z. Boisen, N. R. Jacobsen, K. A. Jensen, P. Møller, G. Brunborg, K. B. Gutzkow, O. Andersen, S. Loft, *et al.*, "Pulmonary exposure to carbon black by inhalation or instillation in pregnant mice: effects on liver DNA strand breaks in dams and offspring," *Nanotoxicology*, vol. 6, no. 5, pp. 486–500, 2012.

[224] O. Safety, H. Administration, *et al.*, "Introduction to nanomaterials and occupational safety and health," *William Marsh Rice University*, vol. 48, 2018.

[225] M. Bottrill and M. Green, "Some aspects of quantum dot toxicity," *Chemical communications*, vol. 47, no. 25, pp. 7039–7050, 2011.

[226] L. Ma-Hock, P. M. Farias, T. Hofmann, A. C. Andrade, J. N. Silva, T. M. Arnaud, W. Wohlleben, V. Strauss, S. Treumann, C. Chaves, *et al.*, "Short term inhalation toxicity of a liquid aerosol of glutaraldehyde-coated $CdS/Cd/(OH)_2$ core shell quantum dots in rats," *Toxicology letters*, vol. 225, no. 1, pp. 20–26, 2014.

[227] J. A. Conti, K. Killpack, G. Gerritzen, L. Huang, M. Mircheva, M. Delmas, B. H. Harthorn, R. P. Appelbaum, and P. A. Holden, "Health and safety practices in the nanomaterials workplace: results from an international survey," 2008.

[228] D. M. Brown, M. R. Wilson, W. MacNee, V. Stone, and K. Donaldson, "Size–dependent proinflammatory effects of ultrafine polystyrene particles: a role for surface area and oxidative stress in the enhanced activity of ultrafines," *Toxicology and applied pharmacology*, vol. 175, no. 3, pp. 191–199, 2001.

[229] R. Duffin, C. Tran, A. Clouter, D. Brown, W. MacNee, V. Stone, and K. Donaldson, "The importance of surface area and specific reactivity in the acute pulmonary inflammatory response to particles," *Annals of Occupational Hygiene*, vol. 46, no. suppl_1, pp. 242–245, 2002.

[230] R. Duffin, L. Tran, D. Brown, V. Stone, and K. Donaldson, "Proinflammogenic effects of low-toxicity and metal nanoparticles in vivo and in vitro: highlighting the role of particle surface area and surface reactivity," *Inhalation toxicology*, vol. 19, no. 10, pp. 849–856, 2007.

[231] G. Oberdörster, E. Oberdörster, and J. Oberdörster, "Nanotoxicology: an emerging discipline evolving from studies of ultrafine particles," *Environmental health perspectives*, vol. 113, no. 7, pp. 823–839, 2005.

[232] M. J. Clift, J. Varet, S. M. Hankin, B. Brownlee, A. M. Davidson, C. Brandenberger, B. Rothen-Rutishauser, D. M. Brown, and V. Stone, "Quantum dot cytotoxicity in vitro: an investigation into the cytotoxic effects of a series of different surface chemistries and their core/shell materials," *Nanotoxicology*, vol. 5, no. 4, pp. 664–674, 2011.

[233] U. Pison, T. Welte, M. Giersig, and D. A. Groneberg, "Nanomedicine for respiratory diseases," *European journal of pharmacology*, vol. 533, no. 1-3, pp. 341–350, 2006.

[234] M. Clift, D. Brown, B. Rothen-Ruthishauser, R. Duffin, K. Donaldson, L. Proudfoot, K. Guy, and V. Stone, "Comparing a panel of commercially available quantum dots and polystyrene nanoparticles with differing surface characteristics; an analysis of their uptake and toxicity in a murine macrophage cell line," *Toxicol Appl Pharm*, vol. 232, pp. 418–427, 2008.

[235] J. Lovrić, S. J. Cho, F. M. Winnik, and D. Maysinger, "Unmodified cadmium telluride quantum dots induce reactive oxygen species formation leading to multiple organelle damage and cell death," *Chemistry & biology*, vol. 12, no. 11, pp. 1227–1234, 2005.

[236] Y. Kim, R. C. Johnson, and J. T. Hupp, "Gold nanoparticle-based sensing of spectroscopically silent heavy metal ions," *Nano Letters*, vol. 1, no. 4, pp. 165–167, 2001.

[237] J. Newman, J. Roberts, and G. Blanchard, "Optical organophosphate sensor based upon gold nanoparticle functionalized fumed silica gel," *Analytical chemistry*, vol. 79, no. 9, pp. 3448–3454, 2007.

[238] M. Lü, J. Li, X. Yang, C. Zhang, J. Yang, H. Hu, and X. Wang, "Applications of graphene-based materials in environmental protection and detection," *Chinese Science Bulletin*, vol. 58, no. 22, pp. 2698–2710, 2013.

[239] X. Zhang, Y. Lai, M. Ge, Y. Zheng, K.-Q. Zhang, and Z. Lin, "Correction: Fibrous and flexible supercapacitors comprising hierarchical nanostructures with carbon spheres and graphene oxide nanosheets," *Journal of Materials Chemistry A*, vol. 3, no. 25, pp. 13577–13577, 2015.

[240] I. V. Lightcap and P. V. Kamat, "Fortification of CdSe quantum dots with graphene oxide. excited state interactions and light energy conversion," *Journal of the American Chemical Society*, vol. 134, no. 16, pp. 7109–7116, 2012.

[241] M. Li, X. Zhou, S. Guo, and N. Wu, "Detection of lead (II) with a turn-on fluorescent biosensor based on energy transfer from Cdse/ZnS quantum dots to graphene oxide," *Biosensors and Bioelectronics*, vol. 43, pp. 69–74, 2013.

[242] H. Zhu, W. Zhang, K. Zhang, and S. Wang, "Dual-emission of a fluorescent graphene oxide–quantum dot nanohybrid for sensitive and selective visual sensor applications based on ratiometric fluorescence," *Nanotechnology*, vol. 23, no. 31, p. 315502, 2012.

[243] M. Li *et al.*, "Detection of mercury(II) by quantum dot/DNA/gold nanoparticle ensemble based nanosensor via nanometal surface energy transfer," *Analytical Chemistry*, vol. 83, no. 18, pp. 7061–7065, 2011.

[244] M. Li, S. K. Cushing, Q. Wang, X. Shi, L. A. Hornak, Z. Hong, and N. Wu, "Size-dependent energy transfer between CdSe/ZnS quantum dots and gold nanoparticles," *The Journal of Physical Chemistry Letters*, vol. 2, no. 17, pp. 2125–2129, 2011.

[245] R. Debnath, O. Bakr, and E. H. Sargent, "Solution-processed colloidal quantum dot photovoltaics: A perspective," *Energy & Environmental Science*, vol. 4, no. 12, pp. 4870–4881, 2011.

[246] J. Van de Lagemaat and A. Frank, "Nonthermalized electron transport in dye-sensitized nanocrystalline TiO_2 films: transient photocurrent and random-walk modeling studies," *The Journal of Physical Chemistry B*, vol. 105, no. 45, pp. 11194–11205, 2001.

[247] L. De Trizio, M. Prato, A. Genovese, A. Casu, M. Povia, R. Simonutti, M. J. Alcocer, C. DAndrea, F. Tassone, and L. Manna, "Strongly fluorescent quaternary Cu–In–Zn–S nanocrystals prepared from $\mathrm{Cu_{1-x}InS_2}$ nanocrystals by partial cation exchange," *Chemistry of Materials*, vol. 24, no. 12, pp. 2400–2406, 2012.

[248] S. Kurtz, J. Wohlgemuth, M. Kempe, N. Bosco, P. Hacke, D. Jordan, D. C. Miller, T. J. Silverman, N. Phillips, T. Earnest, *et al.*, "Photovoltaic module qualification plus testing," tech. rep., National Renewable Energy Lab.(NREL), Golden, CO (United States), 2013.

[249] B. Sadeghimakki and S. Sivoththaman, "Toxicity study needs for quantum dots and nanoparticles in PV fabrication," *MRS Online Proceedings Library Archive*, vol. 1638, 2014.

[250] B. Fu, C. Deng, and L. Yang, "Efficiency enhancement of solid-state $\mathrm{CuInS_2}$ quantum dot-sensitized solar cells by improving the charge recombination," *Nanoscale research letters*, vol. 14, no. 1, p. 198, 2019.

[251] G. H. Carey, I. J. Kramer, P. Kanjanaboos, G. Moreno-Bautista, O. Voznyy, L. Rollny, J. A. Tang, S. Hoogland, and E. H. Sargent, "Electronically active impurities in colloidal quantum dot solids," *ACS nano*, vol. 8, no. 11, pp. 11763–11769, 2014.

[252] Ossila, "Dip coating theory: Film thickness," 2020.

[253] J. Gao, C. L. Perkins, J. M. Luther, M. C. Hanna, H.-Y. Chen, O. E. Semonin, A. J. Nozik, R. J. Ellingson, and M. C. Beard, "N-type transition metal oxide as a hole extraction layer in PbS quantum dot solar cells," *Nano letters*, vol. 11, no. 8, pp. 3263–3266, 2011.

APPENDICES

Appendix A

Masks for Small-Area Device

The following images show the mask designs utilized in fabrication of the ZnO/CIS QD heterojunction device. For clarity, all masks are displayed overlaid onto the substrate and ITO mask. The area of the ITO defines the ten separate devices patterned onto one standard 2.2 × 2.2 cm^2 glass substrate.

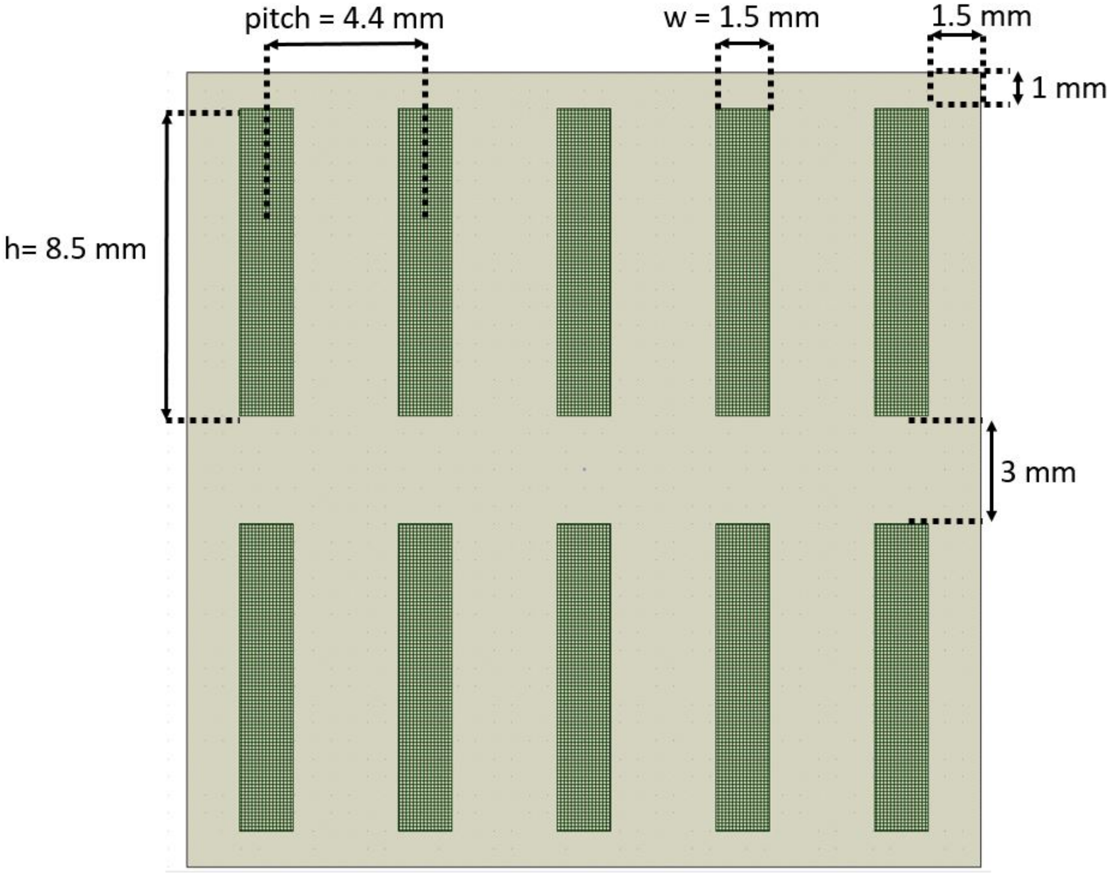

Figure A.1: Photomask design for ITO layer. One standard 2.2 × 2.2 cm^2 (22 × 22 mm^2) substrate is divided into ten discrete devices. Each ITO strip is 8.5 mm in height and 1.5 mm in width, with a 4.4 mm pitch. There are two rows of ITO strips, separated by a vertical spacing of 3 mm.

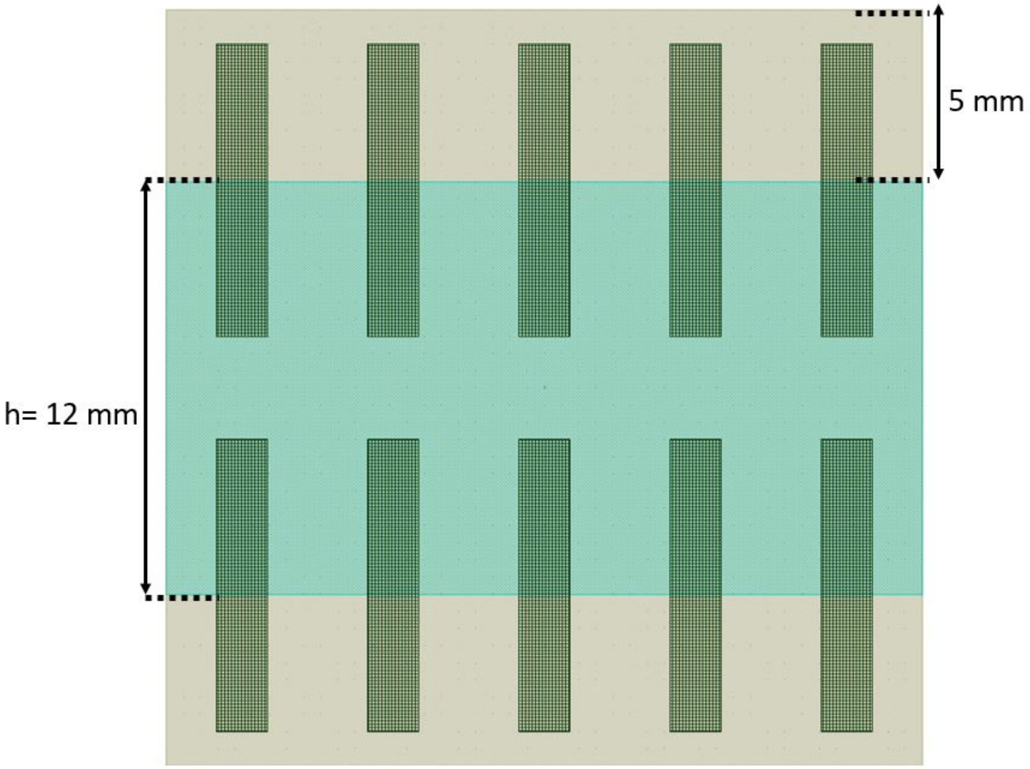

Figure A.2: Photomask design for ZnO layer, with respect to ITO and substrate. The ZnO design is centered across the substrate, placed at a distance of 5 mm from each vertical edge of the substrate. The ZnO design measures 12 mm in height and 22 mm in width.

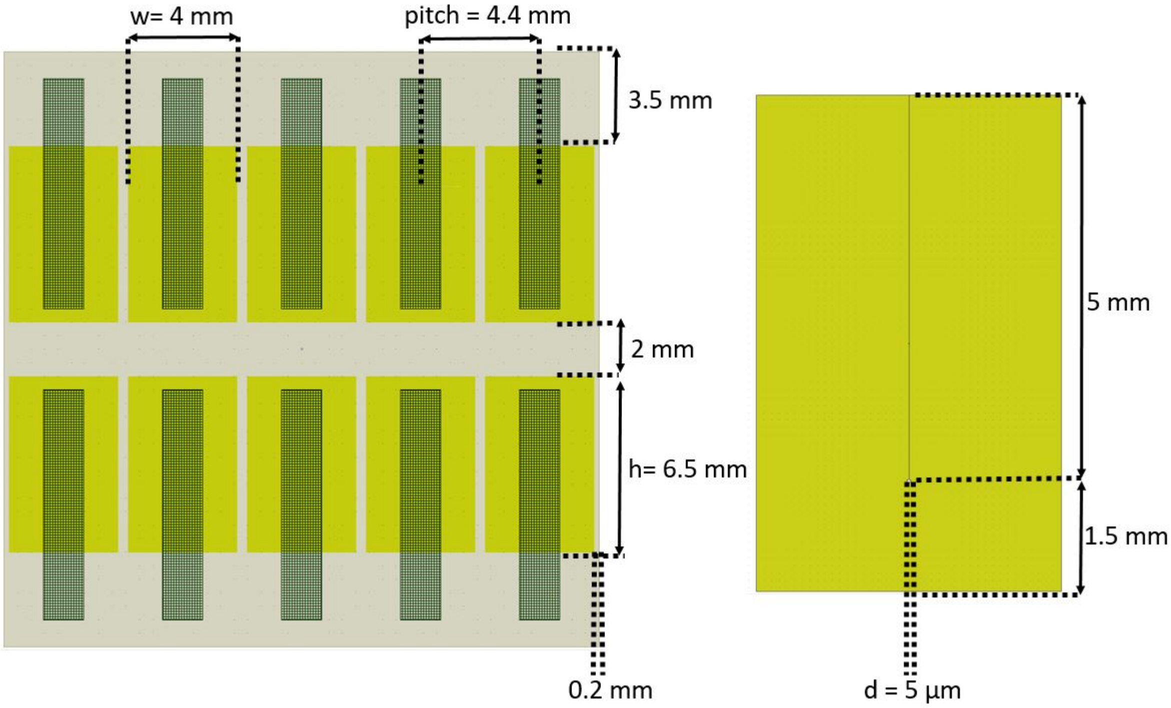

Figure A.3: Photomask design for SU-8 layer, with respect to ITO and substrate. Each SU-8 region is 6.5 mm in height and 4 mm in width. The diagram on the right shows the SU-8 pattern of a single device, which includes a 5 μm-diameter device well located 5 mm from the top, and 1.5 mm from the bottom of the SU-8 region. The size of the device well in this diagram has been increased for visibility.

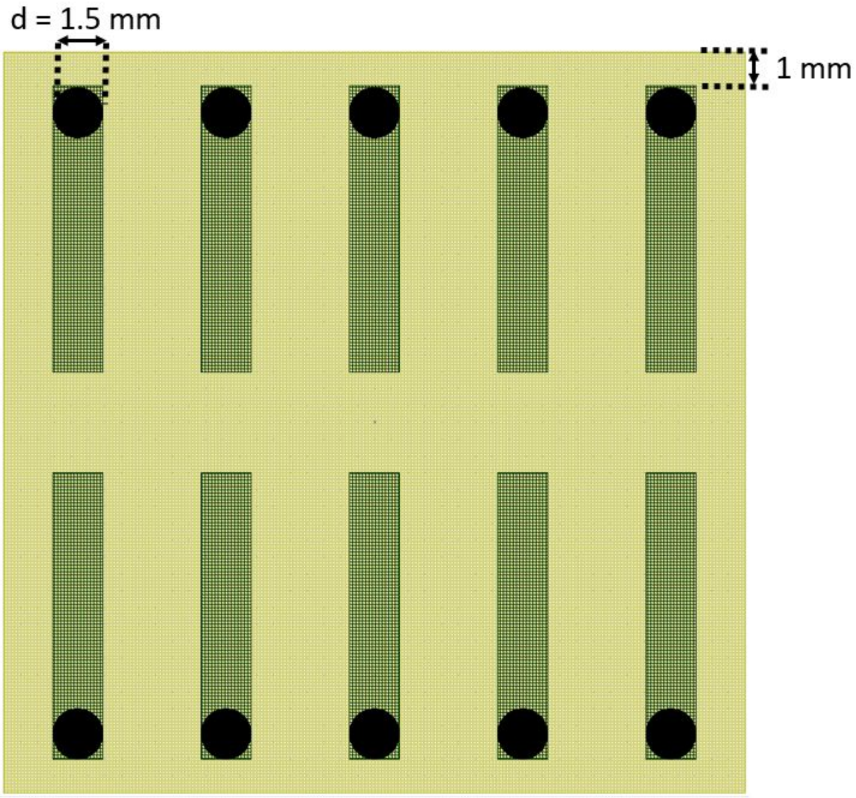

Figure A.4: Photomask design for the bottom contacts, with respect to ITO and substrate. Each contact is 1.5 mm in diameter, and placed on top of the ITO strip, 1 mm from the top and bottom edges of the substrate.

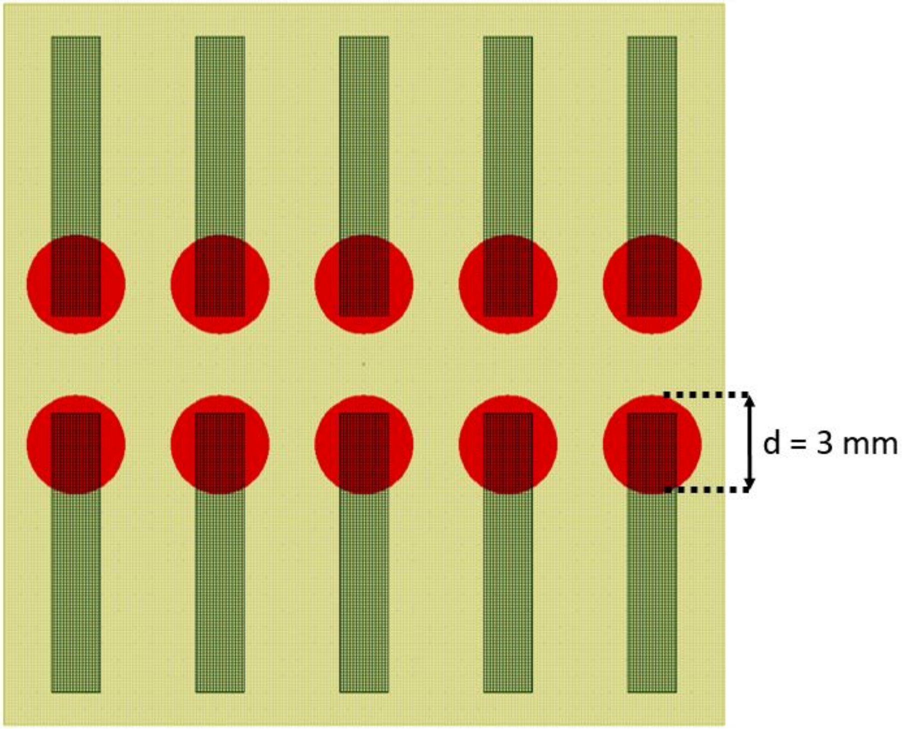

Figure A.5: Photomask design for the QDs, with respect to ITO and substrate. Each QD area is up to 3 mm in diameter, as defined by the inner diameter of the O-rings used in the QD injection system. The centers of the QD areas are aligned with the centers of the 5 μm device wells.

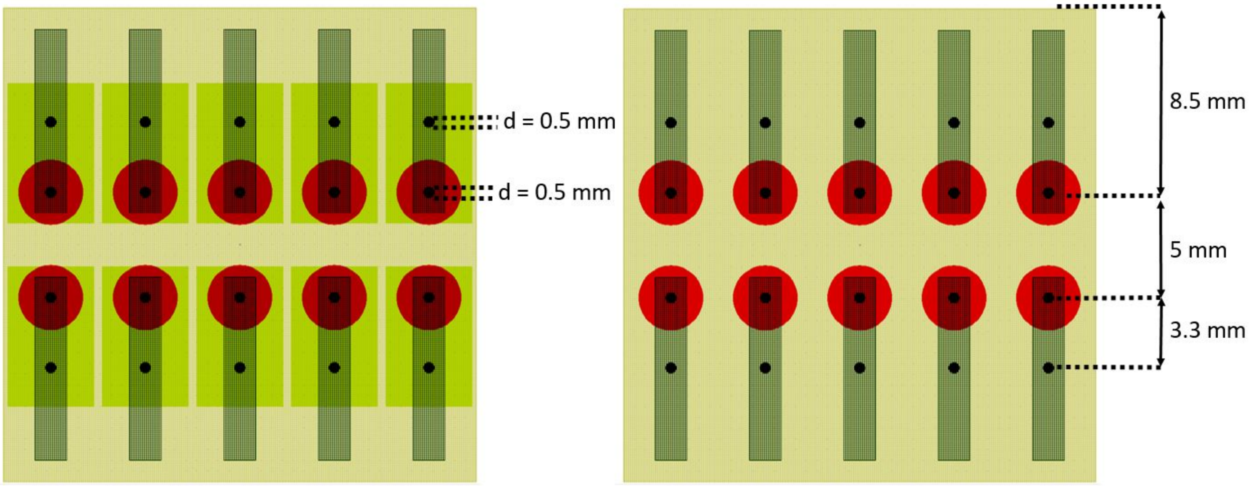

Figure A.6: Photomask design for the top contacts, with respect to QDs, SU-8, ITO, and substrate. Each QD area is up to 3 mm in diameter, as defined by the O-rings used in the QD injection system. The top contacts are 0.5 mm in diameter. The centers of the device top contacts coincide with the centers of the 5 μm device wells. A second top contact is placed onto each device, onto the SU-8, for SU-8 verification.

Appendix B

Quantum Dot Injection System

The following images show the design and deployment of the QD injection utilized in fabrication of the ZnO/CIS QD heterojunction device. This mask is used to place QDs onto the design of the devices on the 2.2×2.2 cm^2 substrate depicted in Appendix A.

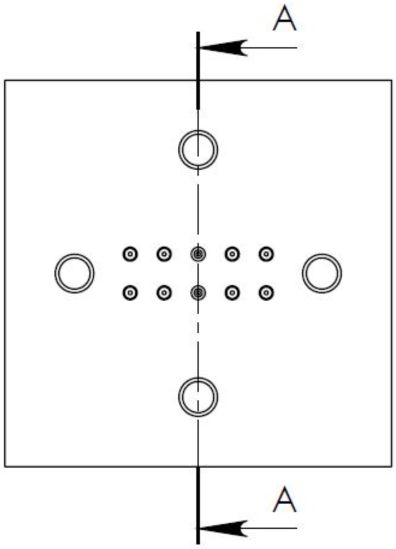

Figure B.1: Top view of the computer aided design (CAD) diagram for the QD injection shadow mask.

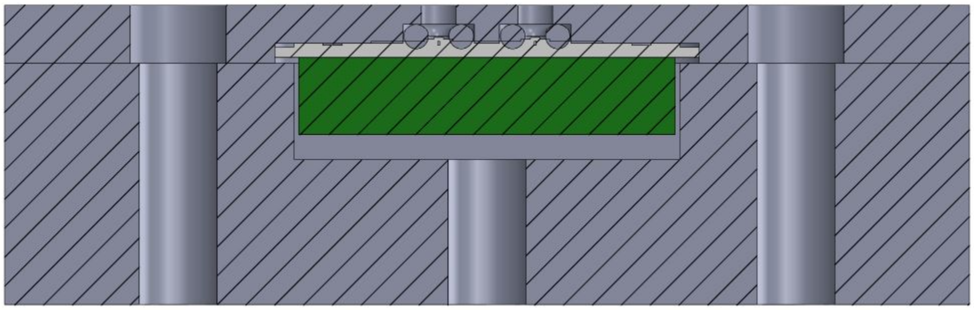

Figure B.2: Cross-sectional view of the CAD diagram for the QD injection shadow mask.

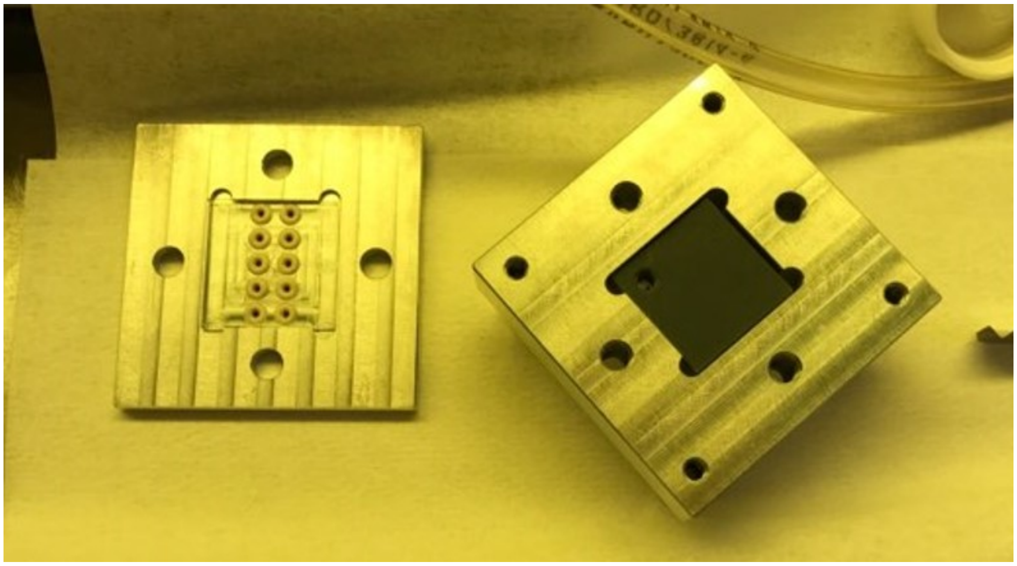

Figure B.3: Photograph of shadow mask for CIS QD injection system.